"Photogrammetric Measurement of the Optical Performance of Parabolic Trough Solar Fields"

"Photogrammetrische Messung des optischen Wirkungsgrades von Parabolrinnenkraftwerken"

Von der Fakultät für Maschinenwesen der Rheinisch- Westfälischen Technischen Hochschule Aachen zur Erlangung des akademischen Grades eines Doktors der Ingenieurwissenschaften genehmigte Dissertation

vorgelegt von

Philipp Christoph Prahl

Berichter: Universitätsprofessor Dr.-Ing. Robert Pitz-Paal
Universitätsprofessor Dr. sc. techn. habil. Hans-Gerd Maas

Tag der mündlichen Prüfung: 2. April 2019

KURZFASSUNG

Erneuerbare Energien sind durch Abweichungen zwischen Bedarf und Angebot gekennzeichnet. CSP (konzentrierende Solarthermie) bietet neben der effizienten und potentiell konkurrenzfähigen Nutzung des Sonnenlichts durch den Einsatz von thermischen Energiespeichern einen Mehrwert, um diesen Schwankungen gerecht zu werden.

Zur Konzentration und Umwandlung des Sonnenlichts in thermische Energie stehen unterschiedliche Technologien zur Verfügung, wobei Parabolrinnen z.Zt. den größten Marktanteil haben. Der optische Wirkungsgrad des Parabolrinnen-Solarfeldes hat einen signifikanten Einfluss auf die Wirtschaftlichkeit des Kraftwerks. Messverfahren zur Bestimmung der geometrischen Genauigkeit von Konzentrator-Systemen sind daher wichtiger Teil bei Forschung & Entwicklung, Aufbau, Inbetriebnahme und laufendem Betrieb.

Diese Arbeit beschreibt die Entwicklung der luftgestützten QFly Messtechnik für die Qualifizierung von Parabolrinnen-Solarfeldern. Gegenüber dem Stand der Technik wurde die stationäre Kamera durch eine Flugdrohne (UAV) mit entsprechender Nutzlast ersetzt. Dies ermöglicht eine vollautomatische Vermessung des gesamten Kraftwerks. Das QFly Verfahren verfolgt zwei Ansätze. Der $\text{QFly}_{\text{HighRes}}$ Ansatz ermöglicht die präzise und differenzierte Vermessung der Konzentrator-Geometrie bei einer räumlichen Auflösung von $6mm/Pixel$ und einer Flughöhe von 30 Metern. Das Messvolumen beträgt ca. 2 Loops pro Tag und ist damit geeignet für die Charakterisierung von Prototypen und zur stichprobenartigen Charakterisierung des Solarfeld. Der $\text{QFly}_{\text{Survey}}$ Ansatz dient dem schnellen Screening ganzer Solarfelder. Bei einer Flughöhe von 120 bis 250 Metern werden in wenigen Stunden die effektive Konzentrator-Form bei reduzierter räumlicher Auflösung und Informationen zur Nachführung gewonnen. Im Rahmen dieser Arbeit werden beide Verfahren beschrieben und einer Unsicherheits-Analyse unterzogen sowie mit unabhängigen Messmethoden validiert.

Letztendlich dienen beide Verfahren dazu, mithilfe der Geometriedaten Bereiche und Phänomene zu identifizieren, welche sich negativ auf den optischen Wirkungsgrad auswirken. Numerische Strahl-Verfolgung ermöglicht die energetische und ökonomische Bewertung potentieller Optimierungsmaßnahmen.

Die QFly Messtechnik kann als ausgereift angesehen werden. Weiterer Handlungsbedarf und Einsatzmöglichkeiten ergeben sich bei der Schnittstelle mit dem Ertragsanalyse, der luftgestützten thermographischen Bestimmung von Wärmeverlusten und der Erweiterung der Messtechnik auf Turmkraftwerke.

ABSTRACT

Renewable energies are characterized by deviations between demand and supply. Concentrating solar power (CSP) offers not only the efficient and potentially competitive use of sunlight, but also the use of thermal energy storage, in order to cope with these fluctuations.

Various technologies are available for the concentration and conversion of sunlight into thermal energy, with parabolic trough collector (PTC) having the largest market share at the time. The optical efficiency of the solar field has a significant influence on the economic viability of the power plant. Measurement methods for determining the geometric accuracy of concentrator systems are therefore an important part of research & development, construction, commissioning and running operation.

This thesis describes the development of the airborne QFly measurement technique for the qualification of PTC solar fields. Compared to the state of the art, the stationary camera has been replaced by a unmanned aerial vehicle (UAV) with corresponding payload. This allows a fully automatic measurement of the entire power plant. The QFly procedure has two approaches. The $\text{QFly}_{\text{HighRes}}$ approach allows the precise and differentiated measurement of concentrator geometry at a spatial resolution of $6mm/pixel$ and a flight altitude of 30 meters. The measurement volume is approx. 2 loops per day and is therefore suitable for the characterization of prototypes and random check of the solar field. The $\text{QFly}_{\text{Survey}}$ method is used for the rapid screening of entire power plants. At a flight altitude of 120 to 250 meters, tracking information and the effective concentrator form can be obtained at a reduced spatial resolution. Within the scope of this work, both methods are described and subjected to an uncertainty analysis and validated with independent benchmark measurement methods.

In the end, the process is used to identify defects with the aid of geometric measured data. Numerical ray-tracing (RT) enables an energetic and economic evaluation of potential optimization measures.

The airborne geometry measurement in parabolic trough power stations can thus be regarded as mature. Further need for action and possible applications arise with the interface with the yield analysis, the airborne thermographic determination of heat losses and the extension of the measuring technology on solar tower power plants.

PUBLICATIONS

Some ideas and figures have appeared previously in the following publications, in chronological order:

- Prahl, C., Stanicki, B., Hilgert, C., Ulmer, S., and Röger, M. (2011). Airborne shape measurement of parabolic trough collector fields. In *Proceedings of the 17th SolarPACES Conference, 20. - 23. September 2011, Granada, Spain*
- Stanicki, B. (2011). Validierung eines Messystems zur Vermessung von Parabolrinnenkollektoren aus der Luft. Master's thesis, Hochschule Ravensburg Weingarten. Contact/Request Dokument: christoph.prahl@dlr.de
- Natho, R. (2012). Thermal evaluation of receivers in parabolic trough collectors using airborne infrared imaging. Master's thesis, Ilmenau University of Technology
- Prahl, C., Stanicki, B., Hilgert, C., Ulmer, S., and Röger, M. (2013a). Airborne shape measurement of parabolic trough collector fields. *Solar Energy*, 91(0):68–78
- Hertel, J. (2013). Study and implementation of an object tracing algorithm for the deflectrometric shape qualification of parabolic trough collectors. Master's thesis, Technische Universität München
- Prahl, C., Ulmer, S., Röger, M., and Pottler, K. (2013b). Verfahren zur Vermessung eines solarthermischen Konzentrators. DE Patent App. DE201110080969
- Prahl, C., Hilgert, C., and Röger, M. (2016a). Luftgestützte optische Qualifizierung von Parabolrinnenkollektoren. In *Kölner Sonnenkolloquium*. Retrieved 2017.05.03, from: `http://elib.dlr.de/108851/`
- Prahl, C., Röger, M., and Hilgert, C. (2016b). Air-borne shape measurement of parabolic trough collector fields. In *Proceedings of the 22nd SolarPACES Conference, 11 - 14 October 2016, Abu Dhabi, UAE*. `http://doi.org/10.1063/1.4984338`
- Prahl, C., Röger, M., Stanicki, B., and Hilgert, C. (2017). Absorber tube displacement in parabolic trough collectors - a review and presentation of an airborne measurement approach. *Solar Energy*, 157:692 – 706. `https://doi.org/10.1016/j.solener.2017.05.023`

CONTENTS

LIST OF FIGURES

LIST OF TABLES

NOMENCLATURE

ABBREVIATIONS

AS3	Andasol III: 50 *MW* PTC plant near Guadix/Spain (SolarMillennium, 2009)
ASCII	American standard code for information interchange
CSP	concentrating solar power
CCS	carbon capture and storage
CMOS	active-pixel sensor for digital imaging produced using complementary metal–oxide–semiconductor technology
CPV	concentrated photovoltaics
CSR	circumsolar ratio (Buie and Monger, 2004)
CTM	camera target method (Lüpfert et al., 2004b)
DPH	dynamic position hold: Preferred flight mode of the md4-1000 UAV when GNSS is available
DGPS	differential global positioning system
DLR	Deutsches Zentrum für Luft- und Raumfahrt e.V.
DNI	direct normal irradiance
DSG	direct steam generation
DO	distant observer (Wood, 1981)
EMM	edge-mismatch: Scalar parameter to compare the result image segmentation for the detection of absorber tube reflection (Hertel, 2013)
ENEA	Italian national agency for new technologies, energy and sustainable economic development
EOR	exterior orientation: Camera positions obtained by photogrammetric evaluation (Luhmann et al., 2006b)
ET	EuroTrough Collector (Geyer et al., 2002)
FEP	front end plate: End face of PTC steel structure orientated towards the drive pylon

FEM	finite element method
FP	false positive: Binary classifier of a confusion matrix
fps	frames per second: Describes the image acquisition rate of a digital camera.
FV	fitness value: Scalar value describing the matching quality between to data-sets
GHG	greenhouse gas
GNSS	global navigation satellite system
GREENIUS	green energy system analysis tool (Dersch et al., 2010)
GSD	ground sample distance (Leachtenauer and Driggers, 2001)
GUI	graphical user interface
GUM	guide to the expression of uncertainty in measurement
GBRP	glass bracket retaining point: Connection between SCE steel structure and mirror panel
HCE	receiver tube (aka.: Heat collecting element)
HTF	heat transfer fluid (Bellos et al., 2017)
IOR	interior orientation: Set of parameters describing the internal geometry and lens distortion of the camera (Luhmann et al., 2006b)
KONTAS	concentrator test bench at PSA, Almeria, Spain (Heller et al., 2011)
LCOE	levelized cost of electricity
LFR	linear fresnel reflector
LiPo	lithium-ion polymer battery
LOC	local controller: Unit to control a single SCA used by Flagsol
LOS	line-of-sight
MATLAB	matrix laboratory: Proprietary programming language developed by MathWorks
MIRVAL	Monte Carlo ray-tracing program developed by SANDIA

MP	mega-pixel: Number of image sensor elements of digital cameras
NREL	national renewable energy laboratory
PDC	parabolic dish concentrator
PG	close range photogrammetry
POI	point of interest
PSA	Plataforma Solar de Almería, Spain
PTC	parabolic trough collector
PV	photovoltaics
PPV	positive predictive value: Proportions of positive results in diagnostic tests (Fawcett, 2006)
PF	penalty factor: Term used in constrained optimization problems
QC	quality control
QDec	deflectometric measurement system for quality control of the shape of solar reflector panels
QFly	airborne qualification of CSP Plants
$\mathbf{QFly_{HighRes}}$	QFly high resolution data acquisition and evaluation mode
$\mathbf{QFly_{Survey}}$	QFly high altitude data acquisition and evaluation mode
$\mathbf{Survey^{Online}}$	solar field status : Solar field in operation $\lvert\phi_\perp\rvert < 0.5^\circ \vee \mathrm{DNI} > 300W/m^2$
$\mathbf{Survey^{Offline}}$	solar field status : Solar field in standby $\theta = 90^\circ \wedge \left(\lvert\phi_\perp\rvert > 10^\circ \vee \mathrm{DNI} = 0W/m^2\right)$
QFoto	in-line quality control system for support structures of CSP collectors
RE	renewable energy
REP	rear end plate: End face of PTC steel structure orientated towards the SCE end
REPA	rotation and expansion performing assembly: Flexible tube connector or ball joint to link HCE with solar field header
RGB	additive color model for digital images using red, green, and blue

ROI region of interest

RP3 PTC mirror quasi standard with a focal length (f) of 1710 mm and a aperture width (D) of 5774 mm

RT ray-tracing

RTK real time kinematic satellite navigation

SANDIA Sandia national laboratories

SCA solar collector assembly: Unit of several SCEs mechanically connected to one drive pylon

SCE solar collector element: Smallest unit of a PTC supported by two pylons

SEGS solar energy generating systems is the world's second largest CSP facility with an installed capacity of 354 *MW*

SPT solar power tower

SPRAY solar power ray-tracing tool (Buck, 2010)

STE solar thermal electricity (same as CSP)

TARMES trough absorber reflection measurement system (Ulmer et al., 2006)

TES thermal energy storage

TOP theoretical overlay photographic approach (Diver and Moss, 2007)

TraCS tracking cleanliness sensor (Wolfertstetter et al., 2012, 2014)

UAV unmanned aerial vehicle

TP true positive: Used in confirmatory data analysis

VSHOT video scanning hartmann optical tester (Wendelin et al., 2006)

VISfield visual inspection system field developed by ENEA (Montecchi et al., 2010)

WP waypoint of autonomous UAV flight route

ROMAN MATH SYMBOLS AND UNITS

CMS	center of mass
CMS_{XZ}	deviation of the SCEs CMS from the axis of rotation
C	PTC concentration ratio using the definition $C = D/(\pi \cdot d)$ (Bendt et al., 1979, p. xiii)
ci	confidence interval of the parameter $\phi_{\perp}$ obtained by the fit of the Gaussian distibution
D	aperture width of a PTC
d	absorber tube diameter
dZ	height deviations of the mirror from the ideal parabola
f	focal length
FD_X	focus deviation in curvature direction
g	gravitational acceleration: $9.81 m/s^2$
k_{SCE}	spring constant describing the torsion stiffness of one SCE
k_{HCE}	spring constant describing the lateral torsion stiffness of the HCE support pivot point at the parabola vertex
L'	active receiver length: Fraction of the HCE which absorbs incoming radiation This is typically only 97% of the total receiver length due to the bellow protections (see Figure 1.1)
MW	megawatt
M_{Abs}	weight of a single HCE filled with HTF
Map^{Sim}	simulated patterns of absorber tube reflections
Map^{Meas}	measured patterns of absorber tube reflections
$\overrightarrow{M_{fr}}$	torque caused by bearing friction
$mrad$	milliradian
$\overrightarrow{N}$	mirror surface normal vector
RMS	root mean square
RMS_{SDX}	RMS value of slope deviation in curvature direction

RMS_{SDXeff}	RMS value of SD_{Xeff}
SD_X	slope deviation in curvature direction
SD_{Xeff}	effective slope deviation in curvature direction: Combination of SD_X, ΔX_{Abs}, ΔZ_{Abs}, and $\phi_\perp$ (see Section 2.2.1)
SD_Y	slope deviation in longitudinal direction
T_{HTF}	heat transfer fluid temperature
$T_{HTF_{nom}}$	nominal operation temperature of a specific SCA
x	global PTC solar field coordinate axis in east-west direction
X_{Reflex}	position of the reflection of the absorber tube edge on the mirror surface in curvature direction
X_{Ortho}	positioning of the orthoimage along the curvature direction
X	local coordinate axis of the PTC perpendicular to Z and Y
Y	local coordinate axis of the PTC representing the parabola vertex
Z	local coordinate axis of the PTC representing the optical axis
#	image index of $\text{QFly}_{\text{Survey}}$ data

GREEK MATH SYMBOLS AND UNITS

α_{Rec}	absorptance of absorber tube
γ	intercept factor: Ratio of solar irradiation hitting the receiver versus solar irradiation available on the aperture, disregarding other optical parameters like reflectivity (Bendt et al., 1979).
$\gamma'_{\phi_{\|\|}}$	effective intercept factor including the influence of the incidence angle ($\phi_{\|\|}$), blocking and shading and thereby the active receiver length (L')
$\gamma'_{\phi_{\|\|}=0}$	effective intercept factor at $\phi_{\|\|} = 0$
$\delta Z_{Abs}(\Delta T)$	relative absorber tube displacement along the optical axis caused by thermal expansion of the absorber tube
ΔX_{Abs}	absorber tube displacement in lateral direction
ΔZ_{Abs}	absorber tube displacement along the optical axis
η_{coll}	solar collector efficiency
η_{opt}	optical efficiency
θ	tracking angle of the parabolic trough collector: 90° corresponds to zenith and 0° corresponds to east.
$\kappa(\phi_{\|\|})$	incidence angle modifier: Ratio of optical efficiency at varying angles of incidence and peak optical efficiency
μ_s	static friction coefficient
μ_k	kinetic friction coefficient
ρ_{Ref}	specular mirror reflectance
Σ_0	*RMS* value of the residuals between detected and projected image coordinates
σ_{SDX}	uncertainty of slope deviation in curvature direction
$\sigma_{SDX_{Eff}}$	uncertainty of effective slope deviation in curvature direction
$\sigma_{X/Z}$	uncertainty of absorber tube position
σ_{X_C}	uncertainty of camera position in X direction
$\sigma_{\overline{X_C}}$	reduced uncertainty of camera position in X direction (Equation 5.18)

$\sigma_{\phi_\perp}$	uncertainty of tracking deviation $\phi_\perp$
$\sigma_{\phi_{\perp eff}}$	uncertainty of *effective* tracking deviation $\phi_{\perp eff}$
τ_{Glass}	transmitance of the glass envelope tube
τ_{Drive}	torque load at the drive pylon required to move the PTC
$\phi_{\|\|}$	incidence angle
ϕ_{Cam}	actual view angle between the optical axis of the SCE and camera position
ϕ'_{Cam}	assumed view angle between the optical axis of the SCE and camera position
$\overrightarrow{\phi'_{shift}}$	vector of discrete shift values to shift Map^{Meas} in vertical direction
$\overrightarrow{\phi''_{shift}}$	vector of discrete shift values to shift Map^{Sim} in horizontal direction
$\phi_\perp$	tracking deviation: also called misalingement angle in (Bendt et al., 1979).
$\phi_{\perp eff}$	effective tracking deviation: Airborne measurement of $\phi_\perp$ returns an *effective* tracking deviation, which also includes the effect of ΔX_{Abs}
χ	cleanliness factor: Ratio of reflectivity of the soiled and the clean mirror

1

INTRODUCTION

Climate change is related to the use of fossil energy carriers like coal, oil, and gas (Rockström, 2014; Stocker, 2013). In addition, relying on fossil energy results in environmental pollution and resource allocation conflicts, with increasing tendency and such gloomy prospects for future generations. There are approaches like carbon capture and storage (CCS) (Haszeldine, 2009) or climate engineering (Keith, 2013) aimed at avoiding or at least reducing the effects of greenhouse gas emission and climate change. However, only the consequent implementation of renewable energy (RE)

> ... may contribute to social and economic development, a secure energy supply, and reducing negative impacts on the environment and health (Edenhofer et al., 2011)...

Except for geothermal energy (Dickson and Fanelli, 2013), biomass (Bhattacharya, 2017), and hydroelectricity (Berga, 2016), all RE carriers are subject to natural fluctuation on different time scales. To a certain degree, some fluctuations match the electricity demand load curve, but in general the large penetration of RE in the electric grid requires a new way of load management including different means of energy storage (Denholm and Mehos, 2014).

The expression *residual load* (Denholm and Hand, 2011) is used to describe the difference between load and fluctuating RE- and non-RE electricity generation to be met by the utility. This is where concentrating solar power (CSP)[1] shows an added value compared to photovoltaics (PV), which has a lower levelized cost of electricity (LCOE) (Kost et al., 2013; Hernández-Moro and Martínez-Duart, 2013). CSP offers the option for relatively cheap thermal energy storage (TES) and makes solar energy dispatchable to periods without sufficient solar radiation.

The terms CSP or STE cover all methods (Lovegrove and Stein, 2012) where solar radiation is concentrated by lens or mirror arrays before harnessing the (thermal) energy of the sun light either by conversion to electricity with a thermodynamic cycle or concentrated photovoltaics (CPV), or by using the thermal energy directly as process heat and to drive chemical reactions. Among the different systems[2] which are commercially available (Irena, 2013), the parabolic trough collector (PTC) (see Figure 1.1) is considered the most mature technology with 4.3 *GW* installed worldwide, which corresponds to a share

1 also known as solar thermal electricity (STE)

2 parabolic trough collector (PTC), linear fresnel reflector (LFR), solar power tower (SPT), and parabolic dish concentrator (PDC)

of 83% of the global CSP installed capacity including all technologies of 5.1 *GW* (CSP-Today, 2017).

Current developments in PTC technology pursue cost reduction, among others, by means of scaling effects, larger aperture areas (Riffelmann et al., 2011), and heat transfer fluid s (HTFs) with higher operation temperatures and/or lower costs like direct steam generation (DSG) (Pitz-Paal et al., 2007), silicone oil (Jung et al., 2015), and molten salt (Ruegamer et al., 2014). Despite these developments, there are some common parameters characterizing nominal performance and collector geometry of "benchmark" PTC power plants, which have been erected so far (see Table 1.1).

Parameter	Value	Unit	Comment / Source
Power plant size	1.340 *x* 1.535	$[km^2]$	
Total aperture area	497.040	$[m^2]$	(Dinter and Gonzalez, 2014)
nominal electric power	49.9	$[MW_{el}]$	
# Loops	152		
Loop length	600	$[m]$	
# SCAs per Loop	4		
SCA length	150	$[m]$	
# SCEs per SCA	12		
SCE length	12	$[m]$	
Mirror geometry	RP3		
HCE length	4.060	$[m]$	(Schott, 2015a) at $20^{\circ}C$
Concentration ratio C	26		(Bendt et al., 1979, p. xiii)
Peak solar field efficiency	70%		(SolarMillennium, 2009)

Table 1.1: Properties of the 50 MW PTC Andasol III power plant with 7.5 h TES. About 50 PTC plants of similar size and nominal output are operational worldwide (CSP-Today, 2017). Most of these plants utilize the PTC mirror quasi standard (RP3) mirror geometry. The smallest concentrator unit is the solar collector element (SCE) supported by two pylons. A solar collector assembly (SCA) denotes all SCEs connected to one drive pylon. A serial connection of SCAs makes up a loop, which connect the cold and hot header pipe.

An overview on the applications and technology of parabolic trough collectors (PTCs) can be found in Price et al. (2002) and Fernandez-Garcia et al. (2010). PTCs are high precision and large scale optical

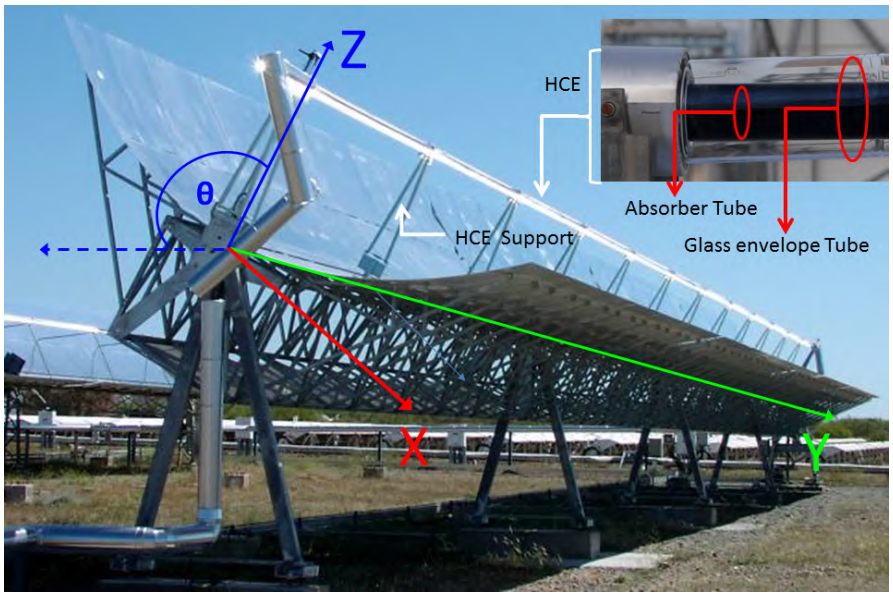

Figure 1.1: EuroTrough (ET) solar collector assembly (SCA) at the Plataforma Solar de Almería (PSA). The coordinate system convention is as follows: The tracking angle (θ) denotes the angle between the Z-axis and the horizontal global PTC solar field coordinate axis in east-west direction (x). The Y-axis denotes the vertex of the parabolic trough, while the X-axis is perpendicular to Y and Z. The receiver tube (HCE) consists of a stainless steel absorber tube surrounded by a glass envelope tube for thermal insulation (Schott, 2015b). The welding connection and the bellow allowing for thermal expansion between the steel absorber tube and the glass envelope tube are protected with aluminum sheet cylinder.

devices. Meeting tight tolerances of the geometry is of prime importance to reach the aimed at optical and thermal performance. Thus, the optical, mechanical, and thermal properties of all components of the solar field are crucial for the final efficiency of the power plant.

The relevance of the optical performance of CSP plants is determined by its influence on the levelized cost of electricity (LCOE), since the optical performance is directly related to the annual total net electrical output and thus important for the economical viability of the power plant (Dieckmann et al., 2017).

With regards to the solar field's optical performance, all influences by the collector geometry are considered by the intercept factor (γ). Three independent geometrical properties determining the intercept factor can be distinguished (Bendt et al., 1979; Pottler et al., 2014). The shape accuracy of the mirror surface is commonly represented by the slope deviation in curvature direction (SD_X) and the slope deviation in longitudinal direction (SD_Y). The tracking deviation ($\phi_\perp$) can be described by the projection of the incidence angle of incoming radiation on the focal plane (Bendt et al., 1979, Sec 2.1, Figure 2.1).

The absorber tube displacement along the optical axis (ΔZ_{Abs}) and the absorber tube displacement in lateral direction (ΔX_{Abs}) are used to describe vertical and lateral deviations of the tube center line from the focal line. In general, the concentrator geometry is also affected by ambient conditions and load cases.

At all stages of technological development[3], the assessment of the performance of CSP systems and components is an important task and a variety of measurement techniques have been adapted or developed for this purpose. Thermal performance measurements are used to characterize the ability of systems and components to harness incoming irradiation, while minimizing thermal losses to the environment (Janotte et al., 2014). Yet, in most cases, the underlying physical effects are not considered in detail. This is the point where the detailed and spatially resolved investigation of the optical properties of CSP-concentrators plays an important role for the comprehensive understanding of the system efficiency.

In view of the above-mentioned geometric characteristics, non-contact, optical measures are established approaches. So far, determination of geometry parameters has been time consuming and applicable to only small fractions of the solar field. Image acquisition for optical measures has been characterized by manual triggering of ground based cameras. Other measures like SCE tracking and torsion characterization were based on inclinometers with high effort for installation and data acquisition. Despite advanced optimization of all processes, the measurement volume has been limited and the effort during evaluation is comparatively high. Such limitations can be partly overcome by coupling a statistical method with samples of geometric ground measurements, as described in Zhu and Turchi (2017).

The technology of unmanned aerial vehicles (UAVs) has made great progress recently. While military applications have permeated public perception of UAVs in a negative way, there is a wide field of civil applications. UAVs are especially useful for image acquisition and surveying of large areas. The advantages of UAVs are high flexibility, large measurement volume and high degree of automation, fast data acquisition, and accessibility. Hence, UAVs offer a smart solution to overcome restrictions of state of the art methods for CSP qualification.

This thesis describes the accurate, comprehensive, large scale and thus airborne assessment of PTC geometrical properties and optical performance and is structured as follows:

3 design, prototyping, solar field erection, operation and maintenance

- Chapter 2 provides an overview on performance parameters of the PTC, in particular deviations of the concentrator from its design shape. The advantages and drawbacks of state of the art measurement techniques are presented. A ray-tracing-based sensitivity analysis of the intercept factor on the collector geometry underlines the importance of complying with tolerances in order to meet the solar field's performance target.

- Chapter 3 presents a holistic optical and mechanical PTC model taking into account variability of the geometry under ambient conditions and operational loads like gravity, wind, friction, and heat transfer fluid temperature (T_{HTF}). This is of particular interest because airborne determination of the PTC geometry is only possible for a certain state (tracking angle $\theta \simeq 90°$), but for reliable forecasting annual yields, it is indispensable to have a comprehensive knowledge about the PTC geometry under all relevant operation conditions.

- Chapter 4 describes the QFly high resolution data acquisition and evaluation mode ($\text{QFly}_{\text{HighRes}}$), which incorporates the use of an UAV for data acquisition and deflectometric methods and close range photogrammetry for evaluation. The method is characterized by low flight altitudes and very detailed and accurate results for SD_X, ΔX_{Abs} and ΔZ_{Abs} for a limited measurement volume (one SCA per flight). As the hardware consists of "off the shelf" components, the main issue are software algorithms for way-point route creation, image processing, camera positioning and approaches to deduce the PTC geometry from airborne images. The expected uncertainty of intermediate and final results is investigated and validated with independent benchmark methods. This validation also involves the comparison of optical and thermal performance measurements for a single SCE.

- Chapter 5 further develops the approach described in Chapter 4 with the objective of geometrical commissioning of entire PTC collector fields called $\text{QFly}_{\text{Survey}}$. While $\text{QFly}_{\text{HighRes}}$ delivers spatially high resolved results for single SCAs, it lacks the possibility for fast screening of entire solar fields. Such an approach is presented and validated here, which delivers low resolution effective slope deviation in curvature direction (SD_{Xeff}) and information on effective tracking deviation ($\phi_{\perp eff}$) and alignment between SCEs from images captured at considerably higher flight altitudes. A reasonable and efficient combination of $\text{QFly}_{\text{Survey}}$ and $\text{QFly}_{\text{HighRes}}$ is presented to outline a methodology for the characterization of entire PTC power plants. This methodology is based on the experience gained with QFly in the Andasol III (AS3) power plant.

- Chapter 6 summarizes the previous chapters and draws conclusions on lessons learned, the progress beyond former state of the art as well as certain drawbacks of airborne PTC characterization. It also provides an outlook and proposes improvements of QFly and future activities to further exploit the large potential of airborne data-acquisition like infrared thermography for heat loss detection and the expansion to the characterization of other CSP technologies like solar power tower (SPT) heliostat field optimization.

Readers familiar with CSP technology in general and PTC characterization in particular are recommended to directly start with Chapter 4.

2

OPTICAL EFFICIENCY OF PARABOLIC TROUGH COLLECTORS

In this chapter, different types of performance parameters of parabolic trough collector systems and their interdependence are described. In this context, the relevance of the intercept factor and the effect of deviations of the concentrator from its design shape are investigated in detail. An overview is given on state of the art measurement approaches to obtain the concentrator geometry. Finally, the sensitivity of the intercept factor on deviations from the design shape is presented for a typical parabolic trough collector[1] concentrator design.

2.1 GENERAL PERFORMANCE MEASURES OF PARABOLIC TROUGH COLLECTOR SYSTEMS

The thermal performance η_{coll} (Equation 2.1) of PTC systems is defined as the ratio between thermal energy $\dot{Q}_{Use}$ released from the collector and solar energy available to the system $\dot{Q}_{Solar}$. $\dot{Q}_{Use}$ is the product of mass-flow $\dot{m}$, specific heat capacity c_p and increase of T_{HTF}. $\dot{Q}_{Solar}$ is quantified as the product of the net collector aperture area A_{Net}, direct normal irradiance (DNI) (= E_b), the cosine of the $\phi_{||}$ and the cleanliness factor (χ) (Janotte, 2012). An updated, more detailed nomenclature on the losses in PTCs can be found in Hirsch et al. (2017).

$$\eta_{coll} = \frac{\dot{Q}_{Use}}{\dot{Q}_{Solar}} = \frac{\dot{m} \cdot c_p \cdot (T_{HTFout} - T_{HTFin})}{A_{Net} \cdot E_b \cdot cos(\phi_{||}) \cdot \chi^{3/2}} \tag{2.1}$$

The optical performance η_{opt} (Equation 2.2) involves only parameters describing the interaction of the concentrator and absorber with incoming radiation. Geometric influences are described by the intercept factor (γ), while specular mirror reflectance (ρ_{Ref}), transmitance (τ_{Glass}), and absorptance (α_{Rec}) characterize the optical properties of the concentrator components. An enhanced definition of the γ involves the interaction of the incoming and reflected radiation with the concentrator structure. This way, the active receiver length (L') and blocking and shading are considered. This quantity is typically returned by ray-tracing (RT) software and is denoted as the effective intercept factor ($\gamma'_{\phi_{||}}$).

$$\eta_{opt} = \rho_{Ref} \cdot \tau_{Glass} \cdot \alpha_{Rec} \cdot \gamma'_{\phi_{||}} \tag{2.2}$$

1 RP3: PTC mirror quasi standard

A parametric description of solar collector efficiency (η_{coll}) (Janotte et al., 2014) as a function of optical efficiency (η_{opt}) is presented in Equation 2.3:

$$\eta_{coll} = \eta_{opt} \cdot \kappa(\phi_{||}) - c_1 \cdot (T_{Out} - T_{Amb}) - c_2 (T_{Out} - T_{Amb})^2 - c_\xi \cdot \left(\frac{\delta T}{\delta t}\right) \tag{2.3}$$

Heat loss to the environment is described by c_1 and c_2, while the term containing c_ξ is only used to model thermal inertia for non-steady state conditions. The dependency of the optical efficiency on the incidence angle ($\phi_{||}$) is described by the incidence angle modifier ($\kappa(\phi_{||})$) (see Equation 2.4). The incidence angle modifier characteristic is derived from the ratio of measured optical efficiency at different incidence angles and the optical peak efficiency:

$$\kappa(\phi_{||}) = \frac{\eta_{opt}(\phi_{||})}{\eta_{opt}(\phi_{||} = 0)} \tag{2.4}$$

The motivation of the following assumptions is to emphasize the impact of the effective intercept factor ($\gamma'_{\phi_{||}}$) on the solar field performance described by the solar collector efficiency (η_{coll}) and because of the difficulties to determine η_{opt} exclusively by thermal performance measurements.

The first assumption deals with the effect of thermal losses to the environment: For a "cold" solar field, the average fluid temperature (Janotte, 2014) equals the ambient temperature:

$$T_{HTF} = \frac{T_{in} + T_{out}}{2} \simeq T_{amb} \tag{2.5}$$

Then, according to Equation 2.3, thermal losses can be neglected.
The second assumption covers the effect of the incidence angle. If the incoming radiations is parallel to the PTCs optical axis, then:

$$\kappa(\phi_{||}) = 1$$

Typical testing conditions in the solar field would hardly include operating periods at normal incidence of solar irradiance (Janotte et al., 2014) and low T_{HTF} at the same time, and at least of all under steady state-conditions.

However, under these assumptions, the importance of the effective intercept factor ($\gamma'_{\phi_{||}=0}$) becomes apparent, as then the solar field performance is primary determined by optical parameters:

$$\left.\begin{array}{c} T_{HTF} = T_{Amb} \\ \phi_{||} = 0 \end{array}\right\} \quad \eta_{coll} \simeq \rho_{Ref} \cdot \tau_{Glass} \cdot \alpha_{Rec} \cdot \gamma'_{\phi_{||}=0} \tag{2.6}$$

Therefore, and also because of the spatial variability of $\gamma'_{\phi_{||}}$, comprehensive and accurate methods to determine geometric properties of CSP concentrators are extremely useful.

According to Equation 2.2, the optical efficiency (η_{opt}) and hence the solar collector efficiency (η_{coll}) are also influenced by the optical and thermal parameters of components like HCEs or mirror panels. These thermal and optical properties can be derived in the first place from laboratory measurement or quality control measures. Temporal and local variability of these parameters attracts more attention, since this has a significant impact on plant performance.
The specular mirror reflectance (ρ_{Ref}) is subject to soiling (Wolfertstetter et al., 2012; Wolfertstetter, 2016) and mirror degradation (Kennedy and Terwilliger, 2004; Wiesinger et al., 2016), so that spatial and temporal variability must be taken in to account especially after several years of operation. Thermal losses from the absorber tube might be affected by H_2 formation and diffusion into the annulus between glass- and steel tube (Kuckelkorn et al., 2016) or by breakage of the glass envelope tube. Here, the spatial distribution of increased heat loss can be investigated by (airborne) thermal imaging (Price et al., 2006; Jorgensen et al., 2009; Natho, 2012; Espinosa-R. et al., 2016a). Also the transmitance (τ_{Glass}) of the glass envelope tube is subject to spatial and temporal variations by soiling (Espinosa-R. et al., 2016b) and degradation of the anti-reflective coating (Chiarappa et al., 2014).

In the further course of this thesis, the briefly mentioned thermal and optical properties and their effect on the optical solar field performance will not be investigated, since the focus is on geometric measures.

2.2 GEOMETRICAL PERFORMANCE MEASURES OF PARABOLIC TROUGH COLLECTORS

Three independent macroscopic[2] geometrical concentrator properties determining the intercept factor (γ) can be distinguished (Bendt et al., 1979; Pottler et al., 2014). In the case of the parabolic trough collector (PTC), these are the slope deviation in curvature direction (SD_X) and the slope deviation in longitudinal direction (SD_Y), displacement of the receiver from the focal line (ΔX_{Abs} and ΔZ_{Abs}) and the tracking deviation ($\phi_{\perp}$). Definitions, causes and effects of these parameters are given in the following sections.

2 microscopic specular errors as mentioned in (Bendt et al., 1979) are not considered as geometric imperfections, since this parameter strongly depends on the type of the used mirror material.

2.2.1 *Mirror shape deviation*

For the mirror shape accuracy, either slope or 3D shape deviations can be measured and assessed. The mirror slope is the relevant parameter for the optical performance, as the deviation of the reflected ray in the receiver region is determined mainly by the direction of the surface normal vector, while the exact position of the point of reflection has a minor effect.

The slope deviation in curvature direction (SD_X) and slope deviation in longitudinal direction (SD_Y) are considered to be the fundamental property for any CSP concentrator system (Lüpfert and Ulmer, 2009). SD_X and SD_Y depend on compliance of the individual components (glass mirrors and support structure) with the tolerances, assembly accuracy, and the interaction of support structure and mirrors for different load cases (see Section 3.1).

Slope deviations are defined as the difference between ideal and real mirror surface normal vector ($\overrightarrow{N}$), projected onto the XZ or YZ plane:

$$SD_{X,Y} = \arctan\left(\frac{N_{X,Y}^{real}}{N_Z^{real}}\right) - \arctan\left(\frac{N_{X,Y}^{ideal}}{N_Z^{ideal}}\right) \tag{2.7}$$

For point concentrating systems like the solar power tower and the parabolic dish concentrator, both SD_X and SD_Y are of equal importance. For line concentrating systems like the parabolic trough collector and the linear fresnel reflector, the relevance of SD_Y depends on the incidence angle ($\phi_{||}$):

SD_Y can be neglected for $\phi_{||} \simeq 0$, while for increasing $\phi_{||}$, SD_Y contributes substantially to the incidence angle modifier ($\kappa(\phi_{||})$) (Bendt et al., 1979, Section 2.2). Generally speaking, the impact of SD_X on the annual energy yield is ten times higher than the impact of SD_Y (Ulmer et al., 2009, p. 5).

For the PTC, a special sign convention (see Figure 2.1) is used to simplify the interpretation of measured data. This is achieved by adapting the sign to the X-coordinate so that negative slope deviations denote too steep mirror areas[3] and positive slope deviations denote too flat mirror areas[4].

The focus deviation in curvature direction (FD_X) (Equation 2.8) combines the SD_X with the distance between mirror and receiver $\overline{|RF|}$.

3 the reflected ray passes below the design focus
4 the reflected ray passes above the design focus

This quantity can be directly compared with the receiver tube diameter (Lüpfert et al., 2004a):

$$FD_X = SD_X \cdot 2 \cdot \overline{|RF|} \tag{2.8}$$

A sample map with typical SD_X and FD_X distribution for an ET collector module is presented in Figure 2.2. The RMS value of slope deviation in curvature direction (RMS_{SDX}) (Equation 2.9) is used as input parameters for the statistical ray-tracing presented in Section 2.4.1. The correct (equal) weighting of single SD_X values to obtain the RMS_{SDX} is achieved by a homogeneous spatial resolution of measurement samples N in the aperture area:

$$RMS_{SDX} = \sqrt{\frac{\sum_1^N SD_X{}^2}{N}} \tag{2.9}$$

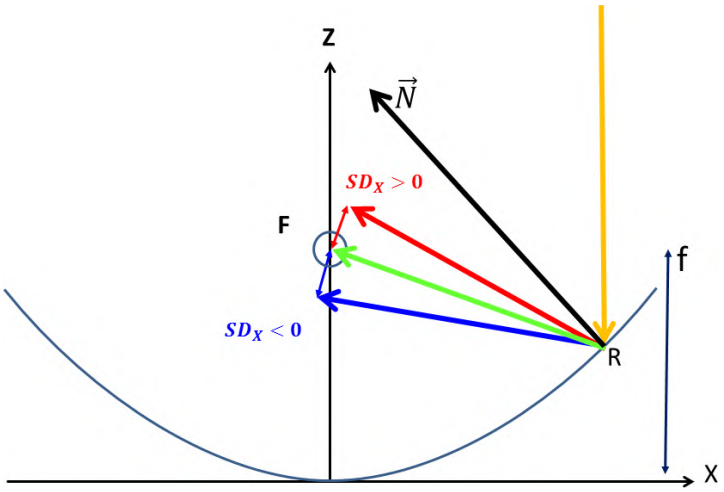

Figure 2.1: Cross section showing incoming radiation (orange), the ideal mirror surface normal vector ($\vec{N}$), and the optimal direction of reflected radiation (green) of the parabolic mirror. Positive and negative slope deviation in curvature direction cause the reflected ray to miss te focal line, as indicated by the red and blue vectors representing not ideally reflected rays. For negative X values, this convention remains valid. The distance between point of reflection R and design focus F is used to calculate the FD_X.

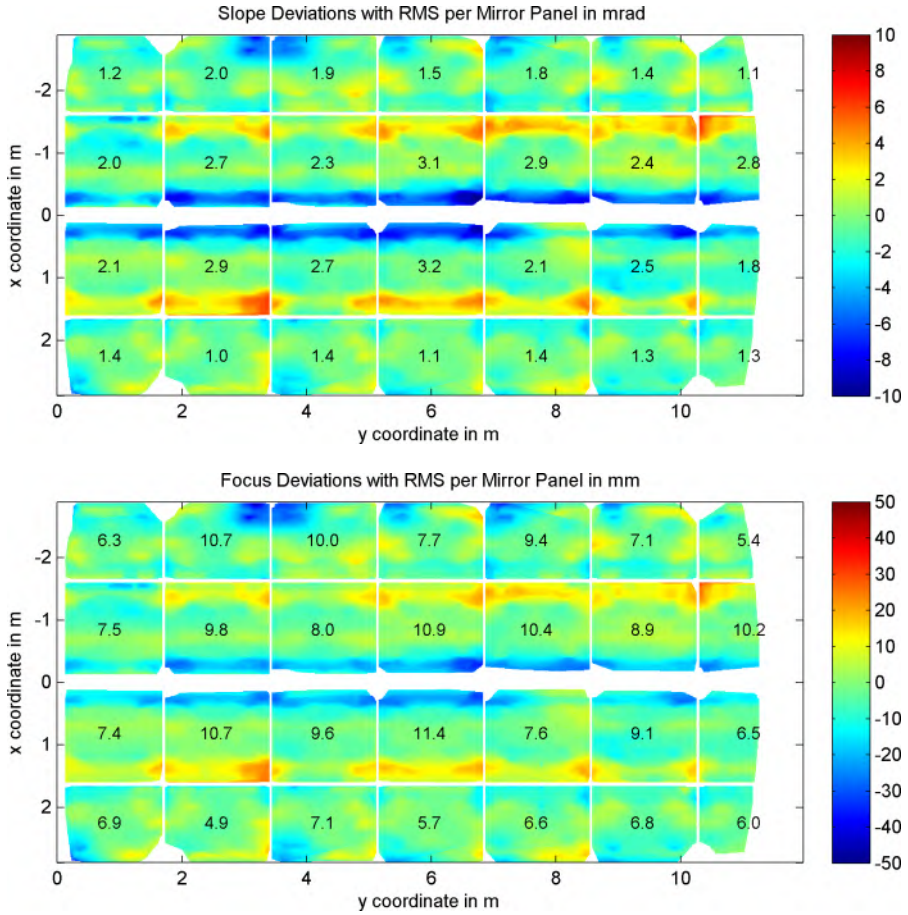

Figure 2.2: SD_X (top) and FD_X (bottom) maps for a RP3 SCE at the concentrator test bench at PSA (KONTAS) facility at PSA. The numbers denote root mean square (RMS) values per mirror panel. Rather high absolute SD_X values close to the parabola vertex (blue in the top figure) are converted into relatively moderate FD_X values due to the short distance between mirror and absorber. On the other hand, SD_X values at the outer mirror rim result in comparatively high FD_X values due to the increased distance to the absorber. The overall performance of this module is excellent with an intercept factor (γ) of $\simeq$ 99%, when neglecting blocking and shading of the HCE bellow protections and the effect of the glass envelope tube. The data was acquired with $\text{QFly}_{\text{HighRes}}$ (see Section 4).

2.2.2 *Effective mirror shape deviation*

In some cases, it is necessary to describe the concentrators optical quality even under conditions, where the contributions from slope deviation in curvature direction (SD_X), displacement of the receiver from the focal line (ΔX_{Abs} and ΔZ_{Abs}), and tracking deviation ($\phi_\perp$) cannot be differentiated. It has been suggested to define the effective slope deviation in curvature direction (SD_{Xeff}) (Prahl et al., 2013a, Section 5.1.3) or combined *reflector-absorber angles* (Owkes, 2012, Section 5.1).

Such a definition is especially useful where the concentrator geometry is determined from distant observer (DO) methods using the absorber tube as pattern for deflectometric methods (see Section 2.3.1).

The position of the absorber tube (which actually provides the reflection pattern) has a major impact on the result. For this reason, the assumptions on the yet unknown absorber position must be carefully selected. For absorber tube displacement in lateral direction (ΔX_{Abs}), a optimal position is assumed ($\Delta X_{Abs} = 0$). For the large systematic values of absorber tube displacement along the optical axis (ΔZ_{Abs}) for lower heat transfer fluid temperature (T_{HTF}) (see Section 3.2.3), the assumption of an ideal positioning ($\Delta Z_{Abs} = 0$) would lead to implausible results. To prevent that, the $\Delta Z_{Abs}(T_{HTF})$-model presented in Section 3.2.3 is used. Thereby it is possible to obtain SD_{Xeff} independently from the heat transfer fluid temperature.

Equation 2.10 provides a general definition how SD_{Xeff} can be derived from SD_X, ΔX_{Abs}, $\Delta Z_{Abs}(T_{HTF})$, and $\phi_\perp$, respectively. Here, f^{Abs} describes analytical function to create the *"effective slope error"* from absorber tube displacement according to (Stynes and Ihas, 2012b, Equation 2). The function g^{Track} describes the sign convention that has to be considered when adding the tracking deviation ($\phi_\perp$) to the SD_X map.

$$SD_{Xeff} = SD_X + f^{Abs}(\Delta Z_{Abs}(T_{HTF},), \Delta X_{Abs}) + g^{Track}(\phi_\perp) \quad (2.10)$$

2.2.3 *Absorber tube misalignment*

Typical receiver tubes (HCEs) for PTCs consist of a stainless steel tube with diameter in the range of 70 - 90 mm (Schott, 2015a,b). All HCEs designed for high temperature applications are surrounded by an evacuated glass envelope tube with an anti-reflective coating to minimize convection heat losses and to maximize the transmitance (τ_{Glass}). A spectral selective coating of the steel tube assures high absorptance (α_{Rec}) and low radiative heat losses. The cost share of the HCEs is about 7 % of the total investment cost of the entire plant (WorldBank, 2010, page 75, Table 8). Thus, HCEs can be regarded as a sensitive key component.

In order to harness the full performance, the deviation of the tube center line from the focal line (ΔX_{Abs} and ΔZ_{Abs}) must not exceed the specified tolerances. These tolerances are mainly determined by the aperture width of the PTC and the absorber tube diameter. In Figure 2.10, the sensitivity of the intercept factor on absorber tube misalignment is shown. For the given RP3 mirror geometry and quality, deviations up to $5\,mm$ are tolerable without significant performance

loss. The national renewable energy laboratory (NREL) (Owkes, 2012; Stynes and Ihas, 2012b) and DLR (Lüpfert et al., 2007) highlight the necessity to measure deviations of the receiver tube from the focal line, as their impact on the optical efficiency is in the same order as slope deviations of the mirror surface.

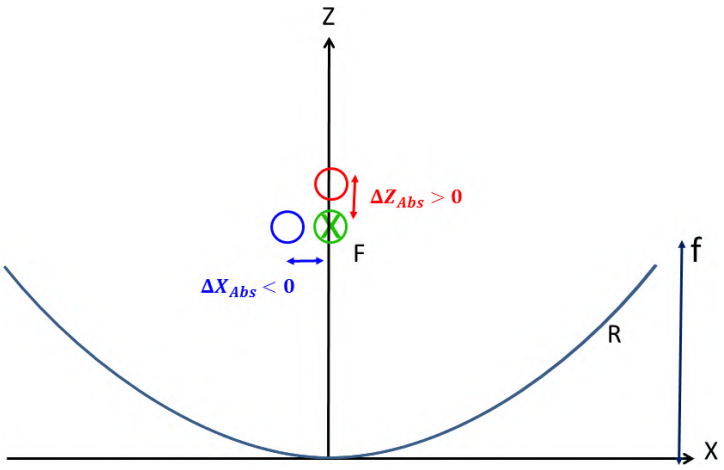

Figure 2.3: Cross Section showing the ideal absorber tube position (green) and vertical (ΔZ_{Abs}) and lateral (ΔX_{Abs}) deviations from the focal line.

The following list provides a brief overview on causes for absorber tube misalignment and corresponding research findings:

- **Mounting accuracy**: Assembly of the (steel-) structures of state of the art PTCs is carried out upside-down on a carefully adjusted jig (Geyer et al., 2002). This jig comprises the exact locations of mirror mounting points, axis of rotation and the focal line. With these measures, tolerances for the absorber tube supports of less than $2\,mm$ can be complied with. In case of a an defective or incorrectly positioned jig, or in the absence of such a device, much larger deviations have been observed.

- $\boldsymbol{T_{HTF}}$: HCEs are connected to the PTC structure via supports, which keep the tube in a position coaxial with the focal line during tracking (see Figure 1.1). The supports are connected to the concentrator structure via a link or spring plate close to the parabola vertex which allows for motion in longitudinal direction in order to compensate for the thermal expansion of the tubes between ambient and operation temperature (see Figure 3.4). As a consequence, the absorber tube center-line deviates from the design focal line, if the heat transfer fluid temperature (T_{HTF}) is below the nominal operation temperature ($T_{HTF_{nom}}$). Details of the dependency of the absorber tube displacement along the optical axis (ΔZ_{Abs}) on the heat transfer fluid temperature (T_{HTF}) are described in Section 3.2.

- **Thermal stress and dead load**: Thermal stress caused by inhomogeneous illumination and inadequate heat transfer may cause residual stress and permanent deformation of the steel tube. Since two phase flow in solar direct stem generation is a critical issue, (Flores and Almanza, 2004) reduced deflections by using compound copper steel tubes. Another critical operating condition is stratified flow in the absorber tube in combination with in-homogeneous radiation distribution or instabilities (phase changes) in DSG facilities (Hirsch et al., 2012; Valdes et al., 2014; Almanza et al., 1997). Investigations concerning HCE deformation and the influence on the intercept factor (γ) in case of molten salt HTF antifreeze installations have been reported in Iverson et al. (2011). Here, deflections up to 16.4 *mm* are reported when hot molten salt flushes the tube.

2.2.4 *Tracking deviation*

PTCs require precise and reliable adaption of tracking angle (θ) under all operating conditions, according to location, time of the year and tracking axis orientation. The angle between the optical (Z-) axis of the concentrator and the sun position, projected on the X/Z (focal) plane of the concentrator must be close to zero with tolerances in the range of $\pm 5\,mrad$ (see Fig. 2.11). The term tracking deviation is used if:

$$|\phi_\perp| > 0 \tag{2.11}$$

This deviation can be caused by malfunction of the tracking system (mechanics, sun position algorithm, and optional sun-sensors), or misalignment of adjacent SCEs during solar field assembly. The local direction of the optical axis along the SCA may also be altered by operational loads like wind, static unbalance and bearing friction. A comprehensive analysis of dynamic tracking deviation under operational loads will be presented in Section 3.3.

The response of the intercept factor on $\phi_\perp$ depends on the concentration factor and the overall geometric accuracy. Systems with large geometrical errors or those with a low concentration factor are less susceptible to tracking deviations, while high accurate and high-concentrating systems react very sensitive to any misalignment between the incoming solar radiations and the optical axis of the concentrator.

An expanded definition of $\phi_\perp$ also involves the role of systematic absorber tube displacement in lateral direction (ΔX_{Abs}). On the one hand, ΔX_{Abs} influences the result of airborne measurement of $\phi_\perp$ (Section 5.2.3). On the other hand, both ΔX_{Abs} and $\phi_\perp$ are correlated concerning the effect on the intercept factor (see Figure 2.11). As

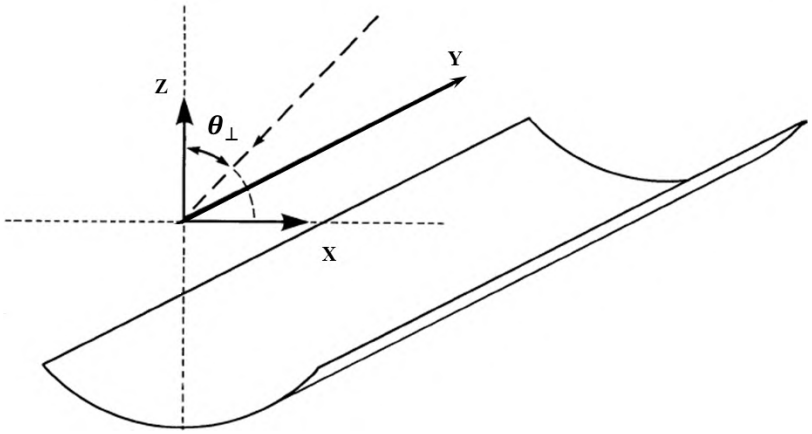

Figure 2.4: Definition of tracking deviation ($\phi_\perp$) according to Bendt et al. (1979). The dashed line represents the direction of incoming solar radiation. $\phi_\perp$ is the angle between the optical Z-axis and the incoming radiation projected into the XZ-plane.

a consequence, the effective tracking deviation ($\phi_{\perp eff}$) acquired by airborne methods[5] is introduced:

$$\phi_{\perp eff} = \phi_\perp + \arctan\left(\frac{\Delta X_{Abs}}{f}\right) \tag{2.12}$$

The difference between $\phi_\perp$ and $\phi_{\perp eff}$ is particularly relevant during uncertainty analysis and validation of airborne measurements (see Section 5.3.3, page 136).

2.3 STATE OF THE ART MEASUREMENT METHODS TO DETERMINE THE CONCENTRATOR GEOMETRY

The following section provides an overview on existing methods for the geometrical characterization of entire CSP concentrators in the solar field, focusing on PTC specific approaches. Laboratory and/or in-line production quality control measures[6] and thermal performance measurements of the solar field (García et al., 2011; Janotte, 2012) are not portion of the discussion.

2.3.1 *Measurement of mirror geometry*

For the measurement of the mirror geometry, a distinction is necessary between shape and slope measurement. Shape measurements provide 3D coordinates, in general at a comparatively low spatial resolution. Subsequent triangulation is required to obtain the local mirror slope,

5 using the absorber tube reflection DO principle
6 e.g.: QFoto (Pottler et al., 2011) and QDec (Weber et al., 2014))

which finally determines the direction of the reflected light.
The latter approach of direct slope measurement delivers the relevant data for performance analysis. Shape deviations of state of the art CSP concentrators are comparatively small[7], so during the acquisitions of slope deviations, an ideal concentrator shape can be assumed in a first order approximation. On the other hand, the shape can be deduced from slope data by integration. Different methods for mirror shape- and slope measurement are presented hereinafter, in which a distinction is made between scanning and screening methods. Comprehensive reviews on methods to determine the shape and/or slope deviations of CSP concentrators can be found in Ren (2014), Xiao et al. (2012), and Arancibia-Bulnes et al. (2017).

Scanning methods

Scanning a reflective surface with a well-defined light source and observing the direction of the reflected ray is the most intuitive and directly arising approach. The measurement uncertainty is related to the accuracy of the position of light-source, point of reflection, and detected hit point of the reflected ray[8]. Among the available methods for scanning CSP collector slope measurements, the video scanning hartmann optical tester (VSHOT) is the most advanced laser ray-trace system, which can be applied to both point- and line-focusing CSP concentrators (Wendelin et al., 2006; Lewandowski and Gray, 2010).

Deflectometric methods

Deflectometry or fringe reflection uses known regular stripe patterns on a screen or target whose reflection in a specular surface is observed by a digital camera (Knauer et al., 2004). From the deformation and distortion of the stripe pattern in the reflection, the local normal vectors of the mirror can be calculated. This method is applied to measure the geometry of heliostats of solar power tower plants (Ulmer et al., 2011), parabolic dish concentrators (Ulmer et al., 2008), linear fresnel reflector mirror panels (Heimsath et al., 2008) or single mirror panels of PTCs (März et al., 2011) and has reached the maturity of a commercial system called QDec[9] for in-line mirror production quality assurance (Weber et al., 2014; CSPServices, 2015). The application of this method to a full-size PTC module in production environment has been also successfully implemented (Ulmer et al., 2012). However, the need for large screens and disturbance by ambient light complicates the implementation deflectometry as an outdoor field measurement tool. In order to overcome these restrictions, there are several methods that use the absorber tube as a "pattern" to determine slope deviation

7 in the range of *mm*
8 usually on a diffusely reflecting surface
9 deflectometric measurement system for CSP mirror panels

in curvature direction (SD_X) or at least rough performance measures. These methods are based on the distant observer (DO) method proposed by Wood (1981):

- The theoretical overlay photographic approach (TOP) involves overlaying theoretical images of the absorber tube in the mirrors onto surveyed photographic pictures (Diver and Moss, 2007) and iterative improvement of the mirror alignment. It uses an array of several ground based cameras to align mirror panels of horizontally orientated PTC modules.
- Another ground based tool for the optical alignment of parabolic troughs called visual inspection system field (VISfield) was developed by ENEA. Montecchi et al. (2010) highlights the principal of "ray-reversibility" and states that fortunately quantum effects can be neglected for PTC optics. After manual alignment of the HCE, the local mirror slope and γ values are derived from digital images, and positions of camera, absorber tube, and absorber tube edge reflections.
- The trough absorber reflection measurement system (TARMES) provides high accuracy and high spatial resolution SD_X maps from a set of photos (Heinz, 2005; Ulmer et al., 2006, 2009). Normal vectors of the mirror surface are derived from the spatial coordinates of the absorber tube edges, the position of the absorber tube edge reflection in the mirror surface and the nodal point of the camera. The measurement principle of TARMES is presented in Figure 2.5. A detailed description of the TARMES post-processing can be found in Heinz (2005). Enhancement for automatic evaluation of large airborne data sets will be provided in Section 4.2.4 and 4.2.5.
- NREL has developed an optical measurement tool for PTCs (Stynes and Ihas, 2012a; Owkes, 2012) using the center line of the image of the reflection of the absorber tube that measures the combined errors due to absorber misalignment and reflector slope error. This method contains elements of TOP and TARMES. By measuring the combined reflector-absorber errors, the uncertainty in the absorber location measurement is eliminated. As the intercept factor (γ) depends on the combined effects of absorber alignment and reflector slope errors, it is stated, that the combined effect provides a simpler measurement and a more accurate input for the intercept factor calculation. This method has also been considered for airborne data-acquisition.

Most previously mentioned methods (VSHOT, VISfield, TOP, and TARMES) have in common that the collectors are easily measured

facing horizon, while the measurement of a collector module in its prevailing operating position (around zenith) involves considerably increased effort. The typical scope of one measurement is a single SCE, so these methods are suitable for random sampling but not for field characterization.

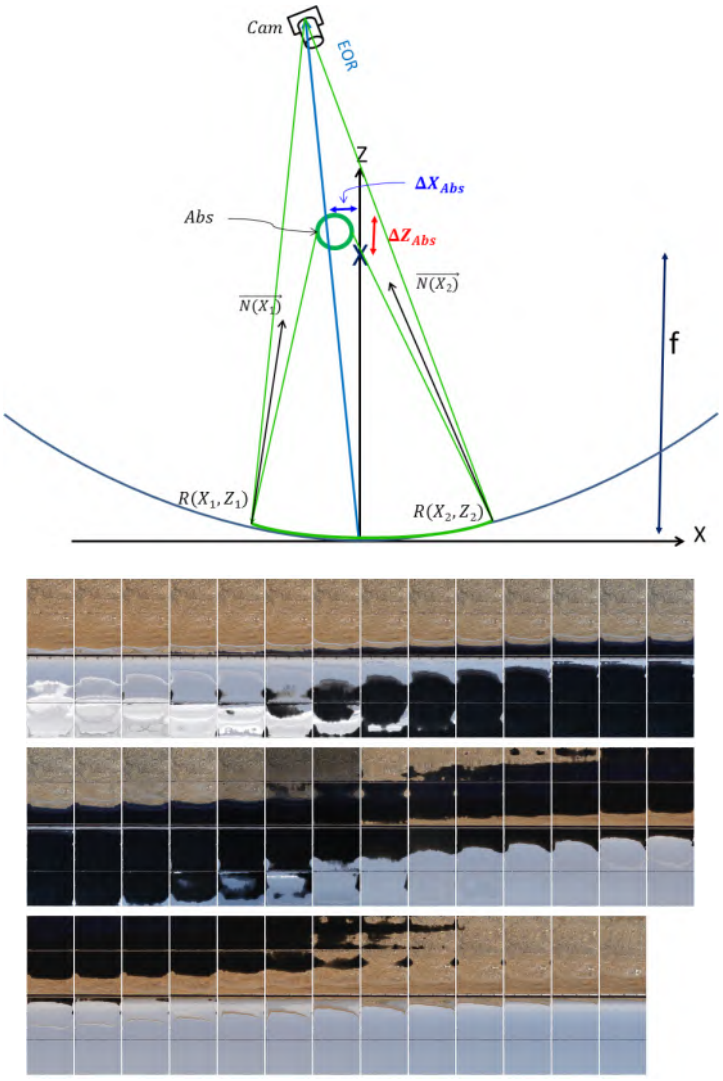

Figure 2.5: Top: Cross section showing the relevant measurement points of the TARMES approach. The reflection of the absorber tube edge in the mirror surface (green) is observed by the camera. Knowing the camera position (EOR), the point of reflection ($R(X, Z)$), and the actual position of the absorber tube (characterized by ΔX_{Abs} and ΔZ_{Abs}), $\overrightarrow{R\,Cam}$ and $\overrightarrow{R\,Abs}$ are created. The bisecting line between $\overrightarrow{R\,Cam}$ and $\overrightarrow{R\,Abs}$ delivers the mirror surface normal vector ($\overrightarrow{N}$). Bottom: Image series of a single mirror row from a TARMES measurement with the SCE facing horizon ($\theta = 0$). The upper half ot the collector shows reflections from the ground, while the lower part reflects the sky. At least $40 - 60$ images are required to achieve sufficient covering of absorber tube edge reflections over the entire mirror surface.

Close range photogrammetry

In contrast to the scanning- and deflectometric slope measurement methods presented so far, which take advantage of the reflective qualities of the investigated surface, close range photogrammetry (PG) (Luhmann et al., 2006b) is a direct 3D measurement technique with wide range of applications. PG has been extensively applied for the qualification to various CSP collectors (Shortis and Johnston, 1997; Pottler et al., 2004; Schiricke, 2008; Fernandez-Reche and Valenzuela, 2012; Garcis et al., 2012).

This method can be applied to any collector orientation and measures 3D coordinates in order to detect characteristic deviations of mirrors, structures and alignment of absorber tubes or rotation axes. It is especially suitable for deformation analyses of prototypes and in cases where no mirrors are attached to the collector structure. As the spatial resolution depends on the density of markers, it generally delivers a lower resolution compared to deflectometric methods. With sufficient spatial resolution, SD_X and SD_Y can be derived by triangulation (Delaunay, 1934) and assigning the mirror surface normal vector ($\overrightarrow{N}$) to each triangle.

The PG measurement procedure for PTCs is as follows: The point of interests (POIs) on the mirror surface, the tracking axis and the absorber tube are highlighted with circular, retro-reflective markers. After image acquisition, 2D image coordinates of the markers are obtained via image processing and the 3D positions of the POIs are calculated by bundle adjustment software. Throughout this work, the DPA Pro software (Bösemann, 2005) from AICON 3d Systems is used. In general, this resulting 3D POI cloud is provided in an arbitrary orientated coordinate system.

The comparison between measured and design coordinates is the objective of the post processing of the 3D data. This procedure involves the transformation of measured points onto the design data, which is described in Section A.1.

Application and results of close range photogrammetry will be used in the following context of this thesis:

- Section 3.1: Derivation of SD_X deformation pattern for different tracking angles θ
- Section 4.2, 4.2.1 and 4.3.1: Calculation and validation of the 3D setup of $\text{QFly}_{\text{HighRes}}$.
- Section 4.3.3: Preparation of benchmark data for the validation of airborne absorber tube positioning.

- Section 4.3.4: Preparation of benchmark data for the validation of airborne SD_X measurement.
- Table 4.2: Camera pre-calibration for $\text{QFly}_{\text{Survey}}$.

2.3.2 *Measurement of absorber tube position*

Despite the relevant impact on the optical performance, relatively few methods for absorber tube positioning have been found in the literature. The most intuitive and straight-forward approach uses cameras attached firmly to the collector structure. This setup (see Figure 2.6) allows to obtain relative values for ΔX_{Abs} and ΔZ_{Abs} with high temporal and spatial resolution. For a two dimensional characterization at least two cameras are required. Lateral deviations can be monitored with a camera mounted close to the vertex, while hight deviations are best observed with camera mounted close to the mirror edge. Such measurements to quantify the effect of thermal or mechanical stress on absorber tubes have been carried out by Iverson et al. (2011), Hirsch et al. (2012), and Wu et al. (2014).

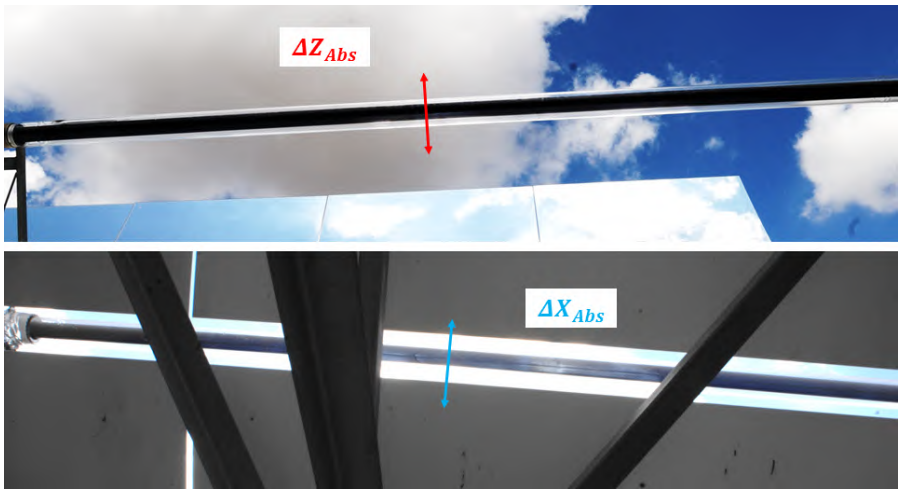

Figure 2.6: Camera based relative measurement of ΔX_{Abs} and ΔZ_{Abs}. The upper picture details originate from a camera mounted close to the rim of parabola. Vertical deflections can be obtained from tube edge detection by image processing. The rigid camera mounting can be cross checked by using the mirror edge as a reference. Bottom: Lateral deviations are obtained by the same approach. The camera is mounted to the torque-box, observing the absorber tube trough the mirror gap at the parabola vertex.

As an add-on to the approach presented by Owkes (2012), NREL has developed an absorber tube alignment measurement technique (Stynes and Ihas, 2012b), which also considers airborne data acquisition and uses a photogrammetric approach with additionally attached markers to determine the camera position relative to the PTC. The interior orientation (IOR) of the camera is acquired by using a checkerboard-based calibration toolbox (Bouguet, 2010). The height and lateral

deviation of the absorber tube are calculated by solving a system of linear equations including the camera position and the absorber tube projected on a plane parallel to the aperture plane including the focal line. The uncertainty analysis published in Stynes and Ihas (2012b) predicts values in the range of $5 - 10\,mm$. The validation of the method with a manually operated camera and a mock collector/receiver without glass envelope tube showed deviations between the absorber alignment measurement technique and a PG reference in the range of $2.1\,mm$ for ΔX_{Abs} and $0.9\,mm$ for ΔZ_{Abs}.

As direct access to the steel tube of the HCE is in general prevented by the glass envelope tube, measurement of ΔX_{Abs} and ΔZ_{Abs} is a two stage process. At first, the axis of the glass envelope tube is measured and then the eccentricity of absorber and glass tube is estimated from digital images. The superposition of glass envelope tube position and eccentricity gives the absolute deviation of the steel tube from the focal line.

The center of the glass envelope tube can be calculated from PG data by fitting a circle to a ring of 3D coordinates from targets attached to the circumference of the glass envelope tube (see Figure 2.7). For this process, the 3D coordinates of all POIs must be transformed into the design coordinate system according to Equation A.1. This photogrammetric approach can hardly be applied to larger numbers of SCEs because it requires substantial preparation efforts. A less precise but much faster approach involves direct manual distance measurement between the glass envelope tube and the outer mirror edges with a hook rod (details see A.2).

To obtain the eccentricity of the steel absorber tube relative to the glass envelope tube, digital images are semi-automatically evaluated (Heinz, 2005) with a MATLAB graphical user interface (GUI) (see Figure 2.7). To obtain ΔX_{Abs}, images are taken along the optical axis (Z) of the PTC. To obtain ΔZ_{Abs}, images are taken perpendicular to the optical axis and the vertex (perpendicular to the Y/Z plane). During the post processing, the user has to select the region of interest (ROI) in the raw images, and the edges of the steel and glass tube are calculated from a cross sections perpendicular to the focal line.

The combination of close range photogrammetry (PG) and edge detection of the the steel tube in digital images yields the relative orientation between the PTC focal line and the steel tube center axis with an accuracy of $\simeq \pm 1.2\,mm$ (see Table 4.5). This method is also used to derive benchmark data for the $\text{QFly}_{\text{HighRes}}$ applications described in Section 4.2.2.

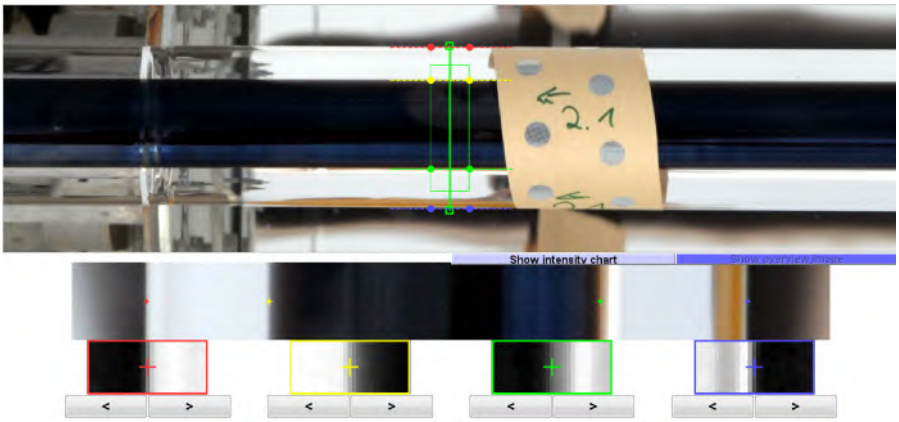

Figure 2.7: Methodology of evaluation of eccentricity image with a MATLAB GUI. The upper area shows the enlarged ROI with the absorber tube in front of the vertex of the parabola. Semi-automatic edge based algorithms help to determine the position of glass- and steel tube edges in the cross-section (lower area). A paper stripe with retro-reflective targets serves to determine the glass envelope tube position by means of photogrammetry in a previous step.

2.3.3 *Measurement of tracking deviation*

A first impression of the PTC tracking deviation ($\phi_\perp$) can be obtained from any asymmetry visible in camera target method (CTM) flux images (Lüpfert et al., 2004b) in the focal region (see Figure 2.8). The CTM methods involves placing a metal plate in the focal region of the PTC while tracking the sun. The metal plate is coated with a diffusely reflecting paint, so that the reflected rays from the mirror can be made visible. This approach also allows for quantitative intercept factor (γ) measurements for a particular Y-position within the collector.

Another option is to use the eccentricity between the shadow of the absorber and the parabola vertex (Fernandez-Garcia et al., 2010). The absorber tube shadow pattern is exploited in a PV cell based sun sensors for closed loop tracking. Two PV cells are aligned symmetrically on both sides of the parabola vertex, so that the electric current of each cell is proportional to the illuminated area. This type of instrumentation is not considered as a measurement technique in the usual sense of the word, as every SCA of the solar field is typically equipped with this sensor as part of the control and regulation in commercial PTC power plants.

Misalignment between neighboring SCEs is another cause for tracking deviation ($\phi_\perp$). During and after the construction phase of solar fields, the measurement of inter-SCE alignment (Pottler et al., 2014) offers large potential for performance enhancement. Angle offsets between neighboring SCEs can be quantified with inclinometers if a reference axis is defined (see also the acquisition of benchmark data with inclinometers in Section 5.3.3). In the absence of such axis, align-

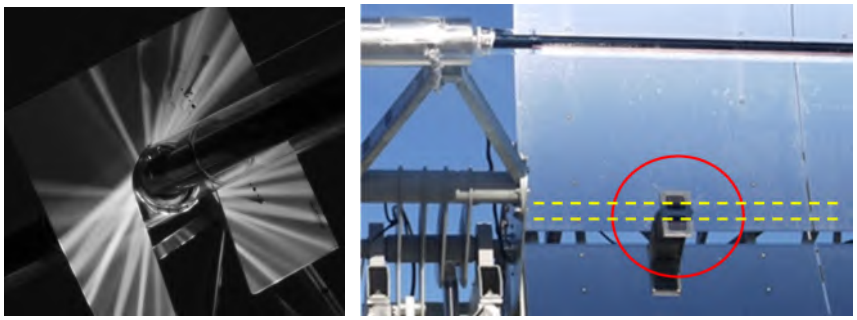

Figure 2.8: Deduction of absorber tube misalignment from optical phenomena. Left: CTM flux images for intercept factor calculation with a pronounced asymmetry, which indicates tracking deviation in the range of $> 10\,milliradian(mrad)$. Right: PV cell based sun sensor assembly for closed-loop tracking control. The absorber tube shadow (dashed yellow lines) is casting the sun sensor (inside red circle). The difference of the current signal from the two PV cells arranged symmetrically with respect to the parabola vertex is used to trigger tracking commands.

ment can be checked via the height level of the outer mirrors or with a water hose level.
The utilization of the imprint of the absorber tube reflection to obtain, among others, effective tracking deviation ($\phi_{\perp\,eff}$) from airborne images has been proposed by NREL (Jorgensen et al., 2009). This idea will be picked up and implemented in Section 5.2.3.
Finally, thermal performance tests with different tracking off-sets may be used to minimize the tracking deviation ($\phi_{\perp}$) by maximizing the solar collector efficiency (η_{coll}).

2.4 DERIVING OPTICAL PERFORMANCE FROM GEOMETRIC MEASURES

The ultimate objective of geometrical measurements presented above is providing information to estimate the optical performance of the CSP system under different operating conditions. As stated by Equation 2.2, besides the intercept factor (γ), the optical efficiency (η_{opt}) also depends on specular mirror reflectance (ρ_{Ref}), transmitance (τ_{Glass}) of the glass envelope tube and absorptance (α_{Rec}) of the selectively coated absorber tube. However, the temporal and spatial variability of these parameter (see page 9) is not subject of this thesis.

The causal relationship between geometric properties of PTCs and the intercept factor has been investigated in detail in Schiricke (2008) and Schiricke et al. (2009). In this section, we will pick up the topic by providing an overview on state of the art methods of intercept factor (γ) calculation. Section 2.4.3 provides examples on the interde-

pendencies of concentrator geometry and optical performance based on measured geometrical data.

2.4.1 *Statistical ray-tracing*

The statistical approach presented in Bendt et al. (1979) consists of folding the sun shape with statistical concentrator shape deviations, that way generating an "effective" source with a wider angle distribution compared to the initial sun shape. Together with an angular acceptance function, the intercept factor for a given set of boundary conditions (e.g. collector design, incidence angle ($\phi_{||}$), RMS_{SDX}, etc) can be derived.

This method works very well when the histogram of concentrator shape deviations can be described with a Gaussian distribution, however, as soon as deviations are distributed in a systematic way, the method reaches is limit (Bendt et al., 1979, page 15). This assumption for Gaussian distributions of concentrator deviations may be a valid approach for large samples as complete solar fields, but the general case is that (e.g. due to mass production of solar field components), systematic errors are very likely to happen. Applications of statistical ray-tracing to PTC fields are presented among others in Lüpfert et al. (2007) and Pottler et al. (2014). A brief explanation on advantages and drawbacks of statistical ray tracing can be found in Zhu and Lewandowski (2012, Section 2.2.2). NREL has developed an analytical approach called FirstOPTIC (Zhu and Lewandowski, 2012; Binotti et al., 2012), which preserves the spatial information of shape- and absorber tube deviations while employing a probability approximation from Bendt et al. (1979) for the sun shape, reflector specularity and tracking accuracy.

In general, statistical ray-tracing is suitable to estimate the performance of CSP systems. However, the numerical ray-tracing presented hereinafter requires less approximations and provides a more detailed description of blocking[10] and shading[11] losses (Lipps et al., 1974). .

2.4.2 *Numerical ray-tracing*

Numerical ray-tracing (RT) is nowadays the state of the art approach to assess the optical performance of CSP systems. Ho (2008) and Bode and Gauche (2012) present a current review on available tools and their features. A comparison of RT-predictions for the performance

10 blocking refers to an object in between the the mirror and the receiver, so that radiation reflected from the mirror can not reach the receiver.

11 shading refers to an object in between the sun and the mirror, so that radiation from the sun can not reach the mirror.

of line concentrating systems (PTC and LFR) is found in Osório et al. (2016).

Most RT tools provide an interface to define the concentrator geometry based on measured data. Similar to the statistical approach, concentrators may also be defined as ideal geometry adding statistically distributed geometrical errors. If the real mirror shape, tracking angle and receiver position is known, numerical RT may predict the optical performance correctly even for cases where systematic errors are present. Another advantage of numerical RT is the fact, that so called blocking and shading elements can be defined in order to determine their influence on the optical performance.

Especially for none-zero values of the incidence angle ($\phi_{||}$), parts of the concentrator structure[12] interfering with incident and/or already reflected radiation have an impact on the intercept factor. The influence of blocking and shading on the optical efficiency (η_{opt}) can be significantly larger than the attenuation of η_{opt} due to geometrical imperfections.

In the context of this thesis, the DLR software SPRAY (Buck, 2010) is used to obtain the intercept factor from measured data obtained with QFly. SPRAY is based on the Monte Carlo ray-tracing program developed by SANDIA (MIRVAL) (Leary and Hankins, 1979) and provides an ASCII file based interface, which makes it a practical solution for batch processing of measured data for different assumptions[13] and to control the in- and output from the QFly master program implemented in MATLAB.

2.4.3 *Relevance of high spatial resolution geometric data*

An approximate figure of the solar field performance can be derived from the statistical RT (Section 2.4.1) in combination with the RMS value of the beam spread (Pottler et al., 2014). However, the RMS_{SDX} values depends always on geometric data with sufficient spatial resolution. In the course of the study, several examples on such data will demonstrate the potential for "debugging" CSP systems.

In order to derive the potential additional yield[14], the annual yield based on measured data from the solar field in its *actual state* is compared with the yield based on assumptions on the *improved* solar field. The expected performance of the *improved* solar field is achieved

12 bellow protections and receivers supports
13 e.g.: Sun-shape or tracking deviation ($\phi_{\perp}$)
14 by improving the collector geometry and/or adapting the operation strategy (e.g. tracking method)

by superimposing measured data with possible modifications of the collector geometry and/or the operation strategy. This comparison assists to find an economically sound decision in favor or against possible corrective actions. To perform this analysis, a coupling of different software tools is required. In particular, the measurement of geometric collector properties must be followed by ray-tracing and yield analysis software (e.g.: GREENIUS), thereby considering different optimization scenarios. This RT- and yield analysis interface of QFly has not yet reached level of detail required for cost-driven performance optimization based on geometrical data for a large data volume. However, some examples on the influence of SD_X (Figure 2.9), combined ΔZ_{Abs} and ΔX_{Abs} (Figure 2.10) and combined $\phi_\perp$ and ΔX_{Abs} (Figure 2.11) are presented hereinafter.

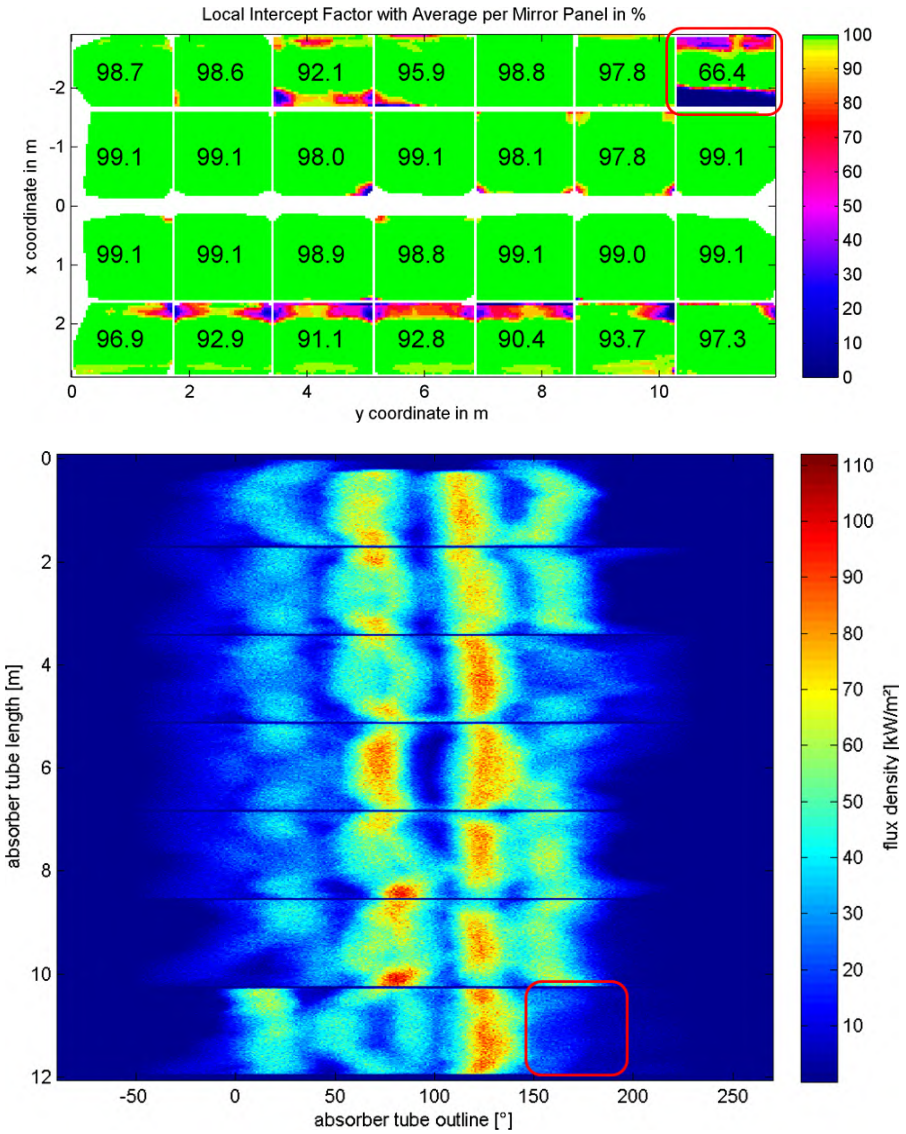

Figure 2.9: Top: ray-tracing based intercept factor (γ) map [%] with average intercept factor values per mirror panel. In the upper right corner of the SCE (marked with a red box), one mirror panel has been mounted the wrong way. The related statistical value reveals the expected reduction of optical performance in this area.
Bottom: Resulting flux density on the absorber tube in $[kW/m^2]$. The vertical axis corresponds to the horizontal Y-axis in the upper graph, while the X-axis represents the circumference of the absorber tube. The lack of concentrated radiation from the wrongly mounted mirror panel can be identified here as well.

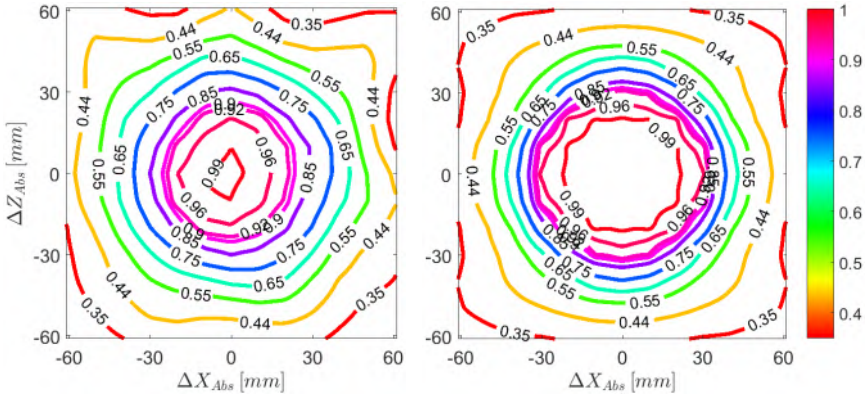

Figure 2.10: RT based sensitivity analysis of the intercept factor (γ) for different ΔZ_{Abs} and ΔX_{Abs} combinations and mirror shapes. The left graph shows results for a real RP3 concentrator with an RMS_{SDX} of 2.1$mrad$. The graph on the right side is based on an ideal mirror. For the given rim-angle, ΔZ_{Abs} and ΔX_{Abs} have similar impact. The characteristics of γ-decrease also depends on the RMS_{SDX}, as an ideal collector has a rather wide plateau without reduction of the performance, but than reacts with a sharp descent of the γ. This can be deduced from the distance between the γ-contour lines. A sun shape with a circumsolar ratio (CSR) of 0.05 was used during the RT simulation.

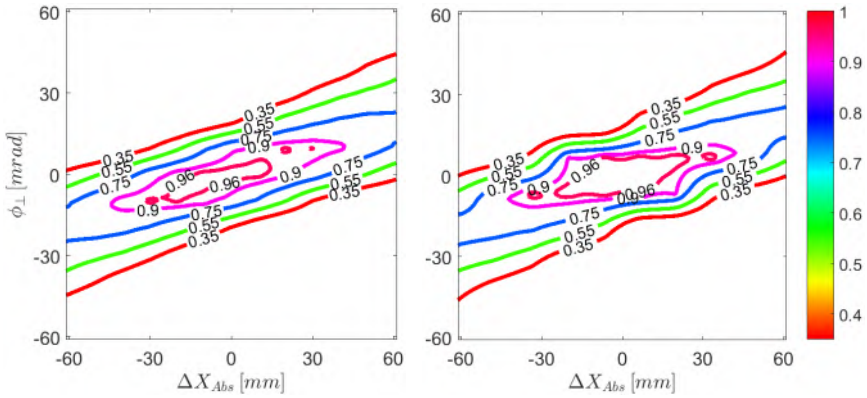

Figure 2.11: RT based sensitivity analysis of the intercept factor (γ) for different $\phi_\perp$ and ΔX_{Abs} combinations and mirror shapes. The left graph shows results for a real RP3 concentrator with an RMS_{SDX} of 2.1$mrad$. The graph on the right side is based on an ideal mirror. $\phi_\perp$ and ΔX_{Abs} may compensate or boost each other. The impact of 1 $mrad$ of $\phi_\perp$ is comparable to 2 mm of ΔX_{Abs} in a certain range. However, γ drops significantly after some $10 - 15\,mrad$. Higher RMS_{SDX} causes a wider beam spread, so that the sensitivity of the γ on $\phi_\perp$ is slightly decreased compared to the ideal mirror geometry. A sun shape with a CSR of 0.05 was used during the RT simulation.

SUMMARY

This chapter has shown that the concentrator geometry has a major influence on the overall performance of parabolic trough collector power plants. Tolerance for deviations from the design geometry are very small and are typically expressed in milliradians (*mrad*s) for slope and tracking deviations, and in *mm* for absorber tube displacement. In turn, the requirements on methods to measure the concentrator geometry are demanding. State of the art approaches are quite accurate, but they lack the possibility to characterize larger areas in an efficient manner.

The next chapter is dedicated to transient alterations of the collector geometry. It will shown that the parameters introduced in Section 2.2 are subject to operation loads (like wind) and operational state (like heat transfer fluid temperature (T_{HTF}) and tracking angle (θ)). In this context, a holistic mechanical PTC model will be developed.

3

OPTICAL AND MECHANICAL PROPERTIES OF PARABOLIC TROUGH COLLECTORS

Geometric PTC performance parameters like tracking deviation ($\phi_\perp$), slope deviation in curvature direction (SD_X), and absorber tube displacement $\Delta X_{Abs}/\Delta Z_{Abs}$ are in general a superposition of initial, static deviations of the mirrors and the structure on the one side, and deformations caused by external loads on the other side. Latter effects are subject to wind, bearing friction, gravitation (dead load), and thermal expansion.

As a consequence, the intercept factor (γ) is a function of the previous mentioned operational loads, and yield analysis must take into account the variability of γ. This chapters is dedicated to state-dependent operational loads and their effect on the geometry. A holistic optical and mechanical PTC model is developed, which takes into account the variability of the geometry under ambient conditions and operational loads.

Typical dependencies of γ on variation of the geometric deviations have been presented in Section 2.4.3. In this chapter, for each of the quantities $\phi_\perp$, SD_X, and $\Delta X_{Abs}/\Delta Z_{Abs}$, relevant operational loads and analytical deformation models are derived and compared with experimental data. This provides supplemental information for geometric information obtained by the airborne methods described in Chapter 4 and 5. That way, the collector geometry, which is in general measured close to zenith position, can be superimposed with relative deformation patterns for any operational state described by the tracking angle (θ) and the heat transfer fluid temperature (T_{HTF}). This is of particular interest because airborne determination of the PTC geometry is only possible for a certain state ($\theta \simeq 90°$), but for reliable forecasting annual yields, it is indispensable to have a comprehensive knowledge about the collector geometry under all relevant operation conditions.

The comprehensive integration of dynamic deformation information into ray-tracing and yield analysis[1] is the logical consequence of this approach. However, this step is beyond of the scope of this thesis. The objective is, at this stage, to develop and validate the state dependent deformation models.

1 including time series of the annual sun positions, corresponding tracking angle (θ), and the operational loads influencing the PTC geometry

3.1 DEPENDENCY OF MIRROR SHAPE ON OPERATIONAL LOADS

The influence of elevation angle, dead load, and metal structure on glass mirror tension, deformation, and hence on the performance of PTCs is a subject of various R&D activities (Möller, 2004; Meiser et al., 2013; Meiser, 2014; Meiser et al., 2015, 2017). The main reason for deformation is the sagging of the mirror panel between the non-rigid support points. The deformation is pronounced in curvature (X) direction, since the parabolic shape enhances the stiffens in Y-direction.

The position of the glass bracket retaining point (GBRP) in curvature direction has a mayor influence on the susceptibility of the mirror shape on dead load. Apparently, the RP3 design did not consider neither Bessel- nor Airy-points (Lewis, 1993, Appendix C.), which might be an explanation for the systematic sagging especially of the inner mirror (see Tab. 3.1 and Figure 3.1). The RP3 design was developed by Luz II Ltd[2] for the LUZ3 collectors deployed in the SEGS 7-9 plants in 1988 (Lovegrove and Stein, 2012, Table 7.2). Since then, the RP3 standard has apparently not been questioned any more.

Parameter	inner mirror	outer mirror
$L[mm]$	1641	1501
$D[mm]$	979	870
$\alpha = D/L$	0.597	0.580
α_{Bessel}	0.559	
α_{Airy}	0.577	
α/α_{Bessel}	1.067	1.036
α/α_{Airy}	1.033	1.004

Table 3.1: Comparison of mirror support point positions of the RP3 design with Bessel- and Airy-points. L and D refer to the arc-length of the extension (L) and the distance (D) between mounting points of the respective mirror panels in X-direction. The use of arc-length instead of true distance of a straight beam is an approximation, which does not affect the ratio α. For the inner mirror, there is a significant deviation from the ideal points of least deflection/bending, which is confirmed by the results of the photogrammetric deformation measurement presented in Figure 3.1

The influence of wind on the dynamic deformation of PTC mirror panels and the development of a suitable deflectometric measurement system was addressed in Wilbert (2009). During deflectometric field measurements, no significant deformations could be detected at wind velocities below $4\,m/s$. Maximum amplitudes obtained from acceleration sensors at higher wind speeds of $\leq 15\,m/s$ were in the range

2 today BrightSource Industries (Israel) Ltd

of $1 - 2.5\,mm$ with frequencies in the range of $1 - 2\,Hz$. Whether these deformations of mirror panels are relevant for the solar field performance was not yet investigated quantitatively, but the impact is expected to be negligible, compared to influence of wind forces on tracking-accuracy and torsion (Geyer et al., 2002; Lüpfert et al., 2001; Hosoya et al., 2008).

The objective of this section is the presentation of a photogrammetric approach to determine the relative deformation patterns as function of the tracking angle θ labeled $SD_{Xrel}(\theta)$, and the superposition of these patterns with absolute SD_X maps derived with QFly in zenith ($\theta = 90°$) position:

$$SD_X(\theta) = SD_X(\theta = 90°) + SD_{Xrel}(\theta) \tag{3.1}$$

This approach is based on the assumption that PTC types based on the same structure and mirror type show identical deformation behavior, so that one single measurement of $SD_{Xrel}(\theta)$ pattern can be applied to any other collector with identical structure and mirror type.

The photogrammetric measurement campaign to obtain relative deformation patterns SD_{Xrel} was carried out at the KONTAS test bench in July 2015 in the context of contributory work to another PhD thesis dedicated to the validation of finite element method (FEM) on the deformation of PTC mirror panels with strain-gauges measurements (Schneider et al., 2015). For this purpose, one row of mirror panels was equipped with retro-reflective marker with a density of 100 targets per m^2. The PG measurement was carried out for 13 different elevation angles. A step-width of 15° between different θ angles was selected, covering the range from 0° to 174°.

Zenith position $\theta = 90°$ was approached twice from both sides, since this position plays a special role as a reference for all other tracking angles. Transformation of the resulting 3D coordinates for each tracking angle into the design collector coordinates system was realized via best-fit of the measured GBRP points (see Equation A.1). Finally, SD_X maps were derived for each value of θ and subtracted from the reference position ($\theta = 90°$), resulting in $SD_{Xrel}(\theta)$.

Figure 3.1 presents the resulting deformation pattern and their influence on a SD_X map derived by $\text{QFly}_{\text{HighRes}}$ by superimposing the deformation pattern $SDx_{rel}(\theta)$ with the QFly result obtained at $\theta = 90°$. The maximum values of the deformation pattern $SD_{Xrel}(\theta)$ are a factor 3 below the absolute slope deviations in this case. Although the SD_X characteristics are notably altered from $\theta = 0°$ to $\theta = 174°$, the influence on the RMS_{SDX} of the mirror row is rather small.

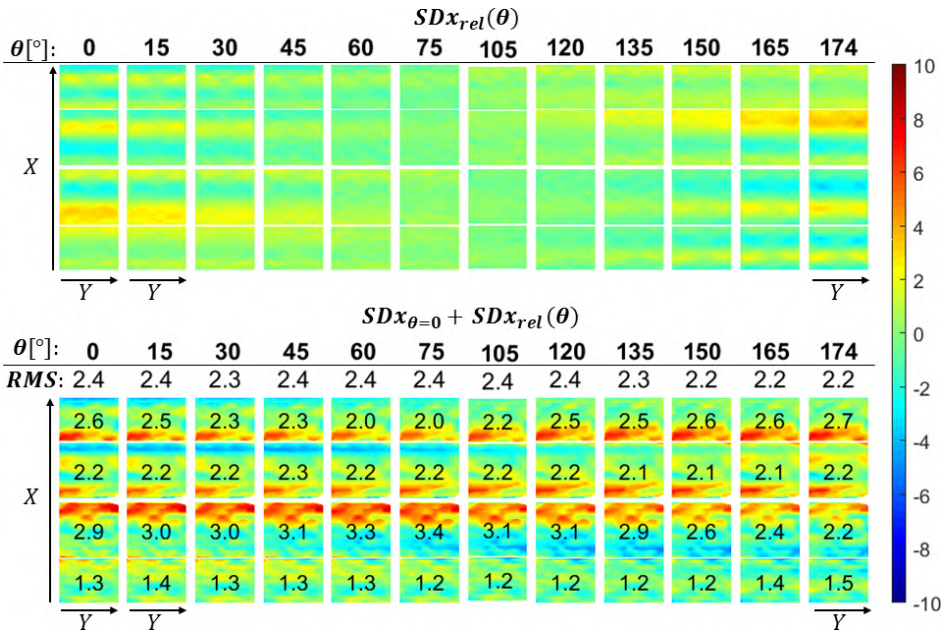

Figure 3.1: Top: $SDx_{rel}(\theta)$ from close range photogrammetry (PG) for all measured elevation angles θ. Each column represents the same mirror panel column next to the front end plate (FEP). Each column is assigned to a certain θ value. The deformation is pronounced for the inner mirror next to the vertex. Qualitative and quantitative accordance with FEM simulations as presented in (Meiser et al., 2013, Fig 6.) is given.
Bottom: $SDx(\theta)$ according to Equation 3.1. $SDx_{\theta=90°}$ was taken from a mirror row from a structurally identical SCE. Despite notably alteration of the slope deviation, RMS_{SDX} values per mirror panel are not altered significantly in this particular case.

3.2 DEPENDENCY OF ABSORBER TUBE POSITION ON HTF TEMPERATURE AND ELEVATION ANGLE

Typical causes for static absorber tube displacement in lateral direction (ΔX_{Abs}) and absorber tube displacement along the optical axis (ΔZ_{Abs}) were described in Section 2.2.3. This section provides a closer look on reversible deviations caused by different load cases and operating conditions. Absorber tubes are connected to the PTC structure via supports, which strive to keep the tube coaxial with the focal line during tracking. Finite lateral stiffness of the supports and the necessity for compensation of thermal expansion causes load-dependent deviations of the absorber tube from the focal line. These dynamic and reversible deviations must be added to static deviations arising from mounting accuracy or residual thermal stress.

The superposition of static and dynamic deformations are described in Eqs. 3.2 and 3.3, assuming that the tracking angle (θ) only affects

ΔX_{Abs}, whilst ΔZ_{Abs} is essentially influenced by the heat transfer fluid temperature (T_{HTF}). Vertical deviation are described by:

$$\Delta Z_{Abs}(T_{HTF} \neq T_0) = \Delta Z_{Abs}(T_0) + \delta Z_{Abs}(\Delta T) \tag{3.2}$$

Here, T_0 refers to the value of T_{HTF} when the absorber tube position measurement (see Section 2.3.2) was conducted. T_{HTF} is usually obtained from the solar field data acquisition system or by independent temperature measurements. A formula to derive relative absorber tube displacement along the optical axis ($\delta Z_{Abs}(\Delta T)$) for different temperatures differences $\Delta T = T_{HTF} - T_0$ is provided by Equation 3.5.

On the other hand, lateral deviations are described by:

$$\Delta X_{Abs}(\theta) = \Delta X_{Abs}(\theta = 90°) + \delta X_{Abs}(\theta) \tag{3.3}$$

The term δX_{rel} depends on the lateral stiffness of the supports and the combined weight of HCE and HTF (see Equation 3.4 and Figure 3.2).

3.2.1 *Lateral absorber tube deviation caused by dead load*

Gravitational effects can be categorized into sagging of the absorber tube between supports and deformation of the supports due to dead load in different elevation angles. For the first mentioned, sagging about $3\,mm$ for empty and $6\,mm$ for tubes filled with molten salt have been reported by Iverson et al. (2011). Relative lateral deviation at the support positions caused by the weight of a single HCE filled with HTF (M_{Abs}) should not exceed the range of $5\,mm$ (see Figure 2.10) taking into account additional geometrical imperfections.

Typical values for M_{Abs} are in the range of $40\,kg$ per support for receiver tubes designed for thermal oil[3]. When the HCE support is exposed to lateral forces (in X-direction, see Figure 3.2), the support itself is not deformed. Instead, the relatively narrow connection element between the support lever and the rest of the concentrator structure acts as a link. Thus, classical beam theory is not adequate to describe the deformation. Rather, the effect of M_{Abs} on absorber tube displacement in lateral direction as a function of the tracking angle (θ) can be described by a lever and a fixed hinge at the parabola vertex:

$$\Delta X_{Abs}(\theta) = k_{HCE} \cdot M_{Abs} \cdot g \cdot \cos(\theta) \cdot f \tag{3.4}$$

The spring constant describing the lateral torsion stiffness of the HCE support pivot point at the parabola vertex (k_{HCE}) is an experimentally determined parameter. The torque on the pivot is described by the

3 HCE: $\sim$ $28\,kg$; HTF per HCE: $\sim$ $12kg$. For direct steam generation PTCs, higher weights are found due to the increased wall strength to enhance the pressure resistance.

weight $M_{Abs} \cdot g$, the lever with length f, and the cosine of the tracking angle (θ).

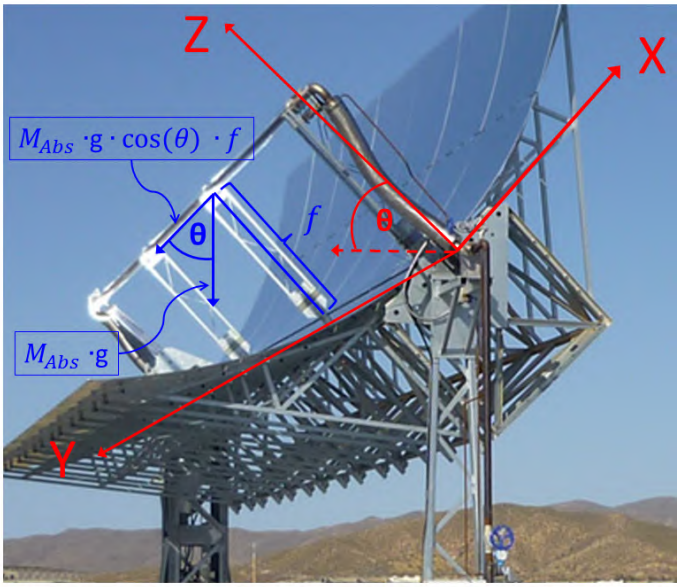

Figure 3.2: Derivation of the gravitational force and the torque acting on the HCE support hinge at the vertex. The absorber tube dead load causes absorber tube displacement in lateral direction (ΔX_{Abs}) as a function of the tracking angle, and depending on the spring constant describing the lateral torsion stiffness of the HCE support pivot point at the parabola vertex (k_{HCE}).

The HCE support lateral stiffness of an ET has been quantified at the KONTAS facility by introducing moderate forces of up to 500 N to the support while measuring the relative lateral deflection, which was in the range of 1 $mm/100\,Nm$. Values for prototypes of other PTC models of up to 30 mm displacement between zenith and horizon position have been reported in Stynes and Ihas (2012a)[Section 8.3], which is far beyond the tolerances.

3.2.2 *Lateral absorber tube deviation caused by REPA forces*

At the outer ends of each solar collector assembly (SCA), rotation and expansion performing assemblys (REPAs) (see Figure 3.5) are installed to compensate for the rotation of the collector and thermal expansion of the absorber tube relative to the plant header and cross over pipes. REPAs introduce additional forces and torque, by dead load and friction. Such deformations have been quantified using the methods described in Section 2.3.2 at a single EuroTrough (ET) SCE mounted at the KONTAS test facility at PSA. A hysteresis can be observed (see Figure 3.3), as friction depends on the previous direction of motion. The influence on the performance of observed moderate deflections

can be neglected in typical solar fields, as only 5% of the HCEs are affected. However, airborne measurements presented in Section 4.2.2 and Figure 4.8 reveal interesting behavior and rather strong lateral deflections probably due to REPA swivel joint friction, which may be used as an indicator for forthcoming REPA failure.

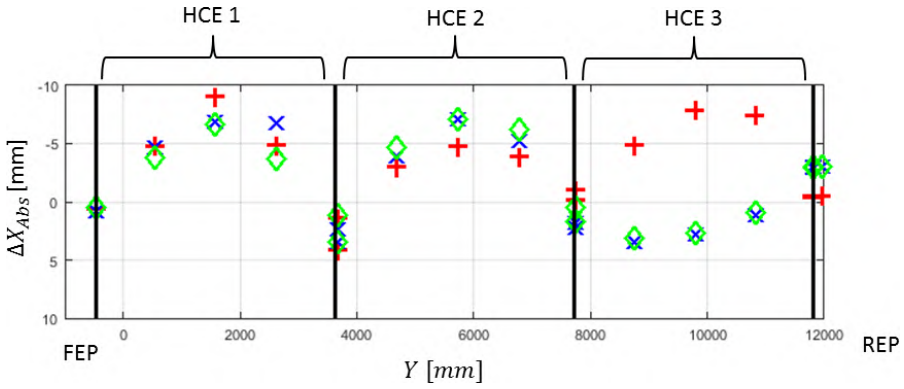

Figure 3.3: Hysteresis of absorber tube displacement in lateral direction (ΔX_{Abs}) measured for $\theta = 90°$ for different directions of motion. For blue and green symbols, the zenith position has been approached repeatedly from $\theta > 0°$, while red symbols refer to approaches from the opposite direction. The HCE towards the rear end plate (REP) suffers significant deformation due to friction loads from the flexible tube connectors. Towards the FEP, deformations are avoided by a reinforced structure.

3.2.3 *Vertical absorber tube deviation caused by thermal expansion*

The nominal operation temperature ($T_{HTF_{nom}}$) of PTC plants using thermal oil as HTF is increasing from the loop inlet ($293°C$) to the loop outlet ($393°C$), on a distance of $\simeq 600\,m$ corresponding to 4 SCAs. The design of individual SCAs is adapted to keep the absorber tube close to the focal line at the local nominal operation temperature by different length of the fixed pipes at the "A-Frame" (see Figure 3.4) at the drive pylon. These fixed pipes have an decreasing length with increasing distance from the cold header inlet. According to the description on page 14, the thermal expansion due to temperature shifts between the early morning before sunrise ($T_{HTF} \sim 150°C$) and nominal operation temperature ($293°C \leq T_{HTF} \leq 393°C$) is compensated by the pivoted HCE supports (see Figure 3.4). The thermal expansion coefficient α_T describes the expansion of the absorber tube (see Equation 3.7).

Height variations of the absorber tube due to thermal expansion $\delta Z_{Abs}(\Delta T)$ can thus be expressed by the tilt angles β of the HCE supports which are determined by the difference ΔY between static base positions and top positions affected by thermal expansion (see Figure 3.5). Base positions refers to the link, where the HCE supports are connected to collector structure. Top position refers to connection between HCE and the support close to the focal line. For $T_{HTF} <$

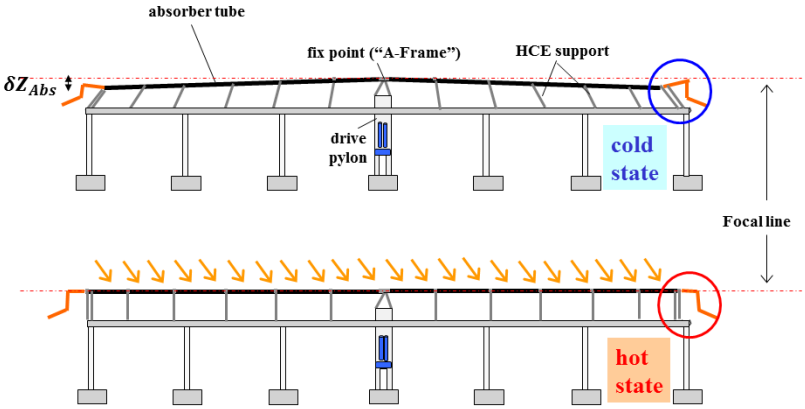

Figure 3.4: Sketch of PTC with HCE at ambient temperature (top, cold state) and at nominal operation temperature (bottom, hot state). Thermal expansion is compensated by tilting of the HCE supports, which leads to increasing ΔZ_{Abs} towards the trough ends in the cold state. The assumptions of vertical supports at nominal operation temperature is only an approximation. Due to design issues, even at $T_{HTF} = T_{HTF_{nom}}$, not all the supports are vertical.

$T_{HTF_{nom}}$, the supports are tilted towards the drive, and the absorber tube center line is located below the focal line.

Equation 3.5 provides an approximation for vertical displacement depending on the thermal expansion of the absorber tubes relative to the fixed points of the supports $dY(\alpha_T, Y, \Delta T)$. Figure 3.5 outlines and explains the assignment of the parameters b, β, l, and dY.

$$\delta Z_{Abs}(\Delta T) = f - b - \cos(\beta) \cdot l \tag{3.5}$$

with

$$\beta = \arcsin\left(\frac{\Delta Y}{l}\right) \tag{3.6}$$

and

$$\Delta Y = Y_{cold} \cdot (\Delta T \cdot \alpha_T + 1) - Y_{Base} \tag{3.7}$$

Y_{cold} refers to the individual Y-position of HCE interconnections at ambient temperature, which is determined by the cold HCE length and the fixed pipes at the "A-Frame". Y_{Base} refers to the HCE-support position at the vertex. Reversible vertical deflections $\delta Z_{Abs}(\Delta T)$ are part of the normal operation procedure and no long term effect on life time of the plant was reported yet. Effects on the optical performance are presented in Figure 2.10. The outer SCEs experience significant reduction of the intercept factor down to $\gamma = 0.75$ during start-up, when the absorber tube displacement along the optical axis (ΔZ_{Abs}) is in the range of $-30\,mm$ (see also Figure 2.10).

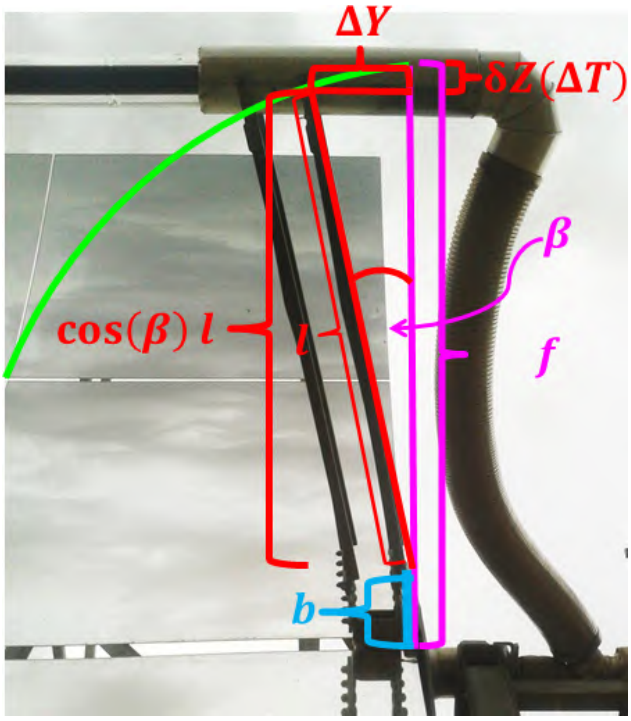

Figure 3.5: Estimation of the relative absorber tube displacement along the optical axis ($\delta Z_{Abs}(\Delta T)$). Here, f is the focal length, b is the distance of the support pivot from vertex. ΔY is the longitudinal displacement caused by thermal expansion, influencing the tilt-angle β. In the right side of the image, a rotation and expansion performing assembly (REPA) is visible.

The equations presented here are in particular used to estimate ΔZ_{Abs} as input parameter for measurements of the effective slope deviation in curvature direction (SD_{Xeff}) with $\text{QFly}_{\text{Survey}}$. When the solar field is not in operation and T_{HTF} is significantly lower than $T_{HTF_{nom}}$, then the appearing vertical absorber tube deflections are so pronounced, that application of Equation 3.5 is essential to derive reasonable SD_{Xeff} results. The presented approach assures, that the SD_{Xeff} result is independent from T_{HTF}.

Figure 3.6 presents a comparison between measured and modeled vertical deflection caused by low T_{HTF} based on $\text{QFly}_{\text{HighRes}}$ data for an entire SCA. The qualitative comparison shows very good matching of model and measurement, in particular if one considers the uncertainty of the initial support tilt angles.

Figure 3.7 presents the range of temperature induced vertical absorber deflection $\delta Z_{Abs}(\Delta T)$ for different values of T_{HTF} and typical uncertainties for the temperature profile along the SCA.

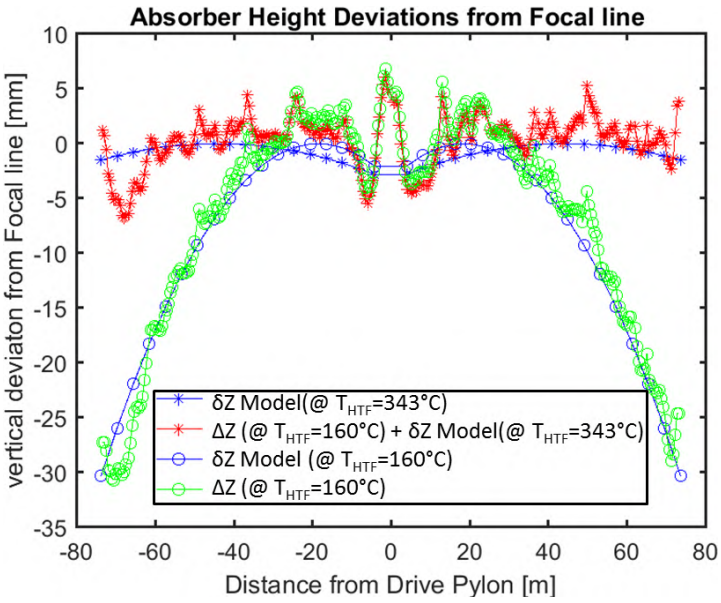

Figure 3.6: Modeled, measured, and temperature-corrected profiles of the ΔZ_{Abs} for an entire SCA . The nominal operation temperature ($T_{HTF_{nom}}$) of this SCA is 343°C, while the measurement of the absorber tube position was carried out $T_{HTF} = 160°C$. Differences between model and measurement are subject to static deviations arising from mounting inaccuracies. Especially the A-Frame at the drive pylon shows a prominent peak.

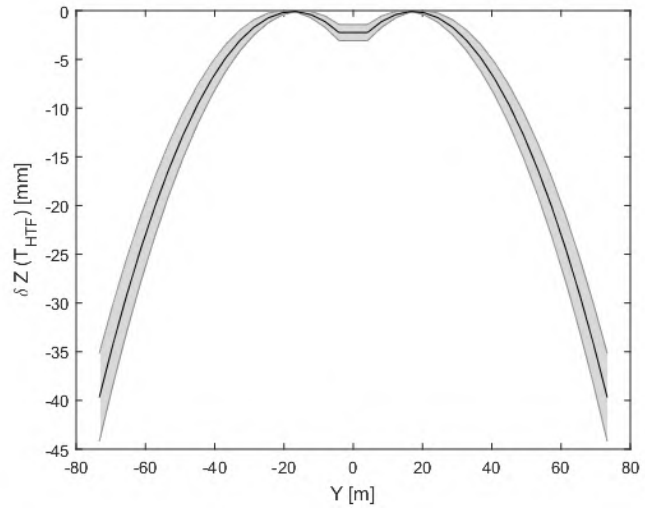

Figure 3.7: Variability of vertical absorber tube deflections due to thermal expansion $\delta Z_{Abs}(\Delta T)$. The uncertainty of the T_{HTF} was set to 5°C, which includes the effect of temperature sensor offset and the rough approximation of a constant T_{HTF} along the whole SCA. The average uncertainty of the vertical absorber tube position is in the rang of $\simeq \pm 4mm$. This variability is used as input parameter for the uncertainty estimation for $\text{QFly}_{\text{Survey}}$ in Section 5.3.2.

3.3 DYNAMIC TRACKING DEVIATION

Similar to the foregoing sections, the tracking deviation ($\phi_\perp$) can be divided in static misalignment[4] and dynamic deviations due to operation loads like unbalance, friction, and wind, as described by Equation 3.8.
The objective of this section is to describe the mechanical behavior of the entire SCA relative to the tracking angle (θ) set by the drive system. This investigation does not provide any information about the correct orientation of the PTC with respect to the incoming solar radiation, as this involves also the performance of the tracking sensors and algorithms.

$$\phi_\perp(\theta, \dot{\theta}, \overrightarrow{V_{Wind}}) = \phi_\perp{}^{initial} + \phi_\perp(\theta, CMS_{XZ}) + \phi_\perp(\dot{\theta}, \overrightarrow{M_{fr}}) + \phi_\perp(\overrightarrow{V_{Wind}}) \tag{3.8}$$

Here, $\phi_\perp{}^{initial}$ represents the static misalignment of each SCE, which is subject to assembly accuracy.
A further term $\phi_\perp(\theta, CMS_{XZ})$ describes the twist of the SCA due to static unbalance. The torque is created by the deviation of the SCEs CMS from the axis of rotation (CMS_{XZ}), depending on the actual value of the θ.
The torque caused by bearing friction ($\overrightarrow{M_{fr}}$) depends also on the history of θ. This is indicated by the functional dependence $\phi_\perp(\dot{\theta}, \overrightarrow{M_{fr}})$, which will result in a hysteresis when the tracking direction is reversed. Finally, wind induced torque and the resulting twist of the SCA can be considered by the term $\phi_\perp(\overrightarrow{V_{Wind}})$.

In order to describe the tracking and torsion behavior of an entire SCA, a semi-analytical model (see Section 3.3.1) was set up in MATLAB. This model provides the option to simulate the tracking behavior for any combination of parameters and motion patterns. In addition, parameters can be fitted to measured inclinometer data, in order to obtain values for the parameters unbalance (CMS_{XZ}) and friction ($\overrightarrow{M_{fr}}$).

Inclinometer measurements were carried out at the first ET prototype located at the PSA for different motion patterns and load cases, delivering information about the mechanical torsion stiffness and the response of the system on operation loads (see Section 3.3.2). Finally, model and measured data are combined in Section 3.3.3 in order to determine parameters for unbalance and bearing friction.

4 due to mounting inaccuracies

3.3.1 *Analytical model*

The response of a mechanical system on external forces is commonly analyzed with finite element method (FEM). For the present scope, setting up a semi-analytical, one-dimensional, and parametrized model is the preferred option, because such a model provides the performance relevant parameter ($\phi_\perp$) as function of only a few parameters describing the collector and operational loads. Such a model can be easily adapted to any collector design without the elaborate procedure of setting up the detailed collector model in the FEM software.

The principle behind this model is to iteratively balance the resulting torque values at each support pylon between adjacent SCEs. The set value of the tracking angle θ is provided by the drive pylon, and the orientation of each solar collector element (SCE) is determined under the boundary condition, that the resulting cumulated torque has to be smaller than the $\overrightarrow{M_{fr}}$ at each bearing or support pylon. Figure 3.8 provides a graphical representation and the definition of involved variables and parameters for a reduced[5] SCA.

The analytical model uses the following approximations:

- The moment of inertia is not considered, e.g. the kinetic energy provided by the angular acceleration and the resulting angular momentum of the SCA are not taken into account by the model. This approximation is justified, because despite the high moment of inertia, angular velocities are very small ($\simeq 3\,mrad/sec$).
- Each SCE, including the connection element to the neighboring SCE, is characterized by a single spring constant describing the torsion stiffness of one SCE (k_{SCE}). As a consequence, the θ-value for the rear end plate (REP) of SCE_I equals the θ-value for the front end plate (FEP) of SCE_{II}, In reality, twist occurs also between adjacent SCEs. However, the behavior of the entire SCA can be modeled that way, since the twist appearing at the connection is considered by the module structure.
- For the calculation of the torque caused by bearing friction ($\overrightarrow{M_{fr}}$), the static friction coefficient (μ_s) is set equal to the kinetic friction coefficient (μ_k). For well lubricated bearings, where no noise indicating stick-slip phenomena is audible, the assumption:

  $$\mu_s \simeq \mu_k$$

  is justified. For sticking bearings, the model will predict an average between μ_s and μ_k under the presented assumption.

5 typical SCAs constellations in commercial CSP see Table 1.1

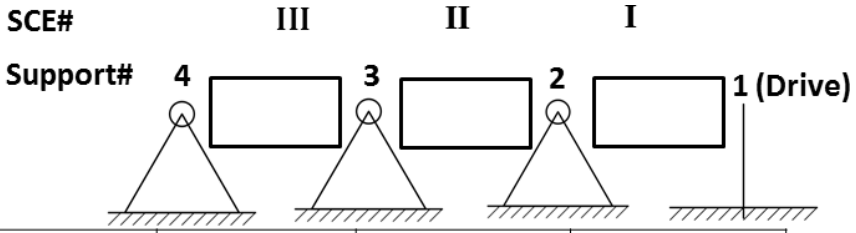

$\tau_{\delta\theta}$	0	$\delta\theta_{III} \times k_{SCE}$	$\delta\theta_{II} \times k_{SCE}$
$\delta\theta$	$\theta(4) - \theta(3)$	$\theta(3) - \theta(2)$	$\theta(2) - \theta(1)$
$Load(iSCE)$	$\tau_{CMS}(iSCE) + \tau_{Wind}(iSCE)$		
$\Sigma\tau(iSupp)$	$\tau_{\delta\theta_{iSCE+1}} + (\delta\theta \times k_{SCE}) + Load(iSCE)$		

Figure 3.8: Sketch of the 1-dimensional SCA model to describe the tracking behavior. The depicted model consists only out of three SCEs for better comprehensibility. Roman numbers denote the SCE ID, while the support pylons are identified by Arabic numbers. The drive pylon provides a fixed support, while the normal pylons allow for rotation around the Y-axis[a].
$\tau_{\delta\theta}$ denotes the torque acting on each SCE from the left (open end). This is zero for the outermost SCE, and $\delta\theta \cdot k_{SCE}$ elsewhere. $\delta\theta$ is the twist between the FEP and the REP of each SCE.
Torques τ are accumulated towards the drive pylon. The sum of torques acting on each bearing is $\sum\tau$, which is composed of the torque acting from the left, the twist of the right SCE, and external loads (unbalance & wind).

a characterized by the torque caused by bearing friction ($\overrightarrow{M_{fr}}$) (see Tab. 3.2)

The simulation is carried out by feeding the model with a vector of equally spaced θ set-points for the drive pylon and a set of parameters describing the mechanical properties of the collector and the load cases. A set of starting values is provided in Tab 3.2. For each θ-value set by the drive pylon, a while loop is repeated and adjusts orientations at each support pylon:

$$\theta_{i+1}(\#_{Supp}) = \theta_i(\#_{Supp}) + \Delta\theta \tag{3.9}$$

until the torques between all SCEs are smaller than the friction coefficient (Equation 3.10):

$$\Delta\theta = \begin{cases} \frac{\sum\tau - \overrightarrow{M_{fr}}}{k} & \text{for } |\sum\tau| > \overrightarrow{M_{fr}} \\ 0 & \text{for } |\sum\tau| \leq \overrightarrow{M_{fr}} \end{cases} \tag{3.10}$$

The results of the simulation based on the initially assumed parameters (see Table 3.2) are presented in Figure 3.9 and 3.10.

Param	Value	Unit	Comment
$\#\,of$ SCEs	6		half SCA
M_{SCE}	2000	kg	(Lüpfert et al., 2001, Table 2)
k_{SCE}	2	$^{kNm}/_{mrad}$	see Section 3.3.2
CMS_x	0.000	m	estimate
CMS_z	0.010	m	estimate
$\overrightarrow{M_{fr}}$	0.15	kNm	estimate
$\overrightarrow{M_{Wind}}$	0	kNm	not considered

Table 3.2: Initial values for the parameters of the tracking model. M_{SCE} denotes the total weight of a single SCE. The spring constant describing the torsion stiffness of one SCE is denoted by k_{SCE}. The CMS_{XZ} denotes the deviation of the center of mass (CMS) from the rotation axis. $\overrightarrow{M_{fr}}$ denotes bearing friction. So far, the model provides no dependence of the wind torque on the tracking angle (θ), which is essential for realistic representation (Hosoya et al., 2008). For this reason, the influence of wind-induced forces is not considered.

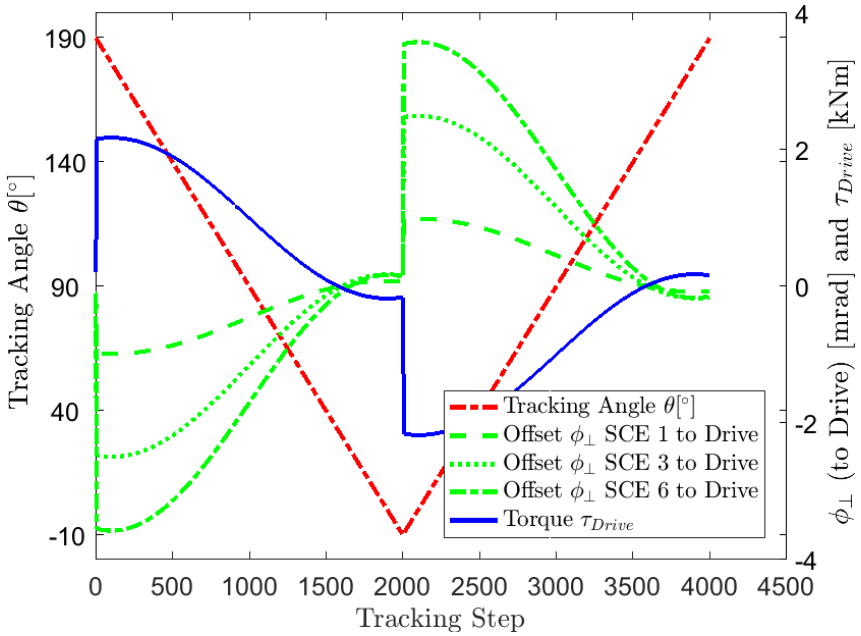

Figure 3.9: Behavior of the semi-analytical tracking model for the parameters defined in Table 3.2. The tracking angle (θ) angle (red line) was altered from $180° \rightarrow 0°$ and back to $180°$ in steps of $0.1°$. Due to the location of the center of mass, the torque load at the drive pylon (τ_{Drive}) (blue) has to work against gravity and friction to lift the SCA to zenith position $[180° \leq \theta \leq 90°]$. After crossing zenith, the unbalance supports the direction of motion, so that the torque required to move the SCA and the twist $\phi_\perp$ between SCEs decreases towards $\theta = 0°$. In the tipping point, τ_{Drive} increases again until the twist (green lines) reaches its maximum value.

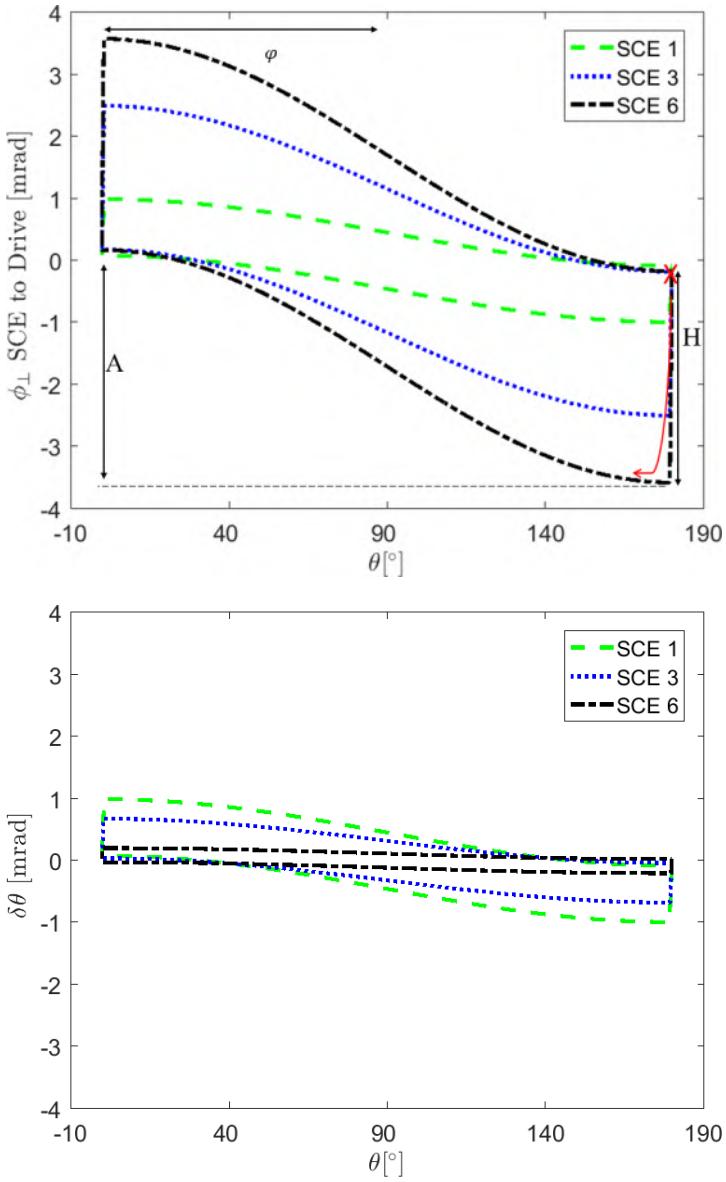

Figure 3.10: Simulated tracking deviation ($\phi_\perp$) of each SCE relative to the drive pylon (top), and twist $\delta\theta$ within each SCE (bottom). The red cross and arrow mark the starting point and motion direction. The largest tracking deviation ($\phi_\perp$) appears at the outer SCE, while the largest twist $\delta\theta$ is observed next to the drive, where all torque is accumulated. Friction can be directly observed from the hysteresis H, while the sinus curve is caused by the unbalance. The phase shift φ and the amplitude A are determined by the location of the CMS_{XZ}.

3.3.2 *Measurement of torsion stiffness*

Measurement of the spring constant describing the torsion stiffness of one SCE (k_{SCE}) is performed by applying a stepwise increasing torque at the REP of the outermost SCE and simultaneously measuring the relative twist at different positions within the SCA with digital inclinometers[6]. Since only relative values are of interest, the mounting of the inclinometers to the SCE end-plates can be performed with comparatively little effort, as the accurate arrangement with respect to the X-axis (see p. 135) is not required.

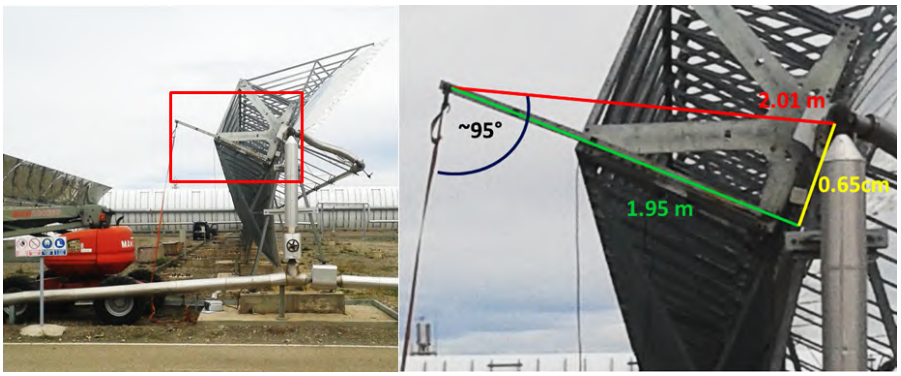

Figure 3.11: Set-up for the the measurement of torsion stiffness: The lever attached to the REP of the last SCE serves to impinge increasing torque for the measurement of k_{SCE}. A securing strap with integrated force meter was used to pull down the lever of 2.01 m length.

Two torsion stiffness measurements were carried out on 2016-03-09 at the ET prototype collector at the PSA (see also Figure A.1). A large lever is attached to the collector structure (see Figure 3.11) in order to achieve high torque values necessary to obtain a clear twist signal. The lever was loaded with up to 1800 N resulting in a maximum torque of 3.6 kNm. Bearing- and REPA friction affects the response of the SCA in successive measurements leading to certain spread of the resulting k_{SCE} values. The k_{SCE} is obtained from a linear fit to the measured τ vs. $\delta\theta$ curve, resulting in an average value of $k = 2.1 \pm 0.25\,[kNm/mrad]$ (see Figure 3.12).

3.3.3 *Twist measurement and comparison with model*

The semi-analytical model presented in Section 3.3.1 was validated with a field measurement by executing the same tracking motion and similar locations of data acquisition. Four inclinometer assemblies[7]

6 Zerotronic Typ C from WYLER (WYLER, 2016)

7 consisting of two inclinometers mounted 90° to each other on magnetic adapter. The 90° tilted mounting extents the $\pm 60°$ measurement range of a single inclinometer to $\pm 105°$ with two overlapping areas of 15° each.

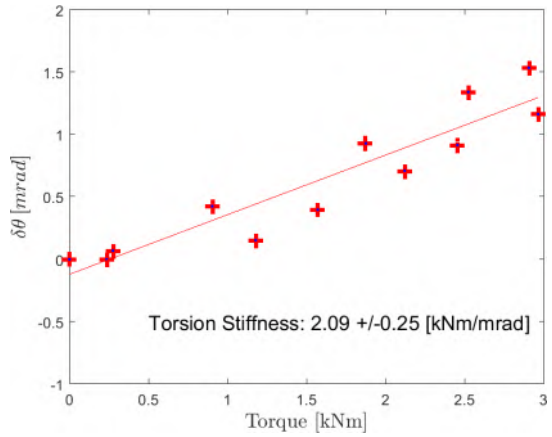

Figure 3.12: Results of the linear regression to determine the spring constant describing the torsion stiffness of one SCE (k_{SCE}). The rather high relative uncertainty of k_{SCE} is caused by the fact that the data was taken from two successive measurements with different boundary conditions (see Figure A.1).

were mounted to the EuroTrough (ET) prototype collector at the PSA as depicted in Figure 3.13.

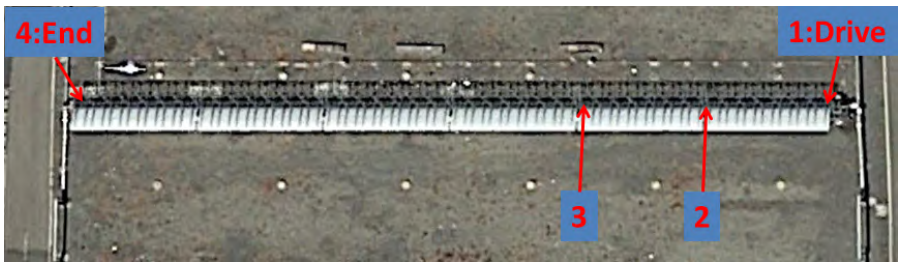

Figure 3.13: Google maps view on the east-west orientated EuroTrough (ET) prototype SCA at the PSA. The SCA extension in east west direction is approximately $70\,m$, which corresponds to a total number of six SCEs. Inclinometer assemblies have been attached to the drive (1), to the FEP of the 2^{nd} SCE (2), to the REP of the 2^{nd} SCE (3), and to the REP of the 6^{th} SCE (4).

Previous experiments lead to the conclusion that inclinometer read-out on the moving SCA is subject to severe synchronization problems. For this reason, the SCA was moved from south ($\theta = 0°$) to north ($\theta = 180°$) and back in $5°$ steps in order to provide sufficient time for inclinometer read-out. The resulting data had to undergo certain corrections (sign convention, off-set correction), until receiving the characteristic curve showing the imprint of friction and unbalance (see Figure 3.14).

The three parameters CMS_x (lateral deviation of the CMS from the axis of rotation), CMS_z (vertical deviation of the CMS from the axis of rotation), and $\overrightarrow{M_{fr}}$ for the friction per support bearing were determined by minimizing the difference between measured data and

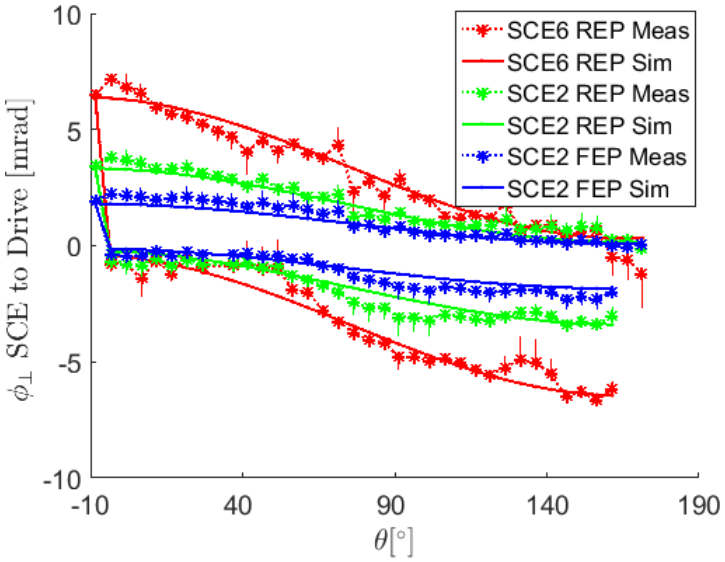

Figure 3.14: Fit of parameters of the analytical tracking model to inclinometer data for three different positions within the SCA. Each curves shows the simulated and measured hysteresis of the tracking deviation ($\phi_\perp$) relative to the drive pylon. Vertical lines at each measurement point represent the residuals between measurement and model. The model describes well the observed behavior of the collector. The *RMS* value of residuals (marked by vertical lines) between model and measurement is 0.4 *mrad*. Deviations are smaller for data gathered close to the drive pylon, compared with the red curve originating from the last SCE. The observed deviations are supposed to arise from local, tracking angle dependent variation of $\overrightarrow{M_{fr}}$, which was approximated by a single, average value representing the whole SCA.

simulation (see Figure 3.14). CMS_x, CMS_z, and $\overrightarrow{M_{fr}}$ are un-correlated, and their effect on the appearance of the $\phi_\perp$ vs. θ curve can be well distinguished. The torque caused by bearing friction ($\overrightarrow{M_{fr}}$) determines the hysteresis, while the *CMS* position determines amplitude and phase-shift of the wave-form (see Figure 3.10). The objective function for this optimization provides the *RMS* values of $\phi_\perp$ difference for corresponding data points. The finally obtained least value for the residuals *RMS* value was 0.4 *mrad*.

The resulting values for the unbalance and friction (see Table 3.3) were considerably higher than the initial assumptions (see Table 3.2). They are not representative for state of the art ET collectors in commercial PTC power plants. Nor is the observed under-performance in terms of increased bearing friction of the collector caused by its operation life. The issues observed here in terms of unbalance were solved in the later SKAL-ET project (Lüpfert et al., 2005).

The combination of inclinometer measurements obtained from a complete tracking cycle and the semi-analytical model allows to determine friction and un-balance of PTCs, which is of prior importance to

Param	Value	Unit
CMS_x	0.004 ± 0.001	m
CMS_z	0.015 ± 0.002	m
$\overrightarrow{M_{fr}}$	0.35 ± 0.05	kNm

Table 3.3: Values for the parameters of the tracking model obtained from the fit of the model parameters CMS_x, CMS_z, and $\overrightarrow{M_{fr}}$ to the measured data. Friction values are atypically high because of poor maintenance. Unbalance is negligible along the X-axis but pronounced along the (optical) Z-axis. The rough uncertainty estimation is based on the RMS value of residuals of the fit, which leads to a relative uncertainty of the model in the range of 15-20%.

the optical performance (see Figure 2.11). Random samples of the inclinometer measurements described here allow to estimate typical friction and unbalance values for certain collector type and solar field, and to determine expected tracking deviation ($\phi_\perp$) for all relevant states of operation. These results may be used in a holistic ray-tracing (RT) and yield analysis, by combining effective slope deviation in curvature direction (SD_{Xeff}) and effective tracking deviation ($\phi_{\perp eff}$) results from airborne qualification in zenith position (see Section 4.2.5, 5.2.2, and 5.2.3) with modeled $\phi_\perp$ for each SCE. A concept to quantify not only static inter-SCE misalignment but also bearing friction with airborne measurements in order to overcome the restrictions of inclinometer based data acquisition will be presented in Section 6.3.

SUMMARY

In this chapter, the dependency of the collector geometry on the operational state and operational loads has been investigated in detail. A holistic, mechanical model for PTCs has been developed. This involves the dependency of the slope deviation in curvature direction on the tracking angle θ, the relation between heat transfer fluid temperature (T_{HTF}) and absorber tube displacement along the optical axis ΔZ_{Abs}, and the relation between tracking angle (θ) and absorber tube displacement in lateral direction ΔX_{Abs}. In addition, a simple but efficient model has been developed, which predicts the torsion of the SCA.

In the future, this holistic PTC model can be used to realize realistic predictions of the γ and such the annual yield, by combining the model with airborne determination of the PTC geometry as presented in the following chapter.

4

AIRBORNE GEOMETRICAL CHARACTERIZATION OF PARABOLIC TROUGH COLLECTORS

Optical measurement techniques are the first choice to determine the geometric, optical, and also thermal[1] properties of PTC solar fields. The application of UAVs is a natural consequence to overcome restrictions arising from state of the art, ground based data acquisition with stationary cameras. Going airborne offers the possibility to automatically obtain high resolution information on the concentrator geometry for large fractions or even the entire solar field with virtually no impact on plant operation. Among approaches[2] to obtain the PTC collector geometry, deflectometric distant observer (DO) techniques exploiting the absorber tube reflection offer unbeatable benefits compared to scanning or pure photogrammetric approaches, because apart from the camera, no additional installations or manipulations in the solar field are required.

Comprehensive investigations on the potential of airborne characterization of PTC solar fields have been conducted by NREL about ten years ago (Jorgensen et al., 2009). At DLR, the first attempt to transfer of the TARMES principle to airborne data data-acquisition is described in Meiser (2008). The topic has been picked up again in 2011 in the scope of the enerMENA[3] project. Since then, the airborne qualification of CSP Plants (QFly) has been continuously developed, culminating in the current thesis.

Public perception of the utilization of UAVs is strongly influenced by non-civil applications and also by news about negligent handling e.g. around airports. On the other hand, civil application in the area of law enforcement (Finn and Wright, 2012), agriculture (Herwitz et al., 2004), disaster management (Maza et al., 2011), and monitoring RE installations like wind turbines (Morgenthal and Hallermann, 2014) and PV power plants (Quater et al., 2014) demonstrate the vast potential of UAV applications for the overall social and economic benefit. Photogrammetry and remote sensing is the primary area of application for UAVs (Colomina and Molina, 2014).

1 infrared thermography to quantify HCE heat loss (Jorgensen et al., 2009)

2 see Section 2.3

3 Project funded by the German Federal Foreign office in order to support a sustainable implementation of CSP Technology in the MENA (Middle East and North Africa) Region (Qoaider et al., 2011)

After a long period with hardly any legal regulation of UAV handling, the commercial and scientific use of small UAVs is subject to national legislation, which complicates the cross boarder application of highly specialized measurement techniques like QFly. This subject will be brought up again in Chapter 6.2.

This chapter describes the $\text{QFly}_{\text{HighRes}}$ mode, which is characterized by a rather complex flight route, low flight altitude and the ability to obtain slope deviation in curvature direction (SD_X), absorber tube displacement along the optical axis (ΔZ_{Abs}), and absorber tube displacement in lateral direction (ΔX_{Abs}) with high spatial resolution and excellent measurement accuracy. Since the $\text{QFly}_{\text{HighRes}}$ approach does not permit to characterize a complete solar field with adequate effort, another measurement mode denoted $\text{QFly}_{\text{Survey}}$ using the same hardware but a different flight mode is presented in Chapter 5. The $\text{QFly}_{\text{Survey}}$ mode enables a quick screening of the entire solar field, obtaining effective slope deviation in curvature direction (SD_{Xeff}) and effective tracking deviation ($\phi_{\perp\,eff}$) at lower spatial resolution. As the hardware of QFly consists of "off the shelf" components, the main issue are software algorithms for way-point route creation, image processing, camera positioning and approaches to deduce the PTC geometry from airborne images.

In the first place, this chapter describes the scope of the $\text{QFly}_{\text{HighRes}}$ approach and the interaction with parameters relevant for the optical performance, that can not be derived by airborne methods. Next, the selected hardware (UAV and camera) will be presented (Section 4.1.1), followed by the description of what is considered the optimal way of data acquisition (Section 4.1.2). The evaluation of the raw data (which exclusively comprises airborne images) to derive the concentrator geometry is described in Section 4.2. Here, mainly deflectometric methods and close range photogrammetry are deployed. Finally, a comprehensive uncertainty analysis and validation is presented in Section 4.3. This validation also involves the comparison of optical and thermal performance measurements for a single SCE.

4.1 SYSTEM DESCRIPTION

The airborne measurement system QFly was developed to obtain spatially high resolved geometric data of PTC collector fields. The data is used in subsequent RT analysis to determine the intercept factor (γ) as a function of geometric properties, mainly the absorber tube deviation ΔZ_{Abs} and ΔX_{Abs} and the mirror shape SD_X. However, there are some variables and effects influencing the intercept factor and finally the optical performance η_{opt}, which can not be determined by QFly, so that additional approaches are required. Table 4.1 provides an overview on

all quantities relevant for the optical performance, and the assigned measurement methods.

The $QFly_{HighRes}$ measurement procedure (see Figure 4.1) can be split into three phases. Preparation involves all pre-flight tasks like creation of waypoint (WP) routes and preparatory work in the solar field like collocation of coded photogrammetric targets and measuring of reference distances. The second step is the image acquisition. All necessary data for a single SCA is collected during a rather short flight of 20 *min*. Last, image processing and evaluation of the collector performance is denoted by post-flight operations. All steps of the work flow are structured in way to enable the evaluation of an arbitrary number of SCEs and SCAs.

Higher flexibility and universal applicability is achieved by a firm distinction between measurement and evaluation. Thereby, airborne image acquisition can be out-sourced to UAV service providers. This is highly relevant, because rapidly evolving national regulations require a certain flexibility like outsourcing the data acquisition and the application of common UAVs with good availability.

Parameter	Method	Variability	Comment
SD_X	$\text{QFly}_{\text{HighRes}}$	$= f(\theta)$	see Section 3.1
SD_{Xeff}	$\text{QFly}_{\text{HighRes}}$, $\text{QFly}_{\text{Survey}}$	$= f(\theta)$	
SD_Y	QDec	$-$	(see Section 2.3.1) (Ulmer et al., 2012; Weber et al., 2014)
ΔX_{Abs}	$\text{QFly}_{\text{HighRes}}$	$= f(\theta, \dot{\theta})$	see Section 3.2
ΔZ_{Abs}	$\text{QFly}_{\text{HighRes}}$	$= f(T_{HTF})$	
$\phi_\perp$	inclinometer	$= f(\theta, \dot{\theta})$	see Section 2.3.3
$\phi_{\perp eff}$	$\text{QFly}_{\text{Survey}}$	$= f(\theta, \dot{\theta}, \Delta X_{Abs})$	see Section 3.3
Blocking and Shading	Modeling, RT	$= f(T_{HTF}, \phi_{\|\|})$	(Lüpfert et al., 2004a)
ρ_{Ref}	Specular Reflectometer (D&S, 2017)	Degradation	(Meyen et al., 2009)
χ	TraCS, Specular Reflectometer	Soiling	(Wolfertstetter et al., 2012)
τ_{Glass} / α_{Rec}	Laboratory- and field measurement	Degradation	(Pernpeintner et al., 2015; Espinosa-R. et al., 2016b)

Table 4.1: List of PTC performance parameters and associated measurement methods. The 3rd column (variability) denotes if the measured parameter is subject to the operational state. All geometric parameters can be determined by QFly, except SD_Y. The variability of SD_Y can be neglected because the mirror shape in longitudinal direction shows low susceptibility to gravitation (Meiser et al., 2013). In addition, the impact of SD_Y on the annual performance yield is a factor 10 below the impact of SD_X (Ulmer et al., 2009). So the inability of QFly to measure SD_Y is not considered a drawback. The position and effect of blocking- and shading objects (mainly bellow protections and HCE supports) is taken from drawings and assessed by RT. Their variable position is obtained similar to the approach described in Section 3.2.3. Optical properties need to be taken from other methods than QFly. The reduction of ρ_{Ref} and τ_{Glass} by soiling is covered by the cleanliness factor (χ).

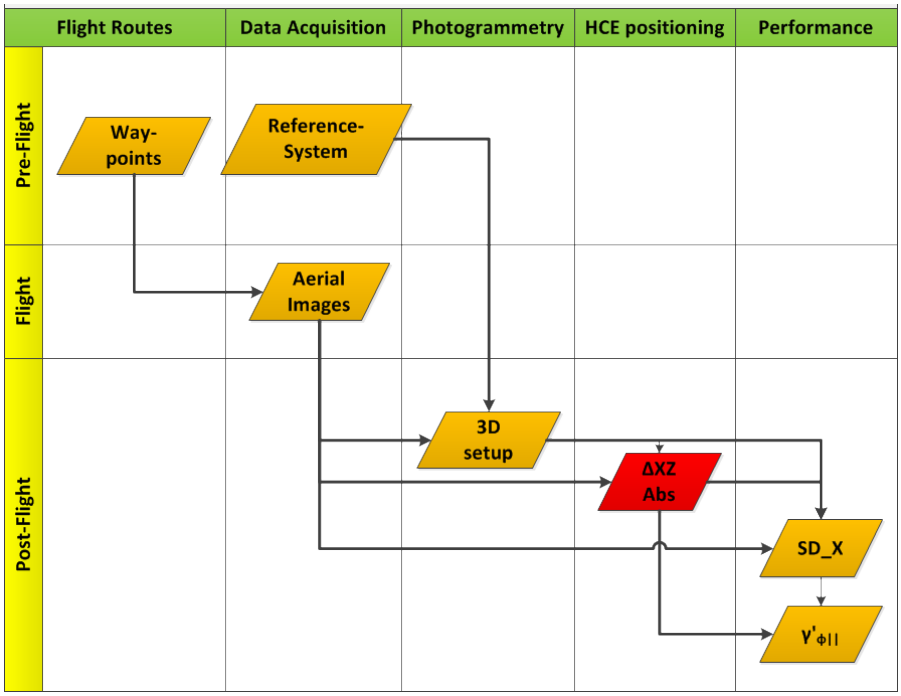

Figure 4.1: Work-flow of $QFly_{HighRes}$. The preparation includes creation of flight routes for the UAV considering the specific SCE- and solar field geometry. A reference system of photogrammetric targets is installed at one SCE defining a initial coordinate system aligned with the solar field. During data acquisition, the UAV takes approx. 800 aerial images per SCA. The first part of the evaluation provides the 3D setup, which is essential for all subsequent geometry calculations. The absorber position ($\Delta X_{Abs}/\Delta Z_{Abs}$) is required to derive SD_X. The last step is the calculation of the effective intercept factor ($\gamma'_{\phi_{||}}$) by ray-tracing.

4.1.1 *Hardware*

The platform carrying the camera to the specified perspectives above the SCA is an unmanned radio controlled multi-copter (referred to as UAV). The applied microdrones md4-1000 (microdrones, 2017a) provides sufficient flight time of up to 45 min, payload of up to 1.2 kg and autonomous WP navigation when GNSS is available. This UAV offers a functionality called dynamic position hold (DPH) to enable stable motion under wind influence. However, the exposure time of the camera must be as short as possible[4] to minimize blurring due to not avoidable tumbling of the drone in wind gusts.

The utilized recording device is a Sony NEX-7 mirror-less interchangeable lens camera (Sony, 2011) with a 16 mm lens and 24 megapixel (MP) resolution. The payload is connected with a 2-axis gimbal (cardanic bearing) to the UAV that enables pitch movement and compensates roll motions during flight. Other cameras than consumer

4 preferable below 1/1000 second

Figure 4.2: Microdrones md4-1000 during a test flight in front of the KONTAS test facility at the PSA.

models have been considered, but this has not been implemented so far. The implementation of GigE Vision or Camera Link devices into the selected flight platform would enable higher frame rates and/or reducing the payload (see Section 6.3).

Further auxiliary equipment to conduct QFly measurements consist of a laptop for flight route generation, communication with the UAV and data post-processing, remote control, telemetry receiver, battery chargers for all devices, and photogrammetric targets for initial PG evaluation (see Section 4.2.1).

4.1.2 *Flight route preparation*

For autonomous WP navigation, so called waypoint files in ASCII format are created with a MATLAB program. The mdCockpit software from microdrones offer the possibility to create and edit these files, but the desired high degree of automation and the dependence of flight route design on solar field properties[5] gives precedence to code-based generation over interactive, manual methods. The WP command reference (microdrones, 2017b) contains a description of all parameters, which are required to define the UAV trajectory, camera orientation and image acquisition settings, and commands for the measures in emergency situation (e.g. no GNSS signal available or critically low battery voltage). Starting from a single SCE measurement,

5 like plant location and orientation, field layout, and collector design

the MATLAB tool for WP creation relocates and adapts the flight path to entire SCAs or loops. Pre-checking the WP routes in Google Earth and simulating the image acquisition from the scheduled camera positions allows for the optimization of WP routes. That way, flight paths can be planned efficiently, and it is ensured that the image series contains all the information necessary for successful image processing and appropriate measurement accuracy.

To obtain accurate results for exterior orientation (EOR) by photogrammetric pose estimation, the demand for sufficient field of view angles requires a rather short focal lengths of the camera of less than $20\,mm$. Thus, to obtain the desired spatial resolution, the flight altitude above the solar field is limited to values below $35\,m$.

The flight route can be separated into two independent sections. The first part consist of a spiral running down a sphere with a radius of $25\,m$. The camera is continuously orientated towards the drive pylon. Images from this part of the WP route assure a robust determination of the interior orientation (IOR) by fulfilling the requirements for simultaneous camera calibration (Remondino and Fraser, 2006, Section 4.1 and 5).

The second part of the flight route provides the images for the estimation of the absorber tube position (ΔX_{Abs} and ΔZ_{Abs}) and mirror shape (SD_X). Each SCE flyover consists of horizontal part and a rising and descending wing (see Fig 4.3). The horizontal part delivers about 40-60 images for SD_X calculation (reflection of the absorber tube is visible) and lateral absorber tube positioning ΔX_{Abs}. The accuracy of ΔZ_{Abs} calculation is enhanced by images taken from the wings, as then the view angle on the absorber tube provides better vertical information (see Section 4.3.3 and Figure 4.14).

4.1.3 *Data acquisition*

Due to the largely automated data acquisition by the UAV, the measurement process consist mainly of preparatory steps. Section A.4 describes the order of relevant steps of the data acquisition for $\text{QFly}_{\text{HighRes}}$. This description is subject to up-dates and provides only a rough overview.

Section 6.2 provides an outlook how to deal with regulatory issues in the context of cross-boarder deployment of QFly.

4.2 EVALUATION

The evaluation is implemented in matrix laboratory (MATLAB) using the image-processing- and curve-fitting toolboxes. Some task are

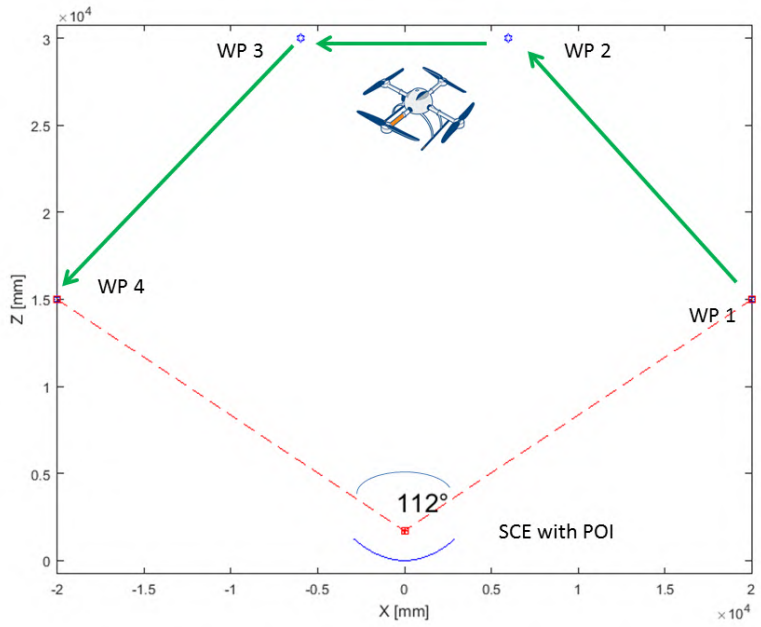

Figure 4.3: Cross section perpendicular to the focal line showing the parabolic mirror with the WPs of each SCE flyover. Images relevant for the mirror shape are taken along $\overline{WP2WP3}$, while additional images for the HCE positioning are taken along $\overline{WP1WP2}$ and $\overline{WP3WP4}$.

solved by open source code submissions from the MATLAB file exchange[6]. The $\text{QFly}_{\text{HighRes}}$ post-processing is structured in the following steps:

- Determination of 3D Setup consisting of the camera positions (EOR) relative to the solar collector assembly (SCA) coordinate system (Section 4.2.1)
- Calculation of absorber tube position (ΔX_{Abs} and ΔZ_{Abs}) based on 3D Setup (Section 4.2.2)
- Creation of orthoimages based on 3D Setup (Section 4.2.3)
- Image processing: Detection and assignment of absorber tube reflections in a series of orthoimages belonging to the same SCE (Section 4.2.4)
- Calculation of the slope deviation in curvature direction (SD_X) (Section 4.2.5)
- Calculation of the intercept factor (γ) from numerical RT based on measured PTC geometry (SD_X, ΔX_{Abs}, and ΔZ_{Abs}) (see Section 2.4)

6 http://de.mathworks.com/matlabcentral/fileexchange

4.2.1 *Determination of camera position*

Precise determination of the six parameters of the exterior orientation (EOR) (see Eq. 4.1) has highest relevance for the measurement accuracy. The importance is based in the fact, that the camera position is involved in the final mirror-normal vector calculation (Figure 2.5), the absorber tube displacement (Figure 4.6), and also in every intermediate step of the post-processing.

$$EOR = [X_C,\, Y_C,\, Z_C,\, \omega_C,\, \varphi_C,\, \kappa_C] \tag{4.1}$$

The spatial coordinates X_C, Y_C, and Z_C denote the position of center of projection, while the angles ω_C, φ_C, and κ_C describe the orientation of the optical axis of the camera (Luhmann et al., 2006b). Various options were taken into consideration to determine the EOR. The UAV built-in global navigation satellite system (GNSS) with an accuracy of $\pm 2\,m$ under ideal conditions is not sufficient. Further options to derive at least X_C, Y_C, and Z_C are differential global positioning system (DGPS) or real time kinematic (RTK), but they are not yet available for the md4-1000 at reasonable cost[7].

Attaching a remote prism to the UAV to track its position with a total station (Siebert et al., 2009) was tested (see also Section 4.3.1), but due to increased pay-load and effort as well as problems with synchronization between camera and total station, this approach was rejected. Furthermore, all these localization measurements would only return the camera position in an arbitrary coordinate system without information about the orientation parameters (ω_C, φ_C, κ_C) of the cameras optical axis.

As a consequence, the evaluation of the aerial images by close range photogrammetry (PG) has been considered to be the most appropriate approach to derive the EOR. This means some extra effort in terms of preparation and image processing, but the benefit of this method is, that 3D coordinates of collector features and the EOR are jointly derived in a single coordinate system. In addition, PG delivers precise information on the intrinsic camera parameters (Remondino and Fraser, 2006, Sec 4.1 and 5), when executed with a suitable camera and sufficient data quality. A suitable camera in this context refers to a mechanically stiff camera body and lens, moderate lens-distortion and sufficient resolution. The data quality refers to the spatial distribution and density of POIs and camera perspectives.

7 In addition, both DGPS or RTK rely on external data sources and/or additional hardware, which further increases effort and complexity.

Camera model

A camera model describes the difference between an ideal pin-hole camera and a real camera. The parameters of this model are the interior orientation (IOR). The camera model used throughout this thesis by the PG post-processing software (Aicon DPA Pro) and several MATLAB applications is described in Luhmann et al. (2006b)(Section 3.2.3.2 Eq. 3.32). The model itself reaches its limits for fish-eye optics[8], yet the deployed Sony NEX-7 camera is described well.

Table 4.2 provides a typical result for the IOR derived from airborne images at a focal distance of 35 m for the Sony NEX-7 camera. Due to chromatic aberration, the interior orientation depends in general on the selected color-channel of an RGB-image (Luhmann et al., 2006a). Since the blue channel of aerial images shows the best contrast between the mirror (showing the reflection of the sky) and the ground, results are always based on gray-scale images derived by splitting the RGB-images and using exclusively the blue channel.

Parameter	Value	uncertainty
$C_k\,[mm]$	-15.865	0.0010
$X_h\,[mm]$	-0.118	0.0006
$Y_h\,[mm]$	0.150	0.0007
A1	$-2.6271 \cdot 10^{-4}$	$9.2935 \cdot 10^{-7}$
A2	$1.5255 \cdot 10^{-6}$	$1.1915 \cdot 10^{-8}$
A3	$-1.9537 \cdot 10^{-10}$	$4.8573 \cdot 10^{-11}$
B1	$-8.3804 \cdot 10^{-5}$	$1.0026 \cdot 10^{-6}$
B2	$2.7716 \cdot 10^{-5}$	$1.0659 \cdot 10^{-6}$
C1	$4.3335 \cdot 10^{-3}$	$8.2312 \cdot 10^{-6}$
C2	$3.5641 \cdot 10^{-5}$	$7.0091 \cdot 10^{-6}$

Table 4.2: Parameters and uncertainties of the interior orientation (IOR) for the Sony NEX-7 with a 16 mm focal length lens. *Ck* denotes the distance of the center of projection from the focal plane. X_h and Y_h describe principal points where the optical axis crosses the focal plane. The other parameters describe radial $(A_{1,2,3})$, and tangential $(B_{1,2})$ distortion coefficients, while $(C_{1,2})$ compensate for shear and affinity.

Photogrammetric evaluation

The $\text{QFly}_{\text{HighRes}}$ post-processing begins with the photogrammetric evaluation. At first, the images are evaluated by the AICON DPA Pro software in order to determine the image- and 3D-coordinates of only the coded markers distributed on and around the PTC. Exploiting the

8 with a focal length of $\lessapprox 10\,mm$

exterior orientation (EOR) derived in that way, the "natural" collector features like corners, gaps, and crosses of the mirror panels are detected in the images and used as additional observations (see Figure 4.4). The artificial coded markers are only used for the first iteration of the photogrammetric evaluation. In subsequent iterations, the number of observations and such the robustness is enhanced by the natural collector features. In addition, the distance between some pairs of the coded and/or natural markers is used as constraint input in the bundle adjustment. That way, a proper scaling of the EOR and SCE feature coordinates is assured.

The detection of the natural collector features (Figure 4.4) has to yield sub-pixel accuracy in order to be beneficial for the combined photogrammetric evaluation of artificial and natural markers. The underlaying image-processing involves creation of orthoimages for each region of interest (ROI), image segmentation to separate the mirror surface from the background, checking the properties of detected objects, edge detection, and finally line detection based on hough-transformation (Hough, 1962; Duda and Hart, 1972; Gonzalez et al., 2004). The intersection of edge lines belonging to the same mirror panel provides the corner coordinates. Gap and cross image coordinates are derived by averaging two or four corner coordinates, respectively. The feature detection method incorporates several quality criteria like size of detected mirror area, contrast, or intersection angle of mirror edge lines. Setting relatively strict thresholds for these parameters reduces erroneous detections.

At the end of that process, the 3D coordinates of all mirror features and camera positions/orientations are known with high accuracy in the same coordinate system. Additional results are the distortion parameters of the camera lens (IOR). Being side-products in the normal bundle-adjustment, these parameters are of high importance in the present case, because they enable completely automated post-processing of the image data. Thus, all information for orthoimage creation, distortion correction and calculation of the slope deviations and absorber tube position is available. The uncertainty analysis presented in Section 4.3 reveals that the EOR is a sensitive parameter and may contribute significantly to resulting collector geometry and thus the optical performance. The estimation of the uncertainty of the photogrammetric localization procedure is described in detail in Section 4.3.1.

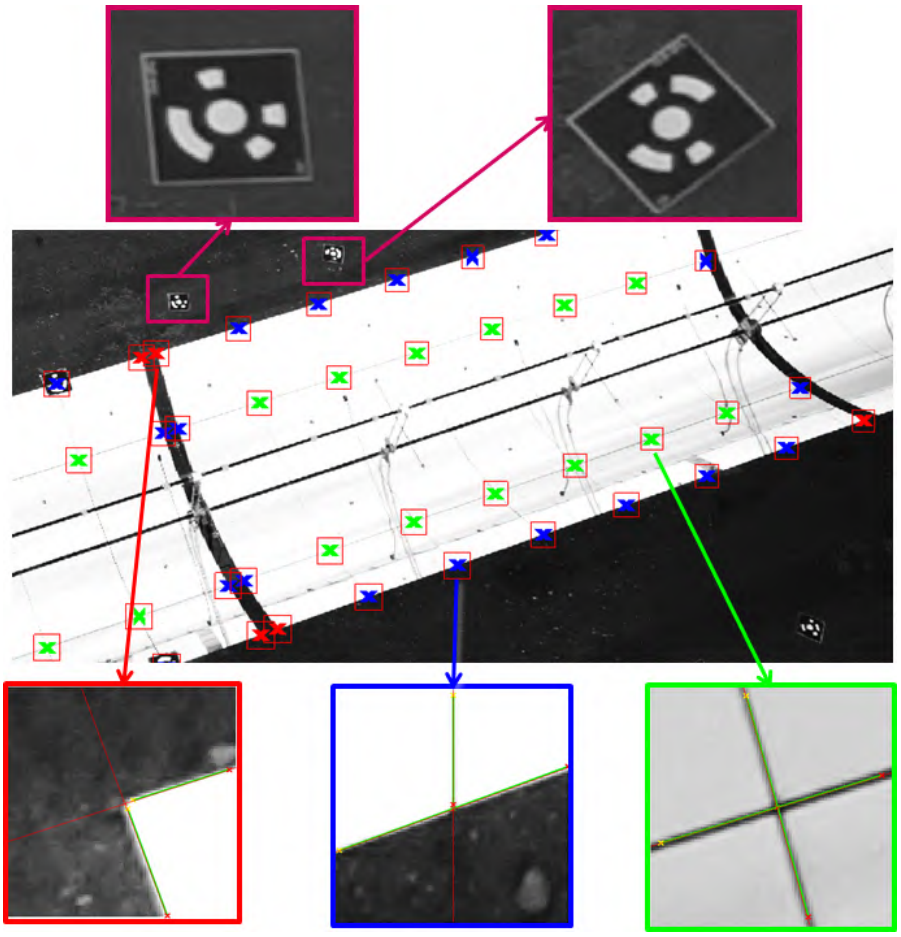

Figure 4.4: Markers used for the photogrammetric evaluation. Artificial coded markers (top) are used to derive start values for the 3D-setup. In subsequent iterations, also mirror-corners (red), -gaps (blue), and -crosses (green) are used as input for the bundle adjustment. The image processing to detect these natural collector features with sub-pixel accuracy involves segmentation, property checking, edge detection, and line detection.

4.2.2 *Airborne measurement of absorber tube misalignment*

Knowing the position of the absorber tube relative to the concentrators focal line is indispensable to fully characterize the optical performance of a parabolic trough collector. On the one hand, the tube serves as pattern for the TARMES principle (see Figure 2.5). In addition, a reasonable statement on the optical performance by means of ray-tracing is only possible if both mirror shape and absorber tube position are available with sufficient spatial resolution and accuracy (see Figure 2.10). So it was necessary to develop a method capable to simultaneously measure the absorber tube position along with the mirror shape from aerial images. In the following section, a fully automated approach to measure ΔX_{Abs} and ΔZ_{Abs} is presented.

The following description is based on a coordinate system convention as shown in Figure 1.1 with the focal line and axis of rotation parallel to $\vec{N}_Y$ and the optical axis represented by $\vec{N}_Z$. 3D-setup data from the photogrammetric evaluation is used as input. The airborne absorber positioning approach (see Figure 4.6) uses observation lines from the camera to the absorber tube center line situated in a reference plane E_{Ref} perpendicular to the focal line (see Figure 4.5). Pairwise intersection of the observation lines delivers ΔX_{Abs} and ΔZ_{Abs}. Typically, the distance in longitudinal Y-direction between measurement positions is set to $0.5\,m$ which delivers sufficient spatial resolution to describe the trend of absorber tube displacement.

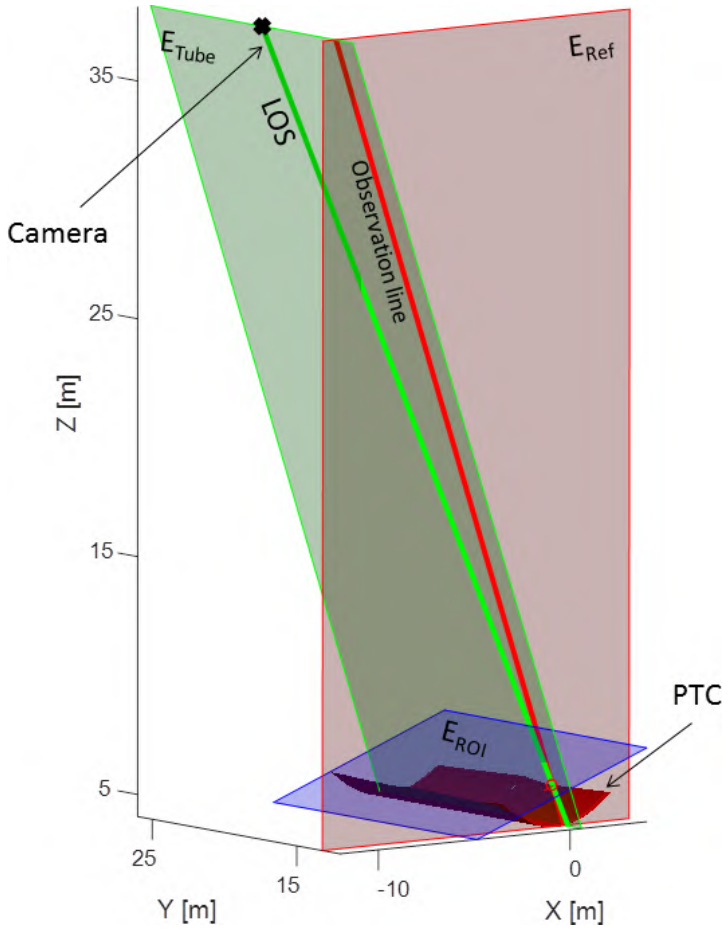

Figure 4.5: 3D visualization of the planes applied to derive the absorber tube position in the ortho-image (see Figure 4.7). Tube detection image processing is carried out inside a fraction of the blue plane E_{ROI} (see Eq. 4.2). The resulting line-of-sight (LOS) (green line) in combination with camera position provides the plane E_{Tube} (Equation 4.4) in green. The intersection of E_{Tube} with E_{Ref} (Equation 4.7, red) delivers a single observation line $\overrightarrow{LOS_{meas}}$ (red).

The first step in the work flow is to determine the absorber tube edges in ortho-images defined by Regions of interest (ROIs). Based on

the cameras IOR and spatial transformation information between each SCE and the camera position (EOR), a grid of 3D coordinates $\vec{x}_{ROI}$ is projected onto the image to obtain an ortho-image (Figure 4.7). The grid $\vec{x}_{ROI}$ is located in a plane fulfilling Equation 4.2:

$$E_{ROI} : (\vec{x}_{ROI} - \vec{p}_{ROI}) \cdot \vec{n}_{ROI} = 0 \tag{4.2}$$

where p_{ROI} is the vector to the current measurement position along the focal line ($\vec{N}_Y$) and $\vec{n}_{ROI}$ is the normal vector of the plane E_{ROI}, defined by $\vec{N}_Y$ and the LOS between camera and measurement position:

$$\vec{n}_{ROI} = (\overrightarrow{LOS_{ideal}} \times \vec{N}_Y) \times \vec{N}_Y \tag{4.3}$$

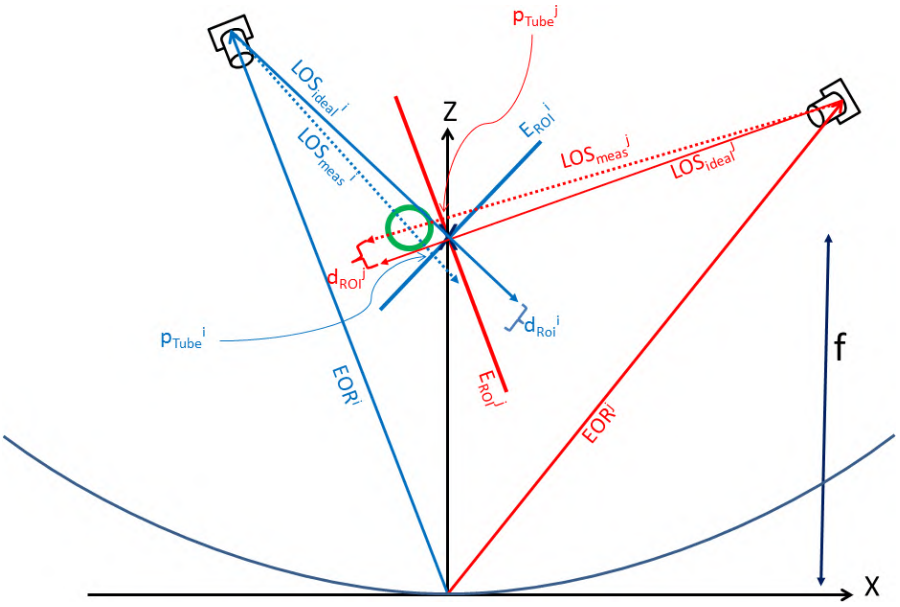

Figure 4.6: Methodology of absorber tube positioning displayed as projection of two observations i and j into a plane E_{Ref} parallel to the XZ-plane. The intersection of E_{Tube} and E_{Ref} is displayed as LOS in this 2D representation. The difference between ideal and measured tube position is denoted as d_{ROI}. Camera distances to the PTC are not drawn to scale in order to improve the presentation.

Within these orthoimages, the deviation of the absorber tube from the focal line d_{ROI} is detected via edge filters and linear regression. Figure 4.7 shows an example of tube detection results.

The result of the image processing is used to define a new plane containing the EOR and the detected tube position within E_{ROI}:

$$E_{Tube} : (\vec{x}_{Tube} - \overrightarrow{EOR}) \cdot (\overrightarrow{LOS_{meas}} \times \vec{N}_Y) = 0 \tag{4.4}$$

with

$$\overrightarrow{LOS_{meas}} = (\overrightarrow{EOR} - \vec{p}_{Tube}) \tag{4.5}$$

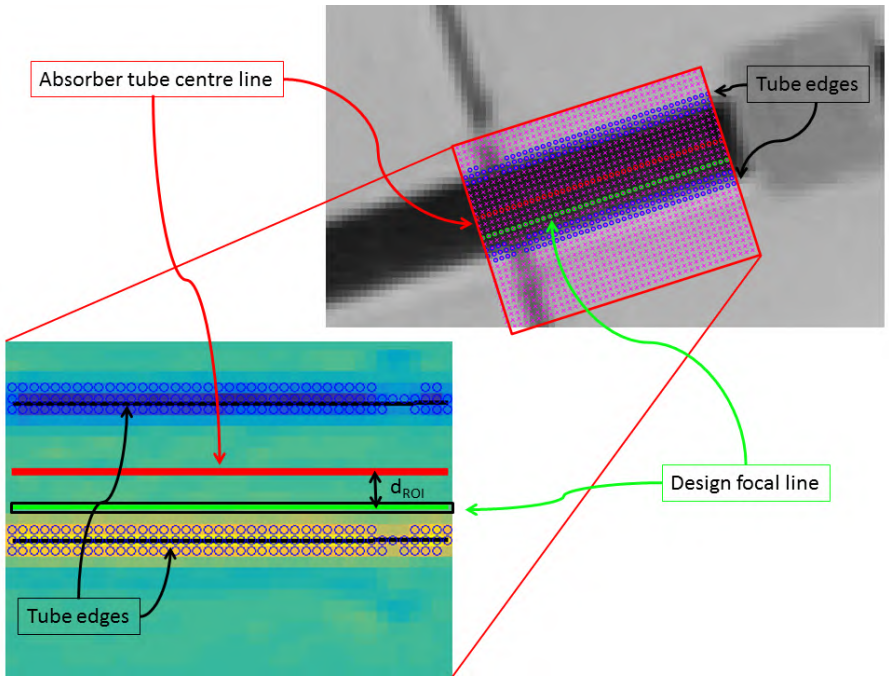

Figure 4.7: Edge based absorber tube detection, reprojected in the original image (top) and within the orthoimage (bottom). Green markers denote the location of the ideal (design-) focal line, and red markers show the tube center deduced from linear intensity weighted regression on tube edge elements (blue circles). The vertical difference in the lower image between ideal focal line and tube center is denoted as d_{ROI} (see Eq. 4.6).

and

$$\vec{p}_{Tube} = \vec{p}_{ROI} + d_{ROI} \cdot (\overrightarrow{LOS_{ideal}} \times \vec{N}_Y) \tag{4.6}$$

The final step to obtain a single observation line is the intersection of E_{Tube} with a reference plane E_{Ref} defined by:

$$E_{Ref} : (\vec{x}_{Ref} - \vec{p}_{ROI}) \cdot \vec{N}_Y = 0 \tag{4.7}$$

The total amount of M observation lines creates a scattered distribution of pairwise intersections $[X_{Abs}, Z_{Abs}]_{i,j}$ within E_{Ref} (see Figure 4.6 and 4.15). Here, i and j denote the indices of intersecting lines. Within E_{Ref}, only the X and Z coordinates are considered.

The tube position and its uncertainty can be derived from the mean value

$$[\overline{X_{Abs}}, \overline{Z_{Abs}}] = \frac{1}{N} \sum_{k=1}^{N} [X_{Abs}, Z_{Abs}]_{i,j} \tag{4.8}$$

and the standard deviation

$$\sigma_{Abs_{Meas}} = \sqrt{\frac{1}{N-1} \sum_{k=1}^{N} ([X_{Abs}, Z_{Abs}]_{i,j} - [\overline{X_{Abs}}, \overline{Z_{Abs}}])^2}. \tag{4.9}$$

Here, N denotes the number of pairwise intersections of observation lines with the indices i and j. That way it is assured to count each intersection only once:

$$N = \sum_{k=1}^{k=M-1} k \tag{4.10}$$

Deviations from the focal line are obtained by:

$$[\Delta X_{Abs}, \Delta Z_{Abs}] = [\overline{X_{Abs}}, \overline{Z_{Abs}}] - [0, f] \tag{4.11}$$

An example of the absorber tube position data is presented in Figure 4.8. The uncertainty analysis for the airborne absorber tube positioning will be presented in Section 4.3.3.

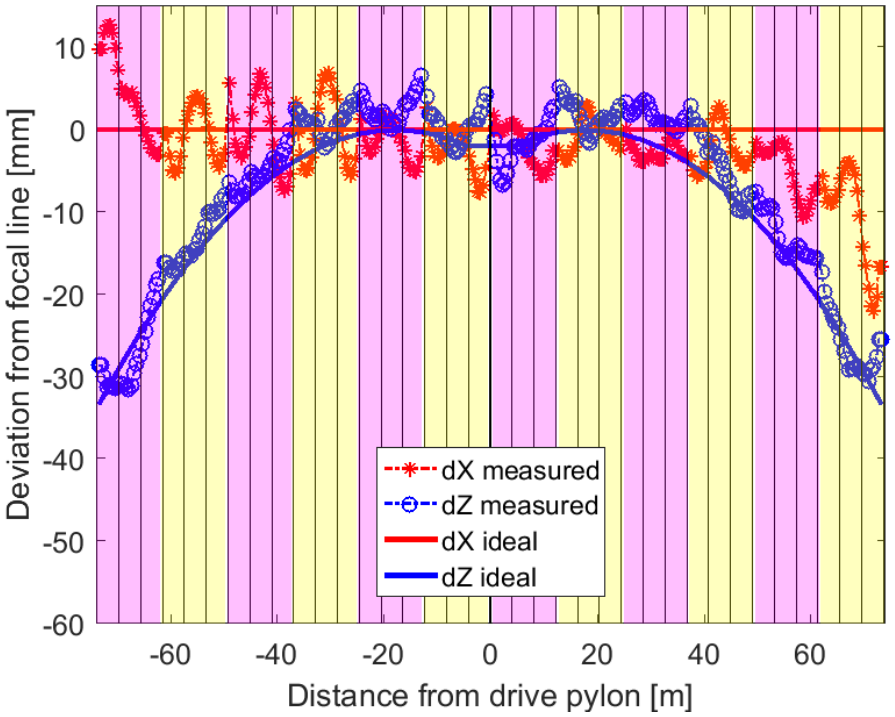

Figure 4.8: Comparison of absorber tube displacement in lateral direction (ΔX_{Abs}) and absorber tube displacement along the optical axis (ΔZ_{Abs}) with the design position according to $T_{HTF} = 147°C$ during the measurement for SCA RH36 from the AS3 plant. Each yellow and magenta stripe represents one SCE. Solid lined denote the ideal position, which for vertical deflections ΔZ_{Abs} already contains the temperature model presented in Section 3.2.3. The northern end ($Y > 70\,m$) shows significant lateral deviations ΔX_{Abs} of up to $20\,mm$, which could be an indicator for increased friction of the REPA swivel joint (see Section 3.2.2).

4.2.3 *Orthoimage creation*

This section describes the motivation and process of orthoimage creation as preparatory step for the final segmentation and geometry calculation.

In order to detect and compare absorber tube reflections from a series of airborne images, while the SCE position within the image varies between consecutive frames, it is indispensable to rectify each image and create matrices with an aspect ratio, that corresponds to the actual collector aperture (see Figure 4.9). Each pixel in the orthoimage matrix can be assigned to a specific location in the ideal concentrator geometry, defined by the horizontal distance from the vertex (X-axis), the position along the vertex (Y-axis), and the height (Z-axis). Same locations of the mirror surface appear at identical positions in the orthoimage matrix, so that subsequent results of the image processing[9] can combined in a single matrix (see Section 4.2.5).

The terms orthophotos or orthoimages (Habib et al., 2007) is mainly used in aerial imagery and describes geometrically corrected raw images by considering topographic relief, lens distortion, and camera tilt. In the present application, spatial information of the 3D-setup (EOR relative to collector module) is used to calculate the 2D transformation from the raw image to the orthoimage. In a first approximation, this is a projective transformation, but the consideration of lens distortion (IOR) and the curved surface requires a pixel-wise transformation, which is described by a look-up table assigning to every pixel in the raw image exactly one pixel in the target matrix (the orthoimage).

For that purpose, an ideal collector grid is created with a spatial resolution (typically $6\,mm/pixel$) according to the actual ground sample distance (GSD). This grid is projected into the image using the EOR and IOR from the photogrammetric evaluation, so that pixel locations in the raw image can be assigned to each grid point of the ideal collector (see Figure 4.9). Gray-values of each color-channel of these pixels are transferred to the corresponding position in the orthoimage matrix. Next-neighbor interpolation is used to smooth the result. The quality of this transformation can be verified by comparing the location of mirror panel crossing points with their design coordinates (see Figure 4.13).

4.2.4 *Detection of the absorber tube reflection*

The final measure before the calculation of SD_X maps is the determination of the position of the absorber tube reflection within the

9 of an entire image series consisting out of $40 - 60$ images

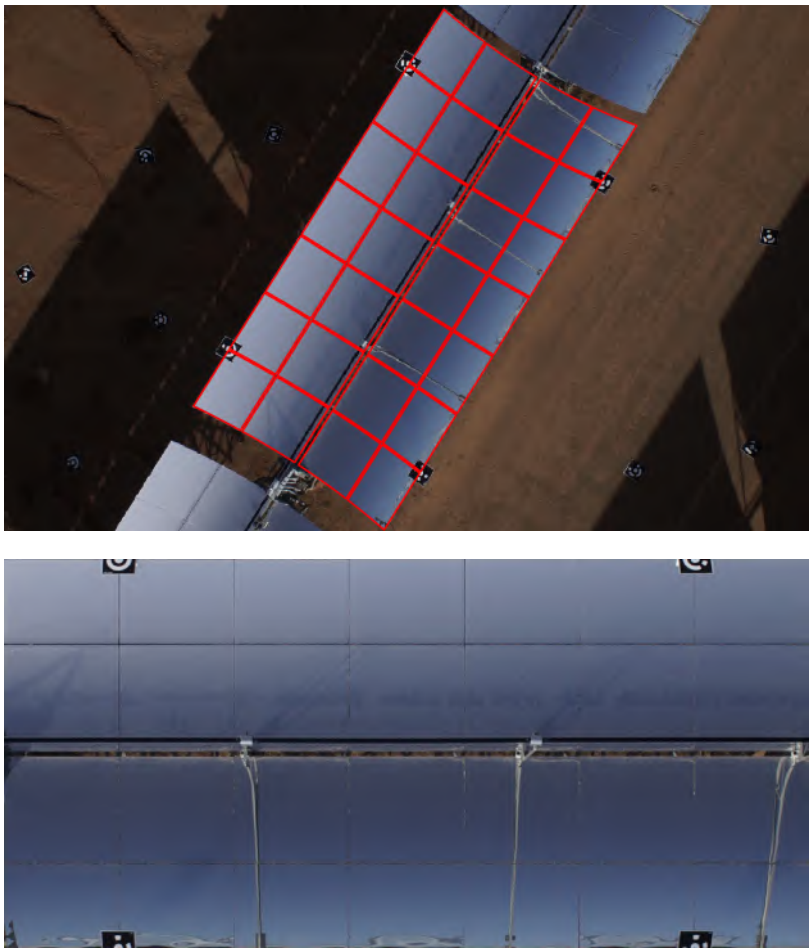

Figure 4.9: Orthoimage creation from an aerial raw image captured at a flight altitude of $\simeq 30\,m$ above the parabola vertex. Top: Projection of the grid of mirror panel boarders into the aerial image. Bottom: Resulting rectified orthoimage considering SCE location and orientation, lens distortion, and camera position. Four coded photogrammetric targets are also visible at the collector boarder. These targets define the initial reference system for the photogrammetric evaluation (see Section 4.2.1). The collocation of targets on the SCA-structure is only required for one SCE within the measurement volume.

mirror area. As a result of the previous orthoimage creation, the reflex position is found within the surface of the ideal parabolic trough, so that the absorber tube edge reflections can be assigned to 3D positions. Uncertainties arising from the assumption of an ideal concentrator geometry for this particular step are discussed in Section 4.3.4.
Basically, the detection of the (dark) absorber tube reflection in front of the (bright) sky background is performed by global thresholding (Otsu, 1975). A binary image (TRUE: Absorber tube reflection, FALSE: Sky) is created by segmenting the gray-scale image, where all pixel with gray-values below the global threshold are set to TRUE while all

other pixel are set to FALSE.

The edges of the binary image represent the coordinates for mirror shape calculation. This straightforward approach (global thresholding, edges of binary image represent absorber tube edge reflection) delivers good results, when the mirrors haven been cleaned prior to the measurement and data acquisition is carried out under overcast sky conditions.

However, the conditions in the solar field may cause unfavorable data quality (see Figure 4.10), that prevents the use of global thresholding without further corrective measures:

- Inhomogeneous background: due to the curvature of the mirror, a wide section of the sky is visible in the mirror. Intensity variations within that background can be caused by bright or dark clouds. But even under clear sky conditions, there is a significant intensity variation between bright areas as the horizon- and circumsolar region and dark areas of the celestial dome (Steven and Unsworth, 1977). The scale of this variation, in combination with other problematic conditions, may result in weak contrast between the tube reflection and dark areas of the clear sky.
- Inhomogeneous illumination: Optimal data is obtained under overcast sky conditions. As CSP plants are preferably installed in regions with high DNI[10], the challenge is to cope with phenomena arising from specular reflection caused by direct radiation from the sun, like shadows, scattering, and specular reflections on the absorber tube.
- Soiling: Dust on the mirror diminishes the overall contrast and tends to enhance the effect of inhomogeneous illumination.

Due to the large amount of data, manual user input to rectify incorrect results of automatic image processing is impracticable. For this reason, different measures to improve the image segmentation under unfavorable conditions were investigated in the course of a master thesis on this topic (Hertel, 2013). The impact of these measures was evaluated by comparing the result of improved image processing algorithms with a ground truth data set. The quality parameter to assess the segmentation result is the edge-mismatch (EMM), which provides a statistical, scalar value for the distance between corresponding edge pixels in the ground truth and in the automatic segmentation result (Hertel, 2013, Eq. 3.1).

For a perfectly segmented image, the EMM is 0 and approaches 1 for a poor segmentation result. In the course of the study, the EMM

10 where overcast sky conditions are rarely encountered

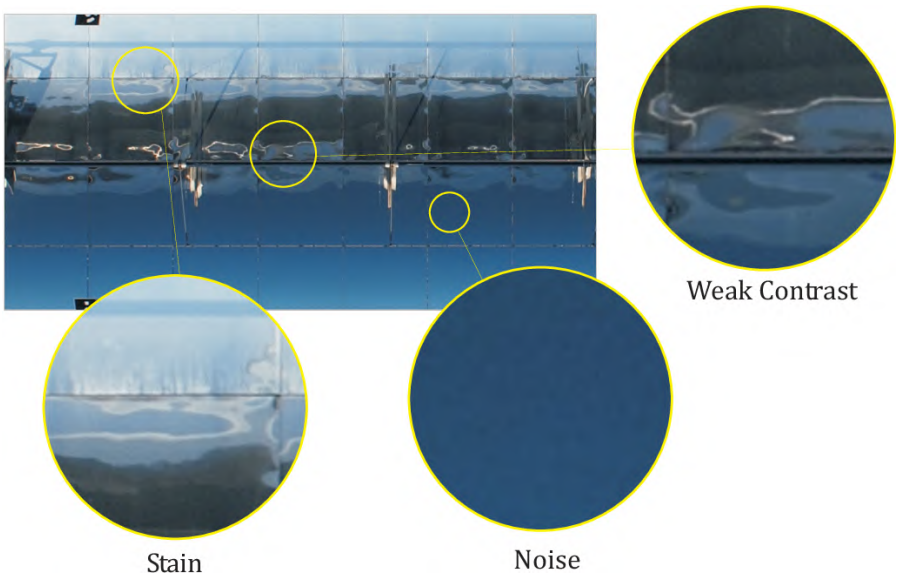

Figure 4.10: Worst case QFly orthoimage with features, that prevent accurate segmentation with straightforward global thresholding. Stain or soiling scatter solar radiation and act as major interfering signal. Noise due to higher gain setting has minor impact. Weak contrast is also caused by a rather dark background and specular direct normal irradiance (DNI) reflections on the absorber tube.

for a worst case data set could be improved from 0.98 to 0.38 for global thresholding and to 0.32 for local thresholding approaches. The individual measures are listed below, in the order of positive impact on the segmentation result:

1. In order to manage inhomogeneous intensity distributions, significant improvement was achieved by background correction (see Figure 4.11). This measure provides a better starting position for global threshold methods by eliminating large scale illumination gradients.

2. Morphological operations (Gonzalez et al., 2004, Chapter 10) in the resulting binary images support the removal of artifacts and thereby improve the plausibility of the segmentation. These operations are:

   - filling of holes and gaps
   - noise removal
   - edge smoothing by dilatation and erosion

3. Edge preserving filtering prior to local thresholding enhances the performance of local thresholding algorithms.

4. Local thresholding may provide even better results than the combination of global thresholding with background correction, at the expense of increased computational effort.

5. For unfavorable low sun elevation angles, specular reflections of direct normal irradiance (DNI) on the absorber tube can be removed by a custom sun-reflex removal application, which considers certain features to identify and remove suspicious objects. A machine learning k-Nearest-Neighborhood (KNN) algorithm is used to classify objects.

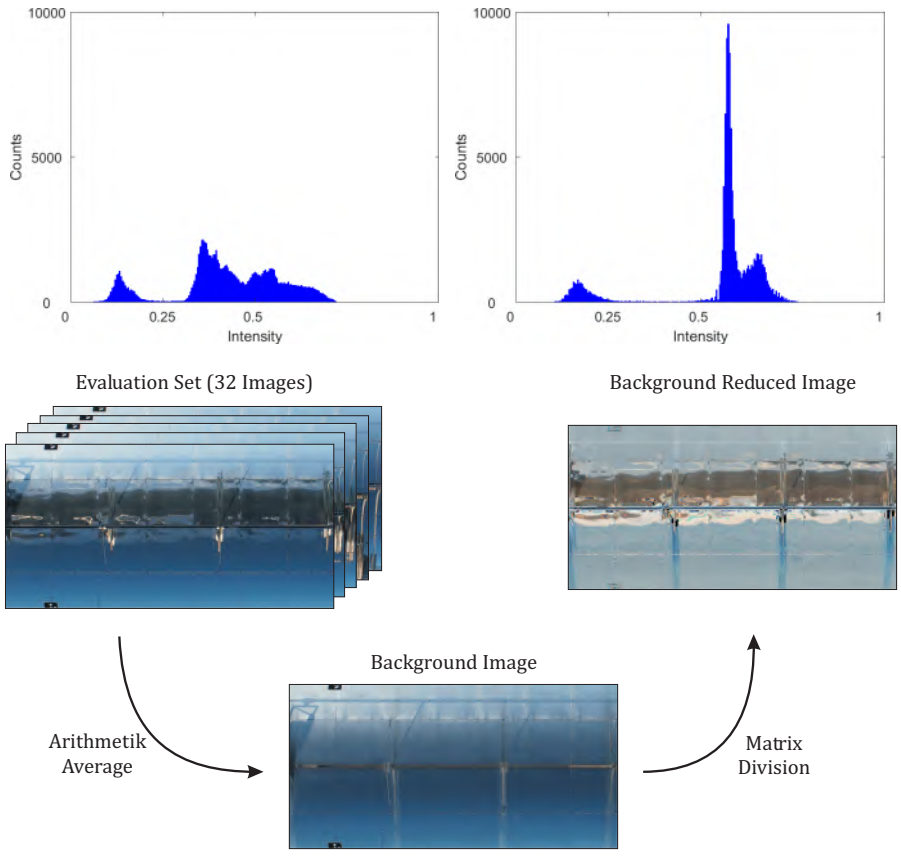

Figure 4.11: Effect of background correction on the histogram and the applicability of a global threshold. Top left: histogram of gray-values of the initial image. The distribution is multi-modal, thus global threshold are prone to return erroneous results. Bottom: Process of background image creation by averaging the entire image series. The resulting image represents very well the prevalent intensity distribution of the background. Top right: Applying the correction matrix to each orthoimage of the series results in un-ambiguous results with bi-modal intensity distribution, which is suitable for global thresholding.

For clean mirrors and adapted flight paths, good segmentation results are achieved by combining methods 1.) and 2.). Attention is paid to adequate conditions during image acquisition to prevent problems during evaluation. However, the presented methods 3.) to 5.) provide excellent fall-back solutions to obtain high quality results even in case of poor data quality.

4.2.5 *Calculation of mirror shape*

The TARMES methodology (see Figure 2.5) of calculating slope deviation in curvature direction (SD_X) from absorber tube reflections is outlined in Ulmer et al. (2009) and described in detail in Heinz (2005). Since the TARMES method has proven its accuracy and applicability in a large number of applications and measurement campaigns, the basic principle has remained unchanged since the first implementation in 2005 (Heinz, 2005; Ulmer et al., 2006). The objective of this section is to provide information on enhancements to assure accurate results with minimized user interaction. In terms of practicability, the largest gain was already achieved by orthoimage creation independent from the camera location (Section 4.2.3) and by automated data-collection (Section 4.1.3) .

In order to obtain reproducible and accurate results, the main point is to provide input without artifacts to the final part of the program, that calculates the mirror slope deviations. This input consists of so called stripe matrices, containing the coordinates of the upper- and lower absorber tube reflection (Ulmer et al., 2009, Figure 3), whereby the value of the actual view angle between the optical axis of the SCE and camera position (ϕ_{Cam}) is assigned to each line. The measures described in the previous section already provide relatively clean absorber tube reflection matrices. However, automatic detection of artifacts in the stripe matrices has improved the reliability of the code. Reliability in this context means, that the appearance of wrong SD_X pattern in the final map is inhibited.

In order to clean the stripe matrix prior to the SD_X calculation, the following measures are applied:

1. Reflection line density check: As the absorber tube reflection is supposed to move across the aperture, the density of tube edge reflection lines within the stripe matrix is expected to be homogeneous and rather low. On the other hand, density peaks in the matrix are good indicators for artifacts arising from dirt or reflections of elements of the structure. The density is calculated by applying an averaging filter to the stripe matrix and then sorting all non zero elements in a histogram. This histogram shows in general a bi-modal distribution, with a large peak at the density of "correct" stripes and a small peak at higher densities arising from repeated faulty detections in the same region. The threshold for this distribution is determined by Otsu's method (Otsu, 1975), in case the effectiveness metric indicates a bi-modal distribution. Stripes within a density region higher than the determined threshold are eliminated.

2. Property check of line objects[11]: Absorber tube reflection line objects are expected to exhibit a certain combination of characteristics regarding the orientation of the major axis of the ellipse, eccentricity of the ellipse, and number of pixel of the line segment. The ellipse refers to a region, that has the same second-moments as the investigated line segment. The combination of orientation and eccentricity provide a measure to identify straight horizontal or vertical lines, which in most cases can be regarded as artifacts. Noise revealed by line segments with a small number of pixel is also removed.

3. Surface Fit: Last but not least, a 2-dimensional surface polygon of 3^{rd} degree is fitted to the remaining lines, whereby the vertical coordinate of the surface represents the actual view angle between the optical axis of the SCE and camera position (ϕ_{Cam}). Then the difference between surface fit and stripe matrix is calculated. Stripes exceeding the double of one standard deviation of the difference are erased.

All measures presented here rely on empirically determined parameters. There is a trade-off between strict detection of artifacts and unintentional deletion of "true" line objects. The validation will show, that the selected measures and settings deliver accurate results without artifacts and without underestimating the slope deviations.

4.3 UNCERTAINTY ANALYSIS AND VALIDATION OF GEOMETRICAL MEASURES

In the previous section, the methods to derive performance relevant geometry parameters of the parabolic trough collector from airborne images have been described. The current section provides the uncertainty analysis and validation measures to prove the predicted accuracy. As the final target figures depend on intermediate results, the uncertainty analysis will follow the same work-flow as outlined in Figure 4.1.

At first, in Section 4.3.1, the uncertainty of the camera position (EOR) is assessed by comparing camera coordinates of airborne images obtained by PG with the coordinates derived with a total station. The plausibility of these results is verified by checking the location of certain collector features within the orthoimage. The accuracy ob the image processing is estimated in Section 4.3.2. The validation of airborne absorber tube measurement with an independent, photogrammetric benchmark will be presented in Section 4.3.3. The impact of prior results on the accuracy of the SD_X maps and RMS values will be investigated in Section 4.3.4. This involves also a brief investigation

11 Using the MATLAB function `regionprops.m`

on how the uncertainty of geometrical measures affects the result of ray-tracing analysis (Section 4.3.5). A comparison between optical and thermal measurements (Section 4.3.6) shows, that results obtained with latest optical and thermal measurement technology predict consistent system performance within the respective error margins.

4.3.1 *Uncertainty analysis and validation of 3D setup*

Uncertainty of camera position

The accuracy of the coordinates and parameters calculated in the photogrammetric bundle adjustment depend mainly on the deployed camera, the perspectives during image acquisition and the distribution of the points of interest (POIs). The bundle adjustment procedure used in the AICON DPA Pro delivers an uncertainty estimation for every calculated parameter. For the exterior orientation (EOR) of a typical $\text{QFly}_{\text{HighRes}}$ set-up, the uncertainty of the camera position (X_C, Y_C, Z_C) is typically in the range of $5 - 10\,mm$. In order to verify these values, the camera position was independently measured with a Trimble 5600 total station (Trimble, 2011), while images for a photogrammetric evaluation were taken. Total station and camera were synchronized, so for each image, the camera position from the bundle adjustment could be assigned by the time stamp to the position measured by the total station.

Best possible measurement accuracy ($< 3mm$) of the total station is achieved when using a prism. Such a tracked prism was attached to the camera, as depicted in Figure 4.12. The measurement point of the prism is located directly above the center or projection of the camera, so that the vertical off-set between both positions could be corrected. Instead being carried by the UAV, the camera was mounted to a man-lift. This was necessary to solve issues related to wind and synchronization between camera and total station. The height of the camera above ground level during the validation measurement as well as the arrangement of coded targets was similar to the first part of the flight routes of $\text{QFly}_{\text{HighRes}}$ (see Section 4.1.2).

The deviations between total station and camera-based EOR at a height above ground of $30\,m$ yielded a *RMS* value in horizontal direction of about $8\,mm$. Estimating the uncertainty of the total station to $\pm 3\,mm$, the uncertainty in center of projection point relative to the prism to $\pm 3\,mm$ and additional influences caused by unintentional movement of the platform to $\pm 3\,mm$, the uncertainty of the absolute horizontal camera position is calculated to be about $\pm 6\,mm$. As for QFly, the relative camera position to the SCE coordinates (estimated uncertainty about $\pm 5\,mm$) is relevant, the total uncertainty in horizon-

tal direction (X and Y) was calculated to $\pm 8\,mm$.

In a former publication (Prahl et al., 2013a) it was postulated, that the horizontal direction is slightly better measured than the vertical coordinate. However, this behavior can not be confirmed for improved flight routes and the detection of additional collector features, where the resulting error ellipsoid for the EOR-coordinates can be approximated by a sphere without any preference for a certain direction.

The results presented here were obtained with an camera with lower spatial resolution[12] (see also Table 4.7). The accuracy of the photogrammetric results obtained with the Sony NEX-7 and adapted flight routes have improved, so that the estimation on EOR and collector features accuracy is adapted. Hence, throughout this thesis an upper limit for EOR uncertainty is used:

$$\sigma_{EOR(X)} = \sigma_{EOR(Z)} = \sigma_{EOR(Z)} = 5\,mm \tag{4.12}$$

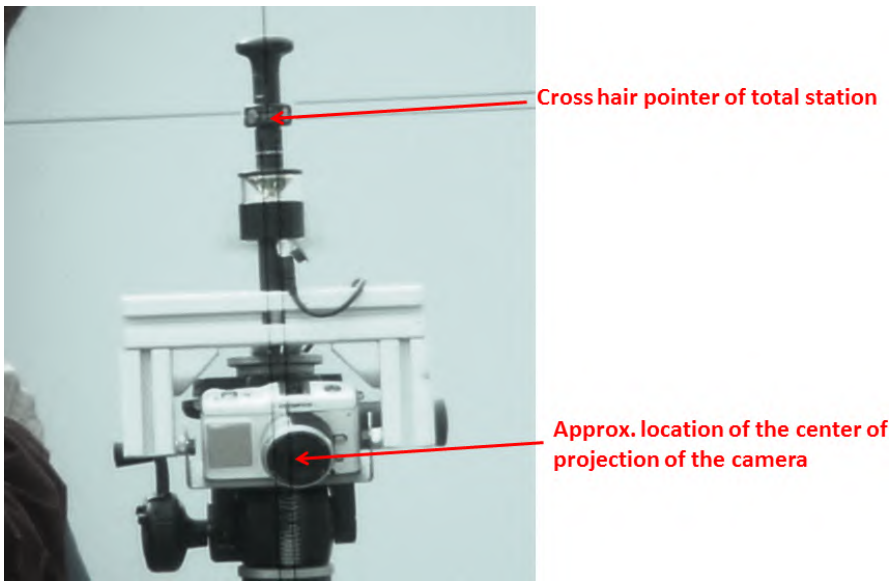

Figure 4.12: Set-up to verify the uncertainty of the camera position. The image was taken by viewing through the telescope of the total station. The cross hair points at the measurement location of the prism, at a fixed distance above the projection center of the camera.

Orthoimage uncertainty

The creation of the orthoimage of the mirror surface is carried out by means of a spatial transformation of the image coordinates. This involves the camera position relative to the collector module and lens distortion parameters. Possible sources for incorrect results are the

12 Olympus Pen E-P1, 12.2 MP

previously estimated EOR uncertainty, systematic errors of the interior orientation (IOR), or mounting inaccuracies of the SCE. The relevant quantity in this context is the positioning of the orthoimage along the curvature direction (X_{Ortho}).

Defective orthoimages lead to a systematic error in the subsequent processing of the stripe matrices. In order to estimate this contribution, the locations of mirror panel cross-points (see Figure 4.4) in the orthoimage were compared to the expected position according to an independent photogrammetric evaluation. Within the orthoimage, these cross-points were re-detected with the same approach as described on page 61, and compared to the benchmark position derived by PG.

That way, the uncertainty of the positioning of the orthoimage along the curvature direction (X_{Ortho})[13] was verified to be less than $3\,mm$ within the complete collector area (see Figure 4.13). This is a good outcome, considering the limited spatial resolution of the orthoimage ($6\,mm/pixel$), and the variability of positioning of photogrammetric markers on the crossing points.

4.3.2 *Uncertainty of the position of absorber tube edge reflection*

Due to vague thresholds, varying image brightness or reflected structures similar to the absorber tube, the uncertainty of X_{Reflex}[14] was empirically estimated to be in the range of $\pm 2\,pixel$, which corresponds to an uncertainty of about $8 - 12\,mm$ for the investigated setup.

Although it seems a straightforward approach, the edge-mismatch (EMM) as implemented in section 4.2.4 can not be be used to quantify the uncertainty of X_{Reflex}, because it involves certain scaling parameters. The EMM was used to assess the performance improvement of segmentation approaches, hence it is only available in conjunction with a ground truth data set. Furthermore, the EMM was determined for a worst case data set, so detection accuracy is expected to be much better for images that comply with the specifications denoted in Section 4.1.3. Outliers, which would far exceed the $\pm 2\,pixel$ estimate are removed by the stripe matrix post-processing presented in Section 4.2.5.

13 *RMS* value of deviations between coordinates measured by PG and the position in the orthoimage

14 position of the reflection of the absorber tube edge on the mirror surface

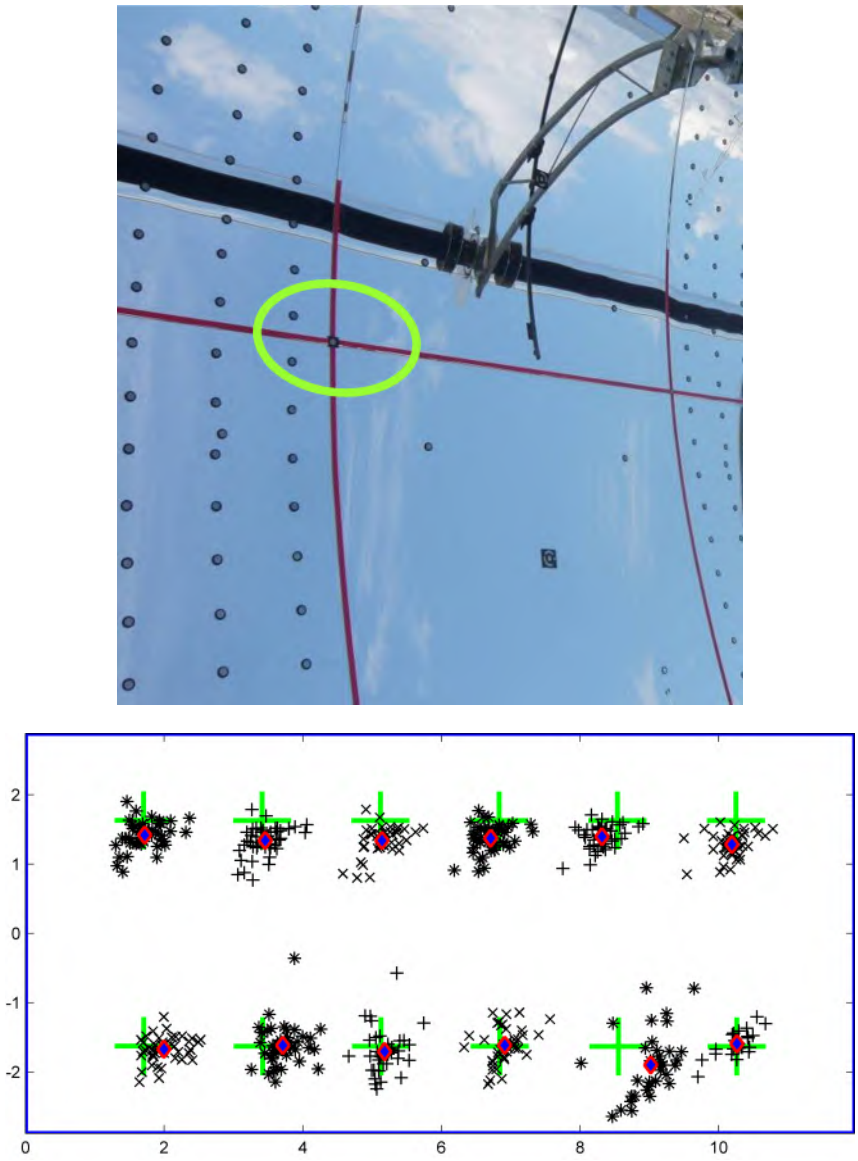

Figure 4.13: Deviation of re-detected mirror panel crossing points from the expected position. Top: part of the mirror surface showing the mirror panel cross point, which was highlighted with red tape for better contrast. A single photogrammetric marker was placed exactly on each crossing point to provide a reference locations. Bottom: Area representing the aperture area of a ET SCE with dimensions in [m]. Green crosses show the benchmark position of the crossing points. Each orthoimage provides a single deviation value (black markers). Averaged values for the whole image series are provided as red markers. Deviation are scaled with a factor of 100 for better visibility. A single coordinate (lower row, second from the right) shows higher deviations, which was probably caused by faulty attached adhesive tape. The position uncertainty (*RMS* value of deviations between coordinates measured by PG and the position in the orthoimage) within the orthoimage was verified to be smaller than 3 mm.

4.3.3 *Uncertainty analysis and validation absorber tube position*

In the following section, error sources are identified and evaluated for both the airborne absorber tube position measurement (introduced in Section 4.2.2), and also for the manual, photogrammetric benchmark measurement. The validation is carried out by comparing airborne- and benchmark data in the context of the estimated error margins.

Uncertainty of airborne measurement

Uncertainties of the camera positioning (σ_{EOR}) and the image processing to derive the tube center displacement (d_{ROI}) cause a fairly wide distribution of the resulting intersection points (see Figure 4.15). The contribution from the camera positioning has been estimated in Section 4.3.1 and is in the range of $\pm 5\,mm$ for both the horizontal fly-over and the ascending and descending wing. The contribution from the image processing ($\sigma_{d_{ROI}} \approx 2.0\,mm$) in the ortho-image plane arises from blurring of the absorber edges and limited resolution (see Figure 4.7). The expected uncertainty of one line-of-sight (LOS) (see Table 4.3) in the focal region is expressed by:

$$\sigma_{LOS} = \sqrt{\sigma_{EOR}^2 + \sigma_{d_{ROI}}^2} \tag{4.13}$$

Param	Value
$\sigma_{EOR}[mm]$	$\simeq$ 5.0
$\sigma_{d_{ROI}}[mm]$	$\simeq$ 2.0
$\sigma_{LOS}[mm]$	$\simeq$ 5.4

Table 4.3: Estimate for the uncertainty of a single observation line LOS in the focal region. As image detection and camera position are independent from each other, the resulting uncertainty is obtained from the sum of squares.

The uncertainty ellipsoid (see Figure 4.14) provides the uncertainty of absorber tube position ($\sigma_{X/Z}$) from single line-line intersection (see Table 4.4). The ellipse shape is determined by the intersection angle of corresponding LOSs. Least major axis lengths are achieved for intersection angles of 90°. The uncertainty of the airborne tube positioning is reduced by the large number N (see Eq. 4.10) of pairwise line-line intersections to a value considerably lower than $\sigma_{X/Z}$:

$$u_{X/Z} = \frac{1}{\sqrt{N}} \cdot \sigma_{X/Z} \tag{4.14}$$

Estimated uncertainty values of single line-line intersections $\sigma_{X/Z}$ (see Tab. 4.4) are confirmed by the characteristics of the distribution of intersection points (see Figure 4.15) .

	Direction	
parameter	X	Z
$\sigma_{X/Z}[mm]$	7.6	20.8
$u_{X/Z}[mm]$	0.21	0.59

Table 4.4: Uncertainty estimates for resulting $\text{QFly}_{\text{HighRes}}$ absorber tube coordinates for vertical and horizontal displacement. The variance in the respective dimension is derived from the semi-minor and semi-major axis according to the visualization of the uncertainty ellipse in Figure 4.14. The resulting measurement uncertainty $u_{X/Z}$ was calculated based on a typical setup with 50 observation lines.

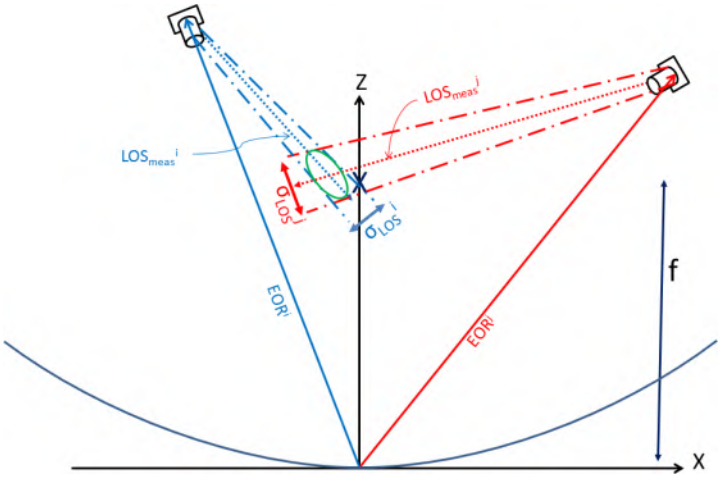

(a)

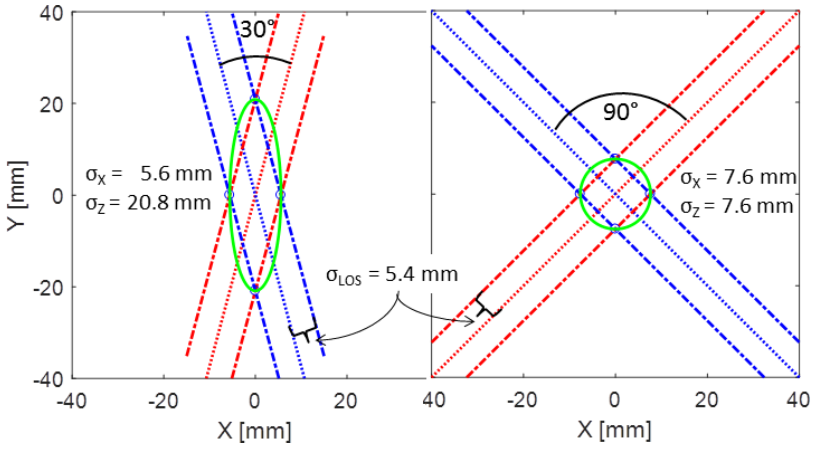

(b)

Figure 4.14: (a): Cross section with intersection measurement error. Uncertainty of the camera position σ_{EOR} and the image processing $\sigma_{d_{ROI}}$ defines the spread of the line-of-sight named σ_{LOS}. The shape of the uncertainty ellipse depends on the intersection angle and σ_{LOS} of each observation. Camera distances to the PTC are not drawn to scale in order to improve the presentation. (b): Examples for uncertainty ellipses for identical σ_{LOS} but different intersection angles of 30° and 90°.

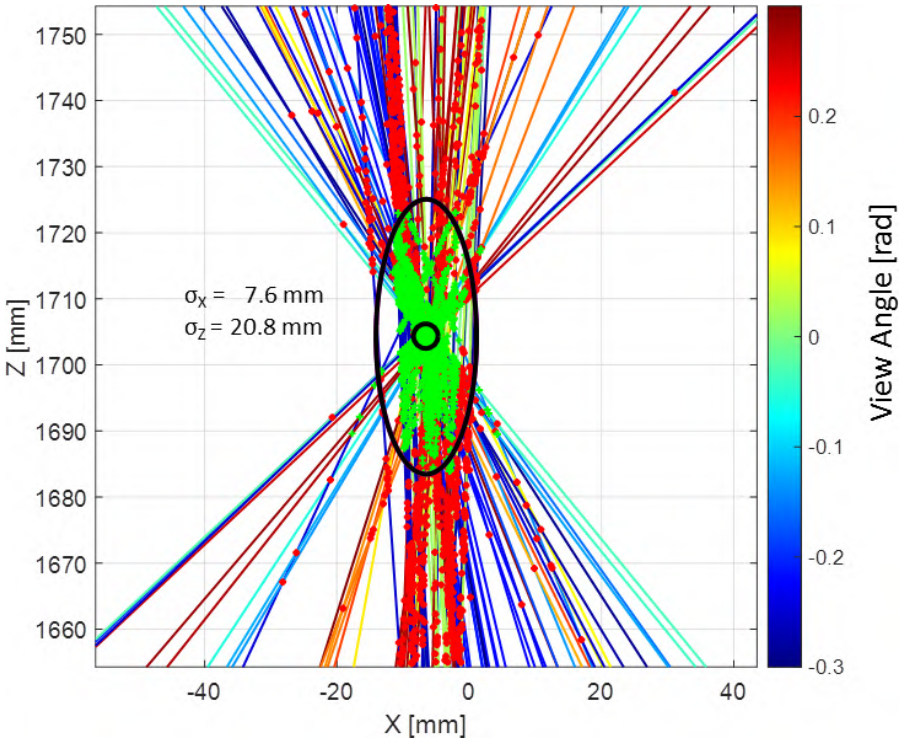

Figure 4.15: Sample distribution of pairwise line-line intersections inside E_{Ref}. Outliers (red dots) are not used to calculate the tube position (small black circle). The main criterion for outliers is the intra-line intersection angle. Intersection points originating from line-of-sights (LOSs) with an intersection angle of less than 10° are rejected.

Line colors correspond to the angle $[rad]$ between the LOS and E_{Ref}, however this parameter does not affect the accuracy. Typical standard deviations for the detected tube position $\sigma_{X/Z}$ from a single intersection are in the range of $7.6\,mm$ in X-Direction and $20.8\,mm$ in direction of the optical axis, in accordance with the ellipse (black) obtained from theoretical uncertainty estimations. The resulting measurement accuracy $u_{X/Z}$ is further reduced by the large number of intersections.

Benchmarking and Validation

The validation of the airborne approach to determine the absorber tube position was carried out by measuring three RP3 type SCEs with close range photogrammetry[15] (benchmark) and $\text{QFly}_{\text{HighRes}}$. HTF was circulated in the corresponding loop at constant temperature ($\simeq 50 \pm 5°C$) during the whole measurement campaign in order to avoid any temperature induced alteration of the absorber tube position (see Section 3.2.3). Any contradiction between benchmark and airborne measurement arising from time delay can be identified by comparing the benchmark measurements before and after the $\text{QFly}_{\text{HighRes}}$ data acquisition (red and green symbols in Figure 4.16). Spatial deviation between both approaches is compensated by interpolating the $\text{QFly}_{\text{HighRes}}$ results on the position of the benchmark measurement.

For the benchmark, retro-reflective markers were attached to the axis of rotation, onto the mirror surface above the mirror attachment points of the support structure and on the glass envelope tube (see Figure 2.7) of the PTC. Three positions per HCE are regarded a reasonable trade-off between spatial resolution and effort. Approx. 550 images were taken with standard equipment[16] and the photogrammetric evaluation was performed with commercial software[17]. The determination of glass envelope tube position and the eccentricity of the steel tube within the glass envelope tube was carried out as described in Section 2.3.2.

Typical manual close range photogrammetry of PTC delivers 3D-coordinates with an absolute uncertainty of less than $0.5\,mm$ for the measurement volume of a single EuroTrough SCE. From the whole dataset, the center of the glass envelope tube is calculated via circle fit of at least eight markers on the circumference. A conservative approach assigns an uncertainty in the same order to the glass tube center line ($\sigma_{X/ZGlass} \approx 0.5\,mm$). Systematic deviations may arise due to misalignment between the rotation axis and the rest of the steel structure. Such deviation, which would lead to inconsistencies between benchmark and $\text{QFly}_{\text{HighRes}}$ measurement are prevented by ignoring the rotation axis coordinates in this case and by using the best fit of mirror coordinates to design values (see A.1).

The semi-automatic determination of the eccentricity of the steel absorber tube relative to the glass envelope tube (see Section 2.3.2, Figure 2.7) is subject to blurring and weak contrast ($\sigma_{X/ZEcc} \approx 1.0\,mm$). The

15 combined with semi-automatic detection of the absorber tube within the glass envelope tube (see Section 2.3.2 and Figure 2.7)

16 Nikon D300s digital SLR camera, ring flash Sunpak Auto 16R Pro

17 AICON DPA Pro

combined uncertainty in X and Z direction is determined according to $\sigma_{X/ZBench} \approx \sqrt{\sigma_{X/Z^2_{Glass}} + \sigma_{X/Z^2_{Ecc}}}$.

Parameter	Value
$\sigma_{X/ZGlass}[mm]$	$\simeq$ 0.5
$\sigma_{X/ZEcc}[mm]$	$\simeq$ 1.0
$\sigma_{X/ZBench}[mm]$	$\simeq$ 1.2

Table 4.5: Uncertainty estimates for photogrammetric benchmark coordinates

About 700 aerial images were captured for the $\text{QFly}_{\text{HighRes}}$ measurement. Most of the images serve to provide a stable configuration for the photogrammetric evaluation (bundle adjustment), which includes a simultaneously optimization of EOR, IOR, and object coordinates. For the absorber positioning, about 50 images captured along the individual flight route above each SCE (see Figure 4.3) are used. Regions of interest (ROIs) are defined approx. $\pm 150\,mm$ along the focal line with respect to PG measurement locations, as the direct view on the glass tube is obstructed in that region by the paper stripe with PG markers (see Figure 2.7). Figure 4.16 shows the result of the comparisons between $\text{QFly}_{\text{HighRes}}$ and benchmark for the first of three investigated SCEs. Table 4.6 provides an overview on the statistics of deviations for all three SCEs.

	RMS [mm]			Mean [mm]		
	X	*Z*	XZ	*X*	*Z*	XZ
SCE1	1.32	1.55	2.04	1.13	1.28	1.85
SCE2	0.92	0.93	1.30	0.47	0.55	0.99
SCE3	0.98	0.82	1.28	-0.86	0.37	1.16

Table 4.6: Statistics of the differences between $\text{QFly}_{\text{HighRes}}$ and benchmark measurement. For each SCE, both the *RMS* and the mean value are provided for each dimension *X* and *Z*. The column denoted XZ represents the the combined measurement uncertainty from both directions. Uncertainties for airborne ($\simeq 0.2 - 0.6\,mm$) and benchmark measurement ($\simeq 1.2\,mm$) are well within the respective margins of the observed differences (see Table 4.4).

The validation shows good agreement between benchmark and airborne measurement within the expected uncertainty margins. Deviations are somewhat larger for SCE1. The primary cause for this is a systematic off-set in the transformation onto the design data. Different POIs were used in either case[18].The manually attached mirror markers have not been positioned with sufficient accuracy for SCE1, while transformation parameters of SCE2 and 3 suggest sufficient accuracy of the transformation parameters here.

18 Mirror corners and gaps for QFly and manually attached markers for the PG measurement

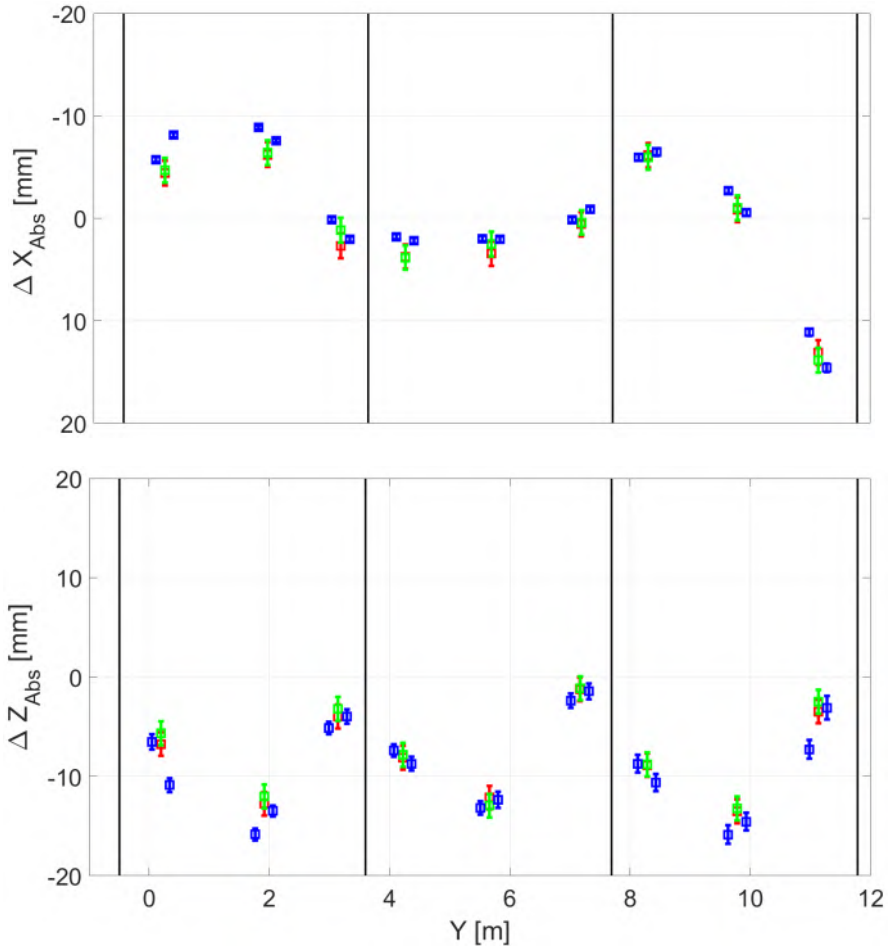

Figure 4.16: Comparison of absorber tube position for the first of three SCEs by $\text{QFly}_{\text{HighRes}}$ (blue), and benchmark measurements before (red) and after (green) the $\text{QFly}_{\text{HighRes}}$ measurement. The photogrammetric benchmarks are consistent. The characteristics of the ΔX_{Abs} (upper) and ΔZ_{Abs} (lower) match well within the expected uncertainty margins. Rather large deviations are due to the fact that data has been acquired from first generation ET collectors within the boiling section of a DSG boiler, where pronounced deflections caused by thermal stress are visible.

The uncertainty for the absorber tube deviation based on the newly developed airborne approach meets the accuracy requirements for the calculation of mirror shape deviations based on the TARMES/QFly approach ($< 2\,mm$, see Section 4.8) and simulation of optical performance with numerical RT. It enables retroactive alignment of the HCE and delivers accurate input for mirror shape measurements based on the distant observer (DO) approach.

The measurement effort for the airborne geometric characterization of the absorber tube position for an entire ET SCA with 12 SCEs is about 30 minutes for preparation and data acquisition, and another

3 h for fully automatic evaluation. The airborne approach is 50 times faster than previous methods with ground based data acquisition.

4.3.4 *Uncertainty analysis and validation of mirror slope deviations*

The following section aims at deriving the uncertainty of slope deviation in curvature direction (σ_{SDX}) from all previously determined input parameters. According to Figure 2.5, the calculation of the SD_X for PTCs using the TARMES/QFly method involves three spatial coordinates:

- The position of the nodal point of the camera and the orientation of its optical axis (EOR).
- The position of the reflection of the absorber tube edge on the mirror surface (X_{Reflex}).
- The position of the edge of the absorber tube, which creates the corresponding reflection on the mirror.

Other parameters which influence the result are concentrator properties like slope deviation in longitudinal direction (SD_Y) and height deviations from the ideal shape. The uncertainties of the input parameters have been deduced in the previous sections. For the calculation of the σ_{SDX}, the software GUM Workbench[19] was used (GUM, 1999). Based on the equations to derive the SD_X from the input data, the GUM Workbench calculates numerically the first order derivates.

The current section deals with two different data-sets. The validation was carried out with data from the KONTAS facility acquired in the year 2011. In the meantime, enhancements of the methodology and the payload have led to improvements of the measurement accuracy. Current evaluations yield improved measurement accuracy. Where necessary, the reader is informed about the use of actual or former data and methods, as listed in Table 4.7.

Year	2011	2016
Location	PSA	AS3
Camera	Olympus PE-1	Sony NEX-7
Resolution	12 MP	24 MP
Airborne Meas. of ΔZ_{Abs} & ΔX_{Abs}	No	Yes

Table 4.7: Different configurations for the $\text{QFly}_{\text{HighRes}}$ SD_X uncertainty analysis.

19 `http://www.metrodata.de/ver14.html`, based on the guide to the expression of uncertainty in measurement (GUM).

The expected measurement uncertainty has been calculated exemplarily for a PTC module with RP3 dimensions. All uncertainties are expressed in terms of one standard deviation. Table 4.8 displays the results obtained with the GUM workbench for a typical flight altitude above the SCE of 30 m. The main contribution to the overall uncertainty is caused by the uncertainty in the absorber tube position. The camera position (X_C, Z_C) has minor influence. Another relevant contribution to the measurement uncertainty is the SD_Y. The estimated order of magnitude of SD_Y was derived from deflectometric measurements of single PTC mirror panels (using the QDec system). A comprehensive overview on the input parameters and their uncertainties is given in Table 4.8.

Input parameter	1σ	mean σ_{SDX}		Value from:
		abs. [$mrad$]	rel.	
ΔX_{Abs} [mm]	2	0.34	0.39	Table 4.6
ΔZ_{Abs} [mm]	2	0.28	0.24	
X_C [mm]	6	0.08	0.02	Section 4.3.1
Z_C [mm]	6	0.00	0.00	
X_{Reflex} [mm]	8	0.00	0.00	Section 4.3.2
X_{Ortho} [mm]	2.5	0.06	0.01	Section 4.3.1
SD_Y [$mrad$]	4	0.15	0.09	QDec/QFoto
dZ [mm]	2	0.28	0.24	
total		0.62		

Table 4.8: Assumptions for the most recent (year 2016) uncertainty of the input parameters and results for the local σ_{SDX} values. The fist block contains the absorber and camera position. The contribution from the uncertainty of the camera position can be neglected, while the absorber tube position has the highest share. The uncertainty of the position of the reflection of the absorber tube edge on the mirror surface (X_{Reflex}) has minor effect, assuming that outliers and artifacts are removed reliably. SD_Y and height deviations of the mirror from the ideal parabola (dZ) also affect the local measurement accuracy.

The formulas for the local uncertainty derived by the GUM Workbench were also implemented in a MATLAB model, in order to provide a σ_{SDX} map over the aperture area of the SCE for the input values presented in Table 4.8. This map is presented in Figure 4.17. The resulting local uncertainty in SD_X is in the range of $0.5 - 0.8\,mrad$, depending on the position within the collector module. The effect of SD_Y increases with increasing distance from the vertex and with increasing incidence angle between LOS and the collectors optical axis (Bendt et al., 1979).

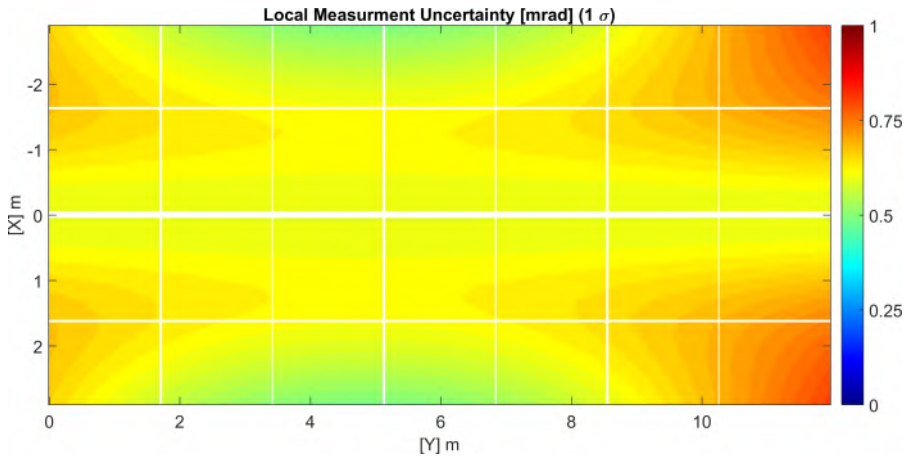

Figure 4.17: $\text{QFly}_{\text{HighRes}}$ σ_{SDX} map for a single SCE in *mrad* based on the values presented in Table 4.8. The asymmetry along the vertex is caused by the eccentric fly-over to avoid specular reflections from the Sun. Symmetrically to the camera positions at $Y = 5\,m$, the influence of SD_Y and height deviations of the mirror surface (dZ) increases towards the end-plates. Close to the vertex, the contribution from uncertainties of ΔX_{Abs} is predominant, while towards the parabola edge the uncertainty of the vertical absorber tube displacement gains influence. σ_{SDX} is in the range of $0.5 - 0.8\,mrad$

Validation

A representative parabolic trough collector SCE[20] was used for the validation measurements carried out in 2011. Three different methods were applied to determine the geometry of this particular SCE in zenith position ($\theta = 90°$):

- A photogrammetric measurement of the SCE was carried out. Since the photogrammetric result is not affected by the uncertainties listed in Table 4.8, this result may serve as an absolute benchmark for both TARMES and $\text{QFly}_{\text{HighRes}}$. Eight mirror panels were equipped with a target raster of $0.15 \times 0.15\,m$ edge length for resolving the long-wave deviations of the mirror panels from the ideal shape. With reasonable effort, this was only possible for two of the seven mirror panel rows. The relative measurement uncertainty of PG between *adjacent* POIs is estimated to be in the range of 0.1 mm, which results in a local uncertainties of the SD_X from close range photogrammetry of $\simeq 0.7\,mrad$.

- A TARMES measurement with a stationary camera on an elevator platform approximately 25 m above the parabola vertex serves as a second benchmark for $\text{QFly}_{\text{HighRes}}$. Using TARMES, the camera position is known with high accuracy due to the use of high resolving inclinometers for the determination of

20 part of the KONTAS facility at PSA

the module orientation[21]. The local measurement uncertainty is estimated to be in the range of $0.6 - 1.1\,mrad$, depending on the position within the collector module.

- The $\text{QFly}_{\text{HighRes}}$ system took images from comparable perspectives relative to the collector as the TARMES measurement. Local values for σ_{SDX} are estimated to be in the range of $0.6 - 1.1\,mrad$, depending on the position within the collector module. The values for σ_{SDX} presented here are slightly higher[22] compared to the ones presented in Figure 4.17 for the latest version of $\text{QFly}_{\text{HighRes}}$. Hence, assumptions on image quality and on the uncertainty of ΔZ_{Abs} had to take into account a higher variance, and led to comparatively higher σ_{SDX}.

These three measurements are expected to deliver the same SD_X results within the presented error budgets. Figure 4.18 shows the results obtained with TARMES and $\text{QFly}_{\text{HighRes}}$. The numbers assigned to each mirror panel in the plot represent the RMS_{SDX}. The SD_X characteristics are almost equal irrespective of small differences in the statistics and local variations.

To assess the differences between both methods, Figure 4.19 shows the difference matrix and the expected measurement uncertainty of $\text{QFly}_{\text{HighRes}}$. The local differences are in accordance with the uncertainty analysis. Some of the deviations may be real deformations of the collector, because during the 2 weeks between both measurements, the collector module was in operation. This might be especially the case for the panels in the lower row of the module, where local deformations close to the GBRPs are visible. On the SCE level, the RMS_{SDX} values was measured to 2.37 *mrad* by QFly and 2.47 *mrad* by TARMES.

Next, $\text{QFly}_{\text{HighRes}}$ results were compared to SD_X maps obtained from the close range photogrammetry measurement. The matched area corresponds to two mirror panel rows at the drive pylon and at the center of the SCE. As the result of the photogrammetric evaluation is not affected by the absorber tube position, it provides a very good benchmark for global deviations, although the spatial resolution and the uncertainty for slope deviations on a small scale are less favorable. Figure 4.20 provides the absolute difference between the PG benchmark and the airborne measurement. Both results match well, considering the fact that the uncertainty of local slope deviations for both measurements is in the range of $0.7\,mrad$. The numbers assigned to each panel represent the difference of the RMS_{SDX} values between

21 expressed by the actual view angle between the optical axis of the SCE and camera position (ϕ_{Cam})

22 When the validation was carried out in 2011, the automatic absorber tube measurement was not yet developed, and a Olympus Pen E-P1 instead of Sony NEX-7 was used.

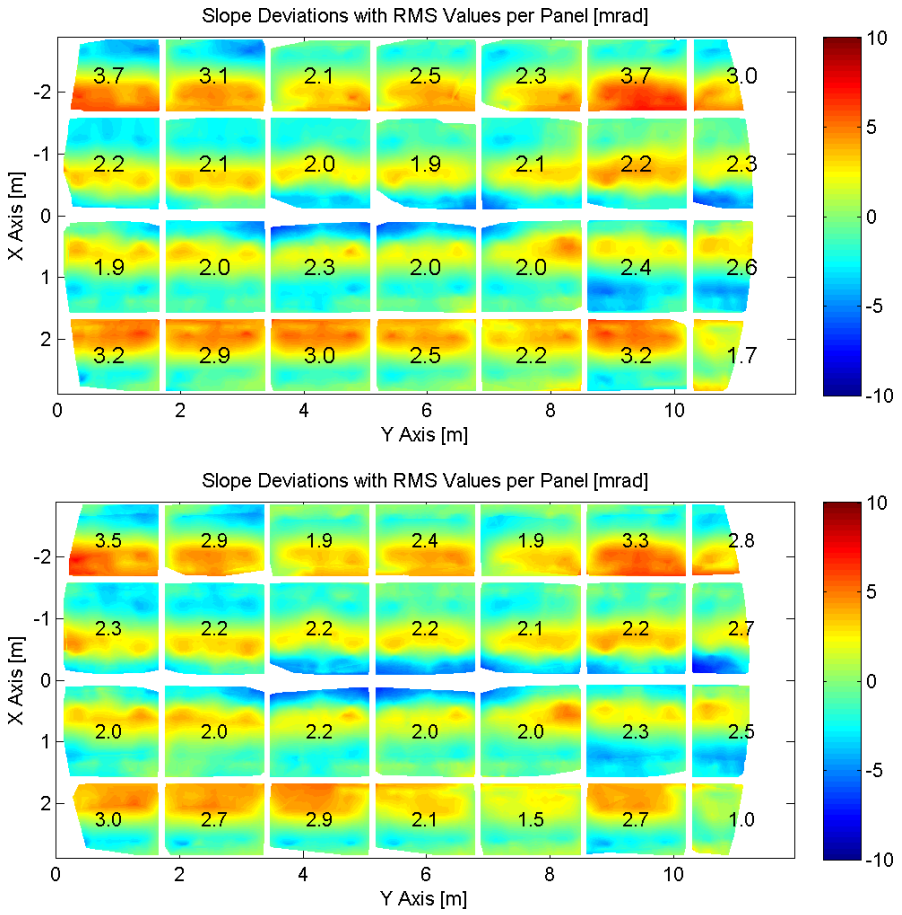

Figure 4.18: Top: TARMES SD_X map. Bottom: $\text{QFly}_{\text{HighRes}}$ SD_X map. The characteristic mirror geometry is well reproduced by both methods. A detailed analysis of the differences is provided in Figure 4.19.

QFly and PG measurement. Here, the deviations of the RMS_{SDX} values of the panels are comparatively small. Local deviations are mainly caused by the limited spatial resolution of the photogrammetric benchmark.

In Figure 4.21, the RMS_{SDX} values are displayed for panels, which have been characterized by all three methods. For each approach, the obtained values are well within the expected uncertainties. The underestimation of the slope deviations by close range photogrammetry is explained by the limited spatial resolution and thus the neglect of small scale slope deviations.

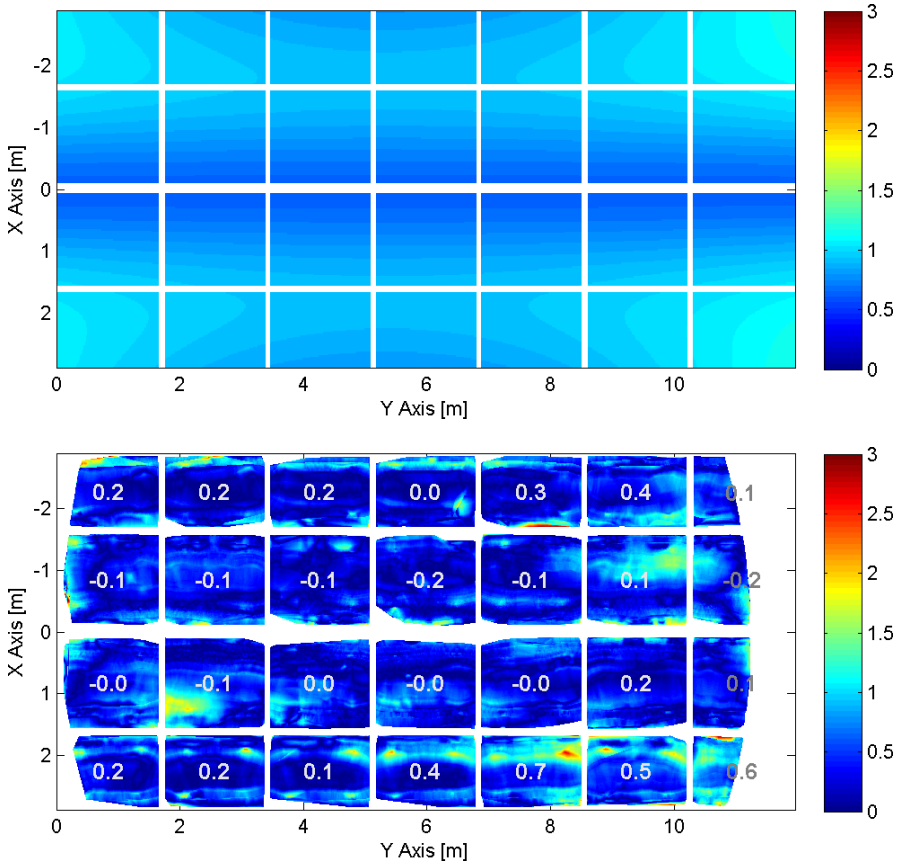

Figure 4.19: Top: Expected absolute measurement uncertainty (1σ) in the range $0.6 - 1.1\,mrad$. The underlying values for the input parameters differ from the values presented in Table 4.8 and Figure 4.17, because the validation in 2011 was carried out with another camera and flight route, and the uncertainty of the absorber tube positioning was higher (see Table 4.7). The scale of the color bar is extended to $3\,mrad$ to match the peaks of the observed absolute differences (Bottom) between TARMES and $\text{QFly}_{\text{HighRes}}$. Except some peaks in the region of the glass bracket retaining points, local differences between both methods are below the 1σ distribution presented above. The difference between both measures is determined also by local variations of the density of absorber tube edge reflection. The numbers assigned to each mirror panel provide the difference of RMS_{SDX} between TARMES and $\text{QFly}_{\text{HighRes}}$.

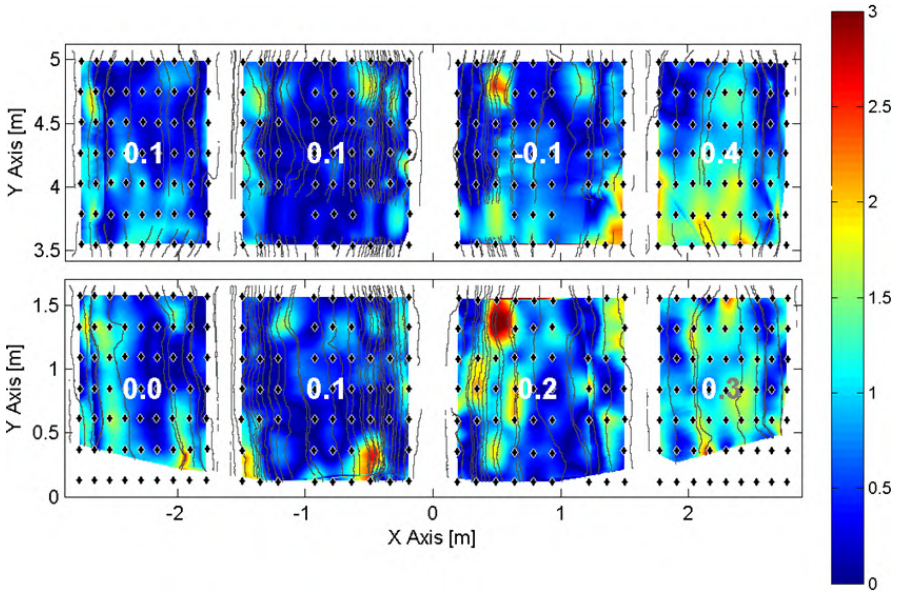

Figure 4.20: Difference of SD_X determined by $\text{QFly}_{\text{HighRes}}$ and close range photogrammetry (PG) for two mirror panel rows in $[mrad]$. The numbers assigned to each mirror panel represent the difference of the RMS_{SDX} values between $\text{QFly}_{\text{HighRes}}$ and PG measurement. Black dots are POIs measured by close range photogrammetry. Vertical curved lines represent detected absorber tube edges of the $\text{QFly}_{\text{HighRes}}$ measurement. Most deviations between both methods can be explained by the limited spatial resolution and coarse grid of the PG. Areas with relatively high deviations between PG and $\text{QFly}_{\text{HighRes}}$ at $X \simeq 2\,m$ are subject to the low density of absorber tube edge lines.

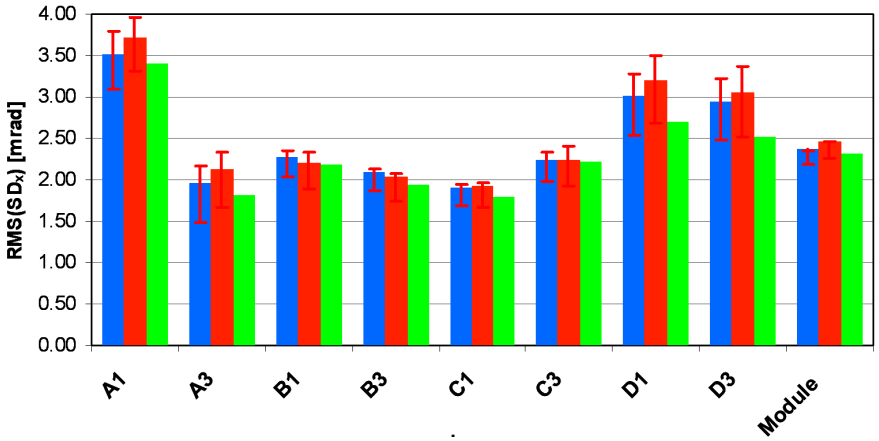

Figure 4.21: Comparison of RMS_{SDX} values for single mirror panels (blue: $\text{QFly}_{\text{HighRes}}$, red: TARMES, green: PG. Panel positions are indicated by A–D (row) and one or three (column number) seen from drive pylon. The underestimation of the RMS_{SDX} by close range photogrammetry is explained by the limited spatial resolution.

Global measurement uncertainty

The RMS_{SDX} value derived from the entire slope deviation map (Eq. 2.9) is an appropriate parameter to describe the optical quality of the concentrator (Lüpfert and Ulmer, 2009). Assuming a Gaussian distribution of the local slope deviations, the RMS_{SDX} value can be used to estimate the optical performance following the statistical approach of Bendt et al. (1979). The uncertainty of the RMS_{SDX} value, however, can not be calculated via an ordinary propagation of uncertainties, since the uncertainties of single measurement points are partly correlated due to widespread influence of input parameters. Furthermore, the definition of the RMS_{SDX} causes an asymmetric distribution of expected measurement results. In other words, even if a perfect concentrator ($RMS_{SDX} = 0\,mrad$) was measured, the inevitable uncertainties of the previously described input parameters always would lead to a $RMS_{SDX} > 0$.

To account for that, a Monte Carlo approach was used to estimate the uncertainty of the RMS_{SDX} value (see Figure 4.22). The input data is based on recent (2016) measurement of an ET collector, with the uncertainties provided in Table 4.8.

Each input parameter was overlaid with a Gaussian distributed noise and an individual spatial pattern to approximate expected correlations between adjacent measuring points. In the first iteration, the resulting asymmetric distribution function of the RMS_{SDX} of repeated measurements has an mean value differing from the measured RMS_{SDX}. In order to cope with that overestimation, the measured slope deviations were iteratively reduced (in total by a factor of 0.9986) until the mean value of simulated RMS_{SDX} matches the measured value. For the investigated SCE the measured RMS_{SDX} value on SCE level amounts to 2.66 $mrad$. By considering the above described effect, the best estimate of the real value was calculated to 2.59 $mrad$ (denoted *best estimate* in Figure 4.22), which in return results in a uncertainty of the measured value in the range of $\pm 0.04\,mrad$ based on a level of confidence of 68.3%. Figure 4.22 shows the distribution of the RMS_{SDX} resulting from the Monte Carlo simulation for an assumption of the uncertainty of the input parameters as described in Table 4.8.

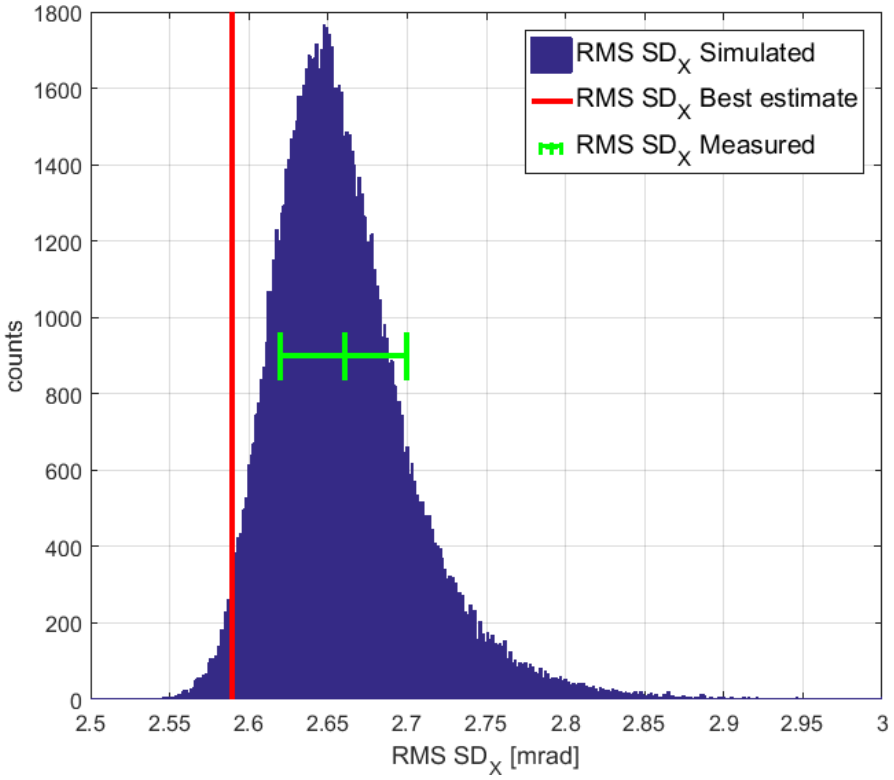

Figure 4.22: Influence of the uncertainties of input parameters on the RMS_{SDX} at module level obtained by a Monte Carlo simulation with 100,000 runs. The red line represents the best estimate of the RMS_{SDX} values so that the measured RMS_{SDX} equals the expectation value of the Monte Carlo simulation. The uncertainty of this assumption is shown by the error bar for a level of confidence of 68.3%.

Influence of sample rate on the RMS_{SDX}

From a single image showing the absorber tube reflection (see Figure 2.5), the SD_X is calculated along the reflection of the absorber tube edges. To obtain information about the entire mirror surface, several images with different view angles are required. As information is only available along these reflection lines, SD_X values between these lines are obtained by interpolation. A critical point is the selection of an appropriate sample rate – the number of images and such observations. For a typical QFly measurement, about 40–60 images must be taken, resulting in about 80–120 absorber tube edge lines distributed over the concentrators mirror surface. Replenishing missing information by interpolation involves neglecting small-scale slope deviations. Consequently, the local SD_X as well as the RMS_{SDX} are assumed to be underestimated with decreasing sample rate. The maximum sample rate in a real measurement is restricted by the affordable effort[23].

23 limited flight time in combination with the limited frame rate of camera.

Several evaluations with decreasing number of images contributing to the calculation of the SD_X map were carried out[24]. The dependency of the RMS_{SDX} on the number of absorber tube edge lines involved in the evaluation is presented in Figure 4.23. It is expected that the RMS_{SDX} approaches the ${RMS_{SDX}}^{True}$ for an infinite number of images.

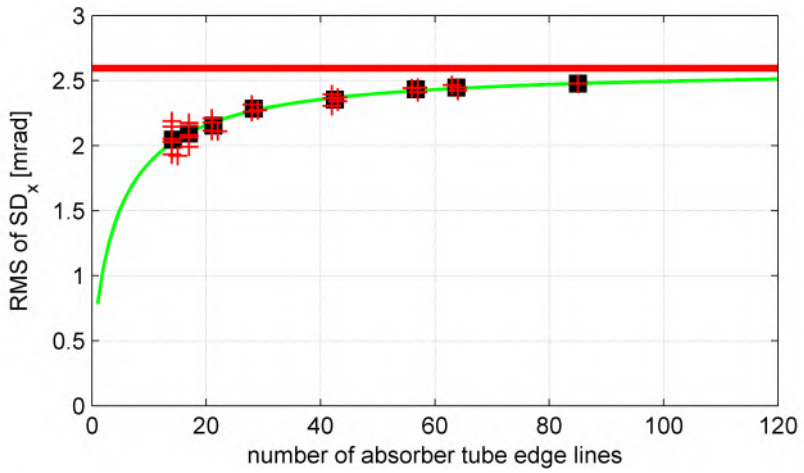

Figure 4.23: The dependency of the RMS_{SDX} on the number of images involved in the evaluation. The RMS_{SDX} measured with highest sample rate of 86 absorber tube edge lines (corresponding to 43 images) yielded 2.48 *mrad* while the ${RMS_{SDX}}^{True}$ derived by extrapolation (red horizontal line) of Equation 4.15 (green curve) yields 2.60 *mrad*. The data points represent different combinations of images. The scattering is due to variations of the RMS_{SDX}, when different combinations of images were used to calculate the slope deviation map.

As expected, the results show an increasing RMS_{SDX} value with increasing number of images and converging towards a value, which is expected to be the true RMS value of slope deviation in curvature direction (${RMS_{SDX}}^{True}$). This value is estimated by fitting the parameters of the function represented by Equation 4.15 to the RMS_{SDX} values obtained for different numbers of images. Equation 4.15 describes the expected value of the chi-squared distribution of RMS_{SDX} values described by the Gamma function Γ:

$$ {RMS_{SDX}}^{Expect}({RMS_{SDX}}^{True}, k) = \frac{{RMS_{SDX}}^{True} \cdot \sqrt{2} \cdot \frac{\Gamma((k+1)/2)}{\Gamma(k/2)}}{\sqrt{k}} \quad (4.15) $$

Here, k is a value proportional to the number of involved images. The extrapolated value ${RMS_{SDX}}^{True}$ could be estimated for the QFly measurement to be 2.60 *mrad*. The closest approximation was reached

24 The data set was the same as the one used for the validation at the KONTAS facility 2011

with the highest number of images and is yet about 0.1 *mrad* lower than the extrapolated value. For the current measurement set up, underestimation of the RMS_{SDX} due to limited sample rate and overestimation due to uncertainties of the input parameters are in the same order of magnitude. For that reason, it is assumed that both effects roughly compensate each other and the overall uncertainty of the RMS_{SDX} is expected to be about 0.1 *mrad* at SCE level based on the statistical uncertainty obtained by the Monte Carlo Simulation and the finite sample rate. A correction of these effects is not foreseen as long the measurement uncertainty and other parameters remain unchanged.

4.3.5 *Sensitivity of the intercept factor on measurement uncertainties*

The characteristic error propagation described for the RMS_{SDX} apply as well for the intercept factor (γ) calculated in a ray-tracing (RT) analysis. Due to the non-applicability of classical propagation of error, the uncertainty of γ can only be determined by varying the geometrical input variable within the respective variance and by checking the distribution of obtained performance values.

In order to determine the uncertainty bandwidth of γ, the evaluation was repeatedly called with the same stripe matrices. The input data for the RT was superimposed with the variation according to the known uncertainties, which then also resulted in a corresponding variation of γ. The result of this variation was uncertainty of γ in the range of 0.2 %, which can be regraded as sufficiently accurate. For typical intercept factor values in the range of $95 - 98$ %, the uncertainty is acceptable in the context of other methods (e.g. yield analysis) to determine accurately the solar field performance.

4.3.6 *Validation of QFly based yield analysis with thermal measurements*

The assumptions and simplifications regarding the heat transfer fluid temperature (T_{HTF}) and the incidence angle ($\phi_{||}$) made in Chapter 2 (Equation 2.6) are not applicable to solar fields of commercial power plants. However, at the KONTAS facility[25], it was possible to compare the optical performance based on thermal measurements with the optical performance based on intercept factor calculations from $\text{QFly}_{\text{HighRes}}$ results and assumptions on the optical properties. Preliminary results of this comparison are available in Janotte et al. (2015). Table 4.9 provides results for $\eta_{opt}(\phi_{||} = 0)$ from both methods. The results for η_{opt} are in good accordance and within the respective error

25 The KONTAS facility provides two-axis tracking and heat transfer fluid temperature (T_{HTF}) control, so that the constraints concerning $\phi_{||}$ and T_{HTF} described in Eq. 2.6 can be fulfilled.

margins.

The optical performance was derived by measuring the geometry of the SCE mounted on the KONTAS with $QFly_{HighRes}$ and determining $\gamma'_{\phi_{||}=0}$ with the ray-tracing software SPRAY. The calculation of $\gamma'_{\phi_{||}=0}$ takes into account the effect of blocking and shading, mainly influenced by the inactive area of the receiver, which corresponds to approx 3.3 % of the total receiver length (Schott, 2015a) at nominal T_{HTF}. The optical properties were taken from the data-sheets of the component manufacturers and correspond to new, state of the art mirrors and receiver tubes.

An often ignored phenomenon is the shading of parts of the mirror surface by the glass envelope tube. In fact, all radiation from the sun traveling through the glass envelope tube before hitting the mirror is deviated from the direction of incoming radiation. The extend of this deviation leads to a focus deviation in curvature direction (FD_X) larger than the absorber tube radius, such that this radiation is lost. This effect diminishes the $\gamma'_{\phi_{||}}$ by another 0.8 % (percentage points). In fact, the mirror gap at the parabola vertex of the RP3 mirror design of 80 mm should match the diameter of the glass envelope tube of 125 mm, since the mirror stripe of 22.5 mm on both sides of the vertex does not contribute to optical performance.

geometrical			thermal		
	Value	$rel.u(1\,\sigma)$		Value	$rel.u(1\,\sigma)$
ρ_{Ref}	0.940	0.010	$\dot{m}$	$2.995\,kg/s$	0.001
τ_{Glass}	0.970	0.010	c_p	$1.62\,kJ/kg\cdot K$	0.010
α_{Rec}	0.955	0.010	$T_{out} - T_{in}$	$10.07°C$	0.010
$\gamma'_{\phi_{||}=0}$	0.942	0.002	DNI	$968\,W/m^2$	0.005
χ	0.990	NaN	χ	0.9902	NaN
$\eta_{opt}(\phi_{||}=0)$	0.804 ± 0.015			0.792 ± 0.012	

Table 4.9: Comparison of the optical efficiency (η_{opt}) from geometrical and thermal measures. The optical properties τ_{Glass} and α_{Rec} were taken from Schott (2015a). The uncertainties of the optical properties are rough estimates. ρ_{Ref} was taken from Meyen et al. (2009). The $\gamma'_{\phi_{||}=0}$ and χ are measured quantities. No uncertainty estimate was available for χ.
For the thermal performance parameters, the values and the relative uncertainty margins were taken from the KONTAS facility. A detailed description of the uncertainty of thermal solar field measurements can be found in Janotte (2012). Although the optical approach tends to slightly overestimate the performance, the results are so far within the current uncertainty margins. The most probable reason is, that the values for the optical performance of the receiver do not correspond to the actually investigated test receiver.

SUMMARY

This chapter has provided an extensive description and validation of the $\text{QFly}_{\text{HighRes}}$ mode. The combination of "off the shelf" hardware with a custom software library provides a unique system for the characterization of parabolic trough collectors and loops, with high spatial resolution and accuracy. A photogrammetric determination of the camera position relative to the collector provides the basis for precise deflectometric determination of the mirror shape and for the photogrammetric evaluation of the absorber tube position. The measurement accuracy of the collector geometry has proven to predict an effective intercept factor $\gamma'_{\phi_{||}}$, which is in excellent agreement with results from thermal performance measurements.

In order to provide an efficient solution for the characterization of the entire solar field, the next chapter is dedicated to the $\text{QFly}_{\text{Survey}}$ approach. By increasing the flight altitude and altering the flight pattern, maps of effective slope deviation in curvature direction ($SD_{\text{X}eff}$) are obtained at slightly reduced accuracy and considerable decreased spatial resolution. The effective tracking deviation ($\phi_{\perp\, eff}$) can be measured by $\text{QFly}_{\text{Survey}}$, which so far has not been accessible at this extent.

5

AIRBORNE QUALIFICATION OF ENTIRE SOLAR FIELDS

This chapter further develops the approach described in the foregoing Chapter 4. The objective is the complete geometrical commissioning of entire PTC collector fields by a method denoted $\text{QFly}_{\text{Survey}}$. The $\text{QFly}_{\text{HighRes}}$ approach with its rather complex waypoint (WP) route has limited measurement capacity due to flight time restrictions ($<= 40min$) and maximum frame rate of the camera ($\simeq 2.5\,fps$). It delivers spatially high resolved results for single SCAs, yet it lacks the possibility for fast screening of entire solar fields. With the current UAV and payload, about one EuroTrough type solar collector assembly (SCA) per flight and up to two loops per day can be measured under ideal conditions in the $\text{QFly}_{\text{HighRes}}$ mode. Hence, a PTC solar field with 152 loops (see Table 1.1) would require 76 days for comprehensive characterization. Experiences during measurement campaigns in commercial power plants have shown that interference with daily plant operation tends to reduce the acceptance and feasibility of solar field qualification methods, even if results are expected to be beneficial for mid- and long term plant performance.

The so called $\text{QFly}_{\text{Survey}}$ concept is presented here, which enables a fast characterization of an entire solar field and such reduces mentioned interference with plant operation. $\text{QFly}_{\text{Survey}}$ provides effective slope deviation in curvature direction (SD_{Xeff}) and the alignment between SCEs (described by the effective tracking deviation $\phi_{\perp\,eff}$) at lower spatial resolution from images taken along straight east-west fly-overs at higher flight altitudes. $\text{QFly}_{\text{Survey}}$ data acquisition for the complete characterization of a PTC power plant with the characteristics presented in Table 1.1 can be implemented in four to eight flights with a total flight-time of 1-2 hours.

The $\text{QFly}_{\text{Survey}}$ approach can be applied to different operational states of the solar field. The solar field status $\text{Survey}^{\text{Online}}$ is characterized by an operational solar field under full solar radiation. Under these conditions, the characterization of the tracking system is possible (Section 5.2.4). However, concentrated radiation on the absorber tube reduces the contrast and thus complicates un-ambiguous detection of the absorber reflection (see Figure 5.1 right).

In contrast, the solar field status $\text{Survey}^{\text{Offline}}$ is characterized by a fix tracking angle (θ) close to zenith position and at least 1 hour

before or after solar noon and/or at cloudy conditions. Under these conditions, the absorber tube reflection is clearly visible (see Figure 5.1 left). In this mode, measurements of the effective slope deviation in curvature direction (SD_{Xeff}) (Section 5.2.2) and effective tracking deviation ($\phi_{\perp eff}$) (Section 5.2.3) are performed, both based on the absorber tube reflection pattern.

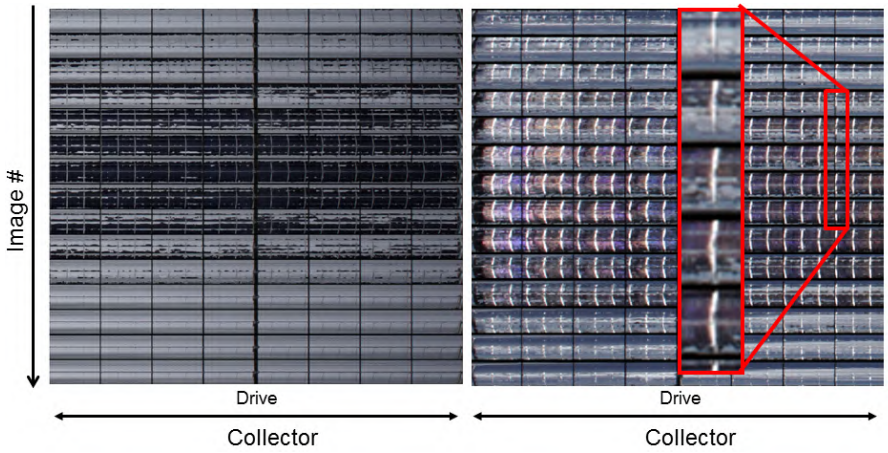

Figure 5.1: Series of orthoimages from $\text{QFly}_{\text{Survey}}$ for different operating conditions of the solar field. All orthoimages show the same SCA from different perspectives during an east-west flyover. Images on the left were captured in $\text{Survey}^{\text{Offline}}$ mode, while images on the right were captured in $\text{Survey}^{\text{Online}}$ mode. The difference between dark (left) and illuminated (right) absorber requires adapted evaluation procedures. Un-ambiguous identification of the absorber tube reflection is only possible in $\text{Survey}^{\text{Offline}}$-mode. The strong signal where concentrated radiation hits the HCE bellow protection shield (highlighted area), is exploited for tracking characterization while the field is in operation (see Section 5.2.4).

The work-flow of $\text{QFly}_{\text{Survey}}$ is visualized in Figure 5.2. Where possible, the methodology and software code of the $\text{QFly}_{\text{HighRes}}$ approach is applied to the $\text{QFly}_{\text{Survey}}$ method. The main differences of the post-processing is found in the calculation of the 3D-setup (EOR in solar field coordinate system). Furthermore, SD_{Xeff} and $\phi_{\perp eff}$ are measured instead of SD_X, ΔX_{Abs}, and ΔZ_{Abs}.

This chapter is structured as follows: Section 5.1 describes the data acquisition and requirements. Section 5.2 is dedicated to the evaluation approaches to obtain SD_{Xeff} and $\phi_{\perp eff}$. Section 5.3 provides results, the uncertainty analysis, and validation against an independent benchmark measures. Finally, in Section 5.4, a concept for comprehensive solar field characterization is presented, combining all approaches used in this thesis in an efficient way. First results from the application of QFly in the AS3 PTC power plant are presented to show the capability of the new system in terms of capacity, accuracy, level of detail, and significance for optimization. The AS3 plant was chosen due to

the long-term collaboration with the operator (Marquesado Solar S.L.) and its proximity to the PSA.

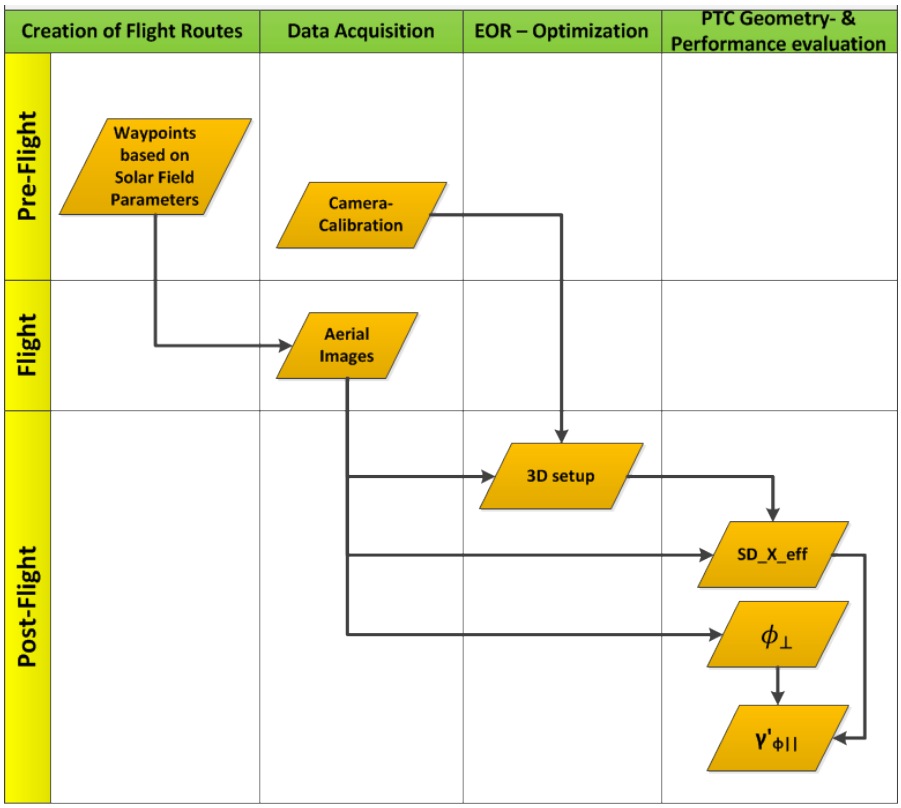

Figure 5.2: Methodology of the $\text{QFly}_{\text{Survey}}$ approach. In comparison with the $\text{QFly}_{\text{HighRes}}$ mode (see Figure 4.1), the camera requires pre-calibration instead of simultaneous calibration in a photogrammetric bundle adjustment. The flight route does not permit the measurement of absorber tube position ($\Delta X_{Abs}/\Delta Z_{Abs}$). However, characterization of the effective tracking deviation ($\phi_{\perp eff}$) is possible.

5.1 SYSTEM DESCRIPTION

5.1.1 *Flight route design and data acquisition*

Flight height, if not limited by law/regulations, should allow for a visible length at ground level covering one loop in north-south direction of the solar field. With the currently used camera (Sony NEX-7 with 16 mm lens) and flight route design, a flight altitude of $\simeq$ 240 m above ground level would be required.

Another possible flight altitude of 120 m provides a view angle sufficient for a single SCA. The corresponding ground sample distance (GSD) and thus spatial resolution of the SD_{Xeff} maps is about 60 $mm/pixel$ at at 240 m flight altitude (factor 10 below $\text{QFly}_{\text{HighRes}}$) and about 30 $mm/pixel$ at at 120 m flight altitude (factor 5 below

$QFly_{HighRes}$). Since UAV regulations in Spain restrict flight altitudes to 120 m above ground level, mainly the second option (120 m) is considered here. The ideal trajectory of such a flight is shown in Figure 5.3.

In order to minimize flight altitude, the "landscape" camera orientation in north - south direction has been chosen for the results presented here, in combination with Nadir mount[1]. However, for reasons described in Section 5.2.1 and 5.3, future flight route designs will make use of different camera orientations (oblique mode) and larger view angle in east west direction for better pose estimation along the relevant X-dimension.

Camera pre-calibration IOR data is obtained from a $QFly_{HighRes}$ measurement carried out before or after the $QFly_{Survey}$ flight, without altering the camera lens and body in between.

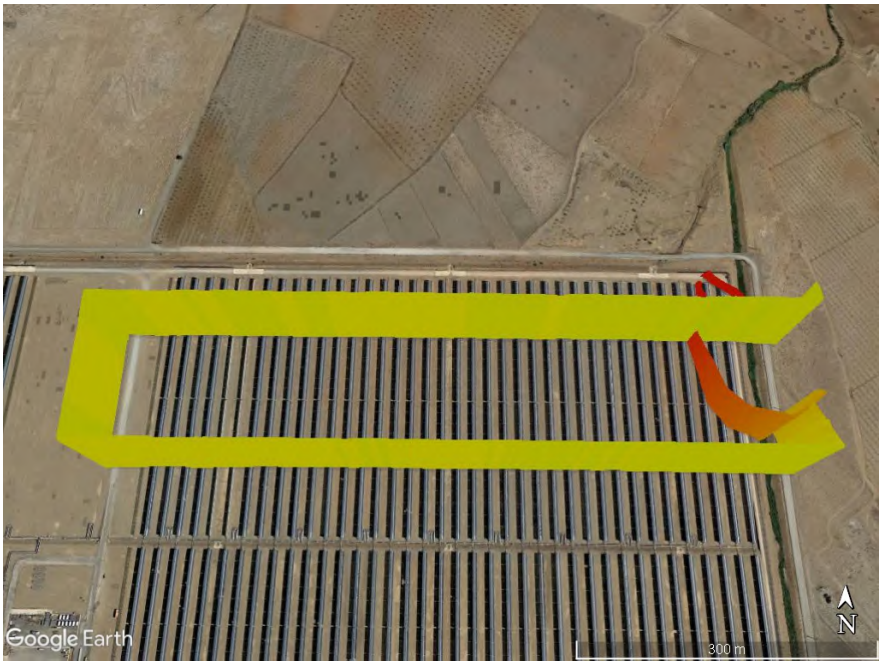

Figure 5.3: Visualization in Google Earth of a $QFly_{Survey}$ WP route at a flight altitude of 120 m for the North East Block of the AS3 CSP plant. The color of the visualization corresponds to the height over ground. Take-off and landing took place in the upper-left corner of the solar field. The data acquired with such a flight of $\simeq$ 15 min duration covers 12.5% of the solar field area.

5.1.2 *Solar field status*

The requirements on the solar field status correspond in general to the points mentioned in Section 4.1.3. Mirrors and absorber glass envelope tubes must be clean and the tracking angle should be close to

1 Camera optical axis vertical

zenith ($\theta = 90 \pm 5°$) for Survey$^{\text{Offline}}$ measurements. For Survey$^{\text{Online}}$ measurements, no θ-constraints have been identified so far. Constant heat transfer fluid temperature (T_{HTF}) and access to the plant data acquisition system is required in order to calculate the temperature dependent absorber tube position in vertical direction (see Section 3.2.3) individually for each SCE. Concerning the ambient conditions, the wind speed at ground level must not exceed $6 - 8\,m/s$. Sufficient ambient light is required to keep exposure times as short as possible ($\leq 1/2000\,sec$) to avoid blurring.

5.2 SURVEY EVALUATION

The evaluation follows to a large extent the work-flow of QFly$_{\text{HighRes}}$. The main difference is the determination of the camera position. Due to the flight route design, the acquired images are not suitable for photogrammetric evaluation. An approach based on assumptions of the solar field coordinates and pre-calibration of the camera in combination with single photo resection is applied here. Orthoimage creation considers the entire SCA instead of single SCEs. The subsequent procedure depends on the measurement mode. In Survey$^{\text{Offline}}$ mode, the detection of absorber tube reflection is similar to the QFly$_{\text{HighRes}}$ approach. The tube pattern are also exploited to calculate the orientation of the optical axis of each SCE. In Survey$^{\text{Online}}$ mode the detection of the absorber tube is not possible to present knowledge. Instead, the clear reflections of the illuminated HCE bellow protection shields (see Figure 5.1) are used to obtain information on the $\phi_{\perp eff}$.

5.2.1 *Determination of camera position*

The position and orientation of the camera relative to the solar field is the key input parameter for all evaluations (mirror shape and tracking characterization). Increasing flight altitude by a factor of five to ten with respect to the QFly$_{\text{HighRes}}$ approach (Section 4.1.2) leads to the fact that the QFly$_{\text{Survey}}$ approach can not exploit the benefits of a bundle adjustment based photogrammetric evaluation. The detection of single mirrors corners and artificial targets with reasonable dimensions (see Figure 4.4) is no longer possible from this altitude and flight routes with appropriate geometry would be far too long.

It is therefore appropriate to assume a given field geometry and pre-calibration of the camera, and only to optimize the exterior orientation by means of single photo resection (Grussenmeyer and Al Khalil, 2002). The whole procedure coincides, of course, with the correctness of the assumptions with regard to the field geometry. The gaps between SCAs are used as "detectable" features for the image processing instead of single mirror panel corner, gaps and crossing points. GNSS data

logged by the UAV is used to obtain proper EOR-starting values. The following list outlines the process of determination of the camera position for a larger image series[2] from a straight east-west solar field overflight, where the image index (#) denotes the image number in the range $\# = [1...N]$:

1. Image processing to detect the pixel position $P_{x,y}^{Meas}$ of collector features in the image #. Search areas are set by ROIs based on rough EOR-estimation (see step 4). For the first image ($\# = 1$), about 8-10 features are detected and assigned interactively to start the process.

2. EOR calculation by means of single photo resection by minimization of residuals (Equation 5.1) between detected $P_{x,y}^{Meas}$ and projected $P_{x,y}^{Proj}$ features[3].

3. Image registration: Identification of identical features in subsequent images ($\# \mapsto \# + 1$). Feature tracking is performed by cross correlation of least ambiguous features and includes an outlier detection and an iterative approach to cope with the challenge of "snapping" forth and back in the repetitive solar field image caused by limited frame rate and tumbling of the camera[4].

4. EOR estimation in image $\# + 1$ with tracked features by minimization of residuals between tracked $P_{x,y}^{Track}$ and projected $P_{x,y}^{Proj}$ features. Start values are the exterior orientation from the previous image or GNSS data.

5. Continue with step 1.

Once the 3D setup in terms of EOR in the solar field coordinate system is known, the process of orthoimage creation and absorber tube detection follows exactly the same methodology as described in Section 4.2.3 and 4.2.4. The following text provides a comprehensive description of the $\text{QFly}_{\text{Survey}}$ EOR estimation task and related constraints. An estimation of EOR uncertainty will be given in Section 5.3.1.

Ideal solar field geometry

The solar field geometry is taken from drawings provided by the plant operator. Once the SCE-geometry in terms of aperture width and length is defined, the geometry of SCAs, loops and entire blocks of the solar field can be established by the parameters presented in Table A.1. Furthermore, the tracking angle (θ) must be considered, as well

2 $N \simeq 800 - 1000$ images

3 also referred to as re-projection error

4 State of the art brush-less gimbals are expected to solve this issue

as the terrain dependent height variation of the SCAs. Such height variations are basically motivated to assure the controlled drainage of surface water.

Survey feature detection

Similar to the $QFly_{HighRes}$ approach, the determination of the exterior orientation (EOR) relies on robust image processing to detect the 2D image coordinates of prominent mirror features with known 3D coordinates. Due to different flight route design and in particular flight altitude, there are some difference between the image processing in $QFly_{HighRes}$ and $QFly_{Survey}$ mode, respectively.

The $QFly_{HighRes}$ image processing is being applied to 32 mirror features per SCE (see Figure 4.4). Due to the reduced ground sample distance (GSD) of the $QFly_{Survey}$ data acquisition and the uncertainty of the initial EOR, these rather small scale features are not suitable in this case. Figure 5.4 provides an overview on the inter-SCE gaps used instead. These features provide a robust alternative to single mirror panel gaps, crossings and corners. The detection process is the same approach as described in Section 4.2.1, page 61.

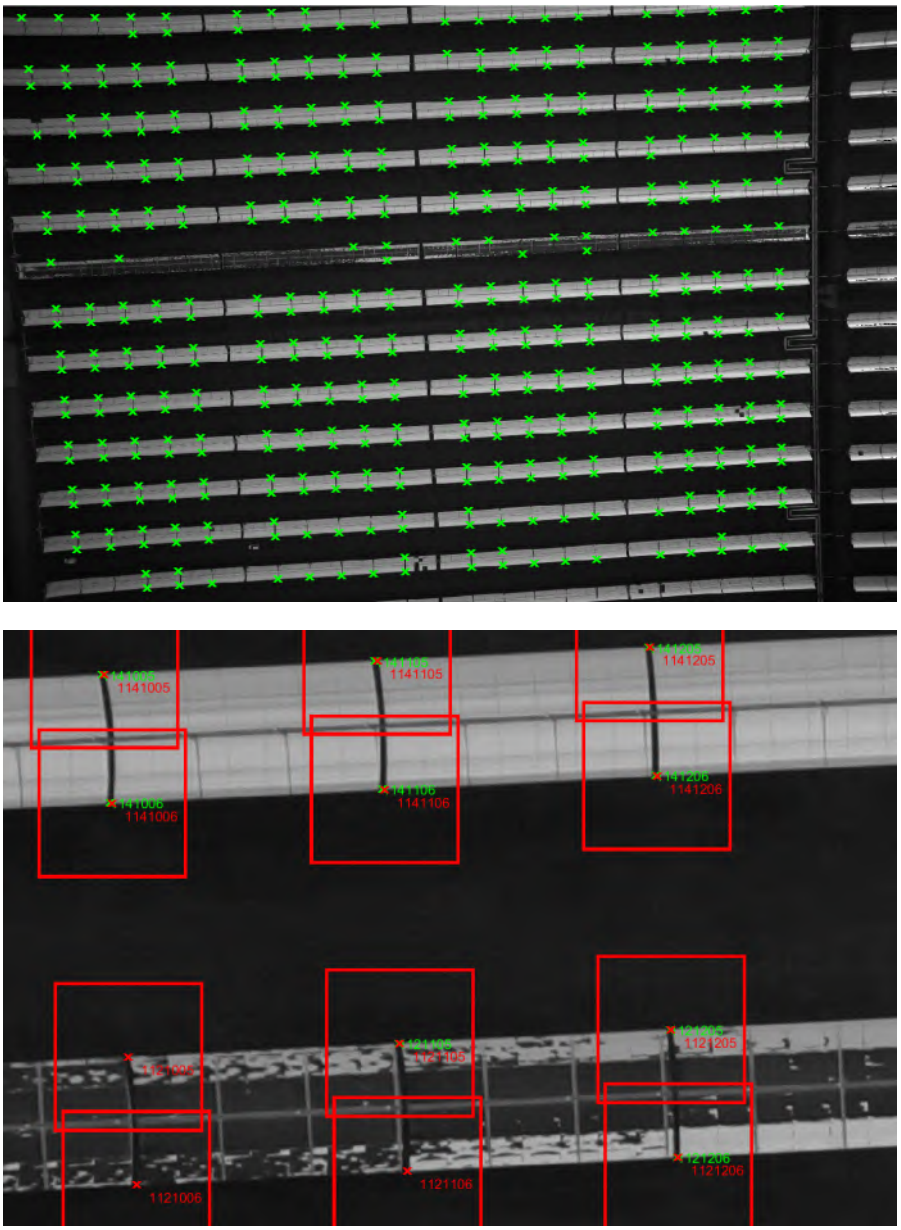

Figure 5.4: Detection of inter-SCA gaps in the $\text{QFly}_{\text{Survey}}$ mode. Top: Full 24 MP image captured at a flight altitude of 250 m with a visible horizontal ground distance of $>$ 300 m, corresponding to an entire loop. The image processing detects about 90 % of the gaps (green markers) and provides a solid basis for the single photo resection. The absorber tube reflection in the center of the image impedes proper feature detection. Bottom: Detailed view on a picture section with search window position and size (red). Strict quality measures assure, that only plausible results are returned. That way, the detection of erroneous features is prevented, especially in regions where the absorber reflection disturbs the gap detection. The numbers assigned to each gap provide a unambiguous identification of each point within the solar field.

Image resection by minimization of 2D residuals

The exterior orientation for each aerial image is determined by single photo resection. 3D-object coordinates[5] and the interior orientation (IOR) are provided as constraints, so that only the six parameters of the EOR (see Equation 4.1) are determined by optimization. The objective function of this optimization is the *RMS* value of the residuals between detected and projected image coordinates (Σ_0):

$$\Sigma_0 = \sqrt{\frac{\sum_{i=1}^{N} \left[P_{x,y}^{Meas}(i) - P_{x,y}^{Proj}(i) \right]^2}{N}} \tag{5.1}$$

Here, $P_{x,y}^{Meas}(i)$ is obtained from the previously described image processing. $P_{x,y}^{Proj}(i)$ is derived from a MATLAB implementation of a holistic camera-projection model based on the collinearity equations (Luhmann et al., 2006b), which constitutes a set of two fundamental formulas to relate 2D coordinates on the camera sensor to object 3D coordinates:

$$P_{x,y}^{Proj}(i) = [x_c^{(i,j)}, y_c^{(i,j)}] \tag{5.2}$$

The collinearity equations to derive the image coordinates $[x_c^{(i,j)}, y_c^{(i,j)}]$ from 3D coordinates, EOR, and IOR are presented in Section A.6.

In order to find the global optimum of the Σ_0 objective function, a genetic algorithm (Houck et al., 1995) is used to provide robust EOR start-values for a MATLAB implementation of the Nelder-Mead simplex algorithm (Lagarias et al., 1998), enhanced by version to admit bound constraints (D'Errico, 2012). There are other, probably more efficient and robust approaches to determine the EOR (Grussenmeyer and Al Khalil, 2002; Davison et al., 2007), but these options have not yet been compared to the currently implemented method.

Image registration

Unlike close range photogrammetry image processing with coded targets, the 3D features used to determine the EOR can not be associated or assigned to a specific SCE with only relying on the information from a single image. In order to trace and assign these features through the images series, image registration (Zitova and Flusser, 2003) is used to match subsequent frames. The time lag between these images is in the range of $\simeq$ 0.3 *sec*. As the aerial image show a repetitive pattern of hardly distinguishable mirror rows, the task of reliable image registration is rather demanding compared to common applications with a unique solution. To cope with that, a MATLAB implementation for image correspondence based on cross correlation (Young, 2011) was

5 inter-SCA-gaps of the solar field

modified slightly to meet the requirements of this application. Due to the mentioned repetitiveness, automatic selection of traceable features was deactivated and the pattern of image sections at the drive pylons and SCA ends were used instead (see Figure 5.5).

The size of patches and search windows is determined empirically and the robustness of the registration process is quite sensitive to these parameters. Various quality criteria are applied to check the consistency of the projective transformation based on the traced features, so that confusing the features is effectively prevented. That way it is possible to automatically process a series of up to 800 images. Measures to further improve the work flow of $\text{QFly}_{\text{Survey}}$ EOR estimation are presented in Section 6.3.

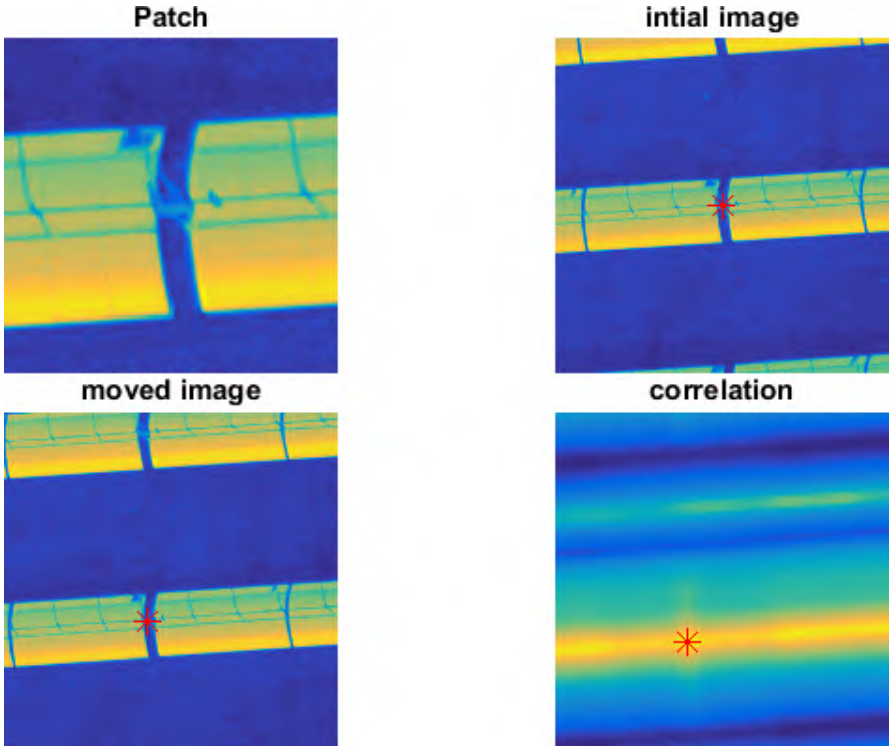

Figure 5.5: Process of image registration to identify corresponding features in consecutive image frames and to derive the projective transformation parameters.
Top left: about 40 patches similar to the presented one are extracted from the current initial image. The patches show the drive- or end-pylon because these features are unique within their closer surrounding. Top right: the red marker shows the center of the patch in the initial image. Bottom left: The search window in the subsequent image, centered at the feature location from the previous image. The search window has approx. three times the size of the patch. Bottom right. Intensity of the cross correlation of patch and search window in the moved image, with the peak of best matching.
The size of the search window has major effect on the result. To large windows involve the risk of "flipping" to the wrong collector row. Too small windows may result in failing to detect the corresponding feature. The problem was solved by starting with reasonable small search windows, and increasing both patch and window size in the case that the methods does not find a unique solution. As the shift between images is directly correlated to angular motion (tumbling) of the UAV and the elapsed time between subsequent image frames, the best option to make the process more robust is a higher image capture frequency (2.5 $frames per second$(fps) for the current Sony NEX-7 payload, up to 30 fps for forthcoming payloads).

5.2.2 *Calculation of low resolution effective mirror shape deviation*

The $QFly_{Survey}$ flight route design[6] does not permit the simultaneous and independent measurement of the absorber tube position (ΔX_{Abs}, ΔZ_{Abs}) and slope deviation in curvature direction (SD_X). Hence, the information derived for the concentrator geometry is the effective slope deviation in curvature direction (SD_{Xeff}) (see Section 2.2.2).

The remaining procedure (ortho-image creation, detection of absorber
shape) follows exactly the way described in Section 4.2.3 to 4.2.5. The main difference is the evaluated unit (SCA instead of SCE) and the spatial resolution ($30 - 60\,mm/pixel$ instead of $4 - 6\,mm/pixel$).

5.2.3 *Calculation of effective tracking deviation in Survey^{Offline} mode*

A major advantage of the large field of view of the $QFly_{Survey}$ data acquisition is the possibility to derive the effective tracking deviation ($\phi_{\perp eff}$) for each SCE of the solar field, which so far has not been accessible at this scope and spatial resolution. If the orientation of the optical axis of each SCE is known, the inter-SCE alignment and torsion of the entire SCA can be checked, as well as inclinometer offsets[7] of the solar field data acquisition system. These results provide important information for the performance analysis and optimization of the tracking system. This is by far the easiest way to boost the solar field performance.

The approach presented here is based on former investigations by NREL on characteristic pattern or "fingerprints" of the absorber tube reflection caused by concentrator imperfections (Jorgensen et al., 2009). This approach is implemented and enhanced by a robust method to match simulated and measured pattern. The first step is the creation of simulated patterns of absorber tube reflections (Map^{Sim}) based on the camera position, measured SD_{Xeff} maps, and simulated absorber tube displacement along the optical axis (ΔZ_{Abs}) as a function of T_{HTF}.

The second step is the creation of measured patterns of absorber tube reflections (Map^{Meas}) from tube reflex images (see Section 4.2.4). Finally, matching of simulated (Map^{Sim}) and measured (Map^{Meas}) patterns provides an accurate method to derive $\phi_{\perp eff}$.

---

6 the straight fly-overs perpendicular to the collector Y-axis do not provide the necessary variety of perspectives and the distance to the collector is to large to detect the absorber tube.

7 inclinometer offsets refer to a misalignment between the X-axis of the SCE and the inclinometer. In this case, the inclinometer of an SCA in zenith position would return a tracking angle (θ) different from 90°.

Creation of ideal absorber tube reflection patterns

Ideal reflection patterns are created by means of custom MATLAB 2D-ray-tracing (RT) code. A virtual observer is moved in the XZ plane horizontally above the PTC, thereby creating the assumed view angle between the optical axis of the SCE and camera position. This view angle is denoted ϕ'_{Cam}. For each value of ϕ'_{Cam}, the visibility of the absorber tube reflection is generated by analyzing the line-of-sights (LOSs) from the camera to the mirror and checking the intersection of "reflected" LOSs with the absorber tube (similar to Figure 5.12). In order to generate realistic patterns, averaged SD_{Xeff} values from high resolution QFly measurements are used in this RT procedure (see Figure 5.6).

The absorber tube displacement along the optical axis (ΔZ_{Abs}) caused by deviations of T_{HTF} from the nominal operation temperature of the SCA (see Section 3.2.3) is also considered, since rather large systematic deviations occur for typical Survey$^{\text{Offline}}$ conditions[8].

Finally, Figure 5.7 shows three variants of Map^{Sim} for different assumptions concerning the collector geometry. It becomes obvious that a good agreement between simulated (Map^{Sim}) and measured (Map^{Meas}) pattern can only be achieved by considering the real collector geometry.

8 Typical T_{HTF} for a cold solar field: $150°C \leq T_{HTF} \leq 250°C$

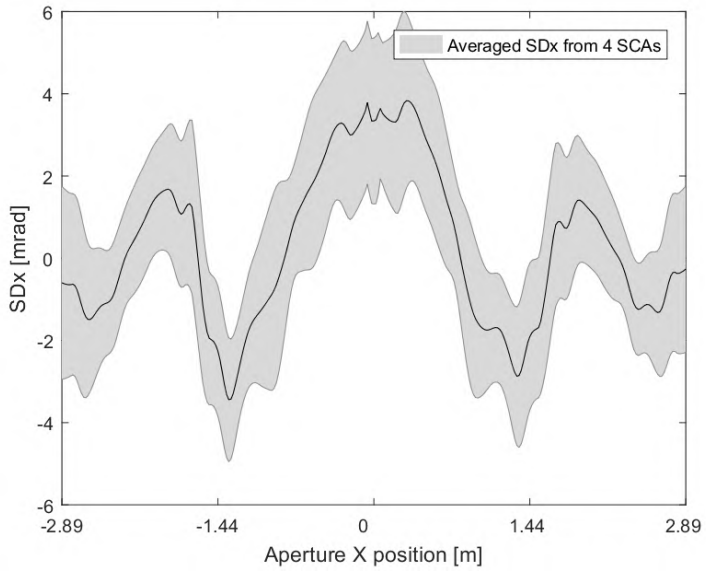

Figure 5.6: Averaged SD_{Xeff} values for the creation of simulated patterns of absorber tube reflections (Map^{Sim}). The SD_{Xeff} values were obtained from four $\text{QFly}_{\text{HighRes}}$ measurements. The SD_{Xeff}-characteristic is used in the 2D-RT to derive realistic pattern (see Figure 5.7 right) in order to maximize the matching quality with measured pattern.

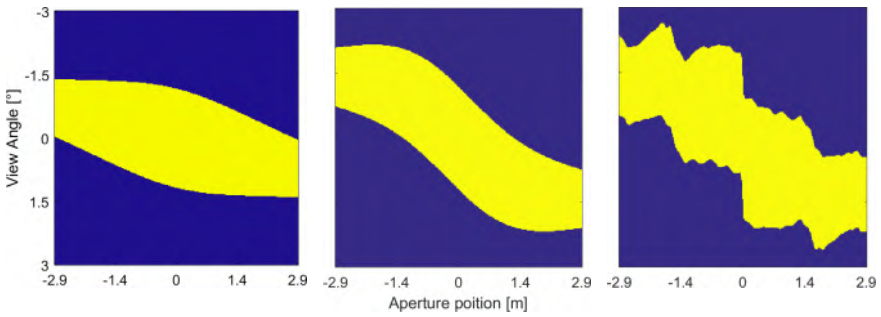

Figure 5.7: Simulated absorber tube reflection pattern (Map^{Sim}) for different different assumptions concerning the collector geometry. The vertical axis denotes ϕ'_{Cam}, while the horizontal axis is associated with the aperture width. Left: Ideal shape and absorber positioning ($SD_X = 0\,mrad$ and $\Delta Z_{Abs} = 0\,mm$). Center: Ideal mirror shape ($SD_X = 0\,mrad$) but consideration of systematic lowered absorber tube position ($\overline{\Delta Z_{Abs}} = -36mm$) due to low HTF temperature at the outer SCEs. Right: Measured mirror shape (SD_X) and absorber tube position ($\overline{\Delta Z_{Abs}} = -36mm$). The assumed flight altitude was $250\,m$.

Creation of measured patterns and pattern matching

The measured patterns of absorber tube reflections (Map^{Meas}) to be matched with the Map^{Sim} are created from a series of absorber tube reflection images (see Section 4.2.4). The the original purpose of these

absorber tube reflection images is the calculation of the SD_X following the TARMES approach. All reflection images associated with one SCE are accumulate in Y-direction to obtain histograms. Histograms are converted into binary vectors (TRUE: Tube detected. FALSE: No tube detected) via thresholding. Finally, these vectors are put in into the corresponding rows of a matrix with the same dimension as the simulated pattern. The row index is determined by the camera position and such by ϕ'_{Cam}. Figure 5.8 illustrates the methodology of the creation of measured pattern, which will hereinafter be referred to as Map^{Meas}.

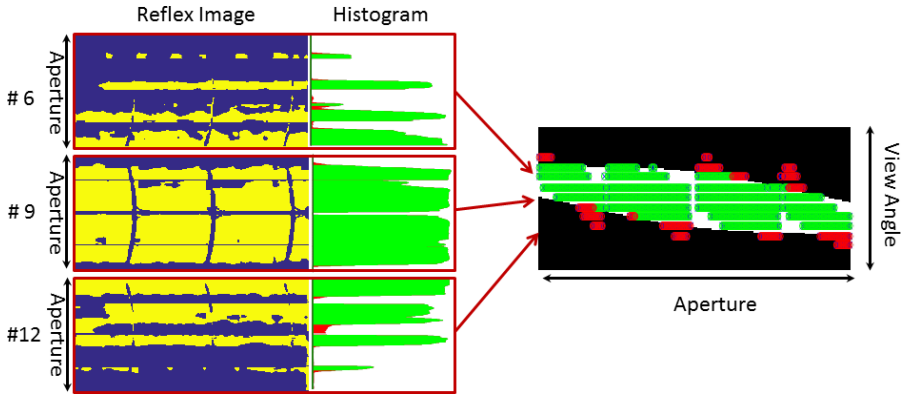

Figure 5.8: Methodology of creation of Map^{Meas} pattern for tracking characterization in Survey^{Offline} mode. A selection of three out of typically 20 absorber reflection images is presented here. Left: Absorber reflection images are accumulated along the Y- direction. Resulting histograms are converted to binary vectors and arranged in the matrix according to the assumed view angle ϕ'_{Cam}. The color coding (red/green) of the non-zero Map^{Meas} entries depends on the logic AND ($\wedge$) operation between Map^{Meas} and Map^{Sim} (see Equation 5.4 and 5.5).

The initial (yet unknown) values of the $\phi_{\perp eff}$ for the creation of Map^{Meas} is set to zero and based on assumption about the collector orientation during the measurement. This angle must be know with an accuracy of $\approx \pm 2°$ in order to implement the previous steps like feature detection and image resection and can be taken from the solar field data acquisition system. The objective of tracking characterization is to determine a possible deviation from the set point. The expected effect is, that $|\phi\perp| > 0$ would shift Map^{Meas} up or down (see Figure 5.9).
This shift of Map^{Meas} is actually the quantity that has to be determined, and is equivalent to the $\phi_{\perp eff}$ assuming that the camera position (EOR) was determined with sufficient accuracy.

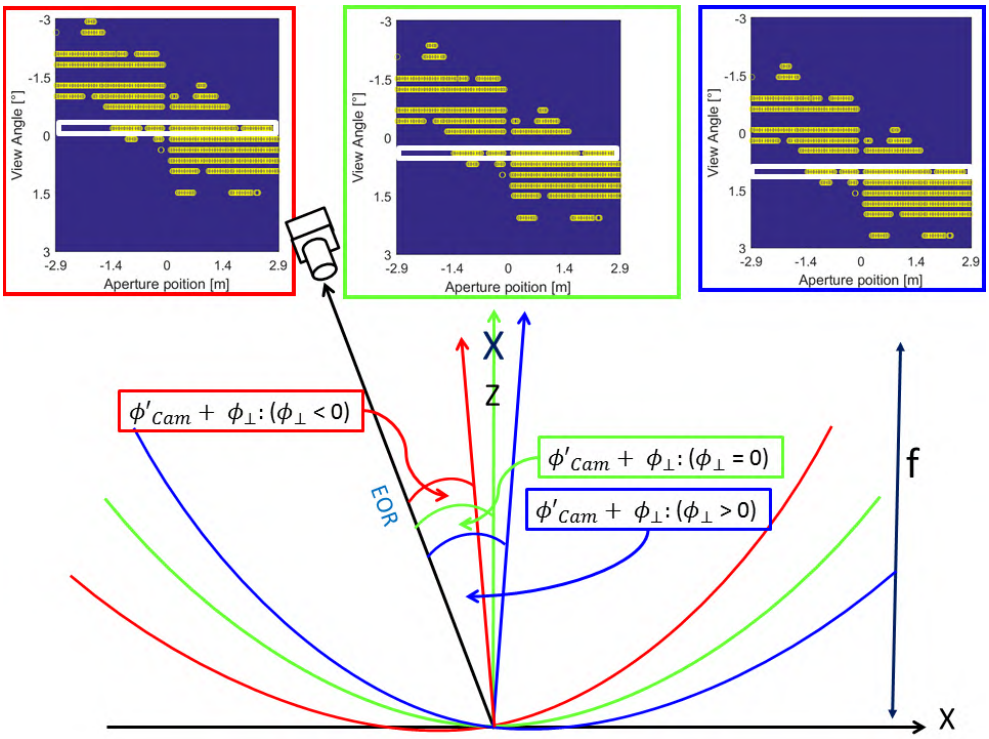

Figure 5.9: Shift of measured tube pattern due to effective tracking deviation ($\phi_{\perp eff}$). ϕ'_{Cam} denotes the view angle between the ideal ($\phi_{\perp eff} = 0$) direction of the optical axis of each SCE and the camera position EOR. In this representation it is assumed that the set-point of tracking angle θ is zenith ($\widehat{=}90°$). For the green parabola, optical axis Z and the green box describe the pattern appearance for $\phi_{\perp eff} = 0$. Red and blue set-ups show the behavior for negative and positive $\phi_{\perp eff}$. The white box in the measured tracking pattern is in every case associated with the same camera position.

In order to find the correct shift value, the vector of discrete shift values ($\overrightarrow{\phi'_{shift}}$) with equal spacing $\Delta\phi$ within the expected range of tracking deviations of $\pm 1.5°$ is defined:

$$\overrightarrow{\phi'_{shift}} = \begin{pmatrix} -\phi_\perp^{max} \\ -\phi_\perp^{max} + \Delta\phi \\ \dots \\ +\phi_\perp^{max} - \Delta\phi \\ +\phi_\perp^{max} \end{pmatrix} \tag{5.3}$$

For every value of $\overrightarrow{\phi'_{shift}}$, the following steps are performed in order to obtain a scalar fitness value (FV) describing the quality of matching between Map^{Meas} and Map^{Sim}.

First, logical operators are applied to the matrices Map^{Meas} and Map^{Sim} in order to identify true positive (TP) and false positive (FP) pixel:

$$\mathrm{TP} = \sum [Map^{Meas}(\overrightarrow{\phi'_{shift}}) \wedge Map^{Sim}] \tag{5.4}$$

$$\mathrm{FP} = \sum [Map^{Meas}(\overrightarrow{\phi'_{shift}}) \wedge \neg Map^{Sim}] \tag{5.5}$$

A variation of the positive predictive value (PPV) (Fawcett, 2006) is used as scalar quality parameter:

$$\mathrm{PPV} = \begin{cases} \left(\frac{\mathrm{TP}-\mathrm{FP}}{\mathrm{TP}+\mathrm{FP}}\right)^2 & \text{for TP} \geq \mathrm{FP} \\ 0 & \text{for TP} < \mathrm{FP} \end{cases} \tag{5.6}$$

The penalty factor (PF) is introduced to consider the RMS value of distances of non-zero Map^{Meas} elements from the next non-zero Map^{Sim} element in the same column j of the matrix:

$$RMS_{Dist} = \sqrt{\frac{\sum_i (FP_{i_1,j} - TP_{i_2,j})^2}{N}} \tag{5.7}$$

$$\mathrm{PF} = RMS_{Dist} \cdot \sqrt[4]{\frac{FP}{TP}} \tag{5.8}$$

Finally, the fitness value (FV) is derived from RMS_{Dist} and PF:

$$\mathrm{FV} = \frac{\mathrm{PPV}}{\mathrm{PF}} \tag{5.9}$$

In order to determine the value of $\overrightarrow{\phi'_{shift}}$ with the best matching of Map^{Meas} and Map^{Sim}, PPV and FV are plotted vs. $\overrightarrow{\phi'_{shift}}$ and the parameters of a Gaussian distribution[9] (see Equation 5.10) are fitted to the resulting curve[10] (see Figure 5.10) .

$$\mathrm{FV}(\overrightarrow{\phi'_{shift}}) = \mathrm{FV}_{max} \cdot \exp - \left(\frac{(\overrightarrow{\phi'_{shift}} - \phi_{\perp\, eff})^2}{\sigma^2} \right) + d \tag{5.10}$$

The approach presented here provides the absolute orientation of the optical axis of each SCE. Due to the combination of all available information in a singe matrix, the pattern matching has proven to be a robust method which yields accurate an reliable results with an uncertainty of 1.6 $mrad$ (RMS). The uncertainty analysis and validation in a commercial power plant's solar field are presented in Section 5.3.3.

9 it is not clear whether a Gaussian distribution is the best choice to describe the resulting FV curve, but it is a robust approach to determine the center of the curve.

10 using the MATLAB Curve Fitting Toolbox^{TM}

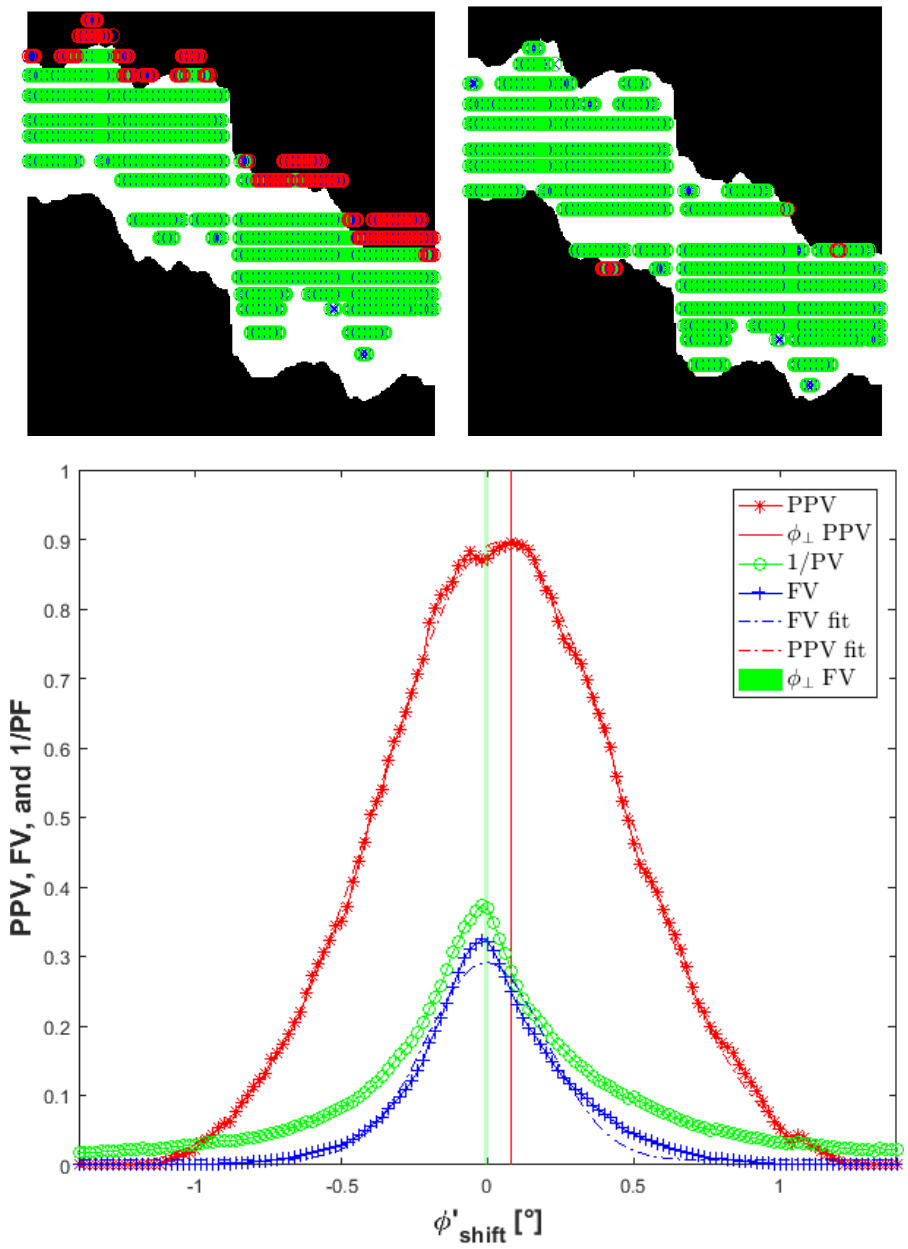

Figure 5.10: Determination of $\phi_{\perp eff}$ in Survey$^{\text{Offline}}$ mode. Top left: Matching of Map^{Sim} and Map^{Meas}, while the Map^{Meas} has been shifted by $\overrightarrow{\phi'_{shift}} = -0.54°$. The overall matching quality is poor, resulting in an FV of 0.05. Top right shows the best possible match for this particular SCE, with $\overrightarrow{\phi'_{shift}} = -0.08°$ resulting in a FV of 0.97. Generally speaking, there is a good qualitative matching between Map^{Sim} and Map^{Meas}.

Bottom: Plot of scalar quality parameters vs. $\overrightarrow{\phi'_{shift}}$ and fitting of a Gaussian distribution to the FV curve to determine $\phi_{\perp eff}$. The FV yields a more clear peak (position and variance highlighted by a vertical green bar), compared to the maximum value of the PPV only (vertical red line).

5.2.4 *Calculation of tracking deviation in Survey^{Online} mode*

While the solar field is in operation, there are two fundamental differences with respect to the image characteristics compared to measurements in Survey^{Offline} mode:

1. Concentrated radiation on the absorber tube strongly decreases the contrast between tube reflection and background (compare Figure 5.1)

2. The tracking angle θ is in general $\neq 90°$. Because of that, the reflections of other objects (terrain and adjacent SCAs) are present in the mirror surface, thus hampering the unambiguous detection of the absorber tube reflection.

Therefore, the shape and tracking characterization of a solar field in operation using the absorber tube reflection seems not feasible, at least at this at this stage and with the available resources and methods. As tracking characterization appears to provide the most relevant and most practical information for plant optimization, a new approach will be presented here, which exploits the clear signal (see Figure 5.1 right) of the illuminated bellow protection shields at the welding connection between adjacent HCEs . A lateral view on the solar field in operation shows the appearance of radiated objects in the focal line (Figure 5.11).

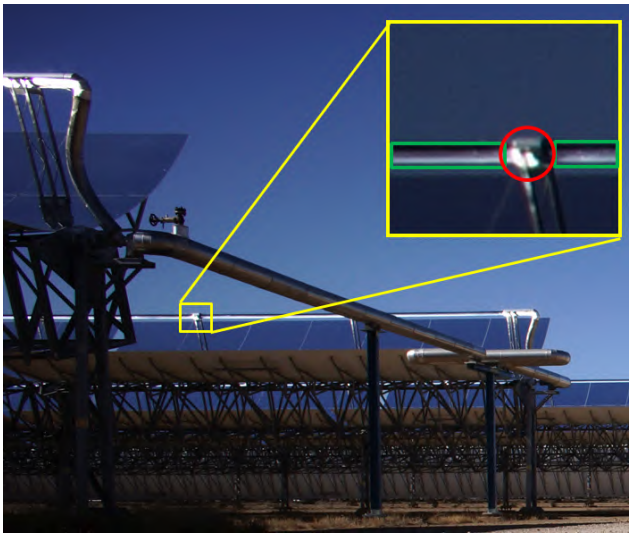

Figure 5.11: Lateral view on solar field in operation. The active area of the HCE within the green rectangle can hardly be used as pattern under operating conditions, since irradiated soiling and specular reflections diminish the contrast. The connections between adjacent HCEs (red circle) show a clear and bright signal, which is exploited to derive the pattern for Survey^{Online} measurement of $\phi_{\perp eff}$.

The first part of this section describes the process of pattern creation, while the second part is dedicated to pattern matching. The concepts introduced in Section 5.2.3 for the Survey^{Offline} tracking characterization will be applied again. The main difference is, that unlike the absorber tube, the shape of the illuminated bellow pattern changes with $\phi_{\perp eff}$, so that we expect an individual "fingerprint" for each value of $\phi_{\perp eff}$. The advantage of this approach is, that the resulting value for $\phi_{\perp eff}$ is directly related to the direction of incoming solar radiation relative to the SCE's optical axis.

Creation of irradiated bellow pattern

The MATLAB 2D ray-tracing (RT) code used for the creation of the absorber tube reflection pattern is employed here twice:

1. For different values of $\phi_{\perp eff}$ the irradiated circumference of the bellow is simulated
2. The reflection of the irradiated (and such visible) part of the bellow in the mirror surface is calculated

In accordance with Equation 5.3, $\phi_{\perp eff}$ values for pattern creation are defined in a similar way by a vector of discrete shift values ($\overrightarrow{\phi''_{shift}}$) :

$$\overrightarrow{\phi''_{shift}} = \begin{pmatrix} -\phi_{\perp}^{max} \\ -\phi_{\perp}^{max} + \Delta\phi \\ ... \\ +\phi_{\perp}^{max} - \Delta\phi \\ +\phi_{\perp}^{max} \end{pmatrix} \tag{5.11}$$

The difference between $\overrightarrow{\phi''_{shift}}$ and $\overrightarrow{\phi'_{shift}}$ is based in the fact, that $\overrightarrow{\phi''_{shift}}$ is applied to create patterns Map^{Sim} of different characteristics, while $\overrightarrow{\phi'_{shift}}$ is again used to shift the Map^{Meas} pattern in vertical direction. For the creation of the Map^{Sim} pattern, sun-shape, measured SD_X values, and modeled $\Delta Z_{Abs}(\Delta T)$ are used in order to obtain good matching quality by using realistic pattern. As a consequence of this approach, look up tables consist now of series of different pattern for each value of $\overrightarrow{\phi''_{shift}}$. Figure 5.12 and 5.13 outline the creation of pattern which originate from reflections of the irradiated bellow shields.

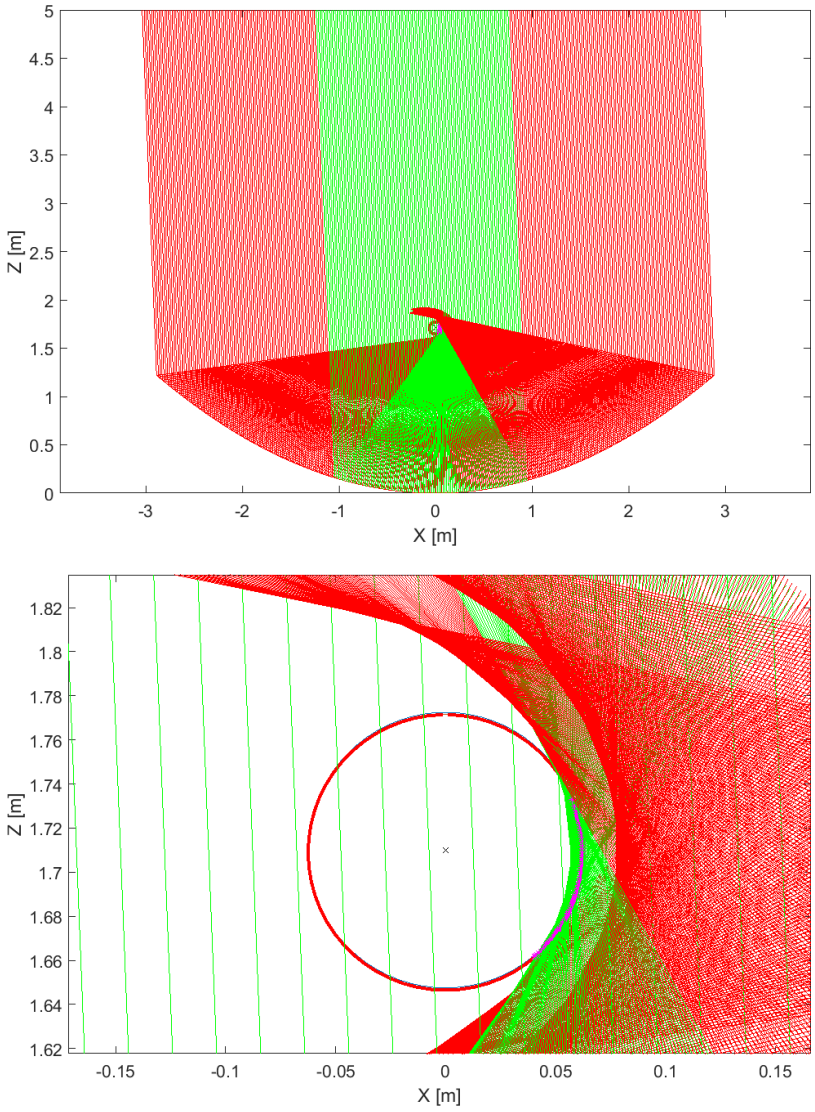

Figure 5.12: 2D RT to create pattern of the irradiated bellow shield reflection. Top: Overview on the entire collector cross-section showing sun rays at $\phi_{\perp eff} = -1.4°$ hitting (green) or missing (red) the bellow with an diameter of 125 mm. Bottom: Zoom into the focal region. $|\phi_{\perp eff}| > 0$ leads to astigmatism and such to asymmetric illumination of the bellow. The imprint of the astigmatism is used to create specific pattern for each value of $\overrightarrow{\phi''_{shift}}$.

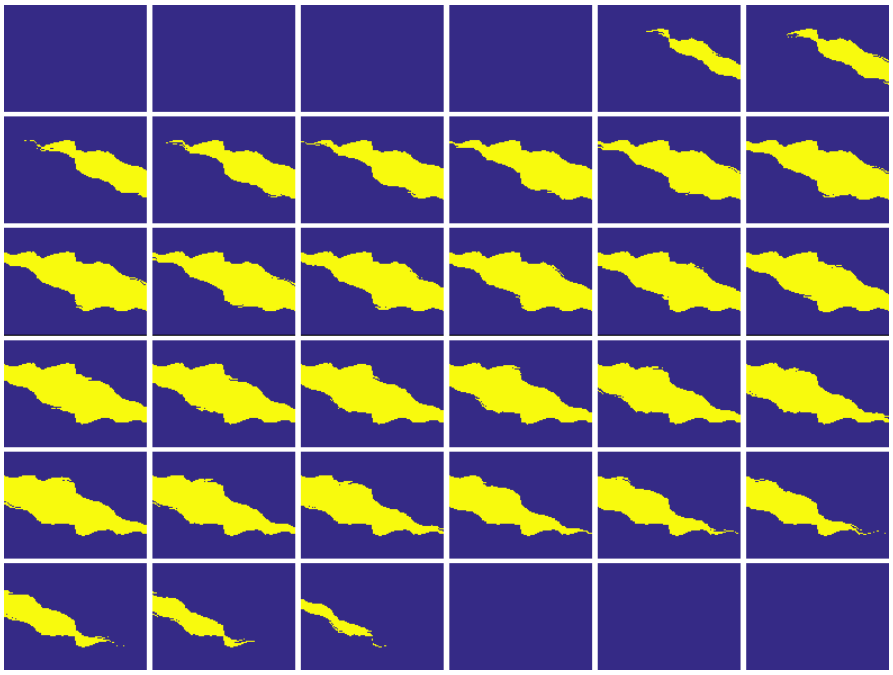

Figure 5.13: Series of ideal pattern (Map^{Sim}) for Survey$^{\text{Online}}$ tracking characterization based on measured slope deviation in curvature direction (SD_X) (see Figure 5.6) and modeled absorber tube position ($\overline{\Delta Z_{Abs}}$) based on considerations on the thermal expansion at the HTF temperature during the measurement. The top left pattern corresponds to $\phi_{\perp\, eff} = -3°$ and the bottom right to $\phi_{\perp\, eff} = +3°$. The angular spacing between successive pattern is $\backsimeq 0.17°$. At a effective tracking deviation value of 2.3°, concentrated radiation starts to hit the bellow protection shield and the bright reflex of the bellow appears in the mirror surface. The pattern is moving from the right to the left through the aperture area. For each value of $\overrightarrow{\phi''_{shift}}$, there is a single unambiguous pattern.

Creation of measured bellow pattern and pattern matching

Pattern to be matched with the Map^{Sim} are created from a series of binary images, which are obtained by simple thresholding of the orthoimages in order to identify overexposed pixel (see Figure 5.14). One difficulty arises from the fact that not only the bellows reflection are detected that way, but also reflections of the upper irradiated part of the HCE-supports. The influence of this systematic false signal will de discussed in the uncertainty analysis. The process[11] of creating Map^{Meas} is identical to the methodology described in Figure 5.8. However, adapted thresholds are used for the conversion of histograms into binary vectors, taking into account the expected fraction of overexposed pixel by considering the active receiver length (L') of 96.7 % (Schott, 2015a).

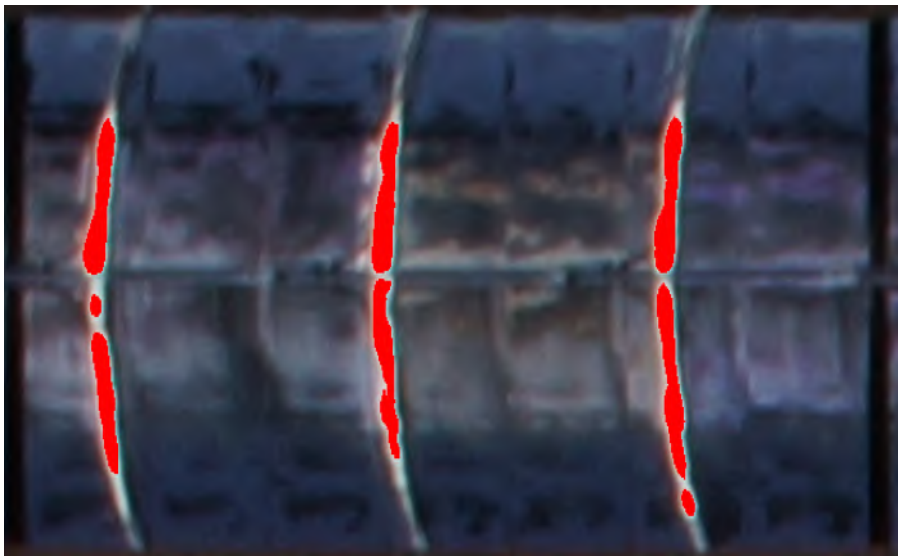

Figure 5.14: Orthoimage in Survey^{Online} mode with detected reflections of irradiated bellow shields (red). The graph also illustrates the complexity of detection of the absorber tube reflection under these particular conditions. In large fractions of the image, bright areas from illuminated soiling and/or specular reflections result in weak contrast and impede unambiguous detection.

The one-dimensional optimization process described for the Survey^{Offline} tracking characterization (see Equation 5.4-5.10) is changed into a two dimensional problem. The main objective is the identification of the angle $\overrightarrow{\phi''_{shift}}$ for which the simulated pattern ($Map^{Sim}(\overrightarrow{\phi''_{shift}})$) fits best to the measured pattern ($Map^{Meas}(\overrightarrow{\phi'_{shift}})$). The best match using only $\overrightarrow{\phi'_{shift}}$ can not be used here, because it is only valid for the Survey^{Offline} mode. A certain correlation between $\overrightarrow{\phi'_{shift}}$ and $\overrightarrow{\phi''_{shift}}$ is expected, but

11 summation in Y-direction, histogram creation, conversion to binary vector, and assignment of vectors to matrix rows

the main information on $\phi_{\perp\,eff}$ comes from the characteristic lateral shift displayed in Figure 5.13

For the Survey$^{\text{Online}}$ mode, assumptions for continues tracking of the solar field[12] were made to obtain the camera position in each single SCA coordinates system. As displayed in Figure A.4, this assumption is only approximate, as non-continuous tracking introduces a systematic deviation between assumed and reals 3D-coordinates of the solar field. However, this deviations is negligibly small, as the EOR positioning algorithm is not sensitive to such small deviations. This approximation is also the reason for the mismatch between $\overrightarrow{\phi'_{shift}}$ and $\overrightarrow{\phi''_{shift}}$ visible in Figure 5.15.

The positive predictive value (PPV), penalty factor PF and FV are calculated similar to Equation 5.6 - 5.9, but the input quantities TP and FP are functions of two shift vectors:

$$TP = \sum[Map^{Meas}(\overrightarrow{\phi'_{shift}}) \wedge Map^{Sim}(\overrightarrow{\phi''_{shift}})] \tag{5.12}$$

$$FP = \sum[Map^{Meas}(\overrightarrow{\phi'_{shift}}) \wedge \neg Map^{Sim}(\overrightarrow{\phi''_{shift}})] \tag{5.13}$$

A typical result of the distribution of FV in the co-domain of $\overrightarrow{\phi'_{shift}}''$ is shown in Figure 5.15:

A normal 2-dimensional Gaussian distribution:

$$FV(x,y) = FV_{max} \exp\left(-\frac{x^2}{\sigma'^2} - \frac{y^2}{\sigma''^2}\right) \tag{5.14}$$

delivers rather poor results when fitted to the FV-distribution due to the correlation between $\overrightarrow{\phi'_{shift}}$ and $\overrightarrow{\phi''_{shift}}$, so the general bivariate Gaussian distribution (Equation 5.15) was chosen to model the FV distribution:

$$FV(x,y) = FV_{max} \exp\left(-\frac{1}{2(1-\varrho^2)}\left[\frac{x^2}{\sigma'^2} + \frac{y^2}{\sigma''^2} - \frac{2\varrho xy}{\sigma'\sigma''}\right]\right) \tag{5.15}$$

whereas the following definition used:

$$x = (\overrightarrow{\phi'_{shift}} - \phi'_{\perp\,eff}) \quad \text{and} \quad y = (\overrightarrow{\phi''_{shift}} - \phi''_{\perp\,eff}) \tag{5.16}$$

Results for Survey$^{\text{Online}}$ tracking characterization and validation measurements are presented in Section 5.3.4.

12 The sun position was calculated according to Michalsky (1988)

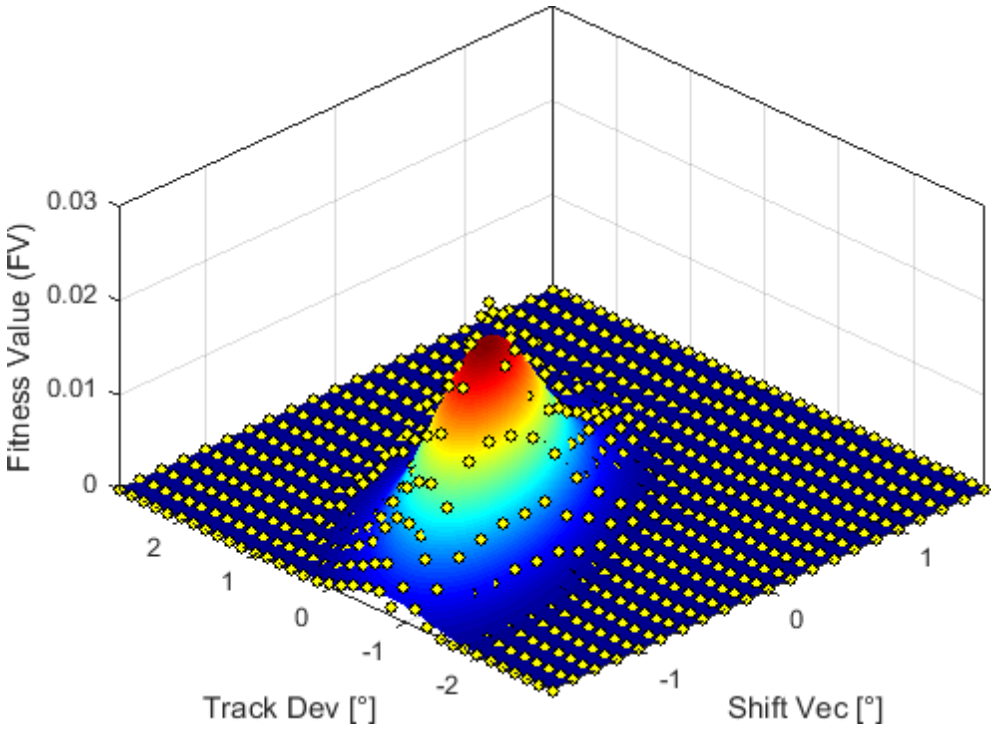

Figure 5.15: $\text{QFly}_{\text{Survey}}$ determination of the $\phi_{\perp eff}$ in $\text{Survey}^{\text{Online}}$ mode. Data points (yellow) of the FV in the co-domain of $\overrightarrow{\phi'_{shift}}(\widehat{=}TrackDev)$ and $\overrightarrow{\phi''_{shift}}(\widehat{=}ShiftVec)$ are shown with the general two dimensional Gaussian distribution fit. Note the different scaling for the horizontal axes. The correlation between $\overrightarrow{\phi'_{shift}}$ and $\overrightarrow{\phi''_{shift}}$ is also visible.

5.3 SURVEY RESULTS, UNCERTAINTY ANALYSIS AND VALIDATION

An extensive measurement campaign was carried out from October 24, 2016 to the November 14, 2016 at the Andasol III (AS3) plant. The objective of this campaign was the demonstration and validation of the $\text{QFly}_{\text{Survey}}$ approach in a commercial CSP-plant. The following task were carried out:

1. $\text{QFly}_{\text{Survey}}$ data acquisition for the complete solar field in $\text{Survey}^{\text{Offline}}$ mode to obtain SD_{Xeff} and $\phi_{\perp eff}$
2. $\text{QFly}_{\text{Survey}}$ data acquisition for the complete solar field in $\text{Survey}^{\text{Online}}$ mode to obtain $\phi_{\perp eff}$
3. $\text{QFly}_{\text{HighRes}}$ for 4 SCAs:
   - SD_{Xeff} data is used as benchmark for $\text{QFly}_{\text{Survey}}$ in $\text{Survey}^{\text{Offline}}$ mode
   - SD_{Xeff} data is used to generate pattern for $\text{QFly}_{\text{Survey}}$ tracking characterization

4. Inclinometer measurements at four SCAs to deliver absolute benchmark data $\phi_{\perp}$ for $\phi_{\perp eff}$ results obtained with $\text{QFly}_{\text{Survey}}$.

The focus of this thesis is on the validation measurements, which took place in the NE-Block of the solar field[13]. Figure 5.16 provides an overview on the location of above mentioned tasks. Figure 5.18 displays basic operation parameters (e.g.: θ, T_{HTF}) of SCA RH35 during the $\text{QFly}_{\text{HighRes}}$ validation measurement.

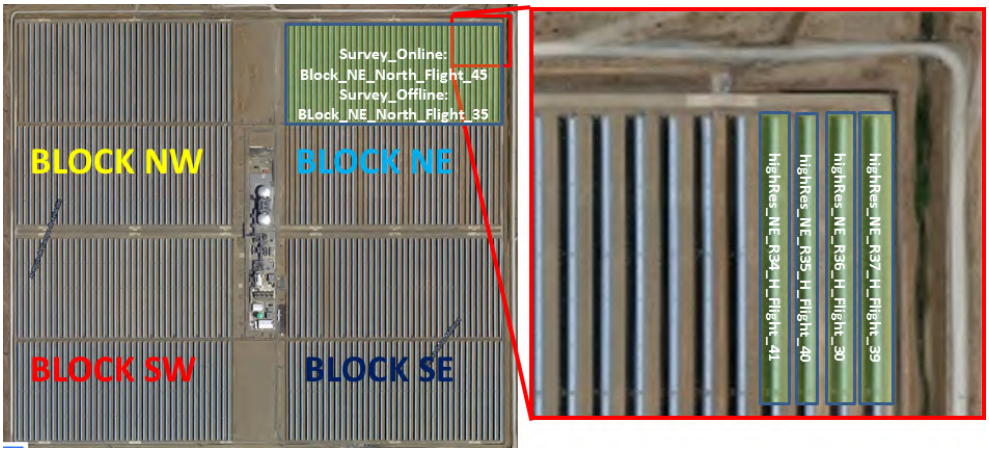

Figure 5.16: Overview on QFly data acquisition at AS3.
Left: Google Earth image of the entire plant. The focus is on the northern part of the NE Block. $\text{QFly}_{\text{Survey}}$ measurements in $\text{Survey}^{\text{Online}}$ and $\text{Survey}^{\text{Offline}}$ mode were carried out here.
Right: Enlarged section on the four SCAs (IDs: RH34-37) where benchmark measurements were carried out by means of $\text{QFly}_{\text{HighRes}}$ and inclinometers.

The first part of this section provides an estimation of the uncertainty of the camera position (EOR) as input parameter for subsequent calculations (Section 5.3.1). Comparison between SD_{Xeff} results obtained with $\text{QFly}_{\text{HighRes}}$ and $\text{QFly}_{\text{Survey}}$ along with an uncertainty estimation will be presented in Section 5.3.2. An uncertainty analysis and the validation of $\text{QFly}_{\text{Survey}}$ tracking characterization for both $\text{Survey}^{\text{Offline}}$ and $\text{Survey}^{\text{Online}}$ mode will be presented in Section 5.3.3 and 5.3.4, respectively.

13 In order to identify the SCAs within the solar field, the "*YX-NN*" nomenclature is used in the following: Here, *Y* denotes the side of the solar field (e.g. L for left (west) and R for right (east)). The second letter *X* describes the position in North-South direction. Here, A-D refers to the southern blocks, and E-F to the northern block. Finally, the number *NN* describes the SCA position within the block from west to east, in the range of 01-38

5.3.1 *Uncertainty analysis of camera position and ortho-image creation*

The approach of $QFly_{Survey}$ EOR estimation presented in 5.2.1 is expected to achieve a lower absolute accuracy than the bundle adjustment based EOR of the $QFly_{HighRes}$ method presented in Section 4.2.1. The reasons for the reduced accuracy are mainly:

1. Fix assumptions on 3D coordinates and the IOR
2. increased flight height
3. sparsely filled images at the boarder of the solar field

Increased EOR uncertainty can be compensated by higher flight altitudes, because ultimately, the relevant contribution to $QFly_{Survey}$ results depends on ϕ_{Cam}, which (for tracking angles exactly at zenith position) is calculated by:

$$\phi_{Cam} = \arctan\left(\frac{X_C}{Z_C}\right) \tag{5.17}$$

The accuracy of ϕ_{Cam} and hence X_C has the greatest relevance for the quality of SD_{Xeff} and $\phi_{\perp eff}$, while the altitude Z_C and the position along the vertex Y_C have minor importance.

The current set-up in terms of field geometry and camera orientation led to a partial correlation between X_C and the camera pitch angle represented by φ_C because of a relatively small view angle in X-direction[14]. Due to that limitation, the EOR returned by the image resection "jumped" back and forth in X-direction occasionally, due to following reasons:

1. At the boarder of the solar field, only a part of the image provides useful information for images resection. This may add a bias to certain EOR parameters and reduce the accuracy.
2. Blur due to quick pitching movements of the camera also reduces the accuracy of single photo resection because in this case, there is no sharp global optimum for the objective function (see Equation 5.1).

Plausibility checks with GNSS data logged by the UAV indicates that horizontal velocity strictly followed the set value of $2.5 \pm 0.2\,m/s$. In order to cope with the mentioned X_C implausibility, piecewise linear regression in a range of 20 images was applied to the X_C-data from the first iteration of EOR estimation. That way it is possible to

14 landscape image orientation was chosen to minimize flight altitude. This provides maximum field of view in north-south directions and allows to capture entire SCAs or loops at minimal altitude. However, this leads to smaller view angles and reduced position accuracy in X-direction

reset single implausible camera positions to a plausible starting point. In the next iteration, EOR optimization was restricted to constraint bounds the range of $[-0.3m, 0.3m]$ in X-direction.

These strict boundary conditions led to reasonable EOR values (see Figure 5.17). These measures may be regarded as a inevitable workaround and will be improved in the future by adequate modifications of the hardware and improved flight route design as outlined in Section 6.3.

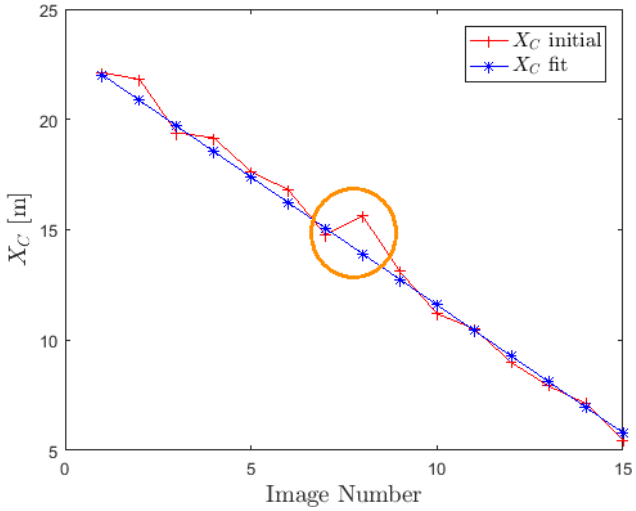

Figure 5.17: Defining constraint boundaries for EOR estimation by linear regression. The red curve show the camera position in X direction, derived by un-constraint single image resection. Due to instable fit configuration at the boarder of the field and correlation between X_C and φ_C, there are evidently implausible results as highlighted by the orange circle. Starting values for a second iteration are derived from the blue curve, based on the assumption that UAV horizontal velocity remains constant.

The RMS value of residuals between projected and measured image coordinates (Σ_0, see Equation 5.1) together with the ground sample distance (GSD) are used to estimate uncertainties for the six EOR parameters (see Table 5.1) for two quality classes of image resection results. The height to width ratio of 4000 to 6000 pixel of the CMOS sensor of the used SONY NEX-7 camera results in different uncertainties of the EOR for the X and Y direction.

Despite the rather high uncertainties for single camera positions σ_{X_C}, the reduced uncertainty of camera position in X direction ($\sigma_{\overline{X_C}}$) derived by averaging over a series of e.g. 20 images is significantly

	Σ_0 (see Equation 5.1)	
σ_{EOR}	$2\,Pixel$	$5\,Pixel$
$\boldsymbol{\sigma_{X_C}}\,[mm]$	~ 180	~ 450
$\sigma_{Y_C}\,[mm]$	~ 120	~ 300
$\sigma_{Z_C}\,[mm]$	~ 120	~ 300
$\sigma_{\omega_C}\,[mrad]$	~ 0.5	~ 1.2
$\boldsymbol{\sigma_{\varphi_C}}\,[mrad]$	~ 0.5	~ 1.2
$\sigma_{\kappa_C}\,[mrad]$	~ 0.5	~ 1.2

Table 5.1: $\text{QFly}_{\text{Survey}}$ EOR uncertainty parameters for a flight altitude of $250\,m$. The ground sample distance (GSD) of $\simeq 60mm/pixel$ in combination with Σ_0-values can be transferred to spatial- and angular uncertainties by simplified geometrical relations. A normal ($\Sigma_0 = 2\,pixel$) and worst-case ($\Sigma_0 = 5\,pixel$) scenario was considered. The two quantities with significant input on the results ($\boldsymbol{\sigma_{X_C}}$ and $\boldsymbol{\sigma\varphi_C}$) are highlighted with bold letters.

smaller. It is assumed that $\sigma_{\overline{X_C}}$ decreases with the square-root of the number of involved images.

$$\sigma_{\overline{X_C}} = \frac{\sigma_{X_C}}{\sqrt{N}} \tag{5.18}$$

This fact is used for the calculation of tracking deviation, where the uncertainty of individual camera positions has minor influence (see Figure 5.23). However, for SD_{Xeff} calculation, the uncertainty of individual camera positions must be considered.

The uncertainty of the positioning of the orthoimage along the curvature direction (X_{Ortho}) (see Table 5.2) is assumed to be directly correlated to Σ_0. All uncertainty values stated here must remain estimations, because no measures have been identified that could serve as a benchmark to crosscheck the estimated values[15]. The validation presented in the following section will show that the estimates on camera position uncertainty are plausible and that the deployed method to derive the camera position is sufficiently accurate to derive reliable results for both SD_{Xeff} and $\phi_{\perp\,eff}$.

5.3.2 *Uncertainty analysis and validation of SD_{Xeff}*

This section follows the approach of mirror slope uncertainty estimation presented in Section 4.3.4. First, the expected SD_{Xeff} uncertainty is obtained by adapting the input parameters to the $\text{QFly}_{\text{Survey}}$ setup. The benchmark is in this case not a completely independent measure,

15 as this was performed for $\text{QFly}_{\text{HighRes}}$ approach (see Section 4.3.1)

but the already validated SD_X maps obtained by $\text{QFly}_{\text{HighRes}}$ (see Section 4.3.4) provides a reliable reference. Next, SD_{Xeff} maps and statistical values from both $\text{QFly}_{\text{HighRes}}$ and $\text{QFly}_{\text{Survey}}$ are compared with the expected uncertainty margins.

Uncertainty analysis

The following characteristics of $\text{QFly}_{\text{Survey}}$ are discussed briefly in order to define the uncertainties of the input parameters in Table 5.2. The list reflects the dependency of SD_{Xeff} on further geometry parameters as described in Equation 2.10 (see definition of SD_{Xeff} in Section 2.2.1):

1. ΔX_{Abs}: absorber tube displacement in lateral direction is not considered in $\text{QFly}_{\text{Survey}}$ mode, so there are no uncertainties defined for this particular quantity .

2. ΔZ_{Abs} (T_{HTF}): absorber tube displacement along the optical axis is considered, in order to obtain plausible results for SD_{Xeff} when the data acquisition was carried out at $T_{HTF} < T_{HTF_{nom}}$ (see Section 3.2.3). The uncertainty of ΔZ_{Abs} in the range of $\pm 4\,mm$ depends on the uncertainty of the T_{HTF} measurement and the Y position with in the SCA (see Figure 3.7).

3. EOR: The estimation of uncertainties in the camera positioning is summarized in Table 5.1.

4. Image processing and detection of the absorber tube reflection in $\text{QFly}_{\text{Survey}}$ mode are affected by the same constraints as described in Section 4.3.2. An adaption of the parameters is mainly required due to the reduced spatial resolution.

Table 5.2 presents the final assumptions for the uncertainty of the used input parameters and the impact on the uncertainty of effective slope deviation in curvature direction ($\sigma_{SDX_{Eff}}$). The values were obtained with the same GUM model as described in Section 4.3.4. The model predicts an average local measurement uncertainty for SD_{Xeff} of about $1\,mrad$, which is $\approx$ 50% higher than the local measurement uncertainty for SD_X in the $\text{QFly}_{\text{HighRes}}$ mode.

The comparison between benchmark data and $\text{QFly}_{\text{Survey}}$ result is presented in Figure 5.19. Figure 5.20 compares the $\sigma_{SDX_{Eff}}$ map with actual deviations between benchmark and the $\text{QFly}_{\text{Survey}}$ result. Similar to the procedure for $\text{QFly}_{\text{HighRes}}$, the effect of uncertainties of the input parameters on the RMS value of SD_{Xeff} (RMS_{SDXeff}) is presented and discussed in Figure 5.21.

Input parameter	1σ	mean $\sigma_{SDX_{Eff}}$	
		abs. $[mrad]$	rel.
$\Delta X_{Abs}\,[mm]$	0	0.00	0.00
$\Delta Z_{Abs}(T_{HTF})\,[mm]$	4	0.57	0.36
$X_C\,[mm]$	180	0.39	0.28
$Z_C\,[mm]$	120	0.00	0.00
$X_{Reflex}\,[mm]$	90	0.00	0.00
$X_{Ortho}\,[mm]$	120	0.09	0.01
$SD_Y\,[mrad]$	4	0.50	0.26
$dZ\,[mm]$	2	0.28	0.09
total		0.96	

Table 5.2: Assumptions for the uncertainty of the input parameters and results for the local $\sigma_{SDX_{Eff}}$. The fist block contains the absorber and camera position. Following the definition of SD_{Xeff}, ΔX_{Abs} is not considered, hence the contribution can be neglected. Uncertainties of absorber tube displacement along the optical axis (ΔZ_{Abs}) due to wrong temperature assumptions are covered by a single valued. This is a rather rough estimate, as the effect is more pronounced to the outer ends of the SCA. The contribution from the EOR in terms of X_C and Z_C considers the *normal* uncertainty from Table 5.1, because worst case positions are assumed to be identified during the rectification of camera positions and during outlier detection. The accuracy of the position of the reflection of the absorber tube edge on the mirror surface (X_{Reflex}) and uncertainties for X_{Ortho} arising from faulty ortho-image creation have a minor share in this set-up. Longitudinal slope deviations SD_Y and height deviations dZ affect the local measurement accuracy due to the large view angles in longitudinal direction.

Creation of benchmark Data

Benchmark data for the validation of the $\text{QFly}_{\text{Survey}}$ SD_{Xeff} results was created by down-sampling and re-arranging of $\text{QFly}_{\text{HighRes}}$ SD_{Xeff} maps. Such maps are appropriate for direct quantitative comparison between $\text{QFly}_{\text{Survey}}$ and $\text{QFly}_{\text{HighRes}}$ results (see Figure 5.19). The $\text{QFly}_{\text{HighRes}}$ approach performs evaluation for each SCE individually, so SD_{Xeff} maps had to be re-arranged according to their position within the SCA taking into consideration the orientation of the local coordinate system[16]. The rearrangement of SD_{Xeff} maps into a map representing the entire SCA does not consider possible misalignment ($\phi_\perp$) between the SCEs. This issues will be picked up again in the following section.

In order to assure comparability between results based on data taken at different values for T_{HTF}, in both cases vertical absorber tube displacement $\Delta Z_{Abs}(T_{HTF})$ (see Section 3.2.3 and Equation 3.5) was

16 Y-axis point from drive towards the REP

utilized under consideration of the position of the SCA within the loop[17]. The heat transfer fluid temperature was taken from the solar field data acquisition system. Uncertainties concerning ΔZ_{Abs} caused by non-steady state temperature have been described in Table 5.2.

Figure 5.18 shows the most relevant SCA parameters for the entire day when RH35 was measured using the $\text{QFly}_{\text{HighRes}}$ and the $\text{Survey}^{\text{Offline}}$ approach.

17 the temperature rise of $\backsimeq 100° K$ from cold- to hot header is compensated by adapting the tube geometry at the drive pylon

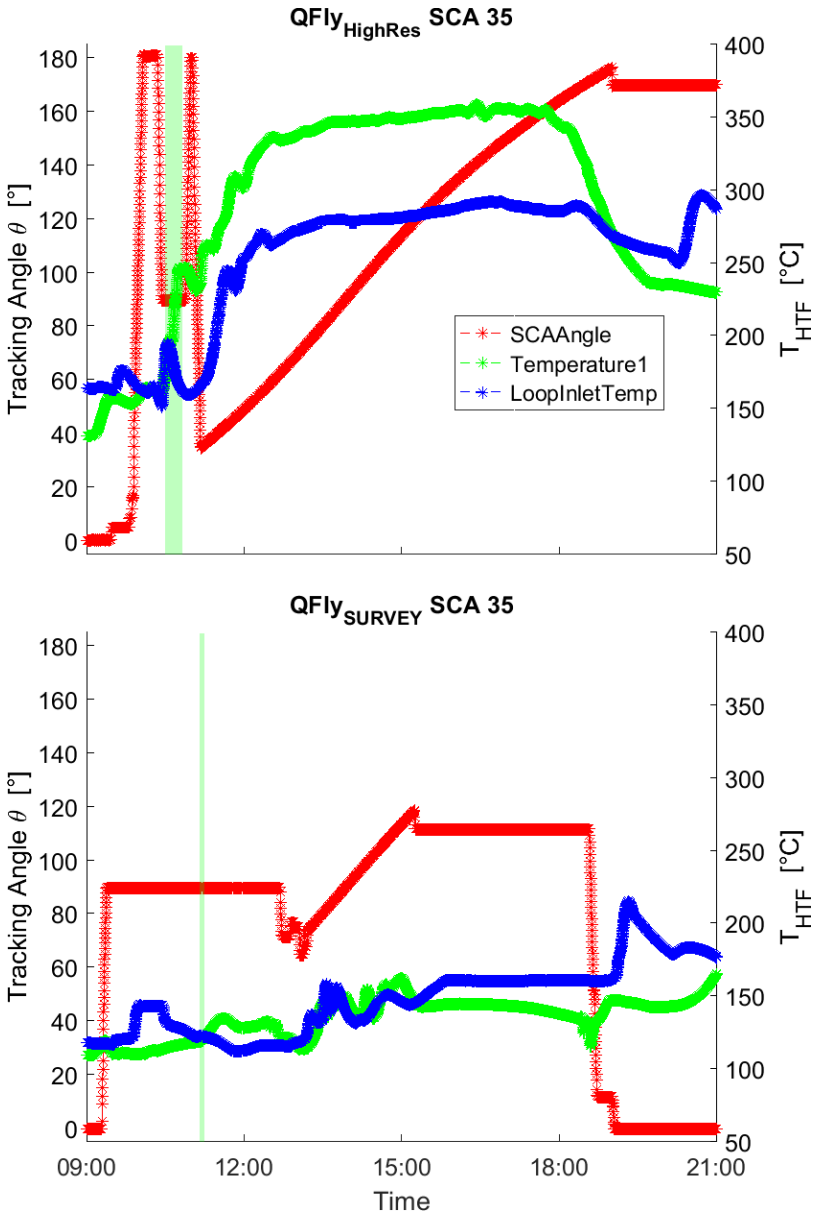

Figure 5.18: Solar field data for SCA RH35 during $\text{QFly}_{\text{HighRes}}$ (top, data acquired on October 28, 2016) and $\text{QFly}_{\text{Survey}}$ in $\text{Survey}^{\text{Offline}}$ mode (bottom, data acquired on October 25, 2016). The red curve shows the tracking angle (θ). Time slots for QFly data acquisition are highlighted by green patches. The time required for the flyover in $\text{QFly}_{\text{Survey}}$ mode is considerably shorter than the time for data acquisition in $\text{QFly}_{\text{HighRes}}$ mode. T_{HTF} is indicated by blue lines (loop inlet) and green lines (drive pylon). Top: The θ movements before and after the benchmark measurement served to attach and remove the coded targets. At 11 AM, the SCA entered in normal operation mode as indicated by the continuous tracking and the increasing fluid temperature. As the SCAs upstream of RH35 were already operational, T_{HTF} was increased from $\sim 160°C$ to $\sim 240°C$ in the course of the $\text{QFly}_{\text{HighRes}}$ measurement, which increased the uncertainty in $\Delta Z_{Abs}(T_{HTF})$. Bottom: Solar field data for RH35 during $\text{QFly}_{\text{Survey}}$ SD_{Xeff} measurement. Zenith was approached from $\theta = 0$, in contrast to the $\text{QFly}_{\text{HighRes}}$ measurement. The reversed motion direction between both measurements and possibly resulting torsion (see Section 3.3) may be the cause for some systematic deviations between $\text{QFly}_{\text{HighRes}}$ and $\text{QFly}_{\text{Survey}}$ as observed in the Figure 5.19.

Validation

The comparison between SD_{Xeff} maps for one SCA is presented in Figure 5.19. Statistical values for all four involved SCAs are presented in Table 5.3. The general characteristics of the SD_{Xeff} are well reproduced by the $\text{QFly}_{\text{Survey}}$ approach. Minor systematic deviations can be explained by the limited sampling rate[18] compared to $\text{QFly}_{\text{HighRes}}$. According to Section 4.3.5, this leads in general to a underestimation of slope deviations. The reduction of the RMS of SD_X according to Figure 4.23 is in the range of $0.2 - 0.3\,mrad$, when the number of images per SCA is reduced from 50 to 15. The diminished sampling rate causes that some areas are flattened by interpolated values, so that slope deviations measured with the $\text{QFly}_{\text{HighRes}}$ approach are not fully reproduced by the $\text{QFly}_{\text{Survey}}$ method.

The statistics show the expected decrease of the RMS_{SDXeff} due to lower sample rate. Future data-acquisition system will be designed to achieve increased camera performance in terms of frames per second (fps) in order to improve both image registration (Section 5.2.1) and accuracy.

SCA	RMS_{SDXeff} $\text{QFly}_{\text{Survey}}$	RMS_{SDXeff} $\text{QFly}_{\text{HighRes}}$	RMS_{SDXeff} $\text{QFly}_{\text{Survey}}$ - RMS_{SDXeff} $\text{QFly}_{\text{HighRes}}$	RMS_{SDXeff} ($\text{QFly}_{\text{Survey}}$ - $\text{QFly}_{\text{HighRes}}$)
RH34	2.39 ± 0.20	2.70 ± 0.10	-0.30	1.41
RH35	2.42 ± 0.20	2.83 ± 0.10	-0.41	1.40
RH36	2.35 ± 0.20	2.46 ± 0.10	-0.11	1.52
RH37	2.45 ± 0.20	2.65 ± 0.10	-0.21	1.69

Table 5.3: Comparison of statistical values RMS_{SDXeff} from $\text{QFly}_{\text{HighRes}}$ and $\text{QFly}_{\text{Survey}}$. The uncertainty of the RMS_{SDXeff} from $\text{QFly}_{\text{Survey}}$ is derived similar to Section 4.3.4 as presented in Figure 5.21. As expected, the $\text{QFly}_{\text{Survey}}$ method tends to underestimate slope deviations by some $1/10$ *mrad*s (3^{rd} column). Statistical values of local differences between $\text{QFly}_{\text{Survey}}$ and $\text{QFly}_{\text{HighRes}}$ are in the range of $1.5\,mrad$, well in accordance with the expected local measurement uncertainties of both approaches ($\text{QFly}_{\text{Survey}}$ $\simeq \pm 0.96 mrad$), $\text{QFly}_{\text{HighRes}}$ $\simeq \pm 0.62 mrad$).

A closer look at the geometric parameters influencing the SD_{Xeff} is necessary to explain some of the observed features in the SD_{Xeff} difference map, which are not subject to the measurement accuracy:

- $\phi_\perp$: Different SD_{Xeff} results may also arise from variable torsion between the SCEs. The $\text{QFly}_{\text{HighRes}}$ evaluation is done individually for each SCE, and the mean value of $\phi_\perp$ is set to zero by

18 in terms of number of images per SCA

virtually "turning" the collector to compensate for offsets in the camera position during the measurement. $\text{QFly}_{\text{Survey}}$ evaluation is carried our for the entire SCA, so misalignment between SCE affects the obtained SD_{Xeff}. The twist or misalignment is moderate for RH35, but the other SCAs exhibit stronger misalignment (see Figure 5.5). This interpretation will be picked up in the discussion of Figure A.2.

- ΔX_{Abs}: When comparing SD_{Xeff} from data from different dates, it must be considered that ΔX_{Abs} is subject to temporal variability (see Section 3.2.2 and 3.2.1). Hence, different results may be obtained for SD_{Xeff}, but this variability is not described by the general measurement uncertainty $\sigma_{SDX_{Eff}}$.
  A prominent feature in the SD_{Xeff} difference map (Figure 5.20) is found in the northern end ($Y \backsimeq 70m$). The most probable explanation for this features are different forces and moments of the rotation and expansion performing assembly (REPA). Such loads are caused by different operating condition, mainly T_{HTF}, and variations of the tracking angle (θ). Different motion directions (see Figure 5.3) in combination with increased friction of the REPA's swivel joint produced opposite forces. These forces produce a local "wave" (ΔX_{Abs}) of the absorber tube, of which the imprint is interpreted as SD_{Xeff}. The reasons of these forces can not be reproduced in detail, but REPAs are known to be problematic in terms of friction and sensitivity to thermal expansion of the header tubes.

The overall conclusion of the validation is, that SD_{Xeff} maps obtained with the $\text{QFly}_{\text{Survey}}$ method provide reliable measurements of the concentrator geometry. However, the diminished spatial resolution and sampling rate tend to underestimate the RMS_{SDXeff} by some 10% in the current configuration. Measures to further improve the measurement accuracy are presented in Section 6.3.

It seems that SD_{Xeff} differences between $\text{QFly}_{\text{Survey}}$ and $\text{QFly}_{\text{HighRes}}$ do not follow the predictions made by the $\sigma_{SDX_{Eff}}$ map displayed in Figure 5.20. This and also the overestimation of the RMS_{SDXeff} predicted in Figure 5.21 lead to the conclusion, that the contributions from $\Delta Z_{Abs}(T_{HTF})$ and/or SD_Y have been overestimated to some degree.

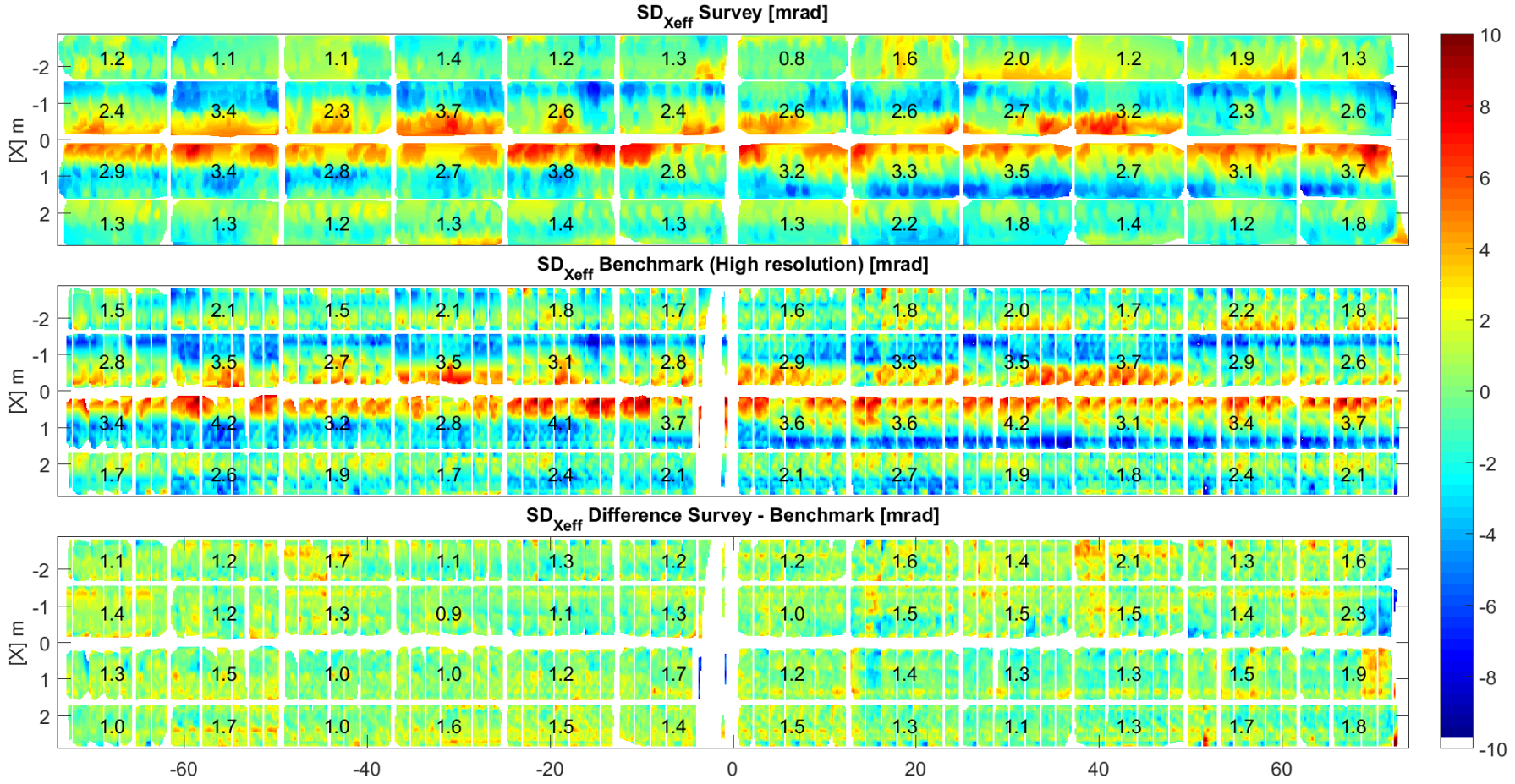

Figure 5.19: $\text{QFly}_{\text{Survey}}$ validation SD_{Xeff} maps in *mrad* for SCA RH35 with statistical values for the mirror panel columns of each SCA. The horizontal axis denotes the distance from the drive pylon in m. Top: $\text{QFly}_{\text{Survey}}$. Middle: $\text{QFly}_{\text{HighRes}}$. The stripe without shape deviation information next to the drive pylon is caused by a defect HCE glass envelope tube. Bottom: Difference $\text{QFly}_{\text{Survey}}$ - $\text{QFly}_{\text{HighRes}}$. Characteristic slope deviation patterns are very well reproduced by the $\text{QFly}_{\text{Survey}}$ method. Mismatches are caused by different sampling rates or false assumptions concerning the ΔX_{Abs}, in particular for the difference visible at $Y \backsimeq 70m$. Different appearance of the white stripes masking mirror boarders are due to fact that that in the $\text{QFly}_{\text{Survey}}$ mode, entire mirror columns (comprising seven mirror panels in Y-direction) are treated as a connected surface, while in $\text{QFly}_{\text{HighRes}}$ mode, mirror panels are separated. Similar visualization about the benchmarking of RH34, RH36, an RH37 can be found in the Appendix (Figure A.2).

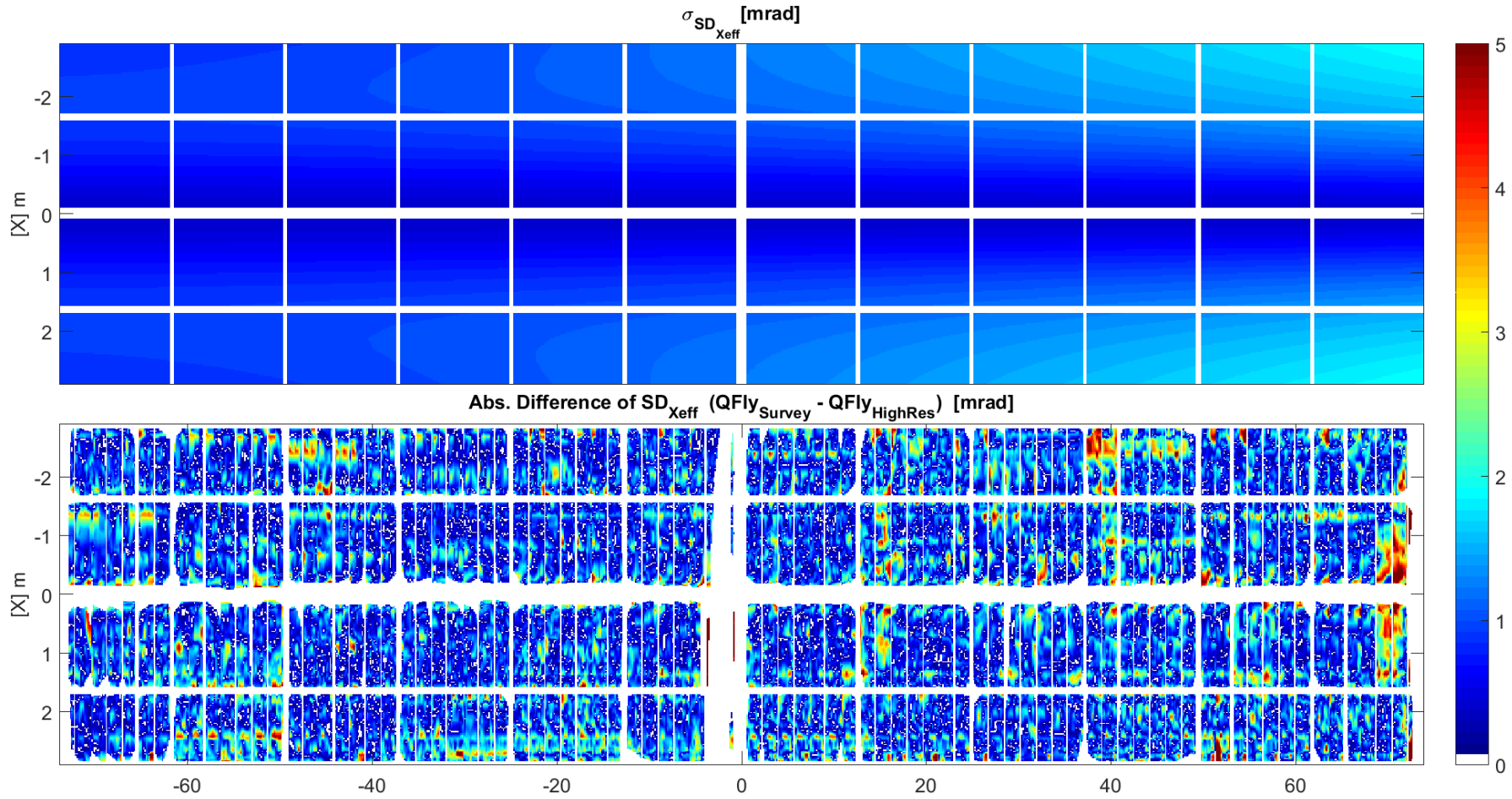

Figure 5.20: TOP: $\text{QFly}_{\text{Survey}}$ uncertainty of effective slope deviation in curvature direction ($\sigma_{SDX_{Eff}}$) map in *mrad* based on the values presented in Table 5.2. The horizontal axis denotes the distance from the drive pylon in *m*. The asymmetry along the vertex is caused by an eccentric fly-over, as in this case the WP route was designed to capture two SCAs in one image. With increasing distance to the camera positions at $Y = -72\,m$, the influence of SD_Y increases towards the northern SCA end. Towards the parabola edge the uncertainty of the vertical absorber tube displacement gains influence. $\sigma_{SDX_{Eff}}$ is in the range of $0.9 - 1.8\,mrad$.
Bottom: Absolute differences of SD_{Xeff} between $\text{QFly}_{\text{Survey}}$ and $\text{QFly}_{\text{HighRes}}$ for SCA RH35. The plot-range was changed with respect to Figure 5.19 to account for the range of differences and uncertainties. About 90 % of the map shows differences below 1 *mrad*. Smaller features with higher differences are subject to lower sampling rate of the $\text{QFly}_{\text{Survey}}$ measurement. At $Y = +72\,m$, there is one features close to the vertex which actually shows higher deviations probably caused by a different ΔX_{Abs} pattern. This is an indicator for increased friction of the REPA swivel joint at the northern end, as both measurements were carried out in zenith position, but approaching zenith from different directions (see Figure 5.18).

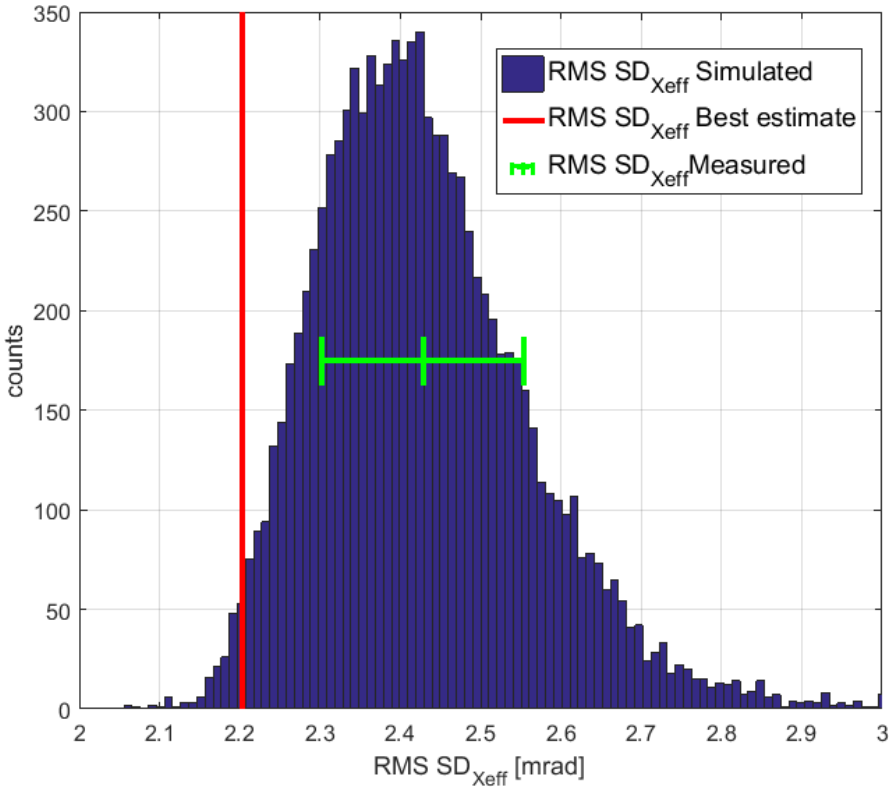

Figure 5.21: Influence of the uncertainties of input parameters on the RMS_{SDX} at SCA level obtained by a Monte Carlo simulation with 10,000 runs. The red line represents the best estimate of the RMS_{SDXeff} values so that the measured RMS_{SDXeff} equals the expectation value of the Monte Carlo simulation. The uncertainty of this assumption is shown by the error bar for a level of confidence of 68.3%. Compared to the $\text{QFly}_{\text{HighRes}}$ RMS_{SDX} uncertainty presented in Figure 4.22, the higher measurement uncertainty of $\text{QFly}_{\text{Survey}}$ results also in a higher uncertainty of the RMS_{SDXeff} value in the range of $\pm 0.2\,mrad$. According to this graph, the RMS_{SDXeff} result obtained by $\text{QFly}_{\text{Survey}}$ is overestimated by the high variance of the input parameters.

The overestimation of the RMS_{SDXeff} due to measurement uncertainty is in this case not completely compensated by the underestimation due to the lower sampling rate. As the RMS_{SDXeff} presented in Table 5.3 tend to confirm the underestimation by the reduced sample rate, it seems that some of the uncertainties of the input parameters (especially $\Delta Z_{Abs}(T_{HTF})$ and SD_Y) have been overestimated.

5.3.3 *Uncertainty analysis and validation of tracking characterization in Survey^{Offline} mode*

The method to obtain the effective tracking deviation ($\phi_{\perp eff}$) from airborne images presented in Section 5.2.3 was validated in the AS3 power plant[19]. This section presents the acquisition of benchmark data and the uncertainty analysis. Results from the following data sources or methods are compared in the course of this validation:

- $\phi_{\perp eff}$ $\text{QFly}_{\text{Survey}}$ results
- $\phi_{\perp}$ values from the solar field data acquisition system (LOC)[20]
- $\phi_{\perp}$ benchmark data acquired with high-precision inclinometers

Obviously, these methods provide different results in terms of the difference between effective tracking deviation ($\phi_{\perp eff}$) and tracking deviation ($\phi_{\perp}$) (see Section 2.2.4). Possible discrepancies arising form this fact are discussed in the validation section.

In order to avoid further contradictions between the results, the camera of the UAV was synchronized with the inclinometer data acquisition system. That way, time-stamps from images showing a certain part of the solar field could be used to access the corresponding time range of benchmark and LOC data.

Inclinometer benchmark data

Per default, a single inclination sensor as part of the LOC is mounted at each SCA in the solar field. Since the mounting and measurement accuracy of these sensors is unknown, a standalone measurement system for the tracking angle (θ) consisting of high precision inclinometers (see also Section 3.3.2), adapters and data acquisition was composed. Thereby, the actual orientation of the optical axis of the SCE in the south of the drive pylon can be assessed independently from the local controller (LOC). The inclinometer set-up (assembly, calibration, and mounting) shall be described briefly hereinafter:

The FEP of each SCE is equipped with two boreholes representing the "water-level" or X-axis, which is used during assembly of the SCE steel structure and for the inter-SCE alignment in the solar field. These boreholes have been used to attach an adapter (see Figure 5.22) carrying a pair of high precision inclinometers (WYLER Zerotronic Typ 3 with a measurement range of $\pm 60°$). Using a pair of inclinometers instead of only single devices allows cross checking of the field measurement with adapter calibration results and a certain degree of redundancy in case of single sensor failure.

19 in the northern part of Block NE, see Figure 5.16

20 called local controller (LOC) in case of the AS3 solar field

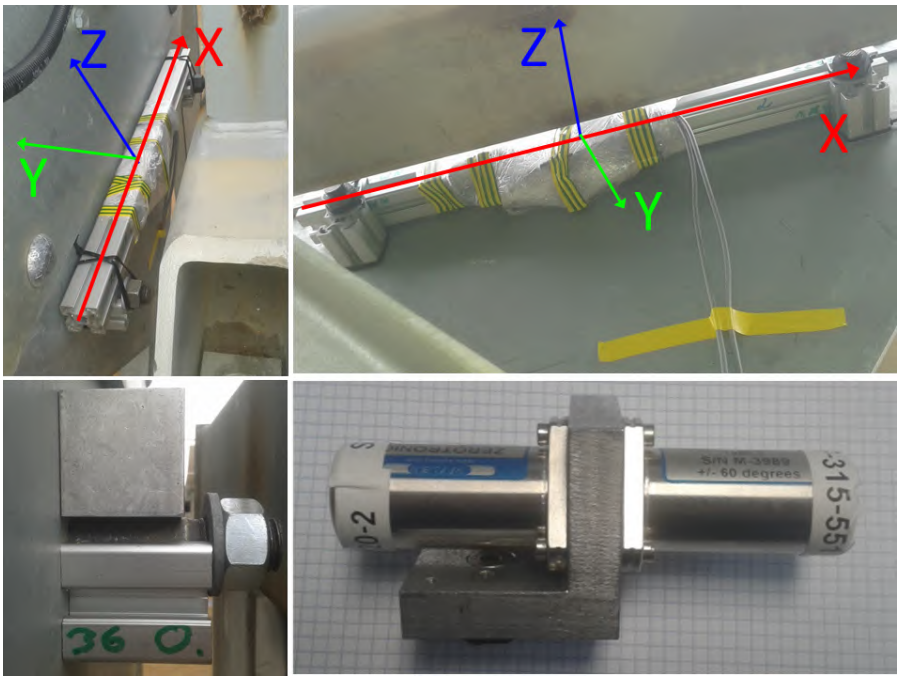

Figure 5.22: Inclinometer setup to measure the tracking angle (θ).
Top: Close-up of the FEP with aluminum profile bridging the boreholes with a distance of 500 mm. The definition of the local SCE coordinates system according to Figure 1.1 is indicated by arrows. Inclinometer sensor assemblies are protected against humidity and are not visible here.
Lower left: Close up of bolt supporting the aluminum profile.
Lower right: Single inclinometer sensor assembly consisting of two WYLER inclinometers mounted to a 90 ∘ precision angle.

After the measurement campaign, the adapters have been calibrated in order to determine inevitable off-sets of the adapters. These off-sets are caused by marginal mounting tolerances, so that even a perfectly horizontally leveled adapter returns non-zero results. In order to determine these off-sets, repeated reversal measurements (WYLER, 2013, Section 10.1) have been carried out on an adjustable reference object (test bench) until all four adapters returned constant results in both orientations (see Figure A.3 and Table A.2). The final uncertainty of the θ_{Bench} also involves tolerances of mounting the adapter to the FEP and uncertainty of alignment between the SCE's X-axis and water level points.

Uncertainty analysis of Survey^{Offline} tracking characterization

The approach of pattern matching is rather robust in terms of sensitivity to outliers, and delivers a clear signal (compare Figure 5.10) by combining all available information in a single binary matrix. Estimating the uncertainty of *effective* tracking deviation ($\sigma_{\phi_{\perp eff}}$) by straight-forward propagation of uncertainty is not suitable, because the process of pattern-matching does not constitute an analytical re-

lation between input values and result. Thus, three complementary error sources are investigated and combined in order to derive a realistic estimation for $\sigma_{\phi_{\perp eff}}$. A graphical representation of the effects originating from the uncertainty of the input parameters can be found in Figure 5.24.

1. The dominant contribution comes from the uncertainty of camera position in X direction (σ_{X_C}). Even tough individual camera positions may contain relatively high values for σ_{X_C} , the reduced uncertainty of camera position in X direction ($\sigma_{\overline{X_C}}$) is estimated to be much lower (Equation 5.18). $\sigma_{\overline{X_C}}$ can be directly converted to a contribution to the $\sigma_{\phi_{\perp eff}}$ by including the flight altitude h:

$$\sigma_{\phi_{\perp eff}}\left(\sigma_{\overline{X_C}}\right) = \arctan\left(\frac{\sigma_{\overline{X_C}}}{h}\right) \tag{5.19}$$

   The effect of σ_{X_C} resulting from wrong EOR estimation is denoted in Figure 5.23 by vertical arrows. The row originating from the image i contributing to the pattern Map^{Meas} is shifted along the vertical dimension by $\sigma_{\phi_{\perp eff}}\left(\sigma_{X_C}\right)$. The entire pattern Map^{Meas} is shifted in the same way by $\sigma_{\phi_{\perp eff}}\left(\sigma_{\overline{X_C}}\right)$ resulting in a systematic contribution to $\sigma_{\phi_{\perp eff}}$.

2. In $\text{QFly}_{\text{Survey}}$ mode, no information for absorber tube displacement in lateral direction and absorber tube displacement along the optical axis is provided. Lateral deviations (ΔX_{Abs}) are assumed to be zero, while systematic vertical deflections (ΔZ_{Abs}) due to $T_{HTF} < T_{Nom}$ are considered. ΔX_{Abs} and faulty detection of the absorber tube reflection ($\Delta X_{Reflection}$) have an identical impact: Alteration of the appearance of the TRUE/FALSE values in the row corresponding to the particular image in Map^{Meas}. This is illustrated in Figure 5.23 by a horizontal arrow. The consequence on $\sigma_{\phi_{\perp eff}}$ is not directly correlated (as in the case of the faulty camera position). Rather there is blurring of the Map^{Meas} appearance leading to a reduced fitness value (FV) during the matching of Map^{Meas} and Map^{Sim}. This will be covered in point 3.
   On the other hand, systematic lateral absorber tube deviations (in terms of $|\overline{\Delta X_{Abs}}| > 0$) will be interpreted as $|\phi_{\perp eff}| > 0$:

$$\sigma_{\phi_{\perp}}\left(\Delta X_{Abs}\right) = \arctan\left(\frac{\overline{\Delta X_{Abs}}}{f}\right) \tag{5.20}$$

   This is not a limiting factor, because that way the effective optical axis is estimated (see Section 2.2.4), which respects the interaction of reflector geometry, absorber position and orientation of the optical axis. As a consequence, $\sigma_{\phi_{\perp}}\left(\Delta X_{Abs}\right)$ is not considered in the estimation of the measurement uncertainty of $\phi_{\perp eff}$.

However, for the validation of airborne $\phi_{\perp eff}$, this contribution will be discussed.

3. The scalar values FV, PPV, and PF (see Equation 5.6 - 5.9) used to determine the best matching provide useful information for the estimation of $\sigma_{\phi_{\perp eff}}$. Example distributions to picture these phenomena are provided in Figure 5.25.
   - Low values for PPV and hence the FV indicate a general poor matching between Map^{Meas} and Map^{Sim}. This may occur when wrong assumptions on the concentrator geometry have been used during the creation of the ideal pattern (p. 109). Another reason for mismatch between Map^{Meas} and Map^{Sim} are wrong results of the image processing as stated above.
   - $1/\mathrm{PF} \ll 1$ also indicates a poor matching between Map^{Meas} and Map^{Sim}, mainly caused by artifacts during reflex detection, which are located far away from the expected pattern. To some degree, such artifacts can be identified and removed by morphological operations in Map^{Meas}.
   - The number of valid images $(\#_i)$ also has an effect on the quality of the result. Augmented distance between successive images or rejection of images during EOR estimation may result in sparsely populated Map^{Meas}. These maps may provide acceptable FV, but in fact the uncertainty of the tracking angle estimation is increased drastically, because there is a wide range with an unclear signal instead of a sharp peak. This situation can be identified by the presence of a plateau with $1/\mathrm{PF} = 1$ and $\mathrm{PPV} = 1$ (see Figure 5.25 bottom).
   - The confidence interval of the parameter $\phi_\perp$ (ci) obtained from fitting the Gaussian distribution (see Equation 5.10) to the FV is also included in the uncertainty estimation.

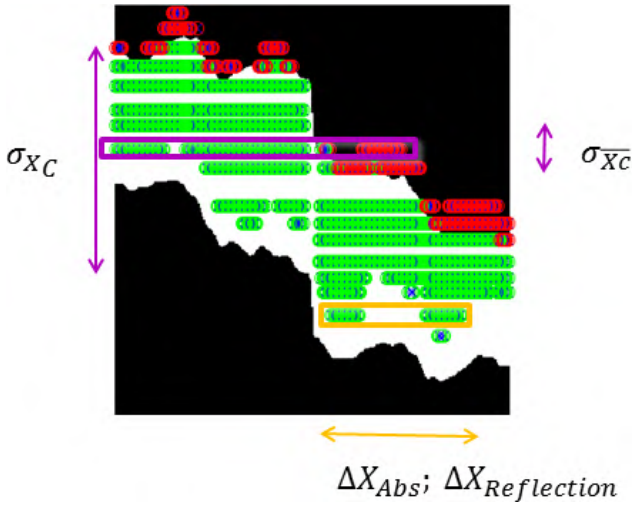

Figure 5.23: Influence of selected error sources on the matching between Map^{Meas} and Map^{Sim}. Uncertainties of the camera orientation (σ_{X_C} and $\sigma_{\overline{X_C}}$: purple arrows. Both not drawn to scale for better visibility) result in ambiguous allocation of the row within Map^{Meas}. Uncertainties resulting from the absorber tube position (ΔX_{Abs}) and reflex detection ($\Delta X_{Reflection}$) affect the appearance of a particular row in terms of width and position of non-zero elements.

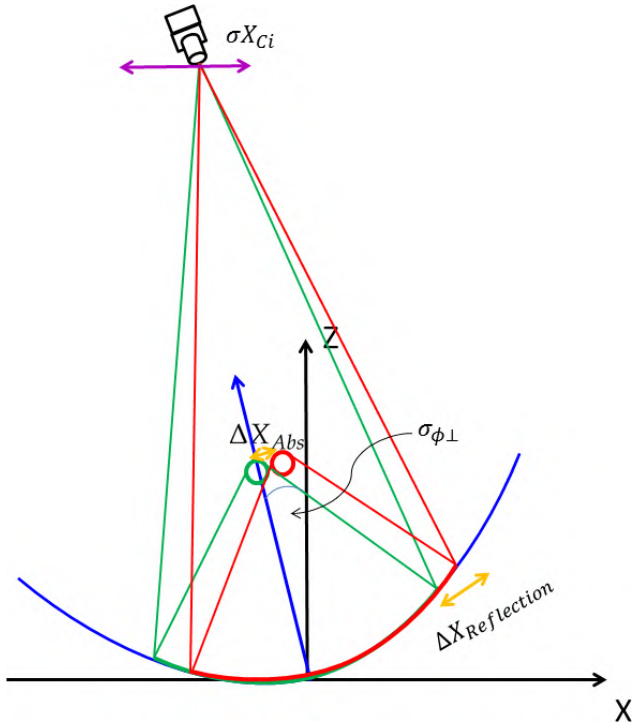

Figure 5.24: Cross section in the XZ plane to point out the qualitative effect of some input values (σ_{X_C}, ΔX_{Abs} $\Delta X_{Reflection}$) for the uncertainty estimation of the tracking measurement. The main sources as displayed in Figure 5.23 are here associated to the collector-camera set-up. Camera distances to the PTC are not drawn to scale.

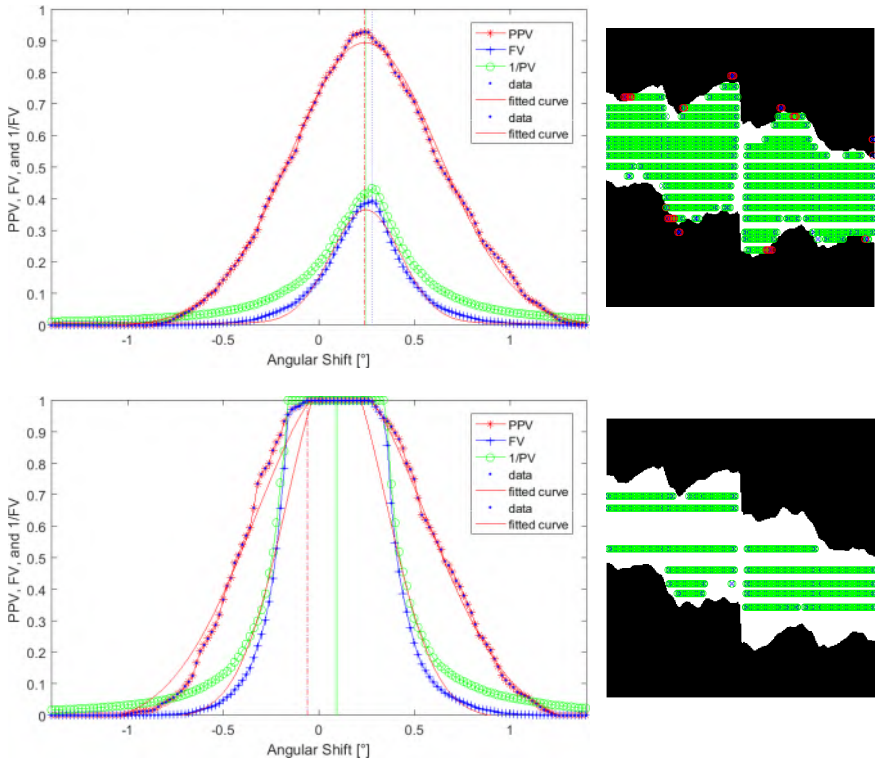

Figure 5.25: Top: Example of un-ambiguous FV curve (left) and initial Map^{Meas}/Map^{Sim} distribution (right). There are sufficient images (#: 18) to verify the good matching between measured and simulated distribution, resulting in a small measurement uncertainty of $\sigma_{\phi_{\perp eff}} = 1.0\,mrad$.
Bottom: for another SCE with only seven valid images, the measurement uncertainty is increased to $\sigma_{\phi_{\perp eff}} = 5.1\,mrad$. The main reason for the increased measurement uncertainties is the wide range without variation of the FV signal, which results in a pronounced plateau of the PF curve.

Table 5.4 provides an overview on the characteristics of the presented error sources. Based on these empirical statements, a formula to estimate $\sigma_{\phi_{\perp eff}}$ from the above mentioned contributions for airborne tracking characterization is presented. The following equation is applied to every measurement point (each SCE):

$$\begin{aligned}\sigma_{\phi_{\perp eff}}{}^2 = &\left(\sigma_{\phi_{\perp eff}}\,(\sigma_{\overline{X_C}})\right)^2 + \\ &\left(ci(\phi_\perp)\cdot(\mathrm{FV}_{max})^{-a}\cdot\frac{\#_i^{max}}{\#_i}\right)^2 + \\ &(\mathrm{PF}_{switch}\cdot\delta\phi_{FV})^2\end{aligned} \tag{5.21}$$

The term $\sigma_{\phi_{\perp eff}}\,(\sigma_{\overline{X_C}})$ corresponds to Equation 5.19. The parameter $\#_i^{max}$ is set to a value[21] of 25. The parameter $ci(\phi_\perp)$ denotes the

21 The number 25 corresponds a the maximal number of images $\#_i$ per SCA achieved during this measurement

Source	Indicator	$\lvert Range \rvert$ $[min - max]$ $[Unit]$	Type
σ_{X_C}	/	$[0.1 - 0.5]$ $[m]$	stat.
$\sigma_{\overline{X_C}}$	/	$[0.1 - 0.2]$ $[m]$	sys.
ΔX_{Abs}	/	$[0.01 - 0.02]$ $[m]$	stat.
$\overline{\Delta X_{Abs}}$ (SCE)	/	$[0.0 - 0.01]$ $[m]$	sys.
Poor matching	$FV \ll 1$	/	stat.
Blur	$FV \ll 1$	/	stat.
number of Images : $(\#_i)$	$1/PF = 1$	$[7 - 25]$	sys.
$ci(\phi_\perp)$	/	$[0.1 - 0.5]$ $[mrad]$	stat.

Table 5.4: Parameters influencing the accuracy of the $QFly_{Survey}$ $\phi_{\perp eff}$ measurement. The parameters are divided in two groups. The first group treats geometric parameters related to the camera- and absorber tube position. Large fluctuations of ΔX_{Abs} will contribute to a poor matching. Systematic absorber tube displacement in lateral direction (ΔX_{Abs}), as they occur, will no be interpreted as an uncertainty, since the orientation of the "effective" optical axis ($\phi_{\perp eff}$) also includes this parameter.
For the second group, the FV, number of images $(\#_i)$, and confidence interval of the parameter $\phi_\perp$ (ci) provide reliable indicators for the uncertainty estimation. Furthermore, the uncertainty contributions are classified whether the are of statistical or systematical nature.

confidence interval of the center of the Gaussian distribution. The exponent a is set to 1 for $Survey^{Offline}$ measurements. $\delta\phi_{FV}$ denotes the width of the plateau in the FV curve, which appears when there is an ambiguous peak. This factor is switched on when the following condition is fulfilled:

$$PF_{switch} = \begin{cases} 1 & \text{for } 1/PF_{max} = 1 \\ 0 & \text{for } 1/PF_{max} < 1 \end{cases} \tag{5.22}$$

Results and validation

The validation of effective tracking deviation ($\phi_{\perp eff}$) method in $Survey^{Offline}$ mode was carried out at the SCEs south of the drive pylon within four SCAs. Calibrated reference inclinometers (see p. 135) have been mounted there in order to acquire benchmark data for the tracking deviation ($\phi_\perp$). The graphical representation of the validation is shown in Figure 5.26, while statistical values are presented in Table 5.5. The expected measurement uncertainty of $\simeq 1.0 - 1.6\,mrad$ for these samples is well within the obtained differences between airborne- and benchmark results.

SCA ID	θ QFly	$\sigma_{\phi_{\perp eff}}$ QFly	θ Bench	$\sigma_{\phi_{\perp}}$ Bench	$\theta^{QFly} - \theta^{Bench}$	θ LOC	$\theta^{QFly} - \theta^{LOC}$
RH34	1570.6	±1.6	1568.9	±1.0	1.7	1571.4	-0.9
RH35	1572.8	±1.1	1574.9	±1.0	-2.1	1576.1	-3.4
RH36	1571.5	±1.1	1572.4	±1.0	-0.9	1573.2	-1.7
RH37	1574.0	±1.2	1575.5	±1.0	-1.5	1574.4	-0.4
RMS					1.6		2.0

Table 5.5: Comparison of $\phi_{\perp eff}$ results derived in Survey$^{\text{Offline}}$ mode with inclinometer benchmark data ($\phi_{\perp}$) and data from solar field data acquisition system (LOC). All angle values are given in *mrad*. The differences between $\text{QFly}_{\text{Survey}}$ and the benchmark values are well within the expected uncertainty margins. Deviations do not exceed 2.1 *mrad* and the *RMS* value of the deviations is 1.6 *mrad*. The largest deviation of 2.1 *mrad* can be explained by one broken glass envelope tube at RH35 and thus reduced accuracy of the detection of the absorber tube refection.
Another reason for the good agreement between $\phi_{\perp eff}$ and $\phi_{\perp}$ is, that the investigated SCEs showed no significant systematic ΔX_{Abs} values (confirmed by the $\text{QFly}_{\text{HighRes}}$ measurements for the involved SCAs).

The uncertainty estimation for the inclinometer-based $\phi_{\perp}$ measurement is only slightly better then the accuracy obtained with $\text{QFly}_{\text{Survey}}$, although the potential concerning mounting accuracy and sensor selection and calibration has been fully exploited.
The striking measurement accuracy of $\phi_{\perp eff}$ is in the same order of typical values obtained with inclinometers and allows to measure the absolute orientation of the optical axis of each SCE for an entire solar field. That way, effects like torsion, and inter-SCE misalignment can be detected with high reliability and spatial resolution. Further $\phi_{\perp eff}$ results for a larger fraction of the solar field will be presented in Section 5.4, providing useful information on straightforward implementable optimization measures for the optical performance.

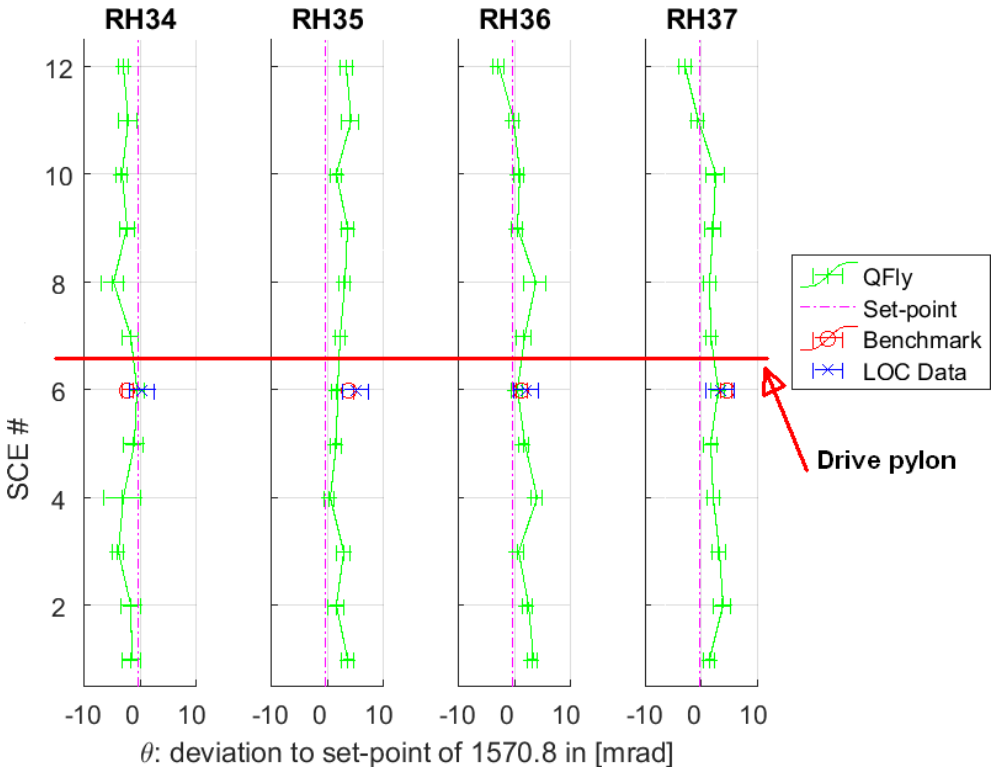

Figure 5.26: Survey$^{\text{Offline}}$ $\phi_{\perp}$ validation results in *mrad* at the SCAs RH34 - 37. The vertical axis denotes the SCE number from south to north. Benchmark data (as well as LOC data) was acquired at SCE # 6. The target value denotes the set point during the measurement (90° $\widehat{=}$ zenith). The difference between $\text{QFly}_{\text{Survey}}$ and the benchmark values is well within the expected uncertainty margins. The tracking angle (θ) values derived from the LOC-inclinometers are in accordance with the independent QFly measures. The presented SCAs show no significant torsion or misalignment, except the northern end of RH37, which deviates $\simeq$ 6 *mrad* from the orientation at the drive pylon.

5.3.4 *Uncertainty analysis and validation of tracking characterization in Survey^{Online} mode*

The validation of effective tracking deviation ($\phi_{\perp\,eff}$) in Survey$^{\text{Online}}$ mode was carried out in the same way and within the same part of the solar field as the Survey$^{\text{Offline}}$ tracking validation. The measurement range of the references inclinometer for the benchmark data (see p. 135) of $\pm 60°$ was not fully exploited, since the validation measurement in Survey$^{\text{Online}}$ mode was carried out approx. one hour before solar noon, so that the tracking angle (θ) set-point values were in range from $-12.5°$ to $-14.5°$ from zenith position (see Figure A.4). Hence, acquisition of benchmark data is similar to Survey$^{\text{Offline}}$ tracking validation. Also the uncertainty estimation requires only small adaptations, as described in the following.

The measurement uncertainty $\sigma_{\phi_{\perp\,eff}}$ is derived by using Equation 5.21. In order to provide reasonable margins, the value of exponent a in was changed from 1 to 2. This was necessary to account for the fact that the fitness value (FV) is typically one order of magnitude lower for the Survey$^{\text{Online}}$ tracking characterization compared to the Survey$^{\text{Offline}}$ results. In general, Survey$^{\text{Online}}$ tracking characterization is less accurate due to the following reasons:

1. The assumption that the bright reflection originates solely from the bellow ignores the influence of other parts of the collector structure. In fact, the HCE supports are exposed to concentrated radiation and generate a wider reflection and/or the support structure blocks part of the signal from the illuminated bellow. These effects depend on the view angle of the camera on the mirror surface and on the incidence angle ($\phi_{||}$).

2. Generation of simulated pattern involves more steps (ray-tracing of solar radiation from the mirror to the bellow, reverse tracing of the signal to the mirror and further to the observer) and is thus prone to be less accurate.

Again, the impact of these effect on $\sigma_{\phi_{\perp\,eff}}$ can be fully quantified by the quality parameters introduced in Equation 5.6 -5.9.

Results and validation

The graphical representation of the validation is shown in Figure 5.27, and statistical values are presented in Table 5.6. The expected measurement uncertainty of $\simeq 2.3 - 2.7\,mrad$ is well within the differences between airborne and benchmark results. Measurement uncertainty increases with increasing distance from the drive pylon due to the effects of structural elements interfering with the signal from the illuminated bellow.

SCA ID	θ QFly	$\sigma_{\phi_{\perp}\,eff}$ QFly	θ Bench	$\sigma_{\phi_{\perp}}$ Bench	$\theta^{QFly} - \theta^{Bench}$	θ LOC	$\theta^{QFly} - \theta^{LOC}$
RH34	1324.7	$\pm$2.7	1322.0	$\pm$1.0	2.7	1324.6	0.1
RH35	1323.5	$\pm$2.4	1324.6	$\pm$1.0	-1.1	1326.9	-3.4
RH36	1326.9	$\pm$2.3	1325.2	$\pm$1.0	1.7	1325.4	1.5
RH37	1327.6	$\pm$2.6	1329.7	$\pm$1.0	-2.1	1331.1	-3.5
RMS					2.0		2.6

Table 5.6: Comparison of $\text{QFly}_{\text{Survey}}$ $\phi_{\perp}$ results in $\text{Survey}^{\text{Online}}$ mode with inclinometer benchmark data and LOC data at the SCAs RH34 - RH37. Deviations do not exceed 2.7 *mrad* and the *RMS* value of the deviations with a value of 2.0 *mrad* is within the predicted uncertainty margins.

The appearance of the torsion/misalignment pattern in $\text{Survey}^{\text{Offline}}$ mode (Figure 5.26) differs slightly from the appearance found in the $\text{Survey}^{\text{Online}}$ validation (Figure 5.27). This observation can be partly explained by the higher measurement uncertainty. Furthermore, $\text{Survey}^{\text{Online}}$ and $\text{Survey}^{\text{Offline}}$ results can hardly be compared with each other in this particular case, because the solar field operation parameters were different:

- heat transfer fluid temperature (T_{HTF})

  $\text{Survey}^{\text{Offline}}$: $\approx 150^{\circ}$

  $\text{Survey}^{\text{Online}}$: $300^{\circ}C < T_{HTF} < 400^{\circ}C$

- tracking angle (θ)

  $\text{Survey}^{\text{Offline}}$: 90°

  $\text{Survey}^{\text{Online}}$: $:-12.5^{\circ} < \theta < -14.5^{\circ}$

As described in Chapter 3, the operational state of the solar field affects both $\phi_{\perp}$ and ΔX_{Abs}, and such way distinct $\phi_{\perp\,eff}$ have to be expected.

To summarize, it can be stated that the estimated measurement uncertainty could be confirmed by the validation. The $\phi_{\perp\,eff}$ characterization in $\text{Survey}^{\text{Online}}$ mode can be used to check the performance of the tracking system under operating conditions. The importance of this method gets obvious when relating the measurement uncertainty ($\approx$ 2 *mrad*) to the typical step width (4 *mrad*) of a single tracking step (see Figure A.4).

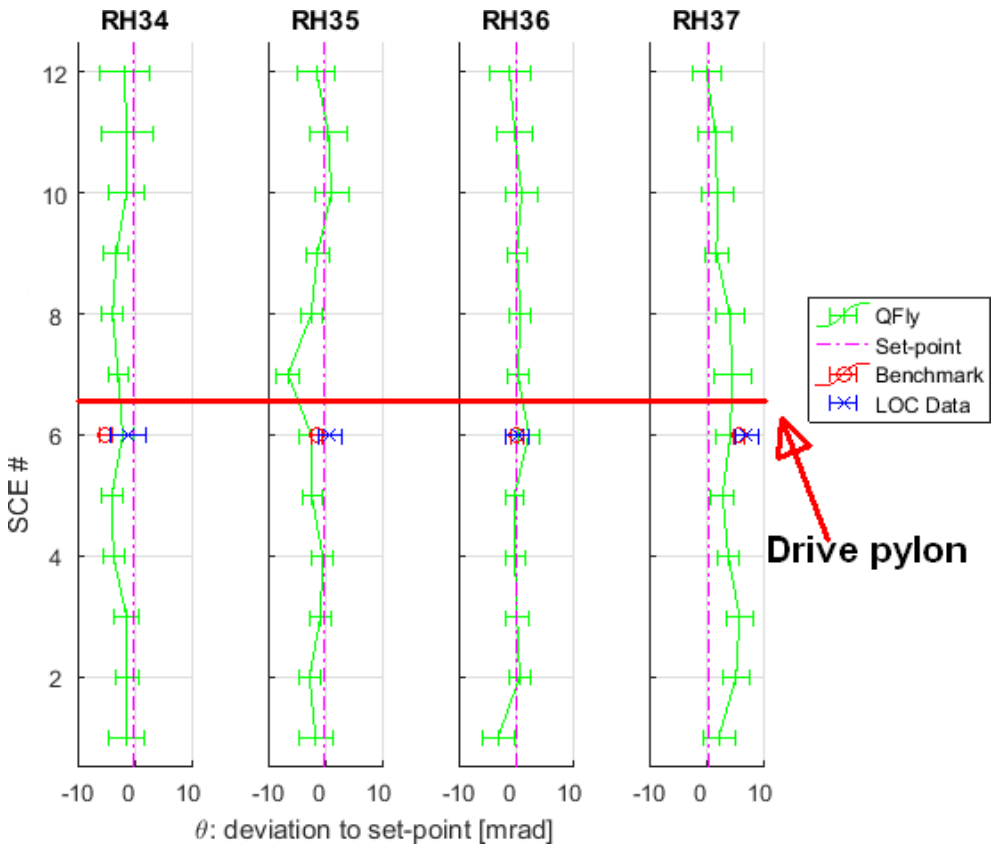

Figure 5.27: Survey$^{\text{Online}}$ $\phi_{\perp eff}$ validation results in *mrad* at the SCAs RH34 - 37. The target value denotes the set point during the measurement ($\simeq -13°$ below zenith position, corresponding to $\theta \simeq 77°$). The difference between Survey$^{\text{Online}}$ and the benchmark values is well within the expected uncertainty margins and tendencies of tracking deviation are well depicted.

5.4 METHODOLOGY FOR SOLAR FIELD COMMISSIONING

The evaluation of the $QFly_{Survey}$ and the $QFly_{HighRes}$ data from the AS3 plant revealed some interesting geometric characteristics and uncovered significant potential for the optimization of the optical performance. A concept for holistic airborne solar field characterization is elaborated based on the following observations:

1. Slope deviations in curvature direction SD_X / SD_{Xeff}:
    - The the four SCEs investigated with $QFly_{HighRes}$ revealed a characteristic SD_X pattern (see Figure 5.6). The geometry is mainly predetermined by the initial shape of the mirror panel, gravitational load, and the interaction[22] of the mirror panel with the collector steel structure.
    - Occasionally, the outer mirror panels are mounted the wrong way round (as in the example presented in Figure 2.9), because the curvature is rather small, so that inner and outer mirror edge can hardly be distinguished. This results in characteristic pattern and strong reduction of the intercept factor (γ).
    - The evaluation of the eastern half of the solar field with $QFly_{Survey}$ revealed the existence of two *"classes"* of SCEs with distinct collector quality. Block NE and a part of Block SE show moderate slope deviations with a RMS_{SDXeff} value in the range of $2-3\,mrad$. Yet, from a certain location in the solar field on, the slope deviation pattern is more pronounced[23], resulting in RMS_{SDXeff} values of up to $4.5\,mrad$.
2. Lateral absorber tube deviation from the focal line (ΔX_{Abs}):
    - Typical lateral deviations from the focal line are in the range of $5-10\,mm$
    - Occasionally, $|\Delta X_{Abs}| > 20\,mm$ are observed at the REPs of the outermost SCAs. Forces and torques from defective[24] REPAs are supposed to be the cause.
    - Lateral deviations at the A-frame may affect the sun-sensor and such way cause systematic tracking off-sets.
3. Vertical absorber tube displacement along the optical axis (ΔZ_{Abs}):
    - Typical vertical deviations from the focal line caused by mounting inaccuracies and bending between the supports are in the range of $5-10\,mm$

22 Mutual alignment of GBRPs at the steel structure and the pads of the mirror panels.
23 see histograms presented in Figure 5.30.
24 increased friction

- Systematic deviations related to the heat transfer fluid temperature (T_{HTF}) are well within the values predicted by the mechanical model (see Figure 3.6). At nominal T_{HTF}, such deviations can be neglected.

4. Effective tracking deviation ($\phi_{\perp eff}$):
   - The data presented for the four SCAs used for validation revealed moderate torsion and misalignment in the range of $\phi_{\perp} = \pm 3 mrad$ (see Figure 5.26).
   - The data presented for the four SCAs used for validation revealed a good compliance between LOC inclinometers, benchmark inclinometers, and $\text{QFly}_{\text{Survey}}$ measured on the other side.
   - The evaluation of all SCAs of northern half of the NE Block revealed larger discrepancies for single samples like misalignment of the LOC inclinometer of $\simeq 20\,mrad$ or pronounced torsion and/or misalignment of $\simeq 10\,mrad$ (see Figure 5.28 and 5.29).

5. Status of solar field components
   - The status of solar field components targets primarily mirrors and absorber tubes. The presence of intact mirrors can be checked with 100% accuracy in $\text{Survey}^{\text{Offline}}$ mode. The $\text{QFly}_{\text{Survey}}$ measurement during the campaign in 2016 Q4 revealed a missing mirror quota in the range of 1.0 to 1.7 ‰.
   - Irregularities of the absorber tube, in particular broken glass envelope tubes, show non-uniform appearance. The characteristics of the bare steel tube depend on how long the unprotected selective coating has been exposed to ambient air. The coating tends to degrade with time so that the tube reflex for recently broken glass envelope tubes is very dark even under concentrated illumination. Degraded coatings provide a very bright signal instead. In any case, broken glass envelope tubes are best detected when the field is in operation ($\text{Survey}^{\text{Online}}$ mode). However, the wide range of possible appearances complicates doubtless identification in the visible range. Data acquisition with an infrared camera is expected to deliver a unquestionable signal in this case.

The procedure depicted in Table 5.7 provides an approach to determine the optical (and thermal) performance of the solar field and to identify measures to improve the plant performance. This methodology was based on the findings from the AS3 plant.

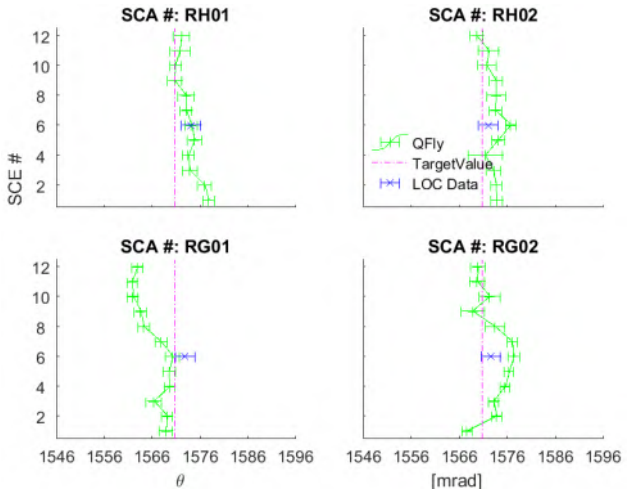

Figure 5.28: Example for possible irregularities concerning SCE alignment. The graphs display the absolute orientation measured by $\text{QFly}_{\text{Survey}}$ of each individual SCE within one loop. The set point is denoted by a vertical red line (target value). The value returned by the inclinometer of the solar field control system (LOC) is marked with a blue symbol. SCAs RG01 & RG02 are examples with significant misalignment and/or torsion.

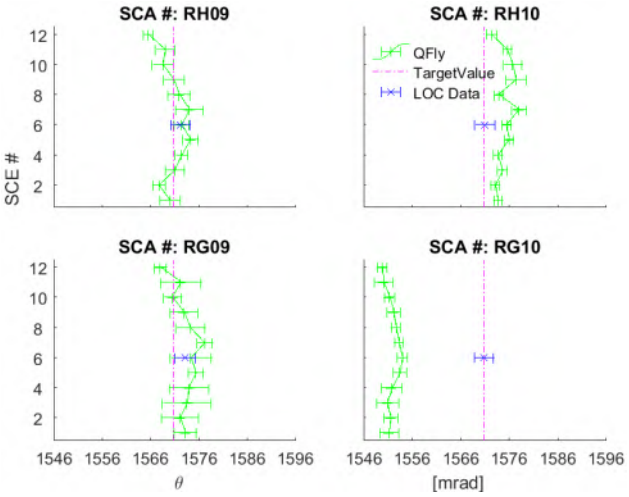

Figure 5.29: Example for possible irregularities concerning inclinometer offsets. Due to erroneous mounting of the inclinometer, the entire SCA RG10 shows a systematic deviation from the set-point. However, $\text{Survey}^{\text{Online}}$ measurements of $\phi_{\perp eff}$ revealed, that even SCAs with wrongly aligned inclinometers show acceptable tracking performance, because the sun sensor signal overruns the inclinometer offset.

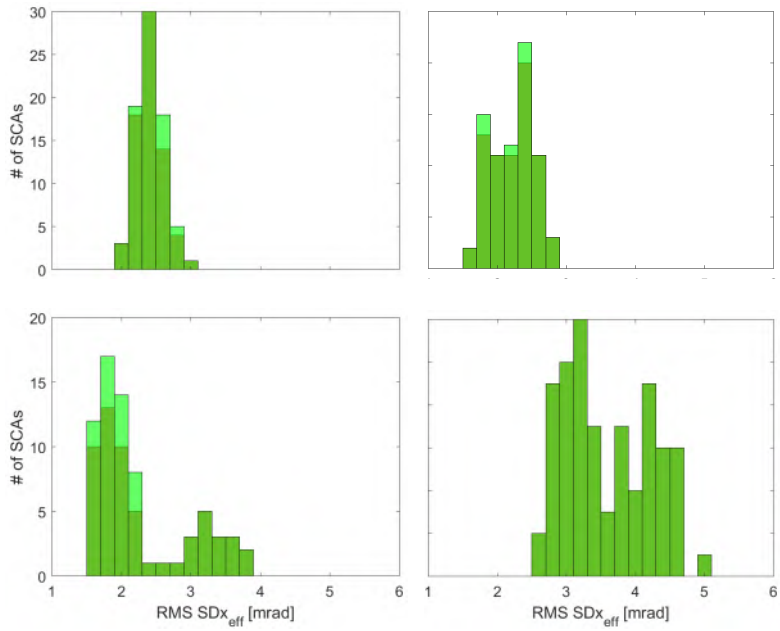

Figure 5.30: Histogram of RMS_{SDXeff} values per SCA for Block NE (top left and right) and SE (bottom left and right). The light green bars refer to results with reduced reliability. While the Block NE shows mono modal slope deviation distribution, there are two types of SCAs with different optical quality present in the northern part of SE (bottom left). The southern part of SE shows consistently a comparatively low shape quality, which could explain the lower thermal performance of this block.

Step #	Scope / data base	Method	Solar field status	Objective
1	Entire solar field	$\text{QFly}_{\text{Survey}}$ $\text{Survey}^{\text{Offline}}$	$\theta = 90°$ approaching zenith from $\theta < 90°$ and $T_{HTF} = const$	SD_{Xeff}, $\phi_{\perp eff}$ (inter-SCE-misalignment, inclinometer offset)
2	Entire solar field	$\text{QFly}_{\text{Survey}}$ $\text{Survey}^{\text{Offline}}$	$\theta = 90°$ approaching zenith from $\theta > 90°$ and $T_{HTF} = const$	$\phi_{\perp eff}$ (torsion by friction by comparison with result from step 1)
3	1 SCA per block (or hot spots detected by $\text{QFly}_{\text{Survey}}$)	$\text{QFly}_{\text{HighRes}}$	$\theta = 90°$ and $T_{HTF} = const$	SD_X, ΔX_{Abs}, and ΔZ_{Abs} for comparison with $\text{QFly}_{\text{Survey}}$ (cross checking) and to provide high resolution data for different plant parts
4	Entire solar field	$\text{QFly}_{\text{Survey}}$ $\text{Survey}^{\text{Online}}$	$60° < \theta < 120°$ and $T_{HTF} = T_{nominal}$	performance of tracking algorithm and sun-sensors/inclinometers
5	Entire solar field	Thermographic inspection of HCEs	$\theta = 90°$ and $T_{HTF} > 250°C$ and preferably after sun-set	thermal losses $[W/m]$
6	Entire solar field with input from step 1-4	RT	(-)	effective intercept factor ($\gamma'_{\phi_{\|\|}}$) for different T_{HTF} and θ
7	entire solar field with input from step 5 and 6 and DNI	Yield analysis	(-)	thermal yield and plant economy for plant "as measured"

Table 5.7: Proposed methodology for solar field characterization. The method presented in step 5 concerning thermographic measurements (Jorgensen et al., 2009; Natho, 2012) is beyond the scope of geometric measurements, however it provides relevant information to assess the thermal performance.

After the evaluation of the data following the steps 1-7 from Table 5.7, the results need to be interpreted in cooperation with the plant operator in order to reveal the potential for optimization. The cooperation with the plant operator is indispensable to evaluate the technical feasibility of suggested optimization measures.

In order to provide substantive arguments in favor of or against certain optimization measures, these measures are virtually implemented and evaluated. This can be achieved by assuming certain improvements of the collector geometry and/or operation strategy. For each scenario, the expected plant performance after implementation of optimization measures is calculated by means of ray-tracing and yield analysis (Steps 6-7). This helps to assess the feasibility of optimization measures from an economic point of view. This approach is presented graphically in Figure 5.31:

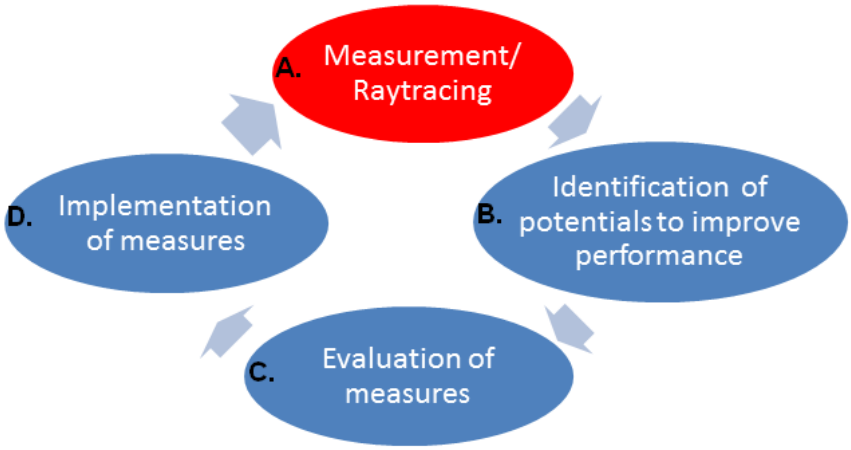

Figure 5.31: Work flow for solar field optimization. The steps A-C of this representation are covered by the methodology described in Table 5.7

SUMMARY

In this chapter, a novel $\text{QFly}_{\text{Survey}}$ approach for the airborne characterization of the optical performance of PTC plants has been presented and validated. With this method, the effective slope deviation in curvature direction SD_{Xeff} and the effective tracking deviation $\phi_{\perp eff}$ can be measured for an entire solar field[25] within a total flight time of less than 2 hours.

Despite the relatively high flight altitude and quick data acquisition, the method has proven to deliver accurate results for both the mirror shape and the individual orientation of the optical axis of each SCE. For the mirror shape expressed by the SD_{Xeff}, local uncertainties are in the range of $1\,mrad$, while the RMS_{SDXeff} of an entire SCE is in the range of $0.2\,mrad$. The uncertainty of the measurement of the absolute orientation of the optical axis, referred to as tracking deviation $\phi_{\perp}$, is in the range of $\simeq 1.6\,mrad$ in $\text{Survey}^{\text{Offline}}$ mode and $\simeq 2.6\,mrad$ in $\text{Survey}^{\text{Online}}$ mode.

Therefor, $\text{QFly}_{\text{Survey}}$ is suitable for the geometrical commissioning of entire PTC collector fields. The $\text{QFly}_{\text{Survey}}$ system has been applied to the AS3 solar field, in order to validate the measurement accuracy, and to unveil the potential of optimization for this particular CSP plant. This measure has lead to the conclusion, that the largest potential for optimization is found in the improvement of the alignment of adjacent SCEs and the correction of inclinometer off-sets.

25 of a 50 megawatt (MW) PTC plant with with the dimensions presented in Table 1.1

6 SUMMARY, CONCLUSIONS AND OUTLOOK

After first attempts at the PSA in 2007, the QFly system has now reached a level of development which allows the holistic characterization of entire PTC solar fields. The following chapter recapitulates results, challenges, and lessons learned. An outlook on further improvements and fields of applications is also provided.

As introduction to the topic, an overview on performance parameters of the PTC and related state of the art measurement methods has been presented. Next, a holistic optical and mechanical PTC model taking into account variability of the geometry under ambient conditions and operational loads was introduced. This model is the basis for a detailed yield analysis by combining the results of airborne measurements with expected deformations of the concentrator during operation. The airborne characterization, as developed and validated in the context of this thesis, can be separated in two different measurement modes, with distinct objectives, scope and accuracy.

The $\text{QFly}_{\text{HighRes}}$ method is characterized by low flight altitudes and very detailed and accurate results for SD_X, ΔX_{Abs} and ΔZ_{Abs} for a limited measurement volume of one SCA per flight.

On the other hand, the $\text{QFly}_{\text{Survey}}$ approach enables the fast characterization of entire PTC plants with reduced spatial resolution and accuracy. An efficient combination of $\text{QFly}_{\text{Survey}}$ and $\text{QFly}_{\text{HighRes}}$ provides a complete methodology for the characterization of entire PTC power plants. The fundamental findings of this work are summarized hereinafter.

6.1 SUMMARY

Analytical collector model

The variability of the measures to characterize the collector geometry under operation conditions was investigated. For each of the quantities slope deviation in curvature direction (SD_X), absorber tube displacement in lateral direction (ΔX_{Abs}), absorber tube displacement along the optical axis (ΔZ_{Abs}), and tracking deviation ($\phi_\perp$), the dependency on operational loads like gravity and thermal expansion is approved with analytical models and exemplary measurements. These models serve to provide additional geometric information for ray-tracing (RT)

and yield analysis. Geometry data obtained with QFly in a certain state described by the heat transfer fluid temperature (T_{HTF}) and tracking angle (θ) can be extrapolated to any other possible operational state. That way, it is possible to provide predictions on the annual yield taking into account all relevant effects.

QFly High Resolution mode

The objective of the $\text{QFly}_{\text{HighRes}}$ mode is to measure SD_X, ΔZ_{Abs}, and ΔX_{Abs} with high spatial resolution ($4\,mm/pixel$ for SD_X) and best possible accuracy. Measurements are carried out close to the zenith position. The waypoint-route for this task is characterized by a flight altitude of $< 30\,m$ and a rather complex flight pattern to provide the variety of perspectives required for simultaneous camera calibration, precise EOR calculation, determination of the absorber tube position, and finally, the measurement of the mirror shape. The measuring volume of this method is up to two loops per day. Typical measurement accuracy for mirror slope measurements is $0.5 - 0.8\,mrad$ (local) and $0.1\,mrad$ for the RMS_{SDX} of an entire SCE. The deviation of the absorber tube from the focal line can be derived with an uncertainty below $2\,mm$ in both X and Z direction.

QFly survey mode

In order to enhance the measuring volume, and to provide information on the effective tracking deviation ($\phi_{\perp eff}$), the $\text{QFly}_{\text{Survey}}$ mode was developed. Aerial image from straight fly-overs perpendicular to the tracking-axis at an increased flight altitude of $120\,m$ provide effective slope deviation in curvature direction (SD_{Xeff}) at a spatial resolution of $30\,mm/pixel$ and the absolute orientation of the optical axis of each SCE. The measurement accuracy for the effective mirror shape is slightly reduced by a less accurate camera positioning and reaches an average value of $\sim 1\,mrad$. The characterization of $\phi_{\perp eff}$ with an accuracy of $2 - 3\,mrad$ offers wide opportunities to detect friction-induced torsion, inclinometer off-sets, and assembly-inaccuracies.

6.2 LESSONS LEARNED

Professional and/or scientific deployment of UAV involves the complex and time-consuming part to fulfill national UAV regulations. The main problem is, that so far there are no international licenses and operational approvals, so that the global application of highly specialized measurement system requires a flexible way for data acquisition and thus a well defined interface between data acquisition and -evaluation.

There is often a conflict of interest between long term optimization objectives and short term operation goals. Thus, any measurement technique for plant optimization must have minimal interference with regular plant operation. The optimum is the airborne characterization of an operational plant without any reduction of the thermal output by measurement-related down-times of the solar field.

Ambient conditions are crucial for successful and efficient data acquisition. To a certain degree, ideal conditions (cloudy sky) for $\text{QFly}_{\text{HighRes}}$ and $\text{QFly}_{\text{Survey}}$ in $\text{Survey}^{\text{Offline}}$ mode fit very well to the objective of the plant operator. In general, the conditions involve very clean mirrors and absorber tubes on the part of the solar field, and wind velocities $< 8\,m/s$ for $\text{QFly}_{\text{Survey}}$ and $< 4\,m/s$ for $\text{QFly}_{\text{HighRes}}$.

6.3 OUTLOOK

One main goal is to further increase of measurement volume and speed. This can be best achieved by enhancing the camera frame rate. This particular constraint shall be resolved by a custom-payload consisting of a CameraLink[1] camera Crevis HV-C2535C ($<$ 30 fps and 25 MP) in combination with a recorder that is capable to handle the data stream of 4,2 Gbit/s (uncompressed) or 25-50 MByte/s with JPEG-compression. The payload involves also the option for on-board image processing and interaction with the UAV, which provides the possibility for autonomous flying. Such a camera with higher frame rate and sub-second image time stamps also provides the potential to further increase the robustness of image registration and to increase the measurement accuracy by providing a higher number of images per SCA.

Although the achieved measurement accuracy fulfills in general the expectations and is sufficient to detect typical anomalies, there are some constraints especially in the $\text{QFly}_{\text{Survey}}$ mode. This is mainly the EOR-estimation, that uses GNSS data from the UAV as starting values, but the obtained results are purely based on image processing. This approach is prone to image quality and constraints of the set-up (solar field geometry and camera perspectives). The increase of measurement accuracy in the $\text{QFly}_{\text{Survey}}$ mode can be achieved among other things by improving the EOR estimation. From the current point of view, the adaption and optimization of WP provides the largest potential for optimization.

Combining the meta data of the UAV with image information has not been fully exploited so far due to poor synchronization between camera and UAV and because of the dull behavior of the deployed

1 Camera Link is a serial communication protocol standard

servo - gimbal. Providing better initial EOR values by improving the synchronization between image time stamps and UAV meta-data in combination with a fast brush-less gimbal is expected to be very beneficial for all QFly applications.

The objective of this adaption is mainly to have the entire image filled with features contributing to the process of the single image resection, even at the boarder of the solar field. This involves adaption of the pitch angle φ_C when approaching and leaving the solar field. Changing from landscape- to portrait-mode provides a larger view-angle in east-west direction a the expense of higher flight altitudes. However, the uncertainty of the camera position in X-direction (X_C) and the partial correlation between X_C and the pitch angle φ_C (see Sec. 5.3.1) can be improved this way.

The potential of effective tracking deviation ($\phi_{\perp\,eff}$) characterization in Survey$^{\text{Offline}}$ mode has not been fully exploited. As denoted in Tab. 5.7, the repeated application of $\phi_\perp$-measurements with different rotation directions to reach zenith position provides the possibility to determine the hysteresis (see Fig. 3.14) and thus the presence of increased bearing-friction by the interpretation of different torsion pattern.

The methods presented in this thesis provide the measurement of all geometric characteristics relevant for the effective intercept factor ($\gamma'_{\phi_{||}}$). However, the interface between QFly and subsequent ray-tracing and yield analysis has not yet reached a level of detail and performance to efficiently handle that data. This interface is mandatory to accurately calculate the annual yield through full exploitation of the available information.

RT analysis shall include all input data for different tracking angle (θ) and heat transfer fluid temperature (T_{HTF}), taking into account static and dynamic geometric deviations (SD_X, ΔX_{Abs}, ΔZ_{Abs}, and $\phi_\perp$) and the position of blocking- and shading objects. The superimposition of QFly$_{\text{HighRes}}$-results with dynamic deformations from the analytical collector model enables the prediction of the intercept factor as function of operational loads: $\gamma'_{\phi_{||}} = \gamma'_{\phi_{||}}(\theta, T_{HTF})$.

That way, the yield analysis is based on effective intercept factor ($\gamma'_{\phi_{||}}$) time series. So far, the $\gamma'_{\phi_{||}}$ of solar field is treated as a constant value without temporal and spatial variability. The correct implementation of this quantity will support the accurate prediction of annual yield and thus the potential for optimization.

The airborne thermography proposed by (Jorgensen et al., 2009) and implemented at SCE-level by (Natho, 2012) will be upscaled in the near future, so that a complete AS3-type solar field can be characterized within less than four nights.

Currently used heat transfer fluid s (HTFs) like Therminol® VP-1 pose a significant threat for the environmental and health. In addition, HTF-leakages can cause fire. For this reason, it shall be investigated, whether portable detectors for Volatile Organic Compounds (VOC) based on photo ionization detector (PID) technology can be added to the UAV-payload. That way, airborne detection missions on a regular basis could help to identify, quantify and monitor HTF-leakages.

The skills and tools from airborne PTC characterization can be transferred to the optimization of heliostat fields. The motivation is here to achieve substantial time saving by airborne tracking characterization instead of time-consuming methods based on flux density measurements of single heliostats.

A

APPENDIX

A.1 SPATIAL TRANSFORMATION OF PHOTOGRAMMETRIC DATA

A sufficient number of reference points[1] in both the measured data A and the design data B is required to determine the spatial transformation parameters (translation: $c_{x,y,z}$, rotation: $r_{x,y,z}$, scaling: μ), which are used to transform the measurement point cloud into the design data coordinate system:

$$\begin{bmatrix} X \\ Y \\ Z \end{bmatrix}^B = \begin{bmatrix} c_X \\ c_Y \\ c_Z \end{bmatrix} + \mu \cdot \begin{bmatrix} 1 & r_Z & -r_Y \\ -r_Z & 1 & r_X \\ r_Y & -r_X & 1 \end{bmatrix} \cdot \begin{bmatrix} X \\ Y \\ Z \end{bmatrix}^A \tag{A.1}$$

A common approach to obtain the above defined transformation parameters is a least-squares fit of all mirror POIs to the design data.
An alternative solution to determine the transformation parameters emphasizes the role of the axis of rotation and the focal line. This method has the advantage, that the resulting performance parameters are derived under consideration of realistic boundary conditions concerning mutual orientation of mirror, tracking axis and absorber.

Translation parameters $c_{x,y,z}$ are determined by moving the origin of the measured data OA to the origin of the design data OB. A reasonable definition of the origin is the front end plate (FEP) (see Figure 1.1).

Rotation angles $r_{x,z}$ to align parabola vertex or the axis of rotation of measured and design data are obtained by merging rear end plates (REPs) of both measured and design data. The rotation angle r_y is calculated by minimizing the difference between measured mirror POIs and corresponding design data points.

A.2 MANUAL GLASS ENVELOPE TUBE POSITION MEASUREMENT

The relation between the difference of opposite hook rod measurements d_{Hook} and lateral glass tube displacement ΔX_{Glass} depends on the parabola width x and f given by:

$$\Delta X_{Glass} = \frac{d_{Hook}}{2} \cdot \cos\left(\arctan\left(\frac{f - \Delta Z_{Glass} - \frac{x^2}{4 \cdot f}}{x}\right)\right) \tag{A.2}$$

1 at least three

The deviation of the glass envelope tube center line from the focal line ΔZ_{Glass} is obtained from HCE support tilt angles β in Y-direction from digital images with the relation: $\Delta Z_{Glass} = cos(\beta) \cdot (f - Z_{Pivot})$. Here, Z_{Pivot} is the distance between the support rotation axis and the vertex. The calculations are based on the assumption of an ideal collector geometry (e.g. outer mirror edges symmetrical with respect to vertex and length of HCE supports fits design criteria). In this case, the assumed uncertainty for the position of the glass envelope tube center relative to focal line is estimated to $\pm 2.0 mm$.

A.3 MEASUREMENT OF SCE TORSION STIFFNESS

The following figure provides the time series of relative twist between inclinometer positions during the torsion stiffness measurement:

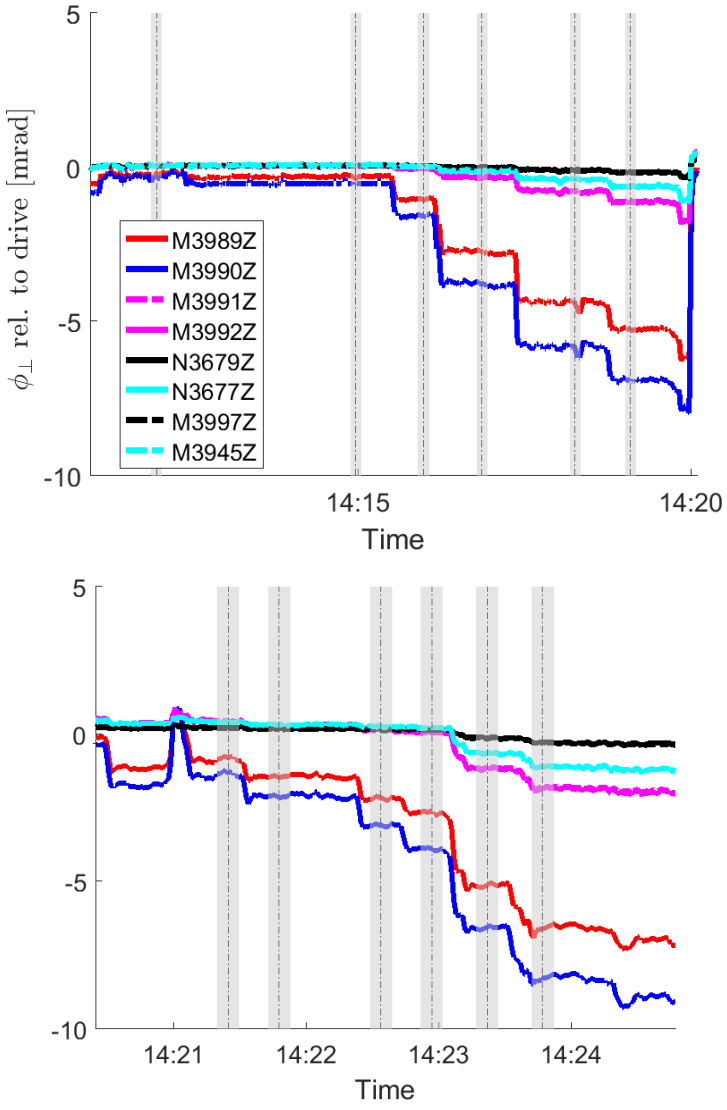

Figure A.1: Raw data of the inclinometer time series used to calculate the spring constant describing the torsion stiffness of one SCE (k_{SCE}). The color of the lines denotes the inclinometer mounting position relative to the drive pylon. The blue curves originates from the inclinometer mounted at the outer end where the torque was applied. The black line denotes the drive position, which, as expected, shows no significant alteration. Grey vertical bars mark selected periods for inclinometer value read-out, corresponding to a certain torque value. Fluctuations of the curves are caused by wind-gusts.

A.4 QFLY MEASUREMENT PROCEDURE

The following list provides a brief introduction into the data acquisition procedure:

1. Determination of SCE-, SCA-, and solar field geometry from drawings
2. Get latitude, longitude, and altitude of the drive pylon selected as origin of the local Cartesian coordinate system by using appropriate web-tools. GNSS measurements in the solar field are prone to systematic errors caused by shading of satellites and the influence on the metal structure, so that using the coordinates from `http://www.geoplaner.com/` is much more reliable. Timing of the data acquisition must consider solar position and orientation of the solar field to avoid specular reflections of solar radiation disturbing the absorber tube detection.
3. Create WP route with MATLAB, and cross check with mdCockpit and GoogleEarth
4. Preparations in the solar field:
   - Assure clean mirrors and glass envelope tubes
   - Place at least four photogrammetric targets on the outer mirror boarder of the SCE close to the drive pylon and distribute approx. 100 targets per SCA on the ground (see Figure 4.4 and 4.9)
   - Assure tracking angle (θ) $= 90° \pm 5°$
   - Assure sufficient mass flow to maintain a constant T_{HTF} during data acquisition
5. Transfer WP to the UAV using the provided serial interface or Bluetooth connection
6. Before take-off: it is mandatory to follow the QFly pre-start checklist covering all safety issues and measures to obtain high quality data. The condensed content of the list addresses:
   - UAV preparation and cross-check (mechanical and electric connections, intact structure)
   - Charge level, capacity and temperature of the UAV LiPo batteries
   - Ambient conditions, especially wind speed and landing area
   - GNSS and magnetometer quality check
   - DPH enabled
   - Camera settings check

7. Directly after take-off, the LiPo voltage must be checked by the telemetry
8. Switch the UAV flight mode to automatic WP navigation in order to initiate image acquisition according to settings as described in Section 4.1.2
9. After finishing the WP route, the UAV returns automatically to the take off position. Landing is done manually in DPH mode.
10. Upon landing measure reference distance between at least four pairs of coded targets and check the aerial image quality
11. (Dis-) charge LiPo batteries to recommended storage capacity/-voltage ($\simeq 3.85\,V$ per cell)

A.5 SOLAR FIELD LAYOUT

The following table provides some basic parameters of the solar field layout. These parameters are used in conjunction with the SCE geometry in order to set up a 3D model of the solar field for the EOR estimation by single image resection.

Parameter	Value
N-S Drive Pylon	$\simeq 1.0\,m$
N-S Normal Pylon	$\simeq 0.3\,m$
N-S Shared Pylon	$\simeq 1.5\,m$
E-W Row Spacing	$\simeq 17.2\,m$

Table A.1: Basic parameters to describe the layout of the investigated solar field (see also Table 1.1). The parameters refer to the the distances between SCEs or SCAs in north-south (N-S) and east-west (E-W) direction.

A.6 COLLINEARITY EQUATIONS

The collinearity equations are used to relate coordinates in a sensor plane (2D) to object coordinates (3D). They are used in photogrammetry and remote sensing:

$$x_c^{(i,j)} = C_k \cdot \frac{r_{11}^{(i)} \cdot (x^{(j)} - X_C^{(i)}) + r_{21}^{(i)} \cdot (y^{(j)} - Y_C^{(i)}) + r_{31}^{(i)} \cdot (z^{(j)} - Z_C^{(i)})}{r_{13}^{(i)} \cdot (x^{(j)} - X_C^{(i)}) + r_{23}^{(i)} \cdot (y^{(j)} - Y_C^{(i)}) + r_{33}^{(i)} \cdot (z^{(j)} - Z_C^{(i)})} + X_h + \Delta x \left(x_c^{(i,j)}, y_c^{(i,j)} \right) \tag{A.3}$$

$$y_c^{(i,j)} = C_k \cdot \frac{r_{12}^{(i)} \cdot (x^{(j)} - X_C^{(i)}) + r_{22}^{(i)} \cdot (y^{(j)} - Y_C^{(i)}) + r_{32}^{(i)} \cdot (z^{(j)} - Z_C^{(i)})}{r_{13}^{(i)} \cdot (x^{(j)} - X_C^{(i)}) + r_{23}^{(i)} \cdot (y^{(j)} - Y_C^{(i)}) + r_{33}^{(i)} \cdot (z^{(j)} - Z_C^{(i)})} + Y_h + \Delta y \left(x_c^{(i,j)}, y_c^{(i,j)} \right) \tag{A.4}$$

Here, i denotes the image number and j the index of a 3D object point (x, y, z). The camera constant C_k and the principal points X_h and Y_h have been introduced in Table 4.2. The terms Δx, Δy describe the deviation of the actually used optics from a pin-hole camera. The parameters $(A_{1,2,3})$, $(B_{1,2})$, and $(C_{1,2})$, also introduced in Table 4.2, represent this deviation. The rotation matrix r is describe by the angles ω_C, φ_C, κ_C whereas (X_C, Y_C, Z_C) is the vector to the center of projection of the camera.

A.7 BENCHMARKING OF QFLY SURVEY EFFECTIVE MIRROR SHAPE

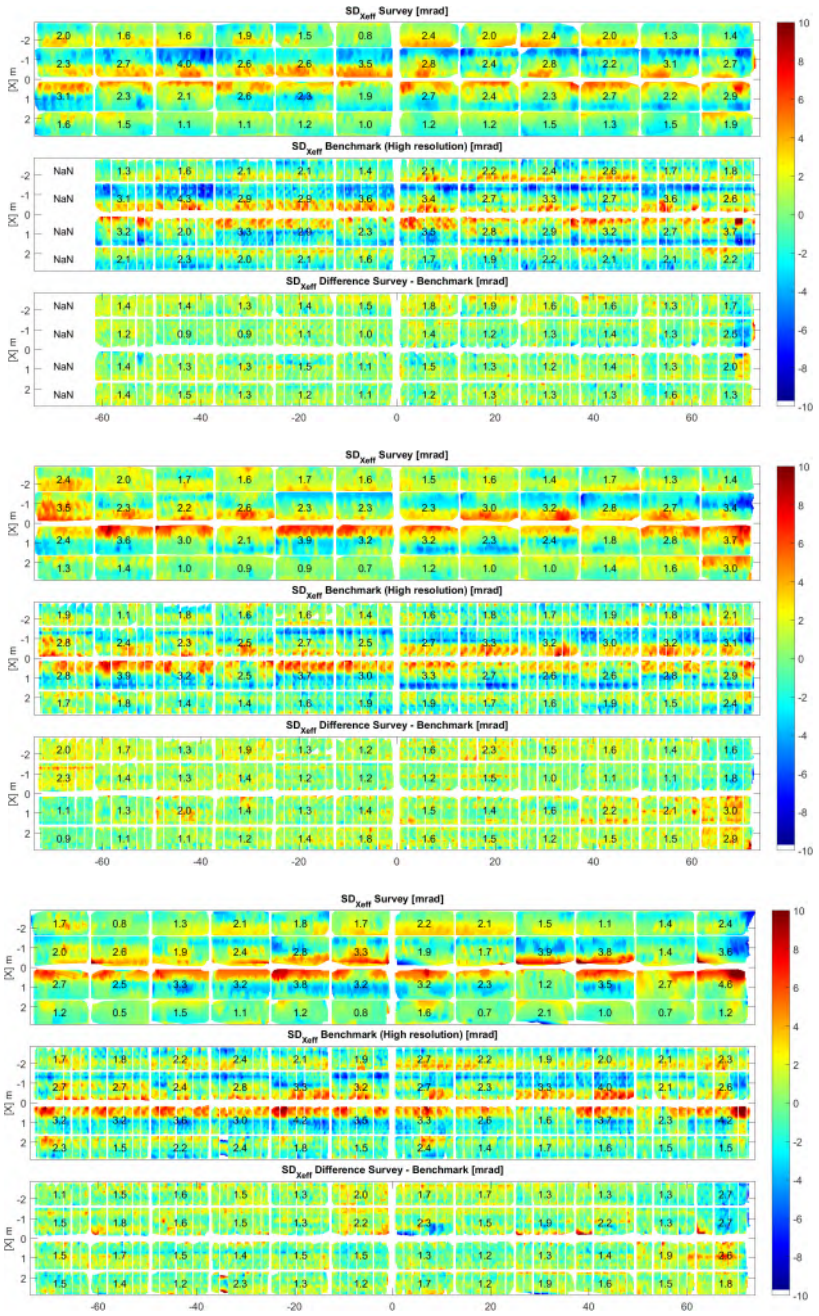

Figure A.2: $\text{QFly}_{\text{Survey}}$ validation SD_{Xeff} maps. Top: RH34. Middle: RH36. Bottom: RH37. The systematic features visible are mainly related to torsion/misalignment between SCEs and alteration of the ΔX_{Abs} between $\text{QFly}_{\text{HighRes}}$ and $\text{QFly}_{\text{Survey}}$ measurements.

A.8 INCLINOMETER ADAPTER CALIBRATION

The following data presents the calibration of the adapters used to derive benchmark data for tracking characterization:

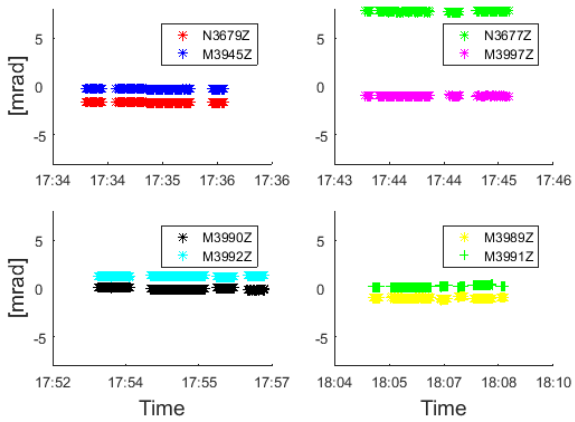

Figure A.3: Inclinometer adapter calibration data from repeated reversal measurements. Each window corresponds to one adapter. Gaps in the data indicates flipping of the adapter on the already leveled test bench. Only the device N3677Z shows a larger calibration value. For further information see Table A.2.

Sensor ID	Position	Calib value [*mrad*]
M3945Z	RH34 W	-0.24 ± 0.02
N3679Z	RH34 E	-1.61 ± 0.02
N3677Z	RH35 W	7.78 ± 0.03
M3997Z	RH35 E	-0.94 ± 0.03
M3990Z	RH36 W	-0.02 ± 0.07
M3992Z	RH36 E	1.34 ± 0.07
M3991Z	RH37 W	0.26 ± 0.08
M3989Z	RH37 E	-0.93 ± 0.08

Table A.2: Inclinometer adapter calibration results. The first row indicates the inclinometer IDs. The second row describes their mounting position (SCA) and orientation (East/West). Calibration values and their uncertainties are used in the benchmark measurements (see Figure 5.26 and 5.27). The uncertainty of the calibration values is derived from the differences between flipping the adapter on the leveled test bench.

A.9 TRACKING BEHAVIOR IN ON-LINE MODE

The following figure provides the time-resolved tracking angle for a short period of 6 minutes in order to demonstrate the width of the individual tracking step.

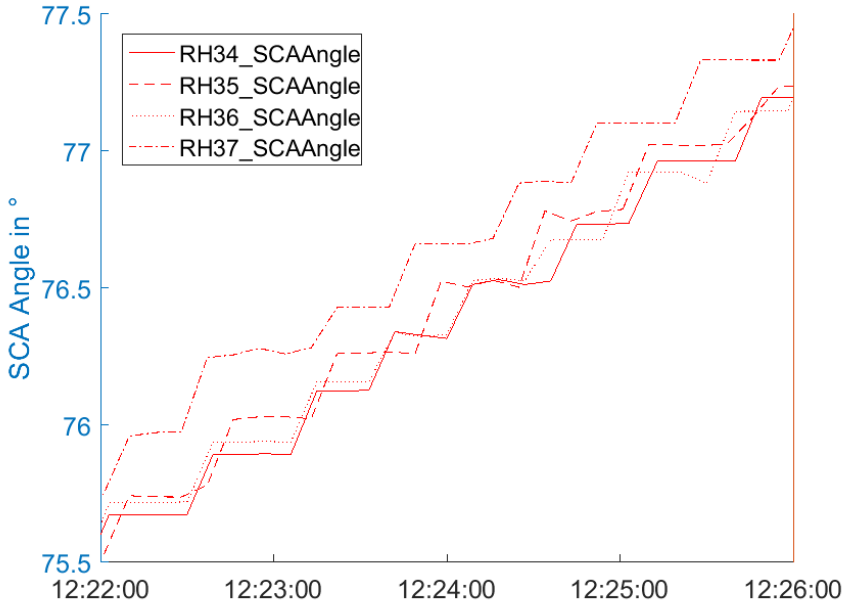

Figure A.4: LOC tracking data during the data acquisition of the Survey$^{\text{Online}}$ validation. During the fly-over with a duration of $\backsimeq 6min$, the tracking angle was altered by 2°. The travel range of one individual tracking step is in the range of $\backsimeq 4mrad$. The final uncertainty of *effective* tracking deviation ($\sigma_{\phi_{\perp eff}}$) must be set in relation to this tracking step value.

BIBLIOGRAPHY

Almanza, R., Lentz, A., and Jimenez, G. (1997). Receiver behavior in direct steam generation with parabolic troughs. *Solar Energy*, 61(4):275 – 278.

Arancibia-Bulnes, C. A., Peña-Cruz, M. I., Mutuberría, A., Díaz-Uribe, R., and Sánchez-González, M. (2017). A survey of methods for the evaluation of reflective solar concentrator optics. *Renewable and Sustainable Energy Reviews*, 69:673–684.

Bellos, E., Tzivanidis, C., and Antonopoulos, K. A. (2017). A detailed working fluid investigation for solar parabolic trough collectors. *Applied Thermal Engineering*, 114:374–386.

Bendt, P., Rabl, A., Gaul, H., and Reed, K. (1979). Optical analysis and optimization of line focus solar collectors. Technical report, Solar Energy Research Institute, Golden, Colorado (USA), Retrieved 2015.03.24 from: www.nrel.gov/docs/legosti/old/092.pdf.

Berga, L. (2016). The role of hydropower in climate change mitigation and adaptation: a review. *Engineering*, 2(3):313–318.

Bhattacharya, S. (2017). State-of-the-art of utilizing residues and other types of biomass as an energy source. *International Energy Journal*, 15(1).

Binotti, M., Zhu, G., Gray, A., and Manzolini, G. (2012). An analytical approach treating three-dimensional geometrical effects of parabolic trough collectors. Technical report, NREL/CP-5500-54712.

Bode, S.-J. and Gauche, P. (2012). Review of optical software for use in concentrating solar power systems. In *Proceedings Southern African Solar Energy Conference*. Retrieved 2015.03.24, from: `sun.ac.za/sterg/files/2012/06/CSP-06.pdf`.

Bösemann, W. (2005). Advances in photogrammetric measurement solutions. *Computers in Industry*, 56(8):886–893.

Bouguet, J. (2010). Camera calibration toolbox for matlab. Retrieved 2015.03.24, from: `http://www.vision.caltech.edu/bouguetj/calib_doc/`.

Buck, R. (2010). Solar power raytracing tool spray user manual ver. 17. Technical report, DLR e.V.

Buie, D. and Monger, A. (2004). The effect of circumsolar radiation on a solar concentrating system. *Solar Energy*, 76. Solar World Congress 2001.

Chiarappa, T., Biancifiori, F., Morales, A., Vicente, G., and Santi, S. (2014). Comparing abrasion testing results on ar-coatings for solar receivers. *Energy Procedia*. Proceedings of the SolarPACES 2014 International Conference.

Colomina, I. and Molina, P. (2014). Unmanned aerial systems for photogrammetry and remote sensing: A review. *ISPRS Journal of Photogrammetry and Remote Sensing*, 92:79–97.

CSP-Today (2017). CSP today global tracker. Retrieved 2017.04.26, from: `http://social.csptoday.com/tracker/projects`.

CSPServices (2015). Deflectometric measurement system qdec. Retrieved 2015-04-23, from: `http://www.cspservices.de/products-services/measurement-systems/qdec`.

Davison, A. J., Reid, I. D., Molton, N. D., and Stasse, O. (2007). Monoslam: Real-time single camera slam. *IEEE transactions on pattern analysis and machine intelligence*, 29(6).

Delaunay, B. (1934). Sur la sphere vide. *Izv. Akad. Nauk SSSR, Otdelenie Matematicheskii i Estestvennyka Nauk*, 7(793-800):1–2.

Denholm, P. and Hand, M. (2011). Grid flexibility and storage required to achieve very high penetration of variable renewable electricity. *Energy Policy*, 39(3):1817 – 1830.

Denholm, P. and Mehos, M. (2014). *Enabling greater penetration of solar power via the use of CSP with thermal energy storage*. CRC Press.

D'Errico, J. (2012). Bound constrained optimization using fminsearch. MATLAB File Exchange. `https://de.mathworks.com/matlabcentral/fileexchange/8277-fminsearchbnd--fminsearchcon` ver 1.4 retrieved 2017-08-15.

Dersch, J., Hennecke, K., and Quaschning, V. (2010). Greenius - A simulation tool for renewable energy utilization. In *Proceedings*.

Dickson, M. H. and Fanelli, M. (2013). *Geothermal energy: utilization and technology*. Routledge.

Dieckmann, S., Dersch, J., Giuliano, S., Puppe, M., Lüpfert, E., Hennecke, K., Pitz-Paal, R., Taylor, M., and Ralon, P. (2017). Lcoe reduction potential of parabolic trough and solar tower csp technology until 2025. In *AIP Conference Proceedings*, volume 1850, page 160004. AIP Publishing.

Dinter, F. and Gonzalez, D. M. (2014). Operability, reliability and economic benefits of csp with thermal energy storage: first year of operation of andasol 3. *Energy Procedia*, 49:2472–2481.

Diver, R. B. and Moss, T. A. (2007). Practical field alignment of parabolic trough solar concentrators. *Journal of Solar Energy Engineering*, 129(2):153–159.

D&S (2017). D&s portable specular reflectometer model 15r-usb technical specifications. `http://www.devicesandservices.com/15r_technical_notes.htm` retrieved 2017-08-09.

Duda, R. O. and Hart, P. E. (1972). Use of the hough transformation to detect lines and curves in pictures. *Communications of the ACM*, 15(1):11–15.

Edenhofer, O., Pichs-Madruga, R., Sokona, Y., Seyboth, K., Matschoss, P., Kadner, S., Zwickel, T., Eickemeier, P., Hansen, G., Schlömer, S., and von Stechow, C. (2011). IPCC special report on renewable energy sources and climate change mitigation - summary for policymakers. Technical report, IPCC. Cambridge University Press, Cambridge, United Kingdom and New York, NY, USA.

Espinosa-R., G., Hermoso, J. L. N., Martínez-Sanz, N., and Gallas-Torreira, M. (2016a). Vacuum evaluation of parabolic trough receiver tubes in a 50 MW concentrated solar power plant. *Solar Energy*, 139:36–46.

Espinosa-R., G., Martinez-Sanz, N., Izquierdo-Nuñez, D., and Osta-Lombardo, M. (2016b). A novel portable device to measure transmittance and reflectance of parabolic trough receiver tubes in the field. *Journal of Solar Energy Engineering*, 138(6):061003.

Fawcett, T. (2006). An introduction to roc analysis. *Pattern recognition letters*, 27(8):861–874.

Fernandez-Garcia, A., Zarza, E., Valenzuela, L., and Perez, M. (2010). Parabolic-trough solar collectors and their applications. *Renewable and Sustainable Energy Reviews*, 14(7):1695 – 1721.

Fernandez-Reche, J. and Valenzuela, L. (2012). Geometrical assessment of solar concentrators using close-range photogrammetry. *Energy Procedia*, 30(0):84–90. 1st International Conference on Solar Heating and Coolingfor Buildings and Industry (SHC 2012).

Finn, R. L. and Wright, D. (2012). Unmanned aircraft systems: Surveillance, ethics and privacy in civil applications. *Computer Law & Security Review*, 28(2):184–194.

Flores, V. and Almanza, R. (2004). Behavior of the compound wall copper-steel receiver with stratified two-phase flow regimen in transient states when solar irradiance is arriving on one side of receiver. *Solar Energy*, 76(1–3):195–198. Solar World Congress 2001.

García, I. L., Álvarez, J. L., and Blanco, D. (2011). Performance model for parabolic trough solar thermal power plants with thermal storage: Comparison to operating plant data. *Solar Energy*, 85(10):2443–2460.

Garcis, S., Bello-Garcia, A., and Ordonez, C. (2012). Estimating intercept factor of a parabolic solar trough collector with new supporting structure using off-the-shelf photogrammetric equipment. *Applied Energy*, 92:815–821.

Geyer, M., Lüpfert, E., Osuna, R., Esteban, A., Schiel, W., Zarza, A. S. E., Nava, P., Langenkamp, J., and Mandelberg, E. (2002). Eurotrough-parabolic trough collector developed for cost efficient solar power generation. In *Proceedings of the 11th SolarPACES Conference, September 2002, Zurich, Switzerland*, pages 04–06.

Gonzalez, R. C., Woods, R. E., and Eddins, S. L. (2004). *Digital image processing using MATLAB*. Pearson Education India.

Grussenmeyer, P. and Al Khalil, O. (2002). Solutions for exterior orientation in photogrammetry: a review. *The photogrammetric record*, 17(100):615–634.

GUM (1999). Env13005: Leitfaden zur Angabe der Unsicherheit beim Messen. Beuth-Verlag, Berlin.

Habib, A. F., Kim, E.-M., and Kim, C.-J. (2007). New methodologies for true orthophoto generation. *Photogrammetric Engineering & Remote Sensing*, 73(1):25–36.

Haszeldine, R. S. (2009). Carbon capture and storage: how green can black be? *Science*, 325(5948):1647–1652.

Heimsath, A., Platzer, W., Bothe, T., and Wansong, L. (2008). Characterization of optical components for linear fresnel collectors by fringe reflection method. In *Proceedings of the 14th SolarPACES Conference, 4. - 7. March 2008, Las Vegas, USA*, pages 1–8.

Heinz, B. (2005). Entwicklung eines optischen Messsystems zur Bestimmung der Steigungsfehler von Parabolspiegeln solarthermischer Kraftwerke. Master's thesis, TU München.

Heller, P., Meyer-Grünefeldt, M., Ebert, M., Jannote, N., Nouri, B., Pottler, K., Prahl, C., Reinalter, W., and Zarza, E. (2011). Kontas–a rotary test bench for standardized qualification of parabolic trough components. In *Proceedings of the 17th SolarPACES Conference, 20. - 23. September 2011, Granada, Spain*.

Hernández-Moro, J. and Martínez-Duart, J. (2013). Analytical model for solar {PV} and {CSP} electricity costs: Present {LCOE} values and their future evolution. *Renewable and Sustainable Energy Reviews*, 20(0):119 – 132.

Hertel, J. (2013). Study and implementation of an object tracing algorithm for the deflectrometric shape qualification of parabolic trough collectors. Master's thesis, Technische Universität München.

Herwitz, S., Johnson, L., Dunagan, S., Higgins, R., Sullivan, D., Zheng, J., Lobitz, B., Leung, J., Gallmeyer, B., Aoyagi, M., et al. (2004). Imaging from an unmanned aerial vehicle: agricultural surveillance and decision support. *Computers and electronics in agriculture*, 44(1):49–61.

Hirsch, T., Bachelier, C., Eck, M., Dersch, J., Fluri, T., Giuliano, S., Goebel, O., González, L., Haller, U., Meyer, R., et al. (2017). The first version of the solarpaces guideline for bankable ste yield assessment. In *AIP Conference Proceedings*, volume 1850, page 160014. AIP Publishing. `http://solarpaces.org/tasks/task-i-solar-thermal-electric-systems/modeling-guidelines`.

Hirsch, T., Ebert, M., Eck, M., Eickhoff, M., Janotte, N., Keller, L., Meyen, S., Meyer-Grünefeld, M., Munini, M., Nanz, L., Prahl, C., Röger, M., and Wittmann, M. (2012). Stratified flow phenomena in parabolic trough systems. In *Proceedings of the 18th SolarPACES Conference, 11. - 14. September 2012, Marrakech, Morocco*.

Ho, C. K. (2008). Software and codes for analysis of concentrating solar power technologies. Technical report, Sandia National Laboratories. Retrieved 2014-07-16, from: `http://energy.sandia.gov/wp/wp-content/gallery/uploads/SAND2008-8053.pdf`.

Hosoya, N., Peterka, J., Gee, R., and Kearney, D. (2008). Wind tunnel tests of parabolic trough solar collectors. Technical Report NREL/SR-550-32282, National Renewable Energy Laboratory, Golden, CO.

Houck, C. R., Joines, J., and Kay, M. G. (1995). A genetic algorithm for function optimization: a matlab implementation. *NCSU-IE TR*, 95(09).

Hough, P. V. (1962). Method and means for recognizing complex patterns. US Patent 3069654.

Irena (2013). Concentrating solar power - technology brief. Technical report, International Renewable Energy Agency.

Iverson, B. D., Flueckiger, S. M., and Ehrhart, B. D. (2011). Trough heat collection element deformation and solar intercept impact. In *Proceedings of the 17th SolarPACES Conference, 20. - 23. September 2011, Granada, Spain*.

Janotte, N. (2012). *Requirements for representative acceptance tests for the prediction of the annual yield of parabolic trough solar fields*. PhD thesis, RWTH Aachen.

Janotte, N. (2014). Guidelines for testing of csp components. Technical report, SFERA (Solar Facilities for the European Research Area).

Janotte, N., Caron, S., Nouri, B., Pernpeintner, J., Prahl, C., and Röger, M. (2015). QUARZ-Receiver-Ringschluss-Vergleich von DLR Labor- und Feldtestmethoden sowie Simulationswerkzeugen zur Bewertung der Leistungsfähigkeit von Parabolrinnenreceivern. *Kölner Sonnenkolloquium*.

Janotte, N., Feckler, G., Kötter, J., Decker, S., Herrmann, U., Schmitz, M., and Lüpfert, E. (2014). Dynamic performance evaluation of the heliotrough® collector demonstration loop–towards a new benchmark in parabolic trough qualification. *Energy Procedia*, 49:109–117.

Jorgensen, G., Burkholder, F., Gray, A., and Wendelin, T. (2009). Assess the efficacy of an aerial distant observer tool capable of rapid analysis of large sections of collector fields. Technical Report NREL/MP-550-44332, NREL.

Jung, C., Dersch, J., Nietsch, A., and Senholdt, M. (2015). Technological perspectives of silicone heat transfer fluids for concentrated solar power. *Energy Procedia*, 69:663–671.

Keith, D. (2013). *A case for climate engineering*. MIT Press.

Kennedy, C. and Terwilliger, K. (2004). Optical durability of candidate solar reflectors. In *ASME 2004 International Solar Energy Conference*, pages 597–606. American Society of Mechanical Engineers.

Knauer, M. C., Kaminski, J., and Hausler, G. (2004). Phase measuring deflectometry: a new approach to measure specular free-form surfaces. In *Photonics Europe*, pages 366–376. International Society for Optics and Photonics.

Kost, C., Mayer, J., Thomsen, J., Hartmann, N., Senkpiel, C., Philipps, S., Nold, S., Lude, S., Saad, N., and Schlegl, T. (2013). Levelized cost of electricity renewable energy technologies. *Fraunhofer Institut For Solar Energy systems (ISE)*. `http://www.ise.fraunhofer.de/en/publications/veroeffentlichungen-pdf-dateien-en/studien-und-konzeptpapiere/study-levelized-cost-of-electricity-renewable-energies.pdf` retrieved 2017-08-15.

Kuckelkorn, T., Jung, C., Gnädig, T., Lang, C., Schall, C., Rajpaul, V., and Richter, C. (2016). Hydrogen generation in csp plants and maintenance of dpo/bp heat transfer fluids–a simulation approach. In *AIP Conference Proceedings*, volume 1734. AIP Publishing.

Lagarias, J. C., Reeds, J. A., Wright, M. H., and Wright, P. E. (1998). Convergence properties of the nelder–mead simplex method in low dimensions. *SIAM Journal on optimization*, 9(1):112–147.

Leachtenauer, J. C. and Driggers, R. G. (2001). *Surveillance and reconnaissance imaging systems: modeling and performance prediction*. Artech House Optoelectronics Library.

Leary, P. and Hankins, J. (1979). User's guide for mirval: a computer code for comparing designs of heliostat-receiver optics for central receiver solar power plants. Technical report, Sandia Labs., Livermore, CA (USA).

Lewandowski, A. and Gray, A. (2010). Video scanning hartmann optical tester (vshot) uncertainty analysis. In *Proceedings of the 16th SolarPACES Conference, 21. - 24. September 2010, Perpignan, France*.

Lewis, A. J. (1993). *Absolute length measurement using multiple-wavelength phase-stepping interferometry*. PhD thesis, Imperial College of Science, Technology and Medicine, University of London.

Lipps, F. et al. (1974). Shading and blocking geometry for a solar tower concentrator with rectangular mirrors. In *American Society of Mechanical Engineers, Winter Annual Meeting*.

Lovegrove, K. and Stein, W. (2012). *Concentrating solar power technology: Principles, developments and applications*. Elsevier.

Luhmann, T., Hastedt, H., and Tecklenburg, W. (2006a). Modelling of chromatic aberration for high precision photogrammetry. In *Commission V Symp. on Image Engineering and Vision Metrology, Proc. ISPRS*, volume 36, pages 173–178.

Luhmann, T., Robson, S., Kyle, S., and Harley, I. (2006b). *Close range photogrammetry: Principles, Techniques and Applications*. Whittles Publishing.

Lüpfert, E., Geyer, M., Schiel, W., Esteban, A., Osuna, R., Zarza, E., and Nava, P. (2001). Eurotrough design issues and prototype testing at psa. *Solar Engineering*, pages 387–392.

Lüpfert, E., Herrmann, U., Price, H., Zarza, E., and Kistner, R. (2004a). Toward standard performance analysis for parabolic trough collector fields. In *Proceedings of the 12th SolarPACES Conference, October 2004, Oaxaca, Mexico*.

Lüpfert, E., Pottler, K., and Schiel, W. (2004b). Optimization of cost and efficiency in concentrating solar power technology trough quality control in large production series for solar fields. *EuroSun2004, 14. Internationales Sonnenforum*.

Lüpfert, E., Pottler, K., Ulmer, S., Riffelmann, K.-J., Neumann, A., and Schiricke, B. (2005). Qualitätssicherung und Ertragssteigerung für Parabolrinnen-Kollektoren (OPAL-2). Technical Report 16UM0004. Retrieved 2017.03.27, from: `http://edok01.tib.uni-hannover.de/edoks/e01fb09/614353335l.pdf`.

Lüpfert, E., Pottler, K., Ulmer, S., Riffelmann, K.-J., Neumann, A., and Schiricke, B. (2007). Parabolic trough optical performance analysis techniques. *Journal of solar energy engineering*, 129(2):147–152.

Lüpfert, E. and Ulmer, S. (2009). Solar trough mirror shape specifications. In *Proceedings of the 15th SolarPACES Conference, 15. - 18. September 2009, Berlin, Germany*.

März, T., Prahl, C., Ulmer, S., Wilbert, S., and Weber, C. (2011). Validation of two optical measurement methods for the qualification of the shape accuracy of mirror panels for concentrating solar systems. *Journal of Solar Energy Engineering*, 133(3):031022.

Maza, I., Caballero, F., Capitán, J., Martínez-de Dios, J. R., and Ollero, A. (2011). Experimental results in multi-UAV coordination for disaster management and civil security applications. *Journal of intelligent & robotic systems*, 61(1):563–585.

Meiser, S. (2008). Entwicklung eines optischen Messsystems zur Bestimmung der Formgenauigkeit von Parabolspiegeln solarthermischer Kraftwerke aus der Luft. Master's thesis, TU Clausthal.

Meiser, S. (2014). *Analysis of parabolic trough concentrator mirror shape accuracy in laboratory and collector*. PhD thesis, RWTH Achen.

Meiser, S., Kleine-Büning, C., Uhlig, R., Lüpfert, E., Schiricke, B., and Pitz-Paal, R. (2013). Finite element modeling of parabolic trough mirror shape in different mirror angles. *Journal of Solar Energy Engineering*, 135(3):031006.

Meiser, S., Schneider, S., Lüpfert, E., Schiricke, B., and Pitz-Paal, R. (2015). Evaluation and assessment of gravity load on mirror shape of parabolic trough solar collectors. *Energy Procedia*, 75:485–494.

Meiser, S., Schneider, S., Lüpfert, E., Schiricke, B., and Pitz-Paal, R. (2017). Evaluation and assessment of gravity load on mirror shape and focusing quality of parabolic trough solar mirrors using finite-element analysis. *Applied Energy*, 185:1210–1216.

Meyen, S., Lüpfert, E., Pernpeintner, J., and Fend, T. (2009). Optical characterisation of reflector material for concentrating solar power technology. In *Proceedings of the 15th SolarPACES Conference, 15. - 18. September 2009, Berlin, Germany*.

Michalsky, J. J. (1988). The astronomical almanac's algorithm for approximate solar position (1950–2050). *Solar energy*, 40(3):227–235.

microdrones (2017a). md4-1000 technical details. Retrieved 2017-03-27, from: `http://wiki.microdrones.com/index.php/md4-1000`.

microdrones (2017b). Waypoint command set for flight controller version 2.8. Retrieved 2017-03-27, from: `http://wiki.microdrones.com/index.php/Waypoint_Command_Set`.

Möller, T. (2004). Messung und Analyse der Verformung von Spiegeln von Parabolrinnenkollektoren durch Eigengewicht. Master's thesis, Hochschule Mittweida, University of Applied Sciences.

Montecchi, M., Benedetti, A., and Cara, G. (2010). Optical alignment of parabolic trough modules. In *Proceedings of the 16th SolarPACES Conference, 21. - 24. September 2010, Perpignan, France*.

Morgenthal, G. and Hallermann, N. (2014). Quality assessment of unmanned aerial vehicle (uav) based visual inspection of structures. *Advances in Structural Engineering*, 17(3):289–302.

Natho, R. (2012). Thermal evaluation of receivers in parabolic trough collectors using airborne infrared imaging. Master's thesis, Ilmenau University of Technology.

Osório, T., Horta, P., Larcher, M., Pujol-Nadal, R., Hertel, J., van Rooyen, D. W., Heimsath, A., Schneider, S., Benitez, D., Frein, A., et al. (2016). Ray-tracing software comparison for linear focusing solar collectors. In *AIP Conference Proceedings*, volume 1734. AIP Publishing.

Otsu, N. (1975). A threshold selection method from gray-level histograms. *Automatica*, 11(285-296):23–27.

Owkes, J. K. (2012). *An Optical Characterization Technique for Parabolic Trough Solar Collectors Using Images of the Absorber Reflection*. PhD thesis, University of Colorado.

Pernpeintner, J., Happich, C., Lüpfert, E., Schiricke, B., Lichtenthäler, N., and Weinhausen, J. (2015). Linear focus solar simulator test bench for non-destructive optical efficiency testing of parabolic trough receivers. *Energy Procedia*, 69:518–522.

Pitz-Paal, R., Dersch, J., Milow, B., Ferriere, A., Langnickel, U., Steinfeld, A., Karni, J., Zarza, E., and Popel, O. (2007). Development steps for parabolic trough solar power technologies with maximum impact on cost reduction. *Journal of Solar Energy Engineering*, 129(4):371–377.

Pottler, K., Lüpfert, E., Johnston, G. H., and Shortis, M. R. (2004). Photogrammetry: A powerful tool for geometric analysis of solar concentrators and their components. In *ASME 2004 International Solar Energy Conference*, pages 719–726. American Society of Mechanical Engineers.

Pottler, K., Mützel, M., Engelke, J., Prahl, C., and Röger, M. (2011). QFoto: Automatic inline measurement system for parabolic trough

structures: Experiences and development. In *Proceedings of the 17th SolarPACES Conference, 20. - 23. September 2011, Granada, Spain*.

Pottler, K., Ulmer, S., Lüpfert, E., Landmann, M., Röger, M., and Prahl, C. (2014). Ensuring performance by geometric quality control and specifications for parabolic trough solar fields. *Energy Procedia*, 49(0):2170–2179. Proceedings of the SolarPACES 2013 International Conference.

Prahl, C., Hilgert, C., and Röger, M. (2016a). Luftgestützte optische Qualifizierung von Parabolrinnenkollektoren. In *Kölner Sonnenkolloquium*. Retrieved 2017.05.03, from: `http://elib.dlr.de/108851/`.

Prahl, C., Röger, M., and Hilgert, C. (2016b). Air-borne shape measurement of parabolic trough collector fields. In *Proceedings of the 22nd SolarPACES Conference, 11 - 14 October 2016, Abu Dhabi, UAE*. `http://doi.org/10.1063/1.4984338`.

Prahl, C., Röger, M., Stanicki, B., and Hilgert, C. (2017). Absorber tube displacement in parabolic trough collectors - a review and presentation of an airborne measurement approach. *Solar Energy*, 157:692 – 706. `https://doi.org/10.1016/j.solener.2017.05.023`.

Prahl, C., Stanicki, B., Hilgert, C., Ulmer, S., and Röger, M. (2011). Airborne shape measurement of parabolic trough collector fields. In *Proceedings of the 17th SolarPACES Conference, 20. - 23. September 2011, Granada, Spain*.

Prahl, C., Stanicki, B., Hilgert, C., Ulmer, S., and Röger, M. (2013a). Airborne shape measurement of parabolic trough collector fields. *Solar Energy*, 91(0):68–78.

Prahl, C., Ulmer, S., Röger, M., and Pottler, K. (2013b). Verfahren zur Vermessung eines solarthermischen Konzentrators. DE Patent App. DE201110080969.

Price, H., Forristall, R., Wendelin, T., Lewandowski, A., Moss, T., and Gummo, C. (2006). Field survey of parabolic trough receiver thermal performance. In *ASME 2006 International Solar Energy Conference*, pages 109–116. American Society of Mechanical Engineers.

Price, H., Lüpfert, E., Kearney, D., Zarza, E., Cohen, G., Gee, R., and Mahoney, R. (2002). Advances in parabolic trough solar power technology. *Journal of solar energy engineering*, 124(2):109–125.

Qoaider, L., Röger, M., Heller, P., and Fend, T. (2011). enermena: Eine Initiative zur Unterstützung der nachhaltigen Implementierung der CSP-Technologie in der MENA Region. *14. Kölner Sonnenkolloquium*.

Quater, P. B., Grimaccia, F., Leva, S., Mussetta, M., and Aghaei, M. (2014). Light unmanned aerial vehicles (uavs) for cooperative inspection of pv plants. *IEEE Journal of Photovoltaics*, 4(4):1107–1113.

Remondino, F. and Fraser, C. (2006). Digital camera calibration methods: considerations and comparisons. *International Archives of Photogrammetry, Remote Sensing and Spatial Information Sciences*, 36(5):266–272.

Ren, L. (2014). A review of available methods for the alignment of mirror facets of solar concentrator in solar thermal power system. *Renewable and Sustainable Energy Reviews*, 32(0):76–83.

Riffelmann, K.-J., Graf, D., and Nava, P. (2011). Ultimate trough: The new parabolic trough collector generation for large scale solar thermal power plants. In *ASME 2011 5th International Conference on Energy Sustainability*, pages 789–794. American Society of Mechanical Engineers.

Rockström, J. (2014). Climate change: The necessary and the possible and the desirable earth league climate statement on the implications for climate policy from the 5th IPCC assessment. *Earth's Future*, 2(12):606–611.

Ruegamer, T., Kamp, H., Kuckelkorn, T., Schiel, W., Weinrebe, G., Nava, P., Riffelmann, K., and Richert, T. (2014). Molten salt for parabolic trough applications: system simulation and scale effects. *Energy Procedia*, 49:1523–1532.

Schiricke, B. (2008). *Optischer Wirkungsgrad von Parabolrinnenkollektoren: Modellierung und Messung*. PhD thesis, RWTH Aachen.

Schiricke, B., Pitz-Paal, R., Lüpfert, E., Pottler, K., Pfänder, M., Riffelmann, K.-J., and Neumann, A. (2009). Experimental verification of optical modeling of parabolic trough collectors by flux measurement. *Journal of Solar Energy Engineering*, 131(1):011004.

Schneider, S., Lüpfert, E., and Schiricke, B. (2015). Optimizing solar thermal power plants: Influences on parabolic mirror shape accuracy. Retrieved: 2017.03.22, from: `http://elib.dlr.de/108855/`.

Schott (2015a). Schott PTR70 4th generation datasheet.

Schott (2015b). Setting the benchmark in receiver technology. Technical report, SCHOTT Solar CSP GmbH. `http://www.direc2010.gov.in/pdf/Setting-Benchmark-Receiver-Technology.pdf` accessed 31-March-2015.

Shortis, M. and Johnston, G. (1997). Photogrammetry: an available surface characterization tool for solar concentrators, part ii: assessment of surfaces. *Journal of Solar Energy Engineering*, 119(4):286–291.

Siebert, S., Klonowski, J., and Neitzel, F. (2009). Unmanned Aerial Vehicles (UAVs) - Historische Entwicklung, rechtliche Rahmenbedingungen und Betriebskonzepte.

https://i3mainz.hs-mainz.de/sites/default/files/public/data/Siebert_Klonowski_Neitzel_Oldenburg_2009.pdf. retrieved 2017-3-28.

SolarMillennium (2009). The parabolic trough power plants andasol 1 to 3. Technical report. www.solarmillennium.de/includes/force_download.php?client=1&path=upload/Download/Technologie/eng/Andasol1-3engl.pdf accessed 14-March-2017.

Sony (2011). Nex-7 datasheet. https://www.sony.de/support/de/content/cnt-specs/NEX-7/list retrieved 2017-03-27.

Stanicki, B. (2011). Validierung eines Messystems zur Vermessung von Parabolrinnenkollektoren aus der Luft. Master's thesis, Hochschule Ravensburg Weingarten. Contact/Request Dokument: christoph.prahl@dlr.de.

Steven, M. D. and Unsworth, M. (1977). Standard distributions of clear sky radiance. *Quarterly Journal of the Royal Meteorological Society*, 103(437):457–465.

Stocker, T. (2013). *Summary for Policymakers*, book section SPM. Cambridge University Press, Cambridge and United Kingdom and New York and NY and USA.

Stynes, J. K. and Ihas, B. (2012a). Slope error measurement tool for solar parabolic trough collectors. In *World Renewable Energy Forum, Denver, Colorado*. NREL/CP-5500-54636.

Stynes, K. and Ihas, B. (2012b). Absorber alignment measurement tool for solar parabolic trough collectors. In *ASME 2012 6th International Conference on Energy Sustainability collocated with the ASME 2012 10th International Conference on Fuel Cell Science and Engineering and Technology*, pages 437–447. American Society of Mechanical Engineers.

Trimble (2011). *Datasheet Trimble 5600*. http://trl.trimble.com/docushare/dsweb/Get/Document-8889/12412G_5600_DS_1006_lr.pdf (retrieved 2017.04.01).

Ulmer, Steffen, Heinz, Boris, Pottler, Klaus, Lüpfert, and Eckhard (2006). Slope error measurements of parabolic troughs using the reflected image of the absorber tube. In *Proceedings of the 13th SolarPACES Conference, June 2006, Seville, Spain*.

Ulmer, Steffen, Heinz, Boris, Pottler, Klaus, Lüpfert, and Eckhard (2009). Slope error measurements of parabolic troughs using the reflected image of the absorber tube. *Journal of Solar Energy Engineering*, 131(1):011014.

Ulmer, S., Heller, P., and Reinalter, W. (2008). Slope measurements of parabolic dish concentrators using color-coded targets. *Journal of Solar Energy Engineering*, 130(1):011015.

Ulmer, S., März, T., Prahl, C., Reinalter, W., and Belhomme, B. (2011). Automated high resolution measurement of heliostat slope errors. *Solar Energy*, 85(4):681–687. SolarPACES 2009.

Ulmer, S., Weber, C., Koch, H., Schramm, M., Pflüger, H., Climent, P., and Yildiz, H. (2012). High-resolution measurement system for parabolic trough concentrator modules in series production. In *Proceedings of the 18th SolarPACES Conference, 11. - 14. September 2012, Marrakech, Morocco*.

Valdes, A., Almanza, R., and Soria, A. (2014). Determining the deflection magnitude of a steel receiver from a {DSG} parabolic trough concentrator under stratified flow conditions. *Energy Procedia*, 57(0):341 – 350. 2013 {ISES} Solar World Congress.

Weber, C., Ulmer, S., and Koch, H. (2014). Enhancements in high-resolution slope deviation measurement of solar concentrator mirrors. *Energy Procedia*, 49:2231–2240.

Wendelin, T., May, K., and Gee, R. (2006). Video scanning hartmann optical testing of state-of-the-art parabolic trough concentrators. In *ASME 2006 International Solar Energy Conference*, pages 699–707. American Society of Mechanical Engineers.

Wiesinger, F., Sutter, F., Fernández-García, A., Reinhold, J., and Pitz-Paal, R. (2016). Sand erosion on solar reflectors: Accelerated simulation and comparison with field data. *Solar Energy Materials and Solar Cells*, 145:303–313.

Wilbert, S. (2009). Weiterentwicklung eines optischen Messsystems zur Bestimmung der Formabweichungen von Konzentratoren solarthermischer Kraftwerke unter dynamischem Windeinfluss. Master's thesis, Universität Bonn.

Wolfertstetter, F. (2016). *Auswirkungen von Verschmutzung auf konzentrierende solarthermische Kraftwerke*. PhD thesis, RWTH Aachen.

Wolfertstetter, F., Pottler, K., Alami, A., Mezrhab, A., and Pitz-Paal, R. (2012). A novel method for automatic real-time monitoring of mirror soiling rates. In *Proceedings of the 18th SolarPACES Conference, 11. - 14. September 2012, Marrakech, Morocco*.

Wolfertstetter, F., Pottler, K., Geuder, N., Affolter, R., Merrouni, A., Mezrhab, A., and Pitz-Paal, R. (2014). Monitoring of mirror and sensor soiling with tracs for improved quality of ground based irradiance measurements. *Energy Procedia*, 49:2422–2432.

Wood, R. (1981). Distant observer techniques for verification of solar concentrator optical geometry. Technical report, Technical Report UCRL-53220 and Lawrence Livermore National Laboratory.

WorldBank (2010). Mena assessment of the local manufacturing potential for concentrated solar power (csp) projects. Technical report, World Bank Group, http://www.cspworld.org/resources/mena-assessment-local-manufacturing-potential-concentrated-solar-power-csp-projects. downloaded 2015-03-30.

Wu, Z., Lei, D., Yuan, G., Shao, J., Zhang, Y., and Wang, Z. (2014). Structural reliability analysis of parabolic trough receivers. *Applied Energy*, 123(0):232–241.

WYLER (2013). Compendium - the secrets of inclination measurement. Available at: `http://www.wylerag.com/fileadmin/pdf/compendium/Compendium_eng_2013.pdf`.

WYLER (2016). Manual sensor zerotronic. Available at: `http://www.wylerag.com/fileadmin/pdf/manuel/zero_e.pdf`; retrieved 2017-03-24.

Xiao, J., Wei, X., Lu, Z., Yu, W., and Wu, H. (2012). A review of available methods for surface shape measurement of solar concentrator in solar thermal power applications. *Renewable and Sustainable Energy Reviews*, 16(5):2539 – 2544.

Young, D. (2011). Image correspondences using cross-correlation. MATLAB File Exchange. `http://de.mathworks.com/matlabcentral/fileexchange/27269-image-correspondences-using-cross-correlation` ver 1.3 retrieved 2016-04-30.

Zhu, G. and Lewandowski, A. (2012). A new optical evaluation approach for parabolic trough collectors: first-principle optical intercept calculation. *Journal of Solar Energy Engineering*, 134(4):041005.

Zhu, G. and Turchi, C. (2017). Solar field optical characterization at stillwater geothermal/solar hybrid plant 2. *Journal of Solar Energy Engineering*, 139:031002–031002–10.

Zitova, B. and Flusser, J. (2003). Image registration methods: a survey. *Image and vision computing*, 21(11):977–1000.